DOCTORAL THESIS

# Observation of Neutrino-Induced Cascades via Radio Detection Techniques

## *Modeling the Cosmic-Ray Background Signal*

*Author:*
Simon DE KOCKERE

*Promotors:*
Prof. Dr. Nick VAN EIJNDHOVEN
Prof. Dr. Krijn D. DE VRIES

*A thesis submitted in fulfillment of the requirements for the degree of Doctor of Sciences*

*in the*

Faculty of Sciences & Bio-Engineering Sciences
Interuniversity Institute for High Energies

November, 2024

**Doctoral examination commission**:

Prof. Dr. Jorgen D'Hondt (Chair)
*Vrije Universiteit Brussel (VUB)*

Prof. Dr. Stijn Buitink (Secretary)
*Vrije Universiteit Brussel (VUB)*

Prof. Dr. Nick van Eijndhoven (Promotor)
*Vrije Universiteit Brussel (VUB)*

Prof. Dr. Krijn D. de Vries (Promotor)
*Vrije Universiteit Brussel (VUB)*

Prof. Dr. Anna Nelles
*Deutsches Elektronen-Synchrotron (DESY)*
*Friedrich-Alexander-Universität (FAU)*

Prof. Dr. Ioana Mariş
*Université Libre de Bruxelles (ULB)*

Prof. Dr. Dominique Maes
*Vrije Universiteit Brussel (VUB)*

Prof. Dr. Michael Tytgat
*Vrije Universiteit Brussel (VUB)*

© 2024 Simon De Kockere

All rights reserved. No parts of this book may be reproduced or transmitted in any form or by any means, electronic, mechanical, photocopying, recording or otherwise, without prior written permission of the author.

*To Caroline Pauwels,*
*and everyone else who dares to wonder*

*"Never a dull moment..."*

- Tav, Baldur's Gate 3

# Acknowledgments

Doing a PhD at the IIHE has been an amazing experience, with lots of opportunities and great adventures. But what made these six years so memorial is, above all, the group of people I spent it with. Trying to address all of these people properly would be another thesis by itself, which forces me to reduce these acknowledgments to a mere synthesis of my impressions. What follows is nothing more than a poor attempt at including everyone that made the IIHE such a wonderful place. However, I'm sure that anyone who has spent some time at the institute can easily extrapolate these words, or better yet, doesn't even need to read these acknowledgments to understand the gratitude I feel to have been part of it.

Starting of course with Nick and Krijn, who have been mentioned many times before in sections like these, and with good reason. Supervising PhD students is only one item on your monstrously long tasklists, yet somehow to me it never really felt like that. The office doors were always open, both online and down the corridor, with maybe one or two exceptions, in case a sailing boat or mountain bike got involved. I have learned a lot, not only about cosmic rays and neutrinos, and I greatly appreciate the trust and autonomy that I was given. Despite your busy schedules you happily made time for spontaneous chats, and I have truly enjoyed all the laughs and cheers on those many occasions that presented themselves. A heartfelt thank you! I would also like to explicitly thank all the other members of my PhD jury, who took the time to go through this work thoroughly, and lent their expertise and critical mind to improve this work.

Next, I would like to express my gratitude towards many fantastic people that were part of countless memorable moments at the IIHE, in no particular order. Orazio, always up for a good joke, even though it might at some point be the end of him. Pablo, whose hilarious vlogs have immortalized some amazing adventures, and encouraged everyone to be part of them. Paul, with his seemingly endless focus and determination, never backing down from a challenge. Nadège, who is always happy to share her knowledge on a variety of things, and definitely knows how to throw a wedding party. Yarno, who has faced many empty Friday halls with me, and whose visits to my office I have always appreciated. Jethro, who provides energy in the corridors with a never-ending enthusiasm, even on an excessive skyr diet. Dieder, our captain, whose great sense of humor is only matched by his kindness. Mitja, always willing to help others, and whose analytical mindset and efforts keep the VUB running. Abby, who can easily lift everyone's mood, through the power of Disney songs and cartwheels. I could go on like this forever, but there are so many people I still need to mention, so I'm forced to cut myself short. Many thanks to Chris, Giovanni, Godwin, Katka, Ben, Else, Ruben, Simona, Juanan, Ioana, Stijn, Felix, Simon, Nhan, Vincent, the people from the secretariats and the IT department, the IIHE directors and the technicians, and so many more.

Special thanks goes to Uzair, who is just an amazing guy, and I don't really need to convince anyone of that. His efforts have been vital to the work presented in this thesis, and he never stopped caring for and supporting the project. Thanks for your dedication and your inspiring, ever positive attitude!

Moving on to the people I probably spent most of my time with during the past six years, whether they liked it or not. Dani, who joined the IIHE with me, and whose boundless creativity can be admired on the cover and the back of this work. Few people possess such an honest kindness, care, and interest for others, and I feel extremely fortunate that I got to see that become a part of my life. El Hombre Mares, nowadays El Doctor Mares, and no doubt one day El Profesor Mares. But to most just Quique. Thanks for being an awesome office mate, and for sticking up with me well beyond those walls. Whether it was catching a seven-legged spider or crashing a nautiloid, I always had an amazing time. Rose, who from the start had to deal with Quique and me, and even though we are technically no monkeys, it might definitely at times have felt like a circus. Without you though, the circus would not have been complete. Thanks for joining, and being such a great friend.

During my PhD I was part of several collaborations, which implies many discussions, teamwork, dinners, and drinks. Thanks to all the members I had the pleasure of meeting, both online and in person. In particular, I would like to thank the people of the deployment teams that I got to be part of, and everyone else I met at Summit Station, who made sure my time up there was filled with fun and truly unforgettable moments.

I have done my fair share of teaching at the VUB, for which I could count on some fantastic people to work with. Stefan, Maria, Nicki, Seppe, Jacob, David, Hans, Kris, all the professors that were involved, and again so many more. Thanks for all your time, dedication, and the great collaboration that made our many achievements possible.

And last but not least, I would like to thank my family, who have been vital in many ways to make all of this possible. Hoewel het de afgelopen jaren niet altijd even gemakkelijk was om mijn avonturen te volgen, en dat wellicht voornamelijk aan mij lag, heb ik jullie interesse, steun en toewijding altijd enorm gewaardeerd.

# Abstract

New methods for detecting neutrino-induced particle cascades in polar ice relying on the observation of radio waves seem like a promising solution to extend the sensitivity range of neutrino astronomy towards energies of $10^{16}$ eV and beyond. Using particle accelerators, the Askaryan radio emission from particle cascades in dense media as well as the radar echo from the associated ionization trail have been observed in controlled environments. However, any proof of the viability of these detection techniques in nature has yet to be delivered.

The observed flux of cosmic rays at these energies is significantly higher than that expected for neutrinos, while cosmic rays are also much more likely to interact. Cosmic rays propagating through polar ice therefore seem like a suitable test beam to verify the feasibility of radio detection techniques in nature. Furthermore, the radiation from cosmic-ray air showers propagating through ice can be expected to mimic that of neutrino-induced particle cascades, forming an important background for neutrino observatories that needs to be identified. In addition, radio emission from cosmic-ray events could potentially be used as an in-situ calibration source.

This work presents FAERIE - the Framework for the simulation of Air shower Emission of Radio for in-Ice Experiments. It is the first Monte Carlo simulation framework that simulates the radio emission created during the propagation of cosmic-ray particle cascades through both air and ice, for observers located below the ice surface. It combines the CORSIKA Monte Carlo Code and CoREAS for the simulation in air with a Geant4-based module for the simulation in ice, and includes ray tracing to describe the propagation of radiation through the non-uniform medium. First, the properties of ultra-high-energy cosmic-ray air showers propagating through ice at altitudes common for polar regions are illustrated with simulation results. At zenith angles up to $\sim 30^\circ$ these air showers contain a very energy-dense core, initiating a particle cascade in ice similar to ultra-high-energy neutrinos interacting in the ice. After explaining the underlying algorithms of the radio calculations in the simulation framework, the associated radio emission of such cosmic-ray events is discussed. They show a unique radio footprint, as a result of the combination of the geomagnetic and Askaryan radiation created in air and the Askaryan radiation created in ice. For most observers the in-ice emission will be delayed with respect to the in-air emission, resulting in a double pulse feature in the electric field traces. As a rule of thumb, the peak amplitude of a cosmic-ray signal corresponds to that of a signal from a neutrino-induced particle cascade with an associated neutrino energy that is one order of magnitude lower than that of the primary cosmic ray.

# Samenvatting

Verschillende huidige generatie neutrinotelescopen gebruiken optische modules om neutrino-interacties in ijs of water te detecteren. Zo is er bijvoorbeeld het IceCube Neutrino Obervatory op de Zuidpool, dat een detectievolume van 1 km$^3$ heeft. Om de extreem lage flux van neutrino's met een energie van 10 PeV en meer te kunnen waarnemen, is echter meerdere kubieke kilometers aan detectiemateriaal nodig. Daarom is er nood aan een nieuwe detectiemethode, waarmee op een praktische en kostenefficiënte manier dergelijke gigantische detectievolumes gerealiseerd kunnen worden. Wanneer een neutrino in het ijs interageert, ontstaat er een lawine aan deeltjes die een netto negatieve lading ontwikkelt. De deeltjeslawine zal daardoor radiogolven uitzenden, die een attenuatielengte van $\sim$ 1 km in ijs hebben. Dit wordt Askaryan straling genoemd. Nieuwe generatie neutrinotelescopen in de poolgebieden onderzoeken momenteel de mogelijkheid om neutrino-interacties in ijs aan de hand van deze straling waar te nemen. Daarnaast wordt ook onderzocht of de deeltjeslawines aan de hand van radar kunnen worden bestudeerd, waarbij een telescoop actief radiogolven uitzendt en vervolgens reflecties op het ionisatiespoor van de lawine detecteert. Hoewel deze technieken er al in geslaagd zijn deeltjeslawines in een dicht medium gemaakt met behulp van deeltjesversnellers waar te nemen, heeft geen enkel experiment tot nu toe kunnen aantonen dat de technieken ook in natuurlijke omstandigheden gebruikt kunnen worden.

Natuurlijke Askaryan radiogolven van kosmische deeltjeslawines in de atmosfeer zijn echter wel al waargenomen door verschillende radiotelescopen. Bovendien bevat zo een atmosferische deeltjeslawine op hoogtes van ongeveer 3 km boven de zeespiegel, wat een typische hoogte is voor poolijskappen, nog steeds een grote fractie van de energie van het kosmische deeltje. Deze energie is voornamelijk geconcentreerd in de kern van de lawine. Wanneer deze kern door het ijs propageert, ontstaat er net zoals bij neutrino-interacties in ijs een deeltjeslawine in het ijs. De kans dat kosmische straling interageert is echter veel groter in vergelijking met neutrino's, en de overeenkomstige waargenomen flux is aanzienlijk hoger. Kosmische straling kan dus gebruikt worden als natuurlijke testbundels van hoogenergetische deeltjes om de nieuwe detectietechnieken in de poolgebieden uit te testen. Verder zorgen ze ook voor een belangrijk achtergrondsignaal dat van neutrinosignalen onderscheiden moet worden, en zouden ze ook gebruikt kunnen worden bij de calibratie van de detectorcomponenten.

In dit werk wordt FAERIE voorgesteld, het eerste Monte Carlo simulatieraamwerk voor de radio-emissie van kosmische deeltjeslawines voor radiodetectoren in ijs dat zowel de component in lucht als in ijs simuleert. Het maakt gebruik van de CORSIKA en CoREAS codes voor de component in lucht, en een module ontwikkeld met de Geant4 simulatie toolkit voor de component in ijs. In beide onderdelen wordt ray-tracing toegepast voor de propagatie van de radiogolven. De belangrijkste kenmerken van kosmische deeltjeslawines in ijs worden gekarakteriseerd. Nadien worden de eigenschappen van de radio-emissie van kosmische deeltjeslawines voor waarnemers onder het ijsoppervlak besproken.

# Preface

When hearing the word "astronomy" we often think about large optical telescopes in dry deserts looking up at the night sky, huge dish-shaped radio telescopes in remote areas peering into the unknown, or maybe even the Hubble and James Webb space telescopes sending us mind-blowing pictures of what at a simple glance looks to be a never-ending emptiness. The aforementioned telescopes all study the Universe through the direct detection of different forms of light, or in more scientifically correct terms *electromagnetic radiation*. Since the very beginning of what could be considered astronomy up to today, electromagnetic radiation has been a very useful astrophysical messenger. These messengers only carry part of the story however, and we need to look for other types of messengers as well to understand all the processes and phenomena in our Universe.

The discovery of *cosmic radiation* in the first half of the 20th century could be considered as the start of multimessenger astronomy. The origin and precise nature of these charged atomic nuclei bombarding our atmosphere still puzzles astronomers today, and their observation has pushed the boundaries of astronomy and particle physics alike. However, just like any other messenger, the information that can be obtained from cosmic radiation has its limits, and soon people started thinking about different types of messengers to add to the palette. Especially the question of where the highest-energy cosmic rays are coming from set astronomers on a challenging expedition, leading up to the birth and development of *gamma-ray* astronomy, *neutrino* astronomy and most recently *gravitational-wave* astronomy, concluding what we know today as multimessenger astronomy.

This work could be thrown into the corner of neutrino astronomy, but take that with a grain of salt, as there are no real corners in multimessenger astronomy. Everything is connected, and focusing on one type of messenger without considering the others is sometimes simply impossible. As will be explained in Chapter 2, the same property that makes neutrinos interesting astrophysical messengers is also the main reason they are so challenging to detect. We have gigaton detectors spanning volumes of the order of 1 km to detect astrophysical neutrinos at a satisfying rate, yet even these observatories turn out to be too small to detect neutrinos at the highest energies. New techniques based on the detection of radio emission from neutrino interactions in dense media like ice are being explored, to extend the current neutrino observation sensitivities towards higher energies. In this thesis I will present a Monte Carlo simulation framework designed to study the properties of radio signals from cosmic-ray induced particle cascades in both air and ice, for observers positioned in ice. These signals could serve as a proof of concept for radio neutrino observatories in ice, and are expected to be a significant type of background as well as a potential calibration source for such type of detectors.

In Chapter 1, I will give a summary of what we know today about cosmic rays, focusing on the key concept of cosmic-ray induced air showers and the corresponding radio emission. In Chapter 2, I will explain the connection between cosmic rays and astrophysical neutrinos, and provide an overview of the latest advances in neutrino astronomy. Although neutrino astronomy has made some great progress during the passed few years, I will mainly focus on its current shortcoming at the highest energies, and in this context introduce two distinct radio detection techniques. In Chapter 3, I will describe the existing radio neutrino projects at Summit Station in Greenland in more detail, and summarize the efforts of the 2023 and 2024 field teams that I was part of. In Chapter 4, I will describe the codes of the simulation framework that forms the main topic of this thesis, and use simulation results to illustrate the properties of ultra-high-energy cosmic-ray air showers propagating through polar ice at high altitudes. Finally, in Chapter 5, I will focus on the simulation of the radio emission associated with these air showers, including both the radiation created in air and the radiation created in ice. I will explain the underlying algorithms that were implemented in the simulation codes, and discuss the first results of the framework. Most of the content presented in Chapter 4 and Chapter 5 is published as part of this thesis work in two peer-reviewed articles [1, 2].

# Contents

# Chapter 1

## Cosmic Rays

### 1.1 Introduction

The discovery of cosmic rays is usually ascribed to Victor Hess, who demonstrated in 1912 through several manned hot air balloon flights that the ionization rate of the air increases significantly at higher altitudes [3]. Since the discovery of natural radioactivity by Becquerel in 1896, it was believed that ionization of the air was due to radioactive decay of elements in the ground. However, when Hess was able to show that ionization increases with increasing altitude, a new hypothesis emerged, proposing that the ionization is due to radiation from extra-terrestrial origin. Not much was known about this radiation at the time, hence the general term "cosmic radiation".

Nowadays we know that this cosmic radiation mainly consists of charged atomic nuclei, and to a lesser extent gamma radiation (i.e. high-energy photons) and free electrons. In the literature however you will find that the term "cosmic rays" usually refers to the charged component of cosmic radiation, treating gamma radiation separately, which is the convention that will be followed in this thesis.

Besides the question of what cosmic rays are, we also have to address the question of where cosmic rays come from. As cosmic rays are charged particles, they are deflected by magnetic fields and interact electromagnetically with other particles, making it hard to track down where exactly a single cosmic ray came from once it has reached Earth. A lot of information of where cosmic rays come from is hidden in the cosmic-ray energy spectrum, representing the number of cosmic rays arriving at Earth as a function of their energy. Amazingly, cosmic rays span a wide range of energies, starting at energies of around $10^9$ eV up to $10^{20}$ eV, the latter corresponding to the energy of a casually thrown tennis ball. This by itself already indicates that cosmic rays do not come from one single type of accelerator in the Universe, and consequently are very likely connected to a wide variety of sources spanning orders of magnitude in size and distance.

The cosmic-ray energy flux is shown in Figure 1.1. In general the number of cosmic rays reaching Earth rapidly decreases with increasing energy, following a power law of the form $\frac{dN}{dE} \sim E^{-2.7}$. Around GeV energies we find more than 1000 particles per square meter per second, while around PeV energies that rate has already dropped to 1 particle per square meter per year. At the highest energies, we only find less than 1 particle per square kilometer per century [4]. There is however a finer structure to the spectrum, most notably the bump around $E = 10^6 - 10^7$ GeV and the dent around $E = 10^9 - 10^{10}$ GeV, usually referred to as respectively the knee and the ankle of the energy spectrum. These features indicate a transition from one main class of sources to another.

A lot of evidence indicates that cosmic rays with an energy below the knee of the spectrum originate from within our own galaxy, the Milky Way, undergoing acceleration for example through shock waves created during supernova explosions

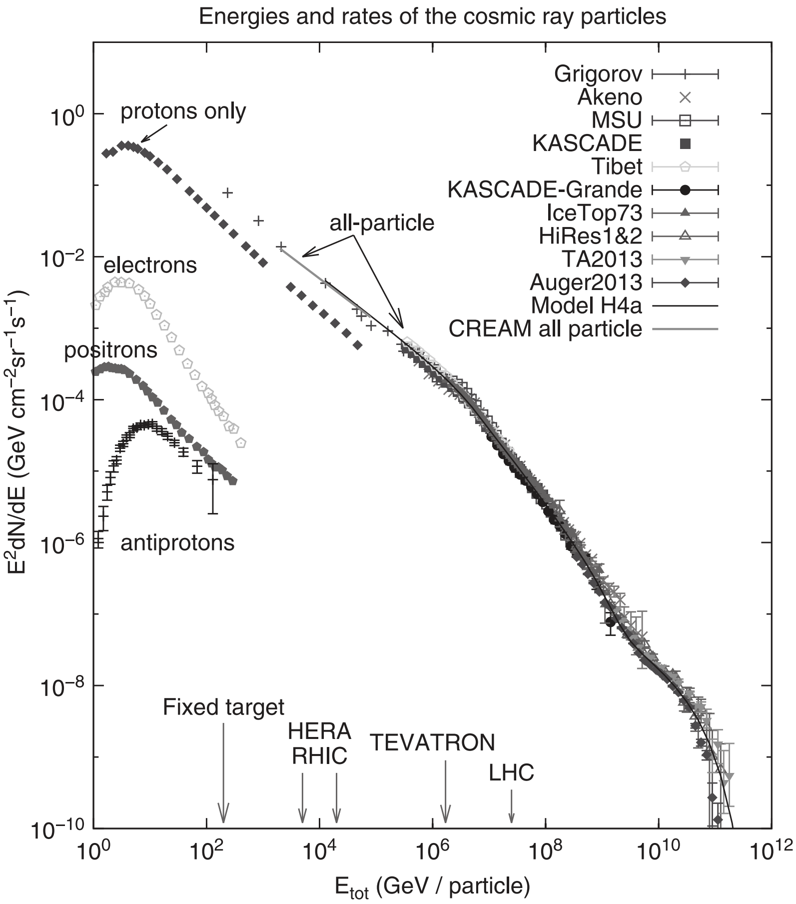


FIGURE 1.1: The combined cosmic-ray flux measurements from different observatories [5]. Indicated below are the center-of-mass energies produced in accelerators on Earth for comparison.

and in supernova remnants [4–6]. Once past the knee the spectrum becomes more inclined, which suggests that at this point galactic supernovae have reached their limit of acceleration, or that cosmic rays are now so energetic they start to leak out of the galaxy. The ankle represents a slight revival of the flux, indicating that a less intense but more persistent extra-galactic component starts to dominate the spectrum. For possible cosmic-ray sources in this energy range we typically look at some of the most energetic processes in the Universe, like gamma-ray bursts (GRBs) and active galactic nuclei (AGN).

Interestingly, starting at an energy around $5 \times 10^{10}$ GeV, protons propagating through the cosmic microwave background (CMB) undergo $\Delta^+$-production [7, 8]. Additionally, at these energies nuclei interact with photons from the CMB and the cosmic infrared background, leading to photodisintegration [9–11]. This implies that the spectrum at the highest energies should have a natural cut-off, referred to as the GZK effect, as this effect was initially predicted for protons by Greisen, Zatsepin and Kuzmin. Recent observations however suggest that starting around an energy of $2 \times 10^9$ GeV the fraction of heavy nuclei contributing to the cosmic ray flux increases, indicating that the steepening at the end of the energy spectrum is a combination of the GZK effect and the associated cosmic accelerators reaching their limits [12, 13].

## 1.2 Air Showers

Low-energy cosmic rays are abundant and can therefore be detected directly using small detectors mounted on balloons and satellites, avoiding interaction of the cosmic rays in the atmosphere. Starting at energies around $10^5$ GeV, the flux of cosmic rays has dropped to a level where we need much larger detection areas in order to have a satisfying detection rate. Mounting these to balloons or satellites is simply impossible, meaning we are bound to stay on the ground and study cosmic-ray air showers instead. Interestingly the same scenario applies for gamma-ray astronomy, where low-energy gammas can be observed using satellites, but high-energy gammas have to be studied through similar air showers.

A cosmic ray or gamma entering Earth's atmosphere will interact with one of the many available nuclei, producing a cascade of secondary particles, called an air shower. By detecting these secondary particles at ground level, we can reconstruct the properties of the air shower and the primary particle that initiated it. A useful illustration of how the properties of the primary particle affect characteristics of the particle cascade as a whole is given by the Heitler model for electromagnetic air showers and the Heitler-Matthews model for hadronic air showers, which give an oversimplified but intuitive picture of air shower development [14, 15].

### 1.2.1 Electromagnetic Air Showers

Figure 1.2a shows a simple diagram of an electromagnetic air shower, i.e. a particle cascade initiated by a photon. The Heitler model assumes only two possible interactions, $e^+e^-$ pair production by a single photon and bremsstrahlung by a single $e^+/e^-$. Both processes start with one particle and end up with two, dividing the energy of the initial particle equally. Furthermore, it assumes the depth travelled before interacting is the same for all electrons, positrons and photons in the particle shower. As illustrated by the diagram, according to this model the number of particles $N$ in the particle shower after $n$ splitting steps should be $N = 2^n$.

The energy of electrons and positrons traveling through a medium is given by $E = E_0 e^{-X/\lambda_r}$, where $E_0$ is its primary energy, $X$ the depth traveled through the

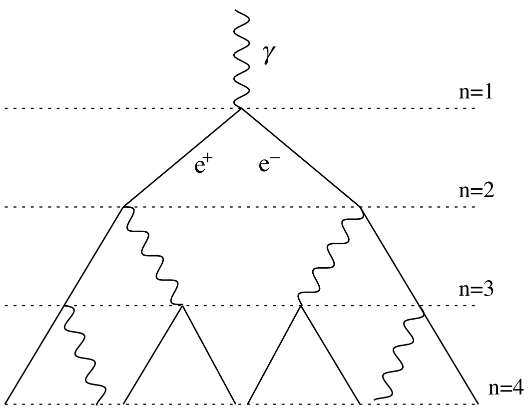


(A)

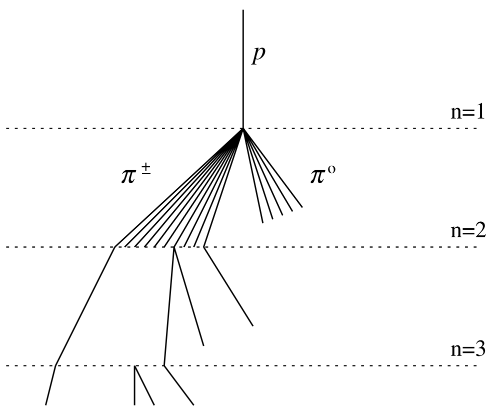


(B)

FIGURE 1.2: A simple diagram of (A) an electromagnetic air shower initiated by a photon and (B) a hadronic air shower initiated by a proton, modified from [14]. For simplicity not all particles in the hadronic shower are shown after the $n = 2$ level, and the electromagnetic subshowers following $\pi^0$ decay are omitted as well.

medium and $\lambda_r$ the radiation length, both typically expressed in units g/cm$^2$. Following this relation, we see that electrons and positrons will lose half of their energy after traveling a depth $d = \lambda_r \ln 2$. Assuming this is a good approximation for the mean free path of pair production by a high-energy photon as well, the depth $d$ can be used as the splitting depth between two vertices in the diagram. This means that after $n$ splitting steps the total depth covered by the shower is $X = n\lambda_r \ln 2$, and the total number of particles in the shower at that point is given by

$$N = 2^n = e^{n \ln 2} = e^{X/\lambda_r}. \tag{1.1}$$

The particle shower will reach a maximum number of particles when the energy of the particles drops below the critical energy $E_c$, at which point collisional energy losses begin to dominate over radiative energy losses. With $E_p$ as the energy of the primary photon initiating the electromagnetic cascade, conservation of energy means that the maximum number of particles in the shower is given by

$$N_{\text{max}} = E_p/E_c. \tag{1.2}$$

Combining Equation 1.1 and Equation 1.2, we find that the depth $X_{\text{max}}$ of the shower at this point follows the relation

$$X_{\text{max}} = \lambda_r \ln(N_{\text{max}}) = \lambda_r \ln(E_p/E_c). \tag{1.3}$$

Equations 1.2 and 1.3 show two important features of electromagnetic air showers that are correctly demonstrated by the model, even though it is somewhat oversimplified. First of all we see that the total number of particles in the shower is proportional to the energy of the primary photon $E_p$. Secondly, we see that the depth at which the shower reaches its maximum number of particles scales logarithmically with $E_p$. This nicely illustrates how the properties of the single particle that initiates the particle cascade influence global air shower characteristics like $N_{\text{max}}$ and $X_{\text{max}}$.

### 1.2.2 Hadronic Air Showers

Figure 1.2b shows a simple diagram of a hadronic air shower, i.e. a particle cascade initiated by a proton. Unlike photons, protons will interact strongly with the air nucleus, and the model assumes that it will create a number of charged pions ($\pi^{\pm}$) given by $N_{\text{ch}}$, and a number of neutral pions ($\pi^0$) given by $\frac{1}{2}N_{\text{ch}}$. The neutral pions will quickly decay to photons, initiating electromagnetic subshowers. The charged pions will continue the hadronic part of the shower, interacting again with air nuclei after traveling a certain distance and creating the next generation of pions. As such the primary energy $E_p$ of the proton is divided into a hadronic channel and an electromagnetic channel.

What we referred to as the splitting depth for the electromagnetic air shower is now replaced by the interaction depth of strongly interacting particles, given by a similar relation $d = \lambda_I \ln 2$. The electromagnetic critical energy $E_c$ indicating the point where collisional energy losses start to dominate, now becomes the critical energy $E_{c,\pi}$ below which charged pions will start to decay into muons instead of interacting with the air nuclei. These muons will then propagate further to the ground level.

According to the model, the number of charged pions after $n$ interaction steps is given by $N_\pi = (N_{\text{ch}})^n$. Together they will carry an energy of $(2/3)^n E_p$, with the remainder of the energy being contained in the electromagnetic part of the shower.

The energy per charged pion at this point is then

$$E_\pi = \frac{(2/3)^n E_p}{(N_{\text{ch}})^n} = \frac{E_p}{\left(\frac{3}{2}N_{\text{ch}}\right)^n}, \tag{1.4}$$

while the energy in the electromagnetic part of the shower is given by

$$E_{\text{em}} = E_p\left(1 - (2/3)^n\right). \tag{1.5}$$

After $n_c$ interaction steps the energy per pion drops below the critical energy $E_{c,\pi}$, which means

$$\frac{E_p}{\left(\frac{3}{2}N_{\text{ch}}\right)^{n_c}} = E_{c,\pi}. \tag{1.6}$$

The number of interaction steps is therefore given by

$$n_c = \frac{\ln\left(E_p/E_{c,\pi}\right)}{\ln(\frac{3}{2}N_{\text{ch}})}. \tag{1.7}$$

With a value of $E_{c,\pi} = 20$ GeV, we find values for $n_c$ in the range $3-6$ for primary energies between $10^{14} - 10^{17}$ eV. Using $\ln(N_\pi) = n\ln(N_{\text{ch}})$ the maximum number of charged pions can be written as

$$N_\pi = \left(\frac{E_p}{E_{c,\pi}}\right)^\alpha = N_\mu, \quad \alpha = \frac{\ln(N_{\text{ch}})}{\ln\left(\frac{3}{2}N_{\text{ch}}\right)}, \tag{1.8}$$

where $N_\mu$ corresponds to the number of muons that will reach ground level. Comparing Equation 1.8 with Equation 1.2, we see that the relation between the maximum number of charged pions in the hadronic air shower and the primary energy of the proton is slightly more complicated than that between the maximum number of particles in the electromagnetic shower and the primary energy of the photon. Especially since $N_{\text{ch}}$, and therefore $\alpha$, depends on the energy of the pion, which changes during the shower development. Equation 1.8 should be taken with care, as the derivation above assumes a constant value for $N_{\text{ch}}$.

Usually $X_{\text{max}}$ is defined as the slant depth of the particle shower at which the electromagnetic component ($e^+$, $e^-$, $\gamma$) reaches its maximum number of particles, also in the case of a hadronic air shower. To find an expression for $X_{\text{max}}$, we would have to take into account all the different electromagnetic subshowers, with different numbers of showers starting at different depths and different starting energies. As a simple approach to this complex problem we will only take into account the first generation of subshowers.

The first interaction of the proton primary happens at a depth of $d = \lambda_I \ln 2$, creating $\frac{1}{2}N_{\text{ch}}$ neutral pions. Each of those pions will quickly decay and create two photons, which means the first generation of subshowers starts off with $N_{\text{ch}}$ photons, each with an energy of $\frac{1}{3}E_p/N_{\text{ch}}$. Combining this with Equation 1.3 we find

$$X_{\text{max}} = \lambda_I \ln 2 + \lambda_r \ln\left(\frac{E_p}{3N_{\text{ch}}E_c}\right). \tag{1.9}$$

From here on we can generalize the results to any nucleus with mass number $A$ as primary particle of the air shower. As the energy during the first interaction of the primary is typically much higher than the binding energy of the different nucleons, we can approximate the nucleus as $A$ independent nucleons with an energy $E_p/A$.

From Equation 1.8 we can derive the total number of expected muons

$$N_\mu = A\left(\frac{E_p/A}{E_{c,\pi}}\right)^\alpha = A^{1-\alpha}\left(\frac{E_p}{E_{c,\pi}}\right)^\alpha, \tag{1.10}$$

and from Equation 1.9 we find that $X_{\max}$ is given by

$$X_{\max} = \lambda_I \ln 2 + \lambda_r \ln\left(\frac{E_p/A}{3N_{\mathrm{ch}}E_c}\right). \tag{1.11}$$

Although Equations 1.10 and 1.11 follow from some limiting approximations, the Heitler-Matthews model for hadronic showers again gives us an intuitive picture of how air shower quantities like $N_\mu$ and $X_{\max}$ are influenced by the energy and the mass of the primary particle that initiated the particle cascade.

Important to note is that at primary energies of $10^{17}$ eV and higher, the first interactions in the shower happen at energies well beyond the center-of-mass energies of particle accelerators on Earth. On top of that, detectors at accelerators are usually not optimized to study particles moving forwards after collision, which is the relevant regime for air shower physics. The hadronic models used to describe the first interactions are therefore not well confined, and carry significant theoretical uncertainties that are hard to estimate [16].

### 1.2.3 Detection Techniques

The models discussed above clearly illustrate that determining global air shower characteristics can give information about the properties of the primary particle. However, in practice, large particle surface detectors are fixed to a certain altitude and can therefore only directly measure the air shower particles at that altitude, which is often referred to as the particle footprint of the shower. Furthermore, at higher energies, these footprints typically span areas of the order of several km$^2$ to hundreds of km$^2$, meaning observatories might only sample a small part of the total footprint. Given these constraints, it requires some special techniques to determine the primary particle's properties using particle detector arrays. Nowadays, many different detection techniques are used to study air showers, supplementing the detection of particles with the detection of atmospheric Cherenkov light, fluorescence light and radio emission [15, 17]. As the radio emission from air showers is particularly relevant for this thesis, it will be covered separately in Section 1.3. A lot can be learned from studying air showers, but in terms of cosmic-ray astronomy the two most important goals are to determine the type of primary particle that initiated the shower, and the primary energy with which it entered the atmosphere.

#### Particle detectors

To sample the particle footprint of air showers, observatories use arrays of scintillator or water-Cherenkov detector units, with the specific dimensions of the array determined by the energy of the air showers to be studied. The detector spacing that is used can vary from $\sim$ 15 m to cover a relatively small surface of the order of $\sim$ 10 km$^2$ like the KASCADE-Grande experiment in Karlsruhe, Germany [21], to more than 1 km spacing to create vast arrays of the order of $\sim$ 1000 km$^2$ like the particle detector arrays of the Telescope Array project in Utah, USA [20] and the Pierre Auger Observatory in western Argentina [22] (Figure 1.3a).

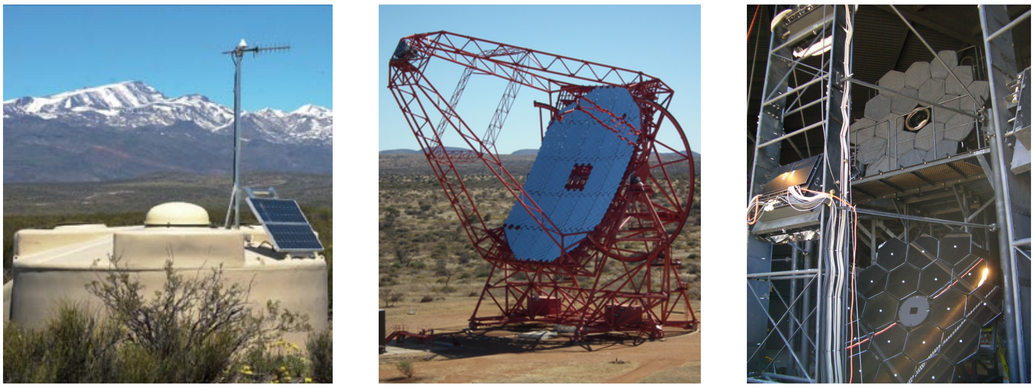

(A) (B) (C)

FIGURE 1.3: (A) One of the many water tanks from the particle detector of the Pierre Auger Observatory [18], (B) the 28 m H.E.S.S. II atmospheric Cherenkov telescope [19], (C) telescopes and cameras from a fluorescence detector station of the Telescope Array project [20].

To distinguish cosmic-ray air shower events from background events, these observatories look for time coincidences of signals in clusters of nearby detector units. From the differences in arrival time of the particles in the different units the arrival direction of the air shower can be determined. The core position of the footprint can be found by fitting a lateral distribution function to the signals of the different detector units. From the lateral distribution function the energy of the primary particle can be reconstructed, by evaluating the distribution at the distance for which the fit of the distribution is the most stable. This value is then compared to simulated events or to events that have been calibrated with other types of detectors.

Determining the primary particle type can be done by measuring the number of muons and electrons reaching ground level. The number of muons is the lowest in photon induced air showers, and increases with increasing primary mass for hadronic air showers, as predicted by Equation 1.10. On the other hand, the number of electrons is the highest in photon induced air showers, and decreases with increasing primary mass for hadronic air showers. Following Equation 1.11, a higher mass number $A$ for the same primary particle energy means the shower will reach shower maximum higher up in the atmosphere, preventing more electrons from reaching ground level.

Particle detectors in principle have a 100% duty cycle, since clouds, sunlight or moonlight do not affect the performance of the detector units.

### Atmospheric Cherenkov light detectors

Charged particles that are moving through a medium faster than the speed of light in that medium emit Cherenkov radiation [23]. Air showers developing in the atmosphere will emit enough Cherenkov photons to be detectable in a wide range of energies. This can be done by either imaging atmospheric Cherenkov telescopes (IACTs) like the H.E.S.S. telescopes in the Khomas highlands of Namibia [24] (Figure 1.3b), or non-imaging Cherenkov detectors like the units from the Tunka Array in Siberia, Russia [25]. IACT's record images of the Cherenkov radiation emitted in the atmosphere, and with enough resolution the distinction between the radiation from the primary particle itself and that of the air shower can be made. Combining the images of multiple IACT's, typically spaced $\sim$ 100 m apart, the arrival direction and the energy of the primary particle can be reconstructed. IACT's are especially efficient in distinguishing photon induced air showers from hadron induced air showers, taking advantage of the more irregular structure of hadronic showers due to the different electromagnetic subshowers from $\pi^0$ decays.

Non-imaging Cherenkov detectors operate more or less like particle detectors, sampling the Cherenkov light footprint of the air shower and fitting a lateral distribution function to the signals of the different detector units. The lateral distribution can then be used to determine the primary energy and the depth of shower maximum, the latter of which relates to the mass of the primary particle.

Since these types of detectors rely heavily on the direct detection of light, they can only operate during clear, moonless nights, which reduces their cycle duty to about $10-15\%$. They are also particularly sensitive to atmospheric conditions, which need to be monitored continuously.

#### Fluorescence detectors

At primary energies above $10^{17}$ eV, the air shower passing through the atmosphere will excite nitrogen molecules, which in turn produce fluorescence light that can be detected on ground level by fluorescence detectors, like the ones operated by the Pierre Auger Observatory and the Telescope Array project (Figure 1.3c). These detectors work somewhat similar to IACT's. They record images of the fluorescence light, which are then used to determine the orientation of the shower axis. A good reconstruction accuracy can be achieved by either using multiple fluorescence detectors, typically separated by distances of the order of 10 km or more, or by independently determining the arrival time of the air shower front at the ground using particle detectors. Once the shower axis orientation is known, the observed light intensities can be used to reconstruct the longitudinal shower profile, i.e. the number of charged particles in function of depth, which relates to the mass of the primary particle. Nowadays also the Cherenkov radiation produced in the atmosphere is measured and provides extra information during reconstruction.

As illustrated by Equation 1.5, around 90% of the energy of a cosmic-ray induced particle cascade is contained in the electromagnetic part of the shower, which is deposited in the atmosphere in the form of ionization energy. This in turn scales with the fluorescence yield, which means a fluorescence detector can perform a calorimetric measurement of air shower cascades and provide a good direct estimator of the energy of the primary particle [26]. The other 10% of the primary energy will be in the hadronic part of the particle shower. Uncertainty on the primary particle mass and the details of the hadronic interactions in the atmosphere translate to some uncertainty on the primary energy of the order of a few percent.

Also these type of detectors rely heavily on the direct detection of light, and just like atmospheric Cherenkov light detectors their cycle duty is therefore only $10-15\%$.

## 1.3 Radio Emission from Air Showers

Particularly relevant for this work is the radio emission of cosmic-ray air showers, created during their propagation through the atmosphere. The existence of radio emission from cosmic-ray air showers was first predicted about 70 years ago [27, 28], and confirmed shortly after [29], but the applications for cosmic-ray physics at the time were limited due to technological challenges [30]. The rise and further development of digital technology during the 21st century have led to a revival of the field, with radio arrays like LOPES in Karlsruhe, Germany [31], CODALEMA in Nançay, France [32], AERA in Argentina, part of the Pierre Auger Observatory [33] and LOFAR, of which the core is located in Exloo, The Netherlands [34] now matching the precision of other established detection methods.

By far most of the radiation comes from the electromagnetic component of the particle shower at the point where the total number of electrons in the shower is the highest, which is the most common definition of $X_{\mathrm{max}}$. Regarding the lateral dimension of the cascade, typically only the first few meters from the shower axis are relevant, which contains most of the high-energy electrons [35]. Furthermore, at any moment in time during the shower development, most of the particles in the cascade are located in the shower front. This could be visualized as a pancake moving down in the direction of the shower axis, with a typical thickness of the order of a meter [36]. This implies that radiation at wavelengths of several meters, i.e. at frequencies below 100 MHz, is coherent and therefore strongly amplified. For incoherent radiation, such as the emission observed by Cherenkov light detectors, the intensity of the radiation is proportional to the number of charges $N$ in the particle shower. For coherent radiation however the intensity of the radiation scales with $N^2$. This means that for air showers initiated by high-energy cosmic rays, the intensity of coherent radiation will be much higher compared to incoherent radiation [37]. In reality the picture is a bit more complicated, as the apparent thickness of the pancake increases with increasing observation angle with respect to the shower axis. Radio emission further away from the shower axis is therefore only coherent at lower frequencies. Furthermore, also the propagation of the cascade front needs to be taken into account, since it moves faster than the speed of light in the atmosphere. Full coherence is only achieved at a specific angle from the shower axis, the so-called Cherenkov angle, which is discussed in more detail in Section 1.3.3 [38].

The radio emission of cosmic-ray air showers consists of two main components, the geomagnetic component and the Askaryan component [30]. Both components are discussed in more detail below and summarized in Figure 1.4.

### 1.3.1 Geomagnetic Emission

Charged particles in the cosmic-ray air shower travelling through the atmosphere will interact with the magnetic field of the Earth. The interaction is determined by the Lorentz force, given by

$$\vec{F} = q\vec{v} \times \vec{B}, \tag{1.12}$$

with $q$ the charge of the particle, $\vec{v}$ its velocity and $\vec{B}$ the magnetic field of the Earth. The direction of the force depends on the sign of the charge of the particle, which means the electrons in the shower will start to drift in one direction, while the positrons will start to drift in the opposite direction. Since the amount of electrons and positrons changes during the shower development, this leads to a time-varying transverse current in the air shower. Just like a time-varying current in a dipole antenna, this will create radio emission polarized in the direction of the current. This is shown on the left of Figure 1.4.

The amplitude of the geomagnetic emission is proportional to the transverse current and therefore the average drift velocity of the charges in the shower [36]. This in turn is proportional to the magnitude of the Lorentz force $|\vec{F}| = qvB\sin(\alpha)$, and therefore to the magnitude $B$ of Earth's magnetic field and $\sin(\alpha)$, with $\alpha$ the angle

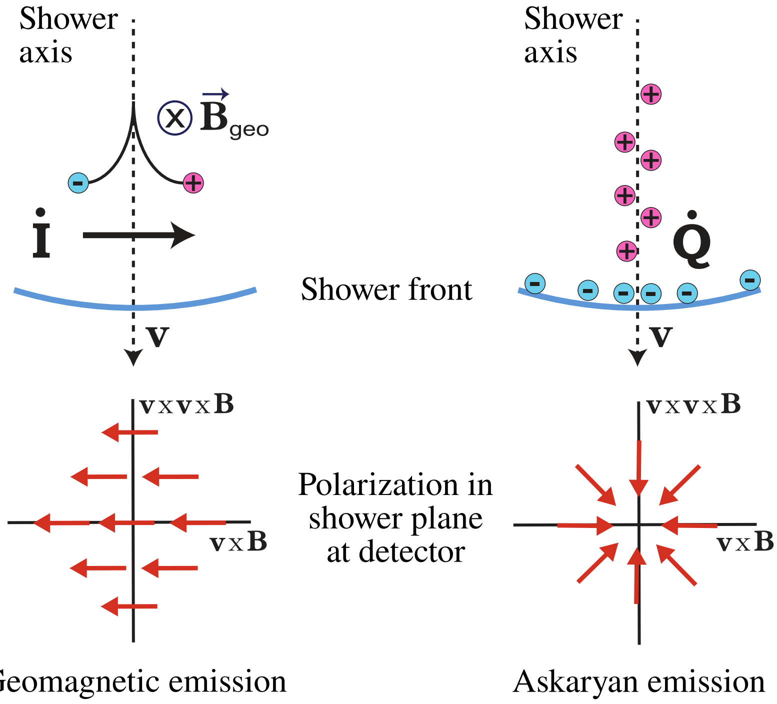


FIGURE 1.4: A summary of the two main components of the radio emission of cosmic-ray air showers: geomagnetic emission (left) and Askaryan emission (right), modified from [39]. The illustrations on the bottom show the polarization in the plane perpendicular to the shower axis.

between the velocity of the particles in the shower and the geomagnetic field. Since the particles in the cascade have very high forward momentum, this angle corresponds to the angle between the shower axis and the geomagnetic field. In general this proportionality to $\sin(\alpha)$ creates an asymmetry in arrival direction of air shower events detected by radio observatories, as demonstrated in Figure 1.5. The geomagnetic emission from particle cascades coming from the direction of the magnetic field will have a lower amplitude compared to showers coming from other directions, and are therefore harder to detect. This property can be used to verify that a set of events are indeed cosmic-ray air shower signals.

The amplitude of the geomagnetic component scales with the drift velocity of the charges in the cascade front [36]. Inclined showers reach their shower maximum higher up in the atmosphere, since they have traversed more medium when reaching a given altitude compared to vertical showers. Consequently, since the density of the atmosphere is lower at higher altitudes, the drift velocity of the charges at shower maximum is higher and the corresponding geomagnetic emission will be stronger [41]. However, for a given observation plane the radio emission from inclined showers will be spread out over a larger surface, since firstly the emission is created higher up in the atmosphere, and secondly the radio footprint will be extended into an ellipse. Furthermore, due to the lower density the particle cascade will be elongated, leading to loss of coherence and therefore decreasing the amplitude of the radio emission [42].

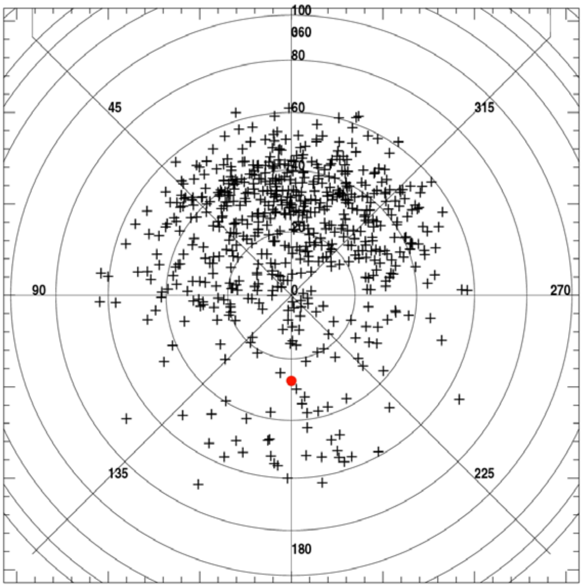


FIGURE 1.5: A sky map of events detected by CODALEMA. The crosses indicate the arrival direction of the detected events, the red dot shows the direction of the local geomagnetic field [40]. The zenith is at the center of the figure and North corresponds to an azimuth angle $\phi = 0$ (top). There is a clear North-South asymmetry in the amount of detected events.

### 1.3.2 Askaryan Emission

During the development of the particle shower in the atmosphere, positrons created during pair production can annihilate with electrons in air molecules. Furthermore, photons can ionize molecules, creating additional free electrons joining the cascade. Both effects together cause the development of a negative charge excess in the shower front, in particular close to the shower axis, of around $20 - 30\%$ of the total number of electrons and positrons. The charge excess varies over time, and therefore generates radio emission. This was first predicted by Askaryan in 1962, which is why we call this the Askaryan effect [27]. For an observer far away from the shower axis, the Askaryan effect could be described using a point-like charge whose strength changes as a function of time. The corresponding radio emission is radially polarized, with no contribution in the center of the shower footprint [36]. This is shown on the right of Figure 1.4. The amplitude of the Askaryan component scales with the magnitude of the charge excess in the shower front [36].

For cosmic-ray air showers the geomagnetic emission usually dominates over the Askaryan emission. The relative strength of the amplitude of the Askaryan radiation to that of the geomagnetic radiation depends on the magnitude of the geomagnetic field and the direction of the shower axis, since both affect the amplitude of the geomagnetic emission. Typical values of the relative strength are around $5 - 20\%$ [30].

### 1.3.3 Cherenkov Cone

As already mentioned in Section 1.2.3, charged particles moving through a dielectric medium faster than the speed of light in that medium will create Cherenkov radiation [23]. The existence of this radiation can be derived directly from Maxwell's equations for electromagnetism, for the first time demonstrated by Ilya Frank and Igor Tamm in 1937 [43]. Cherenkov radiation is emitted in a cone around the charged particle, determined by the Cherenkov angle $\theta_c$

$$\cos\theta_c = \frac{c}{nv}\,, \tag{1.13}$$

with $c$ the speed of light in vacuum, $n$ the index of refraction of the medium and $v$ the velocity of the particle [44]. In case of a particle traveling at the speed of light in vacuum, this relation simplifies to

$$\cos(\theta_c) = \frac{1}{n}. \tag{1.14}$$

To get an intuitive understanding of where this so-called Cherenkov cone comes from, Equation 1.14 can be derived as follows. Figure 1.6 shows a charged particle moving with a velocity $v = c$ through a dielectric medium. The time at which the particle is in point A we define as $t = 0$. The propagation speed of electromagnetic waves though the medium is determined by the index of refraction of the medium, and is given by $c/n$. The time $t_A$ at which the observer, indicated by the black square in the figure, receives the electromagnetic radiation emitted in A is

$$t_A = \frac{nd_A}{c}. \tag{1.15}$$

After traveling a distance $\Delta x$, the emitter will reach point B. For the time $t_B$ at which the observer receives the electromagnetic radiation emitted in B, we find

$$t_B = \frac{\Delta x}{c} + \frac{nd_B}{c}. \tag{1.16}$$

The time difference between both arrival times is therefore

$$\Delta t = t_B - t_A = \frac{\Delta x}{c} + \frac{n}{c}\left(d_B - d_A\right), \tag{1.17}$$

while the time difference between both emission times is simply

$$\Delta t' = \frac{\Delta x}{c}. \tag{1.18}$$

This leads us to the equation

$$\frac{\Delta t}{\Delta t'} = 1 + \frac{n}{\Delta x}\left(d_B - d_A\right). \tag{1.19}$$

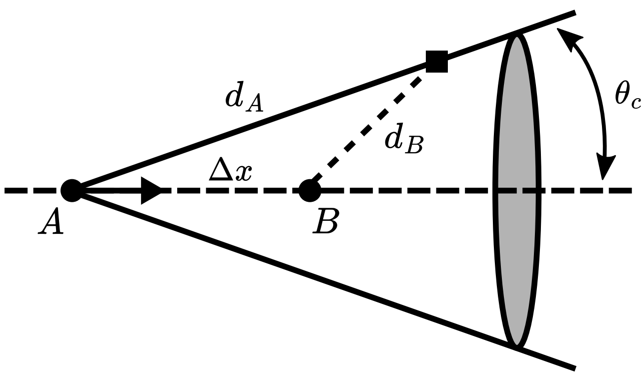


FIGURE 1.6: A sketch of the Cherenkov emission of a charged particle.

From the law of cosines we know

$$d_B = \sqrt{d_A^2 + \Delta x^2 - 2d_A \Delta x \cos(\theta_c)} = d_A \left(1 - \frac{\Delta x}{d_A}\cos(\theta_c) + \mathcal{O}^2\left(\frac{\Delta x}{d_A}\right)\right). \quad (1.20)$$

Combining this with Equation 1.19 and taking the limit $\Delta x \to 0$, we get

$$\frac{dt}{dt'} = 1 - n\cos(\theta_c). \quad (1.21)$$

Following this relation, we see that the expression for the Cherenkov angle given by Equation 1.14 corresponds to an observer time interval $dt = 0$. The Cherenkov angle is therefore the angle at which the radiation emitted over a finite time interval $dt'$ arrives at a single point in time at the observer, which is why the radiation at this angle is the strongest, and coherent up to the highest frequencies. Besides being an intuitive interpretation of the Cherenkov cone, this derivation also underlines an important concept. The existence of the Cherenkov cone is a purely geometric effect. At no point during the derivation anything about the exact nature of the emission was assumed, besides the fact that it propagates at a speed $c/n$ through the medium. Indeed, an analogous derivation can be made for acoustic waves, i.e. sound, which leads to the explanation of the sonic boom.

Since the particles in cosmic-ray air showers move faster than the speed of light in air, at approximately the speed of light in vacuum, the radio emission from these particle cascades will be the strongest and most coherent on the Cherenkov cone following Equation 1.14. With an index of refraction only slightly larger than 1, this leads to a Cherenkov angle in the atmosphere of around 1° [38, 41]. It is important however to keep in mind that the radio emission from air shower cascades is mostly geomagnetic and Askaryan emission, and not Cherenkov emission at lower frequencies.

### 1.3.4 Footprint

The radio footprint of a cosmic-ray air shower is characterized by the interference of the geomagnetic emission and the Askaryan emission [36]. As mentioned in Section 1.3.3, the Cherenkov angle in air is around 1°, which determines the relevant scale of the radio footprint. To illustrate, for a vertical shower reaching $X_{\mathrm{max}}$ around an altitude of 5 km, the Cherenkov angle corresponds to a distance of about $85 - 90$ m from the shower axis at sea level. The exact shape of the observed footprint depends on a variety of parameters, like the distance to $X_{\mathrm{max}}$ of the observer plane, the arrival direction of the particle shower and the frequency band in which the observations are made. Often the radio footprint of a cosmic-ray air shower is visualized by either showing the total electric field strength or some form of energy density as a function of the coordinates in the shower plane, i.e. the plane perpendicular to the shower axis.

In general, the interference of the geomagnetic emission and Askaryan emission leads to a kind of bean shape, which follows directly from the superposition of both pictures in Figure 1.4. The geomagnetic component is polarized along the direction of $\vec{v} \times \vec{B}$ over the whole footprint, and is amplified on the side of the Cherenkov ring where the polarization of the Askaryan emission is aligned. On the other side of the ring, the radial polarization of the Askaryan emission opposes that of the geomagnetic emission, leading to destructive interference between both components.

Figure 1.7 shows a radio footprint of a cosmic-ray air shower measured by the low-band antennas of LOFAR (10 − 90 MHz), together with a radio footprint of a cosmic-ray air shower measured by the high-band antennas of LOFAR (110 − 190 MHz). Both cases feature the bean-shape pattern due to the interaction between the geomagnetic and the Askaryan emission. Comparing the two measurements nicely demonstrates the dependence of the measured footprint on the frequency band in which the observation is made. At higher frequencies coherence is only achieved closer to the Cherenkov cone, which is why the Cherenkov ring is more clearly visible in the second footprint.

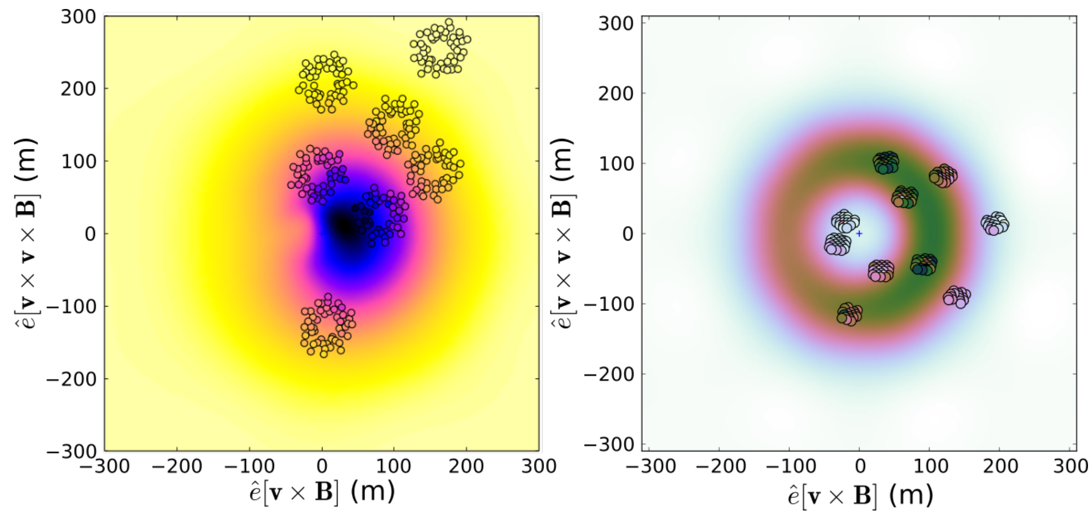


FIGURE 1.7: The radio footprints of two cosmic-ray air showers measured by LOFAR. The color scale indicates power and is given in arbitrary units. The circles on the footprint show the measured signals, the background map shows the best fitting simulation. Left: a footprint measured with the low-band antennas of LOFAR (10 − 90 MHz), modified from [45]. Right: a footprint measured with the high-band antennas of LOFAR (110 − 190 MHz), modified from [46].

### 1.3.5 Determination of Shower Properties

#### Direction

The arrival direction of a cosmic-ray air shower cascade can be determined by comparing the arrival times of the radio signal in different antenna stations. Simple triangulation implies a plane-wave model for the radio wave front, and leads to accuracies of the order of 2° [30]. This can be further improved by using more complicated wave front models.

As already mentioned in Section 1.1, the arrival direction of a single cosmic ray by itself does not contain much information, as cosmic rays are charged particles and therefore deflect in magnetic fields and interact electromagnetically with other particles. It is however an important parameter during the reconstruction of the primary energy and the value of $X_{\max}$ of the particle cascade, as outlined below.

#### Primary energy

Similar to the yield in fluorescence detectors, the strength of the observed radio emission depends on the energy contained in the electromagnetic part of the particle cascade, and can therefore be used to estimate the energy of the primary particle [30].

The absorption of the radio emission by the atmosphere is negligible, so as long as the observer plane is well beyond shower maximum and the measured footprint is sufficiently large, determining the total radiated energy by integrating over the footprint should correlate well with the energy in the electromagnetic part of the shower. Alternatively, the amplitude of the measured electric field at a specific distance from the shower axis can be used, typically close to the Cherenkov ring in the observer plane. This is similar to reconstruction techniques used by particle detectors and non-imaging atmospheric Cherenkov telescopes.

The strength of the geomagnetic emission depends on the geomagnetic angle $\alpha$ of the particle cascade, i.e. the angle between the shower axis and the geomagnetic field, which introduces an uncertainty in both methods. Typical values for the precision and accuracy achieved on energy reconstruction by radio experiments is around $10 - 20\%$, while uncertainties on the mass of the primary particle and the hadronic interaction models lead to a systematic uncertainty of the order of 10%, which is similar to other detection techniques.

Figure 1.8a shows the radiation energy for a set of air shower events measured by AERA, the antenna array integrated in the Pierre Auger Observatory, including a correction for the geomagnetic angle. For each event the primary particle energy is reconstructed by the surface detectors of Auger. Figure 1.8b shows the radio amplitude at a distance of 100 m from the shower axis measured by LOPES and normalized by a factor $\sin(\alpha)$, as a function of the primary particle energy reconstructed by the KASCADE-Grande experiment, which hosts the LOPES antenna array. Both figures nicely show the correlation between the radio observables and the primary energy of the shower cascade, and demonstrate the relevance of observatories employing hybrid detection techniques.

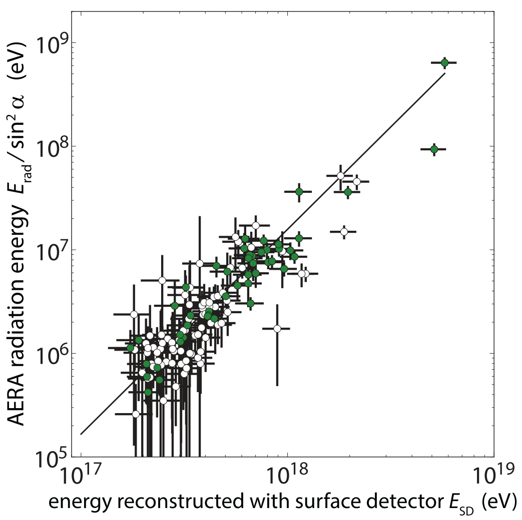


(A)

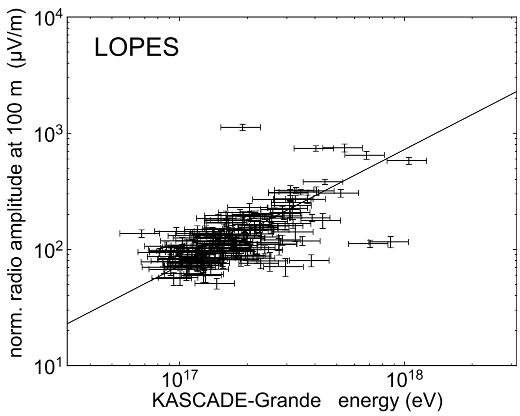


(B)

FIGURE 1.8: (A) The radiation energy measured by AERA corrected for the geomagnetic angle as a function of the primary particle energy reconstructed by the Auger surface detector, modified from [30]. Originally published in [47]. (B) The radio amplitude at a distance of 100 m from the shower axis measured by LOPES and normalized by $\sin(\alpha)$, as a function of the primary particle energy reconstructed by KASCADE-Grande array. Figure modified from [48].

### Shower maximum

As demonstrated in Section 1.2, valuable information about the primary particle can be deduced from the value of $X_{max}$, defined as the depth in the atmosphere where the electromagnetic component of the particle cascade reaches its maximum number of particles. In particular it can give us information about the mass composition of cosmic rays, i.e. what type of primary particles cosmic rays consist of.

The exact value of $X_{max}$ is subject to statistical fluctuations induced by the particle interactions driving the shower development. Even if the energy and arrival direction of the primary particle are known exactly, shower-to-shower fluctuations imply that the observed value for $X_{max}$ can correspond to different primaries. It is however possible to make a discrimination between different primary types in a statistical way, i.e. to get an estimate of the fraction of light and heavy primaries in a set of observed air shower events. This is illustrated in Figure 1.9, which shows measurements of $X_{max}$ over a range of primary energies performed by different observatories (dots), compared to the results from simulations (lines). The closer the measurements lie to the upper blue lines, the higher the fraction of light primaries for that energy seems to be, while measurements close to the bottom red lines suggest a large fraction of heavy primaries.

As mentioned before, at primary energies of $10^{17}$ eV and higher, the first few interactions in the air shower cascade happen at an energy scale beyond the scope of accelerators on Earth in a highly-forward momentum regime. Simulations therefore have to count on hadronic interaction models that can not be verified directly, which introduces systematic uncertainties on mass composition studies. The electromagnetic component and consequently the radio emission from air showers is less dependant on these models, and as such presents itself as a particularly interesting channel to study cosmic-ray mass composition.

Several different observables can be used to determine the value of $X_{max}$ of an air shower particle cascade, including the radius of the Cherenkov ring, the shape of the radio wave front measured at the observer plane, the slope of the frequency

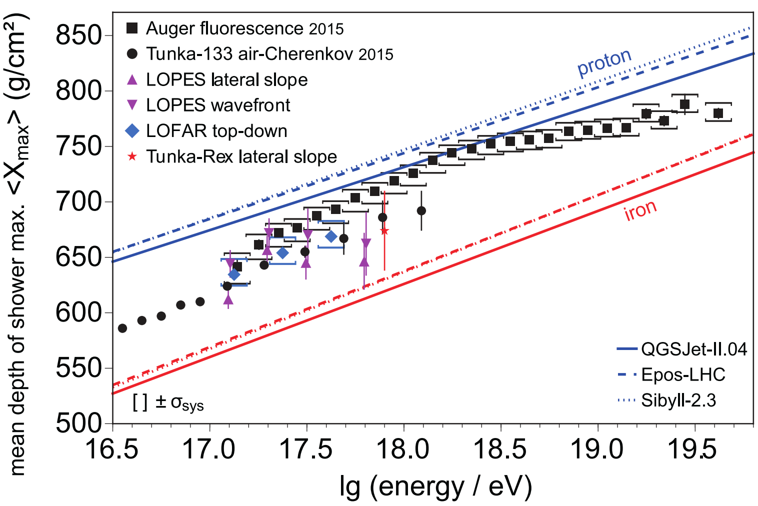


FIGURE 1.9: Measurements of $X_{max}$ in four decades of primary energy, performed by different observatories [30]. The dots show the data from [49–53], the lines show the results from simulations using different primary types and hadronic interaction models from [54].

spectrum at individual antenna stations and the polarization of the signal [30]. Interestingly LOFAR introduced a technique, which similar to fluorescence techniques achieves uncertainties smaller than 20 g/cm$^2$, but comes with a high computational cost [52]. To determine the value of $X_{max}$ for a given air shower event, a library of simulation events is created using the reconstructed incoming direction. To reduce computation cost, the simulated radio footprint is deduced from an interpolation of values on a star grid in the shower plane. Furthermore, only the primary particle type is varied, typically focusing on proton and iron primaries. For the primary energy a simple linear scaling of the radio amplitude is assumed. It is fitted to the data together with the core position of the footprint by minimizing a $\chi^2$ value. These minimum $\chi^2$ values are plotted as a function of $X_{max}$ of the simulated showers, and through a parabolic fit the smallest $\chi^2$ value is determined. The value for $X_{max}$ corresponding to the smallest $\chi^2$ value is then identified as $X_{max}$ of the observed air shower event. This is shown in Figure 1.10 for an air shower event measured by LOFAR.

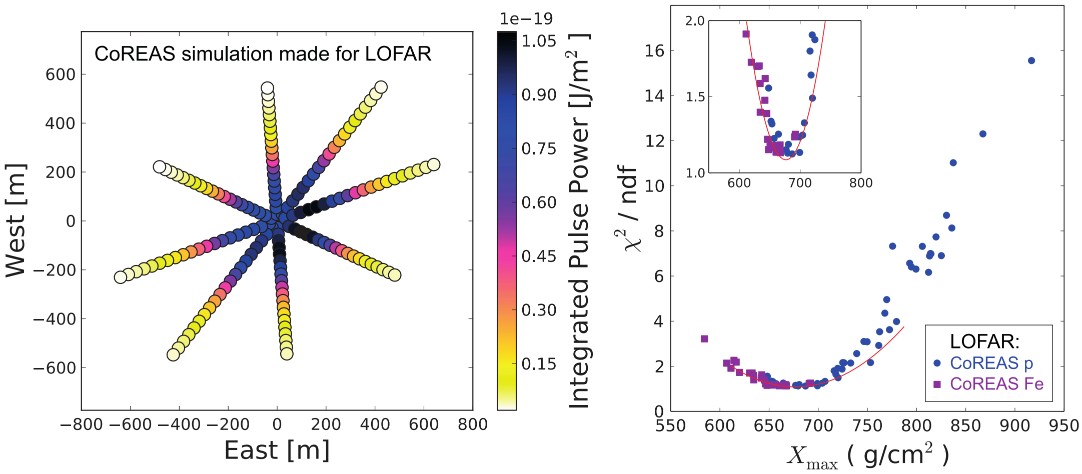


FIGURE 1.10: An illustration of the 'top-down' reconstruction technique of $X_{max}$, modified from [30]. Left: an example of a simulated radio footprint in the observer plane using a star grid for an inclined shower [55]. These are then interpolated in the shower plane and fitted to the data by minimizing a $\chi^2$ value. Right: the minimized $\chi^2$ values of a set of simulations in function of the corresponding $X_{max}$ values, using proton and iron as primaries [56]. The red line shows the parabolic fit, of which the minimum determines the $X_{max}$ value of the observed air shower event.

# Chapter 2

## Astrophysical Neutrinos

### 2.1 Introduction

The neutrino was originally postulated to explain missing spin and energy in the beta decay of atomic nuclei. As a neutral elementary particle it can only interact weakly and gravitationally, which means it hardly interacts at all with its environment, and is therefore notably challenging to detect. In fact, when pointing your thumb to the sun, a well-known source of not only photons but also neutrinos, tens of billions of neutrinos pass through your thumbnail per second without leaving a single trace.

The same characteristic that makes neutrinos so hard to detect also makes them particularly interesting to study, especially in the field of astronomy. As mentioned in Chapter 1, a single cosmic ray arriving at Earth carries little directional information, as during its propagation it deflects in magnetic fields and interacts with other particles. Neutrinos on the other hand can easily travel vast distances without being altered, and thus point back to their sources when they arrive at Earth. Furthermore, they are the only messengers that can convey unaffected information about the inner engines of the cosmic accelerator sites.

Moreover, cosmic-ray accelerators are naturally astrophysical neutrino sources. Accelerated cosmic rays can interact with nearby matter and radiation, mostly creating charged pions, which decay and produce neutrinos [57]. The cosmic rays reaching the GZK energy limit ($\sim 10^{20}$ eV) can even interact with photons from the cosmic microwave background through the $\Delta^+$-resonance,

$$
\begin{aligned}
p+\gamma_{\mathrm{CMB}} &\rightarrow \Delta^+ \rightarrow n + \pi^+ \\
n &\rightarrow p + e^- + \overline{\nu}_e \\
\pi^+ &\rightarrow \mu^+ + \nu_\mu,
\end{aligned}
$$

which creates a natural cut-off for the cosmic-ray spectrum as mentioned in Section 1.1, but also leads to the production of so-called ultra-high-energy cosmogenic or GZK neutrinos ( $\sim 10^{18}$ eV). However, as was also brought up in Section 1.1, recent measurements of the cosmic-ray mass composition at the end of the energy spectrum suggest an increase of the fraction of heavy nuclei. This would imply a reduction of the expected GZK neutrino flux, since it indicates that the suppression of the cosmic-ray energy spectrum at the highest energies is not only a consequence of the GZK effect, but also a result of the associated cosmic-ray accelerators reaching their limits. Additionally, for heavy nuclei the energy is distributed over the corresponding nucleons, resulting in a lower energy per nucleon available for neutrino production.

In general, astrophysical neutrinos seem to be the ideal messengers to identify and study cosmic-ray accelerators. Figure 2.1 gives an overview of the expected neutrino fluxes from different types of sources and interactions with various photon

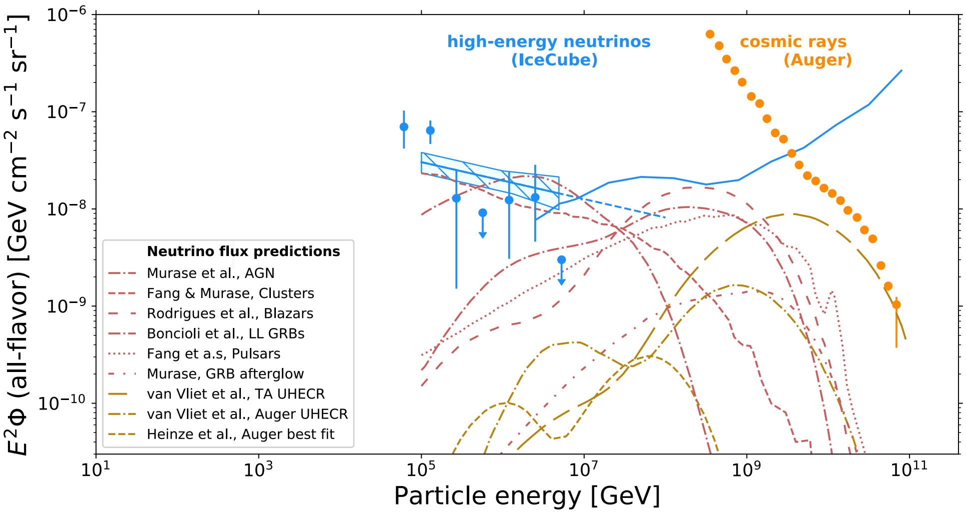


FIGURE 2.1: The neutrino flux measured by the IceCube Neutrino Observatory together with an upper limit towards higher energies (blue), compared to the cosmic-ray flux around the ankle of the spectrum measured by Auger (orange), predictions of astrophysical neutrino fluxes from different types of sources (red lines) and interactions of cosmic rays with various photon backgrounds (dark yellow lines). Figure modified from [58].

backgrounds, compared to the cosmic-ray flux around the ankle of the spectrum. As shown, the expected astrophysical neutrino fluxes are similarly low to that of the high-energy end of the cosmic-ray spectrum, requiring large detection volumes in order to have a satisfying detection rate. Furthermore, the probability of a neutrino interacting in a medium being exceptionally small drives the need for large detection volumes.

The IceCube Neutrino Observatory was the first observatory to measure neutrinos coming from outside of our own solar system, and indeed had to instrument an impressive cubic kilometer of polar ice with optical sensors to achieve that goal [59]. The neutrino flux measured by IceCube is shown in Figure 2.1 as well, and although IceCube's observations are rightfully quoted as an important milestone in neutrino astronomy, it is clear that even the gigantic volume of ice that it constantly monitors does not yet meet the required size for neutrino astronomy at the highest energies. The observatory proves to be insufficiently large to measure the neutrino flux at energies of $10^7$ GeV and beyond, as its given upper limit at these energies lies well above any of the flux predictions shown. Currently, new observation methods based on the detection of radio emission from neutrino-induced particle cascades are being explored, which could provide an effective and cost-efficient way of increasing the detection volume of neutrino observatories. Neutrino astronomy in the energy range of 100 TeV – 10 PeV, currently being probed by observatories like IceCube, is often called "high-energy (HE) neutrino astronomy", and will be summarized in Section 2.2. The work described in this thesis however is connected to the new radio-based observation techniques, aiming to push neutrino astronomy to energies beyond 10 PeV, which will be referred to as "ultra-high-energy (UHE) neutrino astronomy" and described further in Section 2.3.

For completeness the existence of neutrino astronomy in the keV-GeV range, i.e. the low end of the energy spectrum, should also be mentioned. These observatories mostly study neutrinos created within what could be summarized as "our local neighbourhood", for example neutrinos created in the atmosphere by cosmic-ray air showers (atmospheric neutrinos), neutrinos coming from the sun at the center of our solar system (solar neutrinos) or neutrinos created during galactic supernovae [60, 61]. Moreover, neutrino observatories also offer unique ways to test the Standard Model of particle physics, and address open questions such as the nature of dark matter and the neutrino mass ordering [62].

## 2.2 High-Energy Neutrino Astronomy

Detecting astrophysical neutrinos requires especially large detection volumes, to counter both the low flux of neutrinos arriving at Earth as well as the low probability of neutrinos interacting in the detector medium. To this end two main solutions have been put forward by neutrino astronomers, the first one using gigatons of polar ice as detection medium, and the second one monitoring large bodies of natural water. Both ice and water have favourable optical properties for the detection of light [62, 63].

Neutrinos entering ice or water can interact with a nucleus of the given medium, either through a neutral-current interaction (NC) or a charged-current interaction (CC). An example of such an interaction is shown in Figure 2.2. In both cases the interaction leads to the development of a hadronic cascade, containing charges moving faster than the speed of light in the medium. As is the case for air showers, these particles will emit Cherenkov radiation. Cherenkov radiation is the strongest in the high-frequency end of the visible spectrum, and can be detected by digital optical modules (DOMs). The general idea is to install a certain amount of DOMs over a large volume of water or ice to monitor the medium for these neutrino interactions.

The spacing between the optical modules is determined by either the attenuation length or the scattering length of light in the detector medium. For water the attenuation length is the smallest, while for ice the scattering length is the limiting factor [63]. In both cases the typical spacing between the optical modules is around 20 m. Due to the density of the medium, the typical length of the shower cascade is of a similar order as the module spacing. They are therefore hard to resolve and often considered point-like [64].

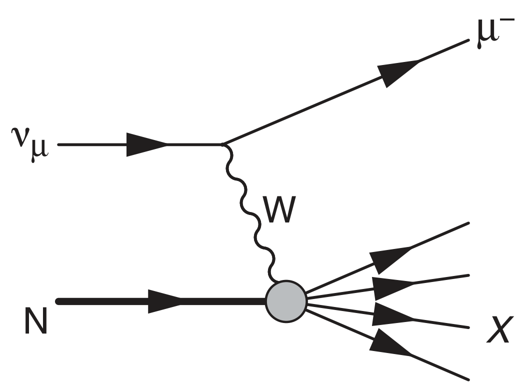


FIGURE 2.2: A muon neutrino interacting through a charged-current interaction with a nucleus, creating a secondary muon and a hadronic cascade. Figure modified from [65]. In case of a neutral-current interaction the hadronic cascade is created through exchange of a $Z$-boson, and a neutrino takes the place of the secondary muon in the diagram.

Especially interesting are the CC interactions with electron neutrinos ($\nu_e$), muon neutrinos ($\nu_\mu$) and tau neutrinos ($\nu_\tau$), which each have their own unique signature. A charged-current interaction with a $\nu_e$ will create an electron with sufficient energy to initiate an electromagnetic particle cascade, merging with the hadronic particle cascade in the medium. If the resulting particle cascade is contained well within the neutrino detector, these events generally yield precise energy measurements. However, since the particle cascade can be considered point-like, these events are usually not well-suited to determine the direction from where the neutrino came from. On the other hand, if a $\nu_\mu$ undergoes a charged-current interaction in the detector, a muon is created that propagates through the medium, often leaving the detection volume. The muon carries away some of the neutrino energy, which is therefore harder to estimate, but in doing so it leaves a track of Cherenkov light behind that is particularly useful for determining the incoming direction of the neutrino. Both interactions define the two most common topologies studied by HE neutrino observatories, namely the cascade topology and the track topology. A charged-current interaction with a $\nu_\tau$ will lead to a combination of both topologies, resulting in a double-cascade signature [66]. The heavy tau lepton created during the initial interaction will escape the hadronic cascade, propagate through the medium and subsequently decay, leading to the development of a secondary cascade. However, since the decay length of tau leptons is about 50 m/PeV, these type of events are usually hard to distinguish from single-cascade events [67–71]. In an ideal-case scenario the tau lepton decays in time so that all energy is contained within the detector medium, but propagates far enough to provide a clear double-cascade signature and excellent direction reconstruction. Interestingly, the distinct signatures following the CC neutrino interactions allow for identification of neutrino flavours, which can provide more information about their astrophysical sources [72].

A common background for neutrino observatories are atmospheric muons, created during the development of cosmic-ray air showers. Compared to astrophysical neutrinos, cosmic rays are much more likely to interact and the corresponding observed flux is significantly higher. The rate of atmospheric muons detected by the DOMs is therefore orders of magnitudes larger than the rate expected for astrophysical neutrinos. To this end HE neutrino observatories usually look down through the Earth, observing the sky from the opposite hemisphere. Neutrinos at energies up to 100 TeV can propagate large distances through the Earth before interacting in the detection volume, while atmospheric muons cannot. Another important background is that of atmospheric neutrinos, also originating from cosmic-ray air showers, which can be distinguished from astrophysical neutrinos based on their more steeply falling energy spectrum.

An illustration of the IceCube Neutrino Observatory is shown in Figure 2.3, which monitors a total volume of $\sim 1\ \mathrm{km}^3$ of polar ice at the South Pole. It consists of 5160 DOMs distributed over 86 vertical strings between depths of 1450 m to 2450 m in the ice, with extra DOMs deployed on the ice surface in tanks of frozen water for the detection of cosmic-ray air showers [73]. The typical spacing of the DOMs in the in-ice array is of the order of $\sim 17$ m. IceCube is currently the only neutrino observatory using optical modules in ice, and was the first to demonstrate the feasibility of the detection technique for HE astrophysical neutrinos [59]. More recently, IceCube revealed possible HE neutrino sources and published the first image of the Milky Way in neutrinos [74–77]. Other observatories are now well on their way to join the HE neutrino astronomy efforts, mostly focusing on water as a detection medium, such as the KM3NeT deep-sea neutrino telescope in the Mediterranean Sea [78] and the GVD neutrino telescope in Lake Baikal [79].

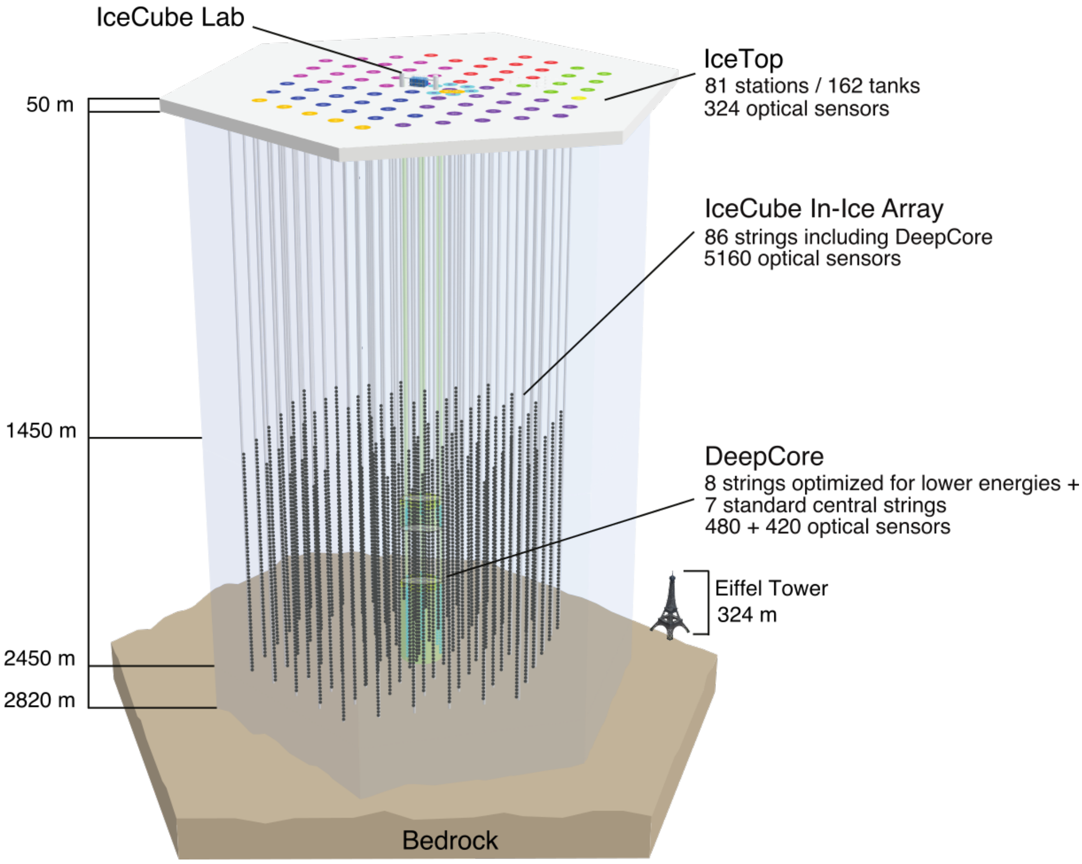


FIGURE 2.3: The layout of the IceCube Neutrino Observatory, located at the South Pole [73]. The detector consists of 5160 DOMs distributed over 86 strings between depths of 1450 m to 2450 m in the ice and is complemented by IceTop, a surface array of DOMs in tanks of frozen water for the detection of cosmic-ray air showers. The Eiffel Tower is shown in the bottom right for scale comparison.

## 2.3 Ultra-High-Energy Neutrino Astronomy

Although the cross section of weak neutrino interactions increases with energy, at the ultra-high-energy range the extremely low neutrino flux calls for even larger detection volumes. In principle the same detection method for HE neutrinos based on the observation of Cherenkov light could be used, simply instrumenting even larger volumes of water or ice with optical modules. This however comes at a great financial and logistical cost, making such an endeavor unfavorable.

Therefore new detection techniques are being explored, with the goal to instrument detection volumes orders of magnitudes larger than the current HE neutrino observatories in a cost-efficient and logistically feasible way. This requires detectors that are much sparser instrumented compared to the typical optical module arrays, and exist of detection units that are able to run autonomously on easily accessible resources like solar or wind power. These requirements force us to move away from the detection of visible light, and instead we turn towards radio, which has an attenuation length of the order of $\sim$ 1 km in ice. For completeness, the possibility of acoustic UHE neutrino astronomy should also be mentioned, which is currently exploring the viability of detecting sound waves created by neutrino interactions in water or ice [80, 81]. As this falls beyond the scope of this thesis, it will not be discussed any further.

In this work the focus lies on the use of radio antennas to detect neutrino interactions in ice, but it should be noted that the use of alternative detection media to detect these interactions are being explored as well, such as large volumes of rock. If a tau neutrino entering a mountain ridge at a near-horizontal incoming direction interacts with the mountain rock, it will create a tau lepton. The tau lepton escapes the mountain ridge, enters the atmosphere and decays, initiating an in-air particle cascade. Similar to air showers initiated by cosmic rays entering the atmosphere, these events create radio emission, providing a possible detection channel to study the initial tau neutrino. Examples of radio detectors exploring this observation method are GRAND [82] and BEACON [83].

In the context of this thesis, a distinction can be made between two types of UHE neutrino radio detectors using ice as a detection medium. The first type is based on the detection of radio waves emitted directly by a neutrino induced particle cascade in ice, which will be referred to as Askaryan radio neutrino detectors. The second type is based on the observation of radio wave reflections, i.e. radar echoes, from the ionization trail associated with the neutrino-induced particle cascade in ice. This technique is currently being explored by the Radar Echo Telescope collaboration.

### 2.3.1 Askaryan Radio Neutrino Detectors

Similar to air showers, neutrino-induced particle cascades moving through ice do not only create Cherenkov radiation in the visible spectrum, but also emit radio waves. For air showers the radio emission has two main components, geomagnetic emission and Askaryan emission. Geomagnetic emission follows from the time-varying transverse current in the shower front due to Earth's magnetic field, and is linearly polarized in the shower plane. The amplitude of the geomagnetic emission scales with the drift velocity of the charges in the current. Compared to particle showers in air, the drift velocity associated with particle cascades in ice will be much smaller, as ice is much denser than air. In ice the Lorentz force from the geomagnetic field will have a negligible effect on the particles in the shower front, and no geomagnetic radio emission is expected.

The Askaryan emission however is determined by the magnitude of the charge excess. Askaryan predicted that the negative charge excess should be mostly independent of the medium density, which means that we can expect neutrino-induced particle cascades in ice to emit Askaryan radiation [27]. As the particles in the cascade move faster than the speed of light in ice, the emission will be concentrated around the Cherenkov cone. Depending on the density, the Cherenkov angle in ice is of the order of $40^\circ - 55^\circ$ [84]. More detailed studies confirmed Askaryan's estimations and modeled the expected Askaryan radiation [85–89]. This led to the deployment of the Radio Ice Cherenkov Experiment (RICE) at the South Pole [90], the first array of radio receivers in ice designed to look for Askaryan emission from neutrino interactions, followed by the Antarctic Impulsive Transient Antenna (ANITA) [91], the Askaryan Radio Array (ARA) [92], the Antarctic Ross Ice-Shelf Antenna Neutrino Array (ARIANNA) [93], and the Radio Neutrino Observatory in Greenland (RNO-G) [58].

The details of these experiments vary, but they all share the common goal of detecting Askaryan radio emission from neutrino-induced particle cascades in ice. Although Askaryan radio neutrino detectors have been around now for more than 20 years, no proof of any measurement of the Askaryan emission of in-ice particle cascades in nature has been presented yet. In principle these detectors rely on predictions from models and simulations, and have so far only been able to produce limits on the UHE neutrino flux. It is however important to note that Askaryan radiation of particle cascades in dense media has been measured in a controlled environment using particle accelerators [94], and as discussed in Chapter 1, the Askaryan emission from particle cascades in air has been observed by multiple air shower detectors. This provides additional confidence in the search for radio signals from in-ice cascades, and underlines again the synergy between cosmic-ray astronomy and neutrino astronomy.

### Types of Askaryan detectors

Several different approaches can be followed for detecting the radio signal created by neutrino interactions in ice [95]. RICE deployed several radio receivers deep in the ice at the South Pole, going as far as 350 m below the surface [96]. Similarly, ARA constructed five autonomous stations at the South Pole with antennas around $\sim$ 200 m in the ice [97]. A single ARA station consists of 4 antenna strings going vertically down into the ice, holding 4 antennas each. The 4 antennas are divided in two pairs separated about $20-30$ m, with each pair consisting of one vertically polarized birdcage dipole and one horizontally polarized quad-slot antenna [98]. The latest station that was deployed also includes a 5$^{\text{th}}$ antenna string, equipped with 7 vertically polarized antennas and 2 horizontally polarized antennas deep in the ice, following a more compact spacing of $1-2$ m. This string is used for beamformed triggering via constructive interference based on predefined phase offsets [97]. The layout of the latest station is shown in Figure 2.4a.

The first $\sim$ 100 m of natural ice sheets, such as the ones at the South Pole and in Greenland, consist of non-uniform compacted snow, referred to as the firn [100]. Deploying antennas in the firn leads to large uncertainties on the detector medium

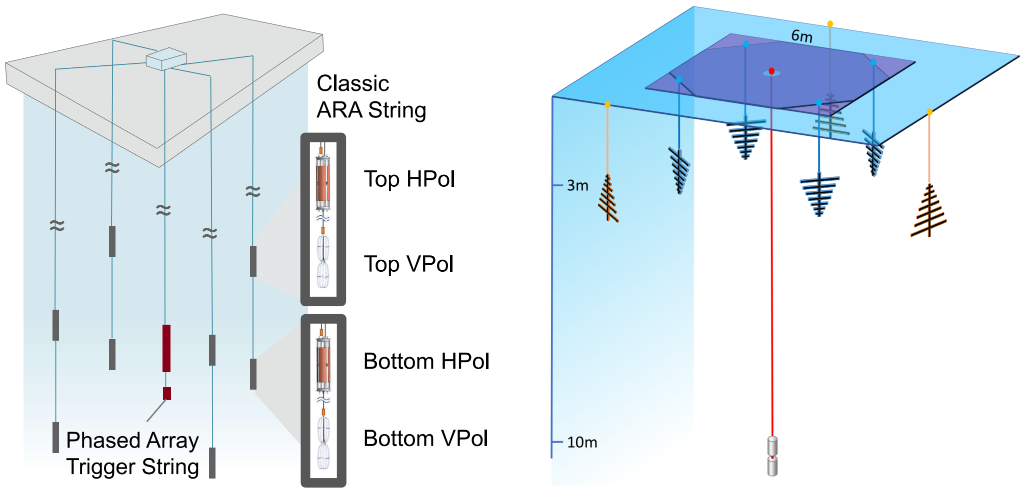


(A) (B)

FIGURE 2.4: (A) The station layout of ARA5, the latest unit deployed by the ARA collaboration. It has 4 antenna strings each holding 4 antennas, and an additional 5th string with 9 more antennas used for beamformed triggering. The maximum depth of the antennas of the ARA detector array is around 200 m. Figure modified from [97]. (B) The station layout of an ARIANNA detector unit. It has 4 downward-pointing LPDA's and 3 upward-facing LPDA's at a depth of 3 m, and a single dipole antenna at a depth of 10 m [99].

and complicated signal propagation effects, influencing the triggering and reconstruction capabilities of the detector [92]. Furthermore, the index of refraction of the firn changes significantly on short length scales, which means radio signals moving through the firn will follow bend trajectories. This leads to so-called shadow-zones, i.e. zones in the ice from which emitted signals cannot reach the radio receivers, which reduces the effective horizon of the detector [101]. The exact properties of the firn depend on the chosen deployment site, but in general the sensitivity of a single radio detector station is higher for antennas deeper in the ice.

Nonetheless, deploying antennas near the ice surface has interesting benefits as well. First of all, the deployment of a radio station using near-surface antennas is less complicated. It usually involves digging antenna trenches, which is significantly more straightforward compared to drilling deep antenna holes. Secondly, depending on the drill technique applied, the typical diameter of deep boreholes in the ice range from $6'' - 11''$ [58]. This means deploying antennas deep in the ice comes with heavy restrictions on the possible antenna designs. In general the better antennas are log-periodic dipole arrays (LPDA's), which are formed by a combination of multiple dipole antennas of different lengths placed on a central arm, forming a tree-like structure [95]. These antennas can be placed in near-surface trenches, but unfortunately do not fit in deep boreholes. Furthermore, calibration and maintenance of near-surface arrays is less complicated, improving reconstruction capabilities of the detector array. The ARIANNA detector consists of 7 identical radio stations, each using 4 downward-pointing LPDA's 3 m below the surface, and a single dipole antenna at a depth of 10 m in the ice to assist during background removal and event reconstruction [99]. The 4 downward-pointing LPDA's are accompanied by 3 upward-facing LPDA's for the detection of radio emission from cosmic-ray air showers. The layout of an ARIANNA station is shown in Figure 2.4b. The stations were deployed on the Ross Ice-Shelf at Moore's Bay in Antarctica, an ice shelf of roughly 570 m thick followed by the Ross Sea beneath [102]. This allows the downward-pointing LPDA's to look for both direct radio signals from skimming neutrino's, as well as signals reflecting on the ice-water boundary coming from downward going neutrino's.

More recently, the RNO-G collaboration has started deploying detector units close to Summit Station in Greenland, combining deep in-ice antennas with LPDA's close to the surface. This so-called hybrid layout will be discussed in more detail in the next chapter.

A third method avoids deploying antennas in the ice altogether. Instead, a payload of radio receivers is mounted on a hot air balloon, which is flown over a large mass of ice such as the continent of Antarctica for several weeks, looking for neutrino signals coming from the ice. With this approach a huge volume of ice can be monitored with a relatively small detector, with a corresponding energy sensitivity shifted towards the highest energies when compared to that of ground-based observatories [103]. The ANITA collaboration has performed 4 flights over a period of 10 years, and is now working towards the next generation of hot air balloon neutrino experiments, the Payload for Ultrahigh Energy Observations (PUEO) [104]. The last balloon launched by ANITA flew for 28 days at a height of $\sim$ 40 km above the Antarctic surface. The payload was about 8 m tall and consisted of 48 horn antennas, arranged in rings around the data acquisition system. A picture of the payload used during the 4th flight is shown in Figure 2.5, as well as a picture taken during the 2nd flight illustrating the enormous size of the hot air balloon.

As already indicated at the start of this section, no proof of any measurement of the Askaryan emission of in-ice particle cascades in nature has been presented yet by any of these radio neutrino observatories. It is however worth mentioning

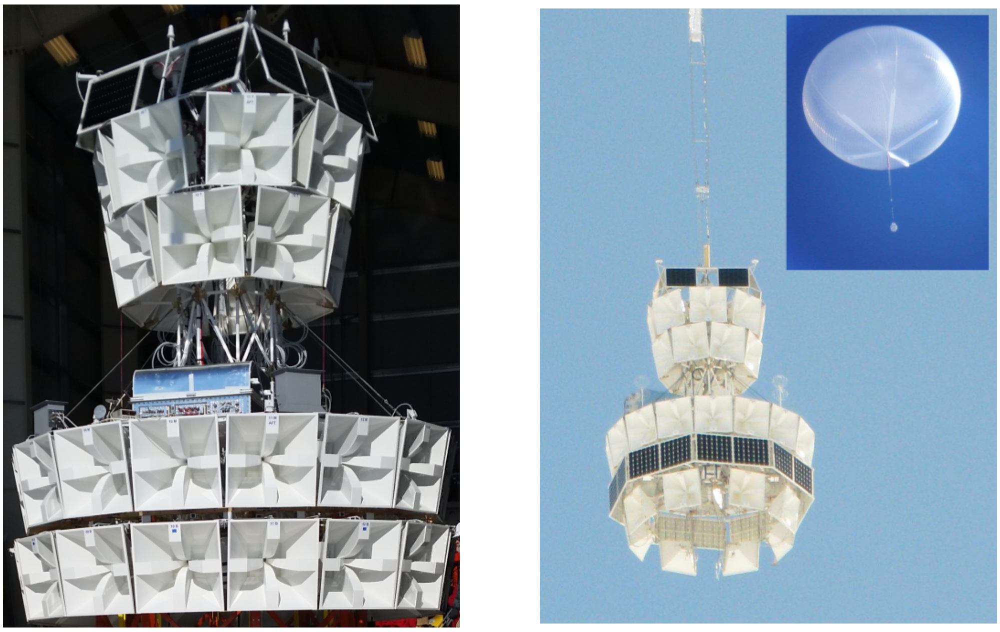

(A) (B)

FIGURE 2.5: (A) The payload of the 4th balloon launched by ANITA [114]. It is about 8 m tall and consists of 48 horn antennas, each roughly 0.95 m wide from edge to edge. After launch an additional row of solar panels dropped down below the bottom ring of antennas, which is not shown in the picture. (B) A picture of the payload used during the 2nd ANITA flight after launch, illustrating the enormous size of the hot air balloon [115].

that other types of signals have been observed, such as radio emission from solar flare events [105, 106] and the radiation emitted by cosmic-ray air showers in the atmosphere [107, 108]. In particular, ANITA reported the observation of anomalous cosmic-ray like events with an unusual signature [109–111]. At the time of writing, the origin of these events has not yet been identified. Furthermore, neutrino searches by these observatories have led to constraints on the UHE neutrino flux [99, 112–114].

#### Neutrino direction

The details of the method applied to reconstruct the arrival direction of a neutrino interacting in the ice depends on the detector layout, but in general follows the process described below [58]. First of all the arrival direction of the radio signal itself is determined. Usually this is done by comparing the arrival time of the signal in different receivers of the detector unit. Using more receivers results in a better resolution, which is typically less than 1°. From the known Cherenkov angle $\theta_c$ in ice and the arrival direction of the signal, a ring on the sky indicating all the possible arrival directions of the neutrino can be constructed. The degeneracy arrives from the fact that the emission propagation alone does not uniquely define the exact orientation of the Cherenkov cone in the ice. However, since the emission only has an Askaryan component, the polarization $\vec{p}$ of the corresponding electric field should be perpendicular to the cone, pointing radially inwards towards the shower axis. By measuring the polarization of the signal the orientation of the Cherenkov cone can be determined, and a unique point in the on-sky ring can be identified as the arrival direction of the neutrino. This process is illustrated in Figure 2.6. Since the electric

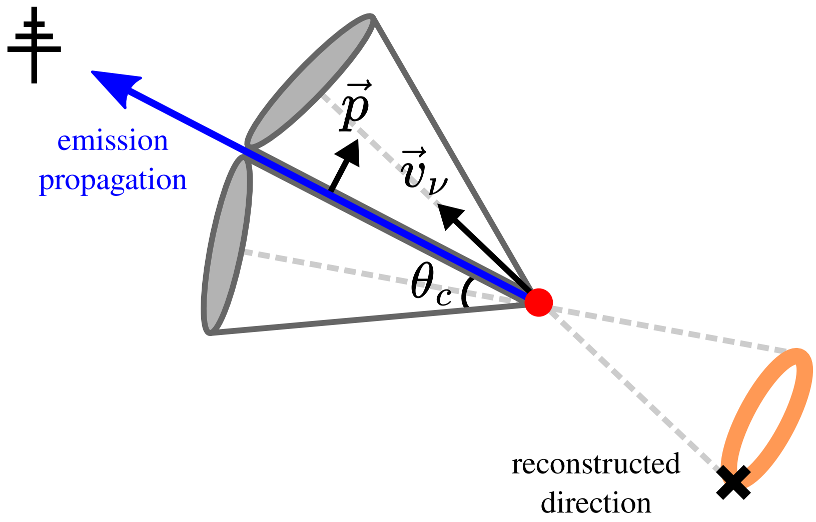


FIGURE 2.6: An illustration showing the basic principle of neutrino direction reconstruction based on the observation of the arrival direction and polarization of the radio emission.

field has no component in the propagation direction, the polarization of the emission can be determined using one vertically polarized receiver and one horizontally polarized receiver, as long as the polarization of both antennas does not coincide with the propagation direction of the emission. An antenna polarized in the propagation direction of the emission will in principle not be sensitive to the corresponding electric field.

Radio emission slightly off the Cherenkov cone can still be detected, which increases the sensitivity of the detector unit, but also complicates the neutrino arrival direction reconstruction. In this case, also the viewing angle with respect to the cone needs to be determined. As the condition for full coherence is only truly fulfilled on the Cherenkov cone, the high-frequency content of the signal quickly disappears for viewing angles further away from the cone. The viewing angle can therefore be reconstructed from the frequency slope of the Fourier transform of the signal.

Extra complications arise when the propagation of the radio emission from the neutrino interaction cannot be approximated by a straight path, but instead bending or refraction due to a changing index of refraction needs to be taken into account. This is especially important when the neutrino interaction happens in the firn, which has a density that changes significantly on short length scales, or when the receiver is situated in the firn or the atmosphere. Good knowledge of the refractive index profile is then needed to determine how the signal propagated from emission point to receiver, and correctly reconstruct the neutrino arrival direction [95].

### Neutrino energy

The energy of the neutrino interacting in the ice can be reconstructed based on the amplitude of the electric field observed by the receiver. The relation between the electric field amplitude $|\vec{E}|$ and the neutrino energy $E_\nu$ is given by

$$|\vec{E}| \propto y \cdot f(\phi) \cdot \frac{\exp(-d/l_{\text{atten}})}{d} \cdot E_\nu, \tag{2.1}$$

with $y$ the fraction of the neutrino energy that goes into the particle cascade, $f(\phi)$ representing the dependency on the viewing angle $\phi$ with respect to the Cherenkov cone, $d$ the distance to the interaction vertex and $l_{\mathrm{atten}}$ the attenuation length of ice [58]. Also here the exact method to reconstruct the energy of the neutrino depends on the detector layout. In general it requires determining the amplitude of the electric field observed by the receiver, the distance from receiver to the interaction point, and the viewing angle between the receiver and the Cherenkov cone, as all of these terms occur in Equation 2.1.

The fraction $y$ is different for each event, which results in a systematical uncertainty factor of $\sim 2$, imposing a hard bound on the resolution that can be achieved [116]. For charged-current interactions of electron neutrinos $y = 1$, since all the energy of the neutrino will be transferred to the particle cascade in the ice. However, at energies above $10^{15}$ eV, the wavelength associated with the momentum of the electrons and positrons becomes larger than the atomic spacing in ice, which reduces the cross-sections for bremsstrahlung and pair production due to the Landau–Pomeranchuk–Migdal (LPM) effect [117, 118]. Electron neutrino CC interactions can therefore lead to multiple displaced electromagnetic showers, developing out of phase and interfering constructively or destructively, justifying using the inelasticity uncertainty bound for these type of events as well [58, 95].

To determine the amplitude of the electric field at the receiver, the measured voltages need to be converted into electric field components, which requires a good understanding of the antenna response. Similar to the polarization of the radio emission, the amplitude of the total electric field can then be determined using two antennas polarized orthogonally to each other, provided that the arrival direction of the emission is known [95].

The distance to the interaction point can be calculated using the differences in arrival time of a deep 3D array of antennas. When the detector unit is located close to the ice surface, the distance to the interaction point can also be determined using a single receiver. In this case both the emission propagating directly between emitter and receiver and the emission reflecting off of the ice-air boundary can be detected. Using the incoming signal direction and the time difference between both signals, the vertex distance can be determined with a precision of  10%, which is similar to the resolution obtained by a deep 3D array of receivers [116, 119].

When the viewing angle with respect to the Cherenkov cone is increased, coherency is lost and the amplitude of the received emission will decrease. The effect of the viewing angle on the measured amplitude can be taken into account by measuring the fluence of the received radio signal, defined by

$$\Phi = \epsilon_0 c_0 \int E^2(t)\mathrm{d}t, \tag{2.2}$$

with $\epsilon_0$ the vacuum permittivity and $c_0$ the speed of light in vacuum. As mentioned in the previous section, the viewing angle influences the slope of the frequency spectrum of the emission. Therefore a slope parameter is defined, as the ratio of the fluence in a low-frequency band to that of the fluence in a high-frequency band. This parameter allows to reconstruct the energy in the shower cascade. Figure 2.7 shows the relation between the square root of the fluence $\Phi$ of the radio signal in the $130 - 300$ MHz band divided by the particle cascade energy, as a function of the ratio of the fluence in the $130 - 300$ MHz band to that of the fluence in the $300 - 500$ MHz band, from simulations for the RNO-G observatory. The relation between both variables can be described by a parabola, which can be used to calculate the energy of the observed particle cascade. The relation was determined for a fixed distance between emitter and receiver of 1 km, without taking into account attenuation by the ice. To

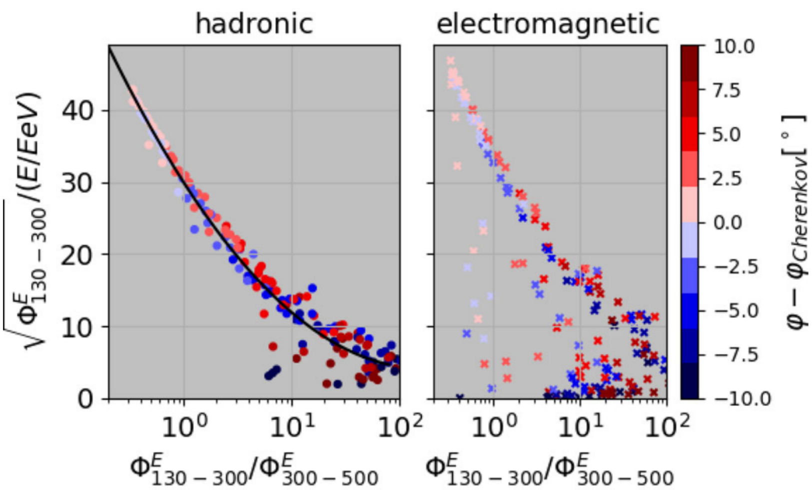


FIGURE 2.7: Square root of the fluence Φ of the radio signal in the 130 − 300 MHz band divided by the particle cascade energy, as a function of the ratio of the fluence in the 130 − 300 MHz band to that of the fluence in the 300 − 500 MHz band, based on simulations for the RNO-G observatory [119]. Colors show the viewing angle relative to the Cherenkov cone. The distance between shower and observer was fixed to 1 km, and attenuation by the ice was neglected. Left: for hadronic showers, with the black line showing a parabolic fit. Right: for electromagnetic showers, showing outliers affected by the LPM effect.

use the parabolic relation, the measured electric field therefore has to be corrected first for the actual distance to the emitter and attenuation.

### 2.3.2 Radar Echo Telescope

A cascade of relativistic particles moving through a medium will not only lead to the emission of electromagnetic radiation, but will also create a trail of non-relativistic electrons and ionized nuclei. Given the right circumstances, this ionization trail can reflect incident radio waves, i.e. radar echoes, providing an alternative way of studying the particle cascade and the primary that initiated it. In contrast to the Askaryan radiation emitted by the cascade, the power of the radar emission can be controlled, which allows for detections at lower energies.

The possibility of detecting radar echoes from ionization trails of cosmic-ray induced particle cascades in air was already being discussed during the Second World War, motivated by the detection of unexplained transient radar echoes originating from the atmosphere [120]. This led to the development of the Jodrell Bank observatory, which showed that these transient radar echoes came from denser ionization trails in the upper atmosphere created by meteors. Nonetheless, multiple other experiments looked for radar echoes from air shower ionization trails [121–124]. No such events were detected, which was subsequently attributed to the short lifetime of the ionization trail, in combination with significant energy losses due to collisions between the ionized electrons and the air molecules [120, 125, 126].

Moving to denser media increases the ionization density, which makes the reflection of radio waves on the ionization trail feasible even for short lifetimes and high collision rates. Although the radar echo technique seems to fail for air shower astronomy, it is therefore still a viable option for the detection of UHE neutrinos creating particle cascades in ice. Indeed, several studies have demonstrated the feasibility of radar detection of neutrino-induced cascades in ice [127–130]. Moreover, radar echoes from ionization trails of high-energy particle cascades have been observed during the T576 experiment at the SLAC National Accelerator Laboratory, where an electron beam was directed into a target to mimic a neutrino interaction [131]. The target was made of high-density polyethylene (HDPE), with a similar density and ionization lifetime as ice and comparable radio properties. A transmitting antenna was directed towards the target, broadcasting continuous-wave (CW) radiation at different frequencies ranging from 1 GHz up to 2.1 GHz. Multiple receiver antennas were placed on the same side of the target as the transmitter to measure the reflections of the emitted radio waves. An illustration of the setup is shown in Figure 2.8. To find evidence of a radar reflection, the data taken during beam injection was compared to so-called null data. The null data consists of background data taken during a period when the transmitter was turned off, supplemented with CW background extracted from signal data. A comparison between an average of 200 signals of a single run and the corresponding null data is given in Figure 2.9, showing a clear excess in the time-frequency region where the radar echo is expected to be.

Following the success of the T576 experiment, the Radar Echo Telescope (RET) collaboration was founded with the goal of deploying and operating the first neutrino telescope relying on the radar echo technique. A possible layout for a Radar Echo Telescope for Neutrinos (RET-N) station is shown in Figure 2.10, consisting of a single string in the center of the station carrying a phased-array transmitter, surrounded by 9 other strings carrying 3 receiver antennas each. The design is currently undergoing optimization studies, and should therefore be considered preliminary. It is located $\sim 1500$ m below the ice surface of a polar ice sheet to suppress radio background signals, to take advantage of the uniformity of the index of refraction profile of deep ice, and to avoid signal interaction with the ice-air boundary [132].

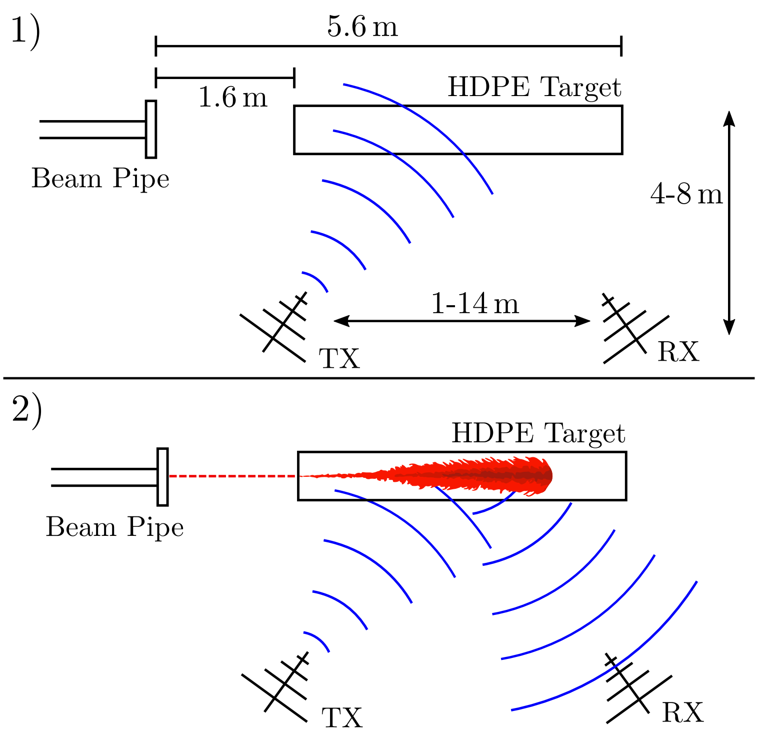


FIGURE 2.8: An illustration of the setup of the T576 experiment at the SLAC National Accelerator Laboratory, before beam injection (top) and during beam injection (bottom) [131]. TX represents the transmitting antenna, and RX represents the receiving antenna.

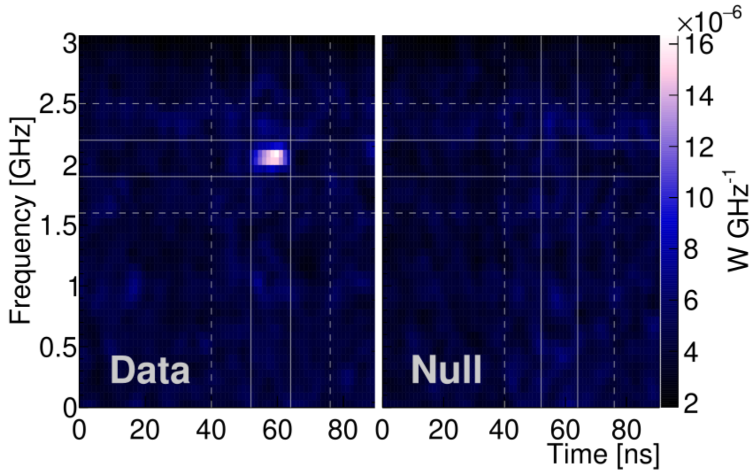


FIGURE 2.9: A comparison between an average of 200 signals of a single run and the corresponding null data, both represented in a frequency versus time spectrogram [131].

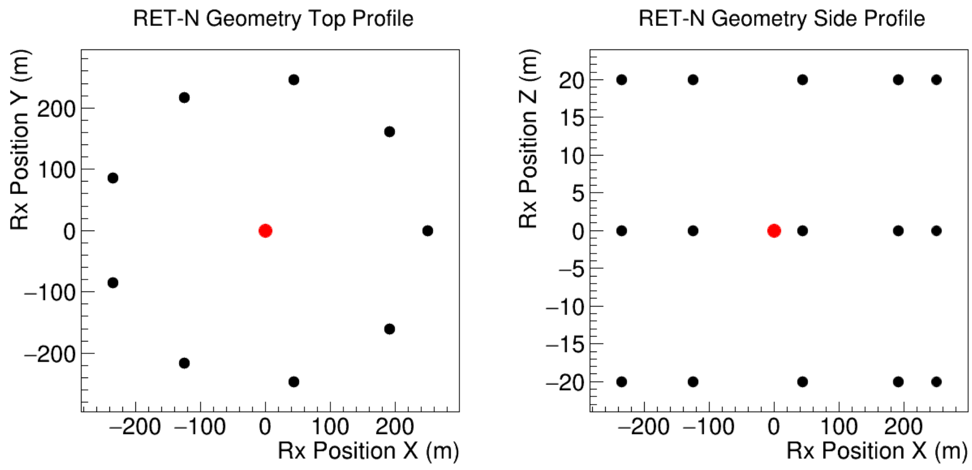


**(a)** **(b)**

FIGURE 2.10: A possible RET-N station layout, presented in a top profile (left) and a side profile (right) with respect to the phased-array transmitter [132]. The phased-array transmitter location is indicated by a red dot, while the receiver locations are indicated by black dots.

Although the T-576 experiment showed the feasibility of radio waves reflecting off of particle cascades in dense media and confirmed the existing radar scattering models, a demonstration of the technique in nature is still missing. To this end, the Radar Echo Telescope for Cosmic Rays (RET-CR) has been deployed close to Summit Station in Greenland, which will be described in the next chapter [133].

### Signal properties

Two independent software modules have been developed to study the properties of the radar echo signals coming from neutrino-induced particle cascades in ice, RadioScatter [128] and MARES [129, 130]. RadioScatter uses a particle-level model, while MARES relies on a macroscopic model.

Not looking for the direct radio emission of particle cascades but instead relying on reflections from controlled transmission comes with some interesting advantages. The power of the transmitter represents an additional degree of freedom that can be used to optimize the detector sensitivity. In addition, radar echoes are not concentrated around the Cherenkov cone. This increases the detection efficiency, since more cascade geometries can be detected. Moreover, the motion of the ionization trail with respect to the transmitter and receivers of the detector unit will induce a Doppler shift of the transmitted radiation. The reflected signal will show a unique chirp-like signature, which can be used for triggering and direction reconstruction [134, 135]. A preliminary study using a simplified detector geometry demonstrates a neutrino arrival direction resolution of $\sim 2^\circ$ [132]. Additional studies of the geometry-dependent features of the reflected signal are currently underway [129, 130].

### Sensitivity

The results of a preliminary sensitivity study using 10 RET-N stations following the layout given in Figure 2.10 is shown in Figure 2.11. Using only a limited amount of stations, RET-N will be able to probe the neutrino flux starting at an energy of $\sim 10^{16}$ eV, where the current sensitivity of the IceCube Neutrino Observatory ends, up to an energy of $\sim 10^{20}$ eV, testing different cosmogenic and astrophysical neutrino models.

Interestingly, since RET-N does not rely on the detection of radio emission emitted by the particle cascade on the Cherenkov cone, it could be particularly suited for neutrino flavour studies [62]. A CC tau neutrino interaction creates a hadronic particle cascade and a tau lepton. Given the ultra-high energy of the neutrino, the tau lepton will propagate several hundreds of meters through the ice and subsequently decay, initiating a second particle cascade in the ice. As mentioned before, such a double-cascade event is a unique signature for identifying tau neutrino interactions. The event geometries that allow for the detection of the direct Askaryan radio emission are limited, since the Cherenkov cone from the second cascade is displaced with respect to that of the first cascade [136]. For distinguishing CC tau neutrino interactions the large angular acceptance of the RADAR echo technique can prove valuable.

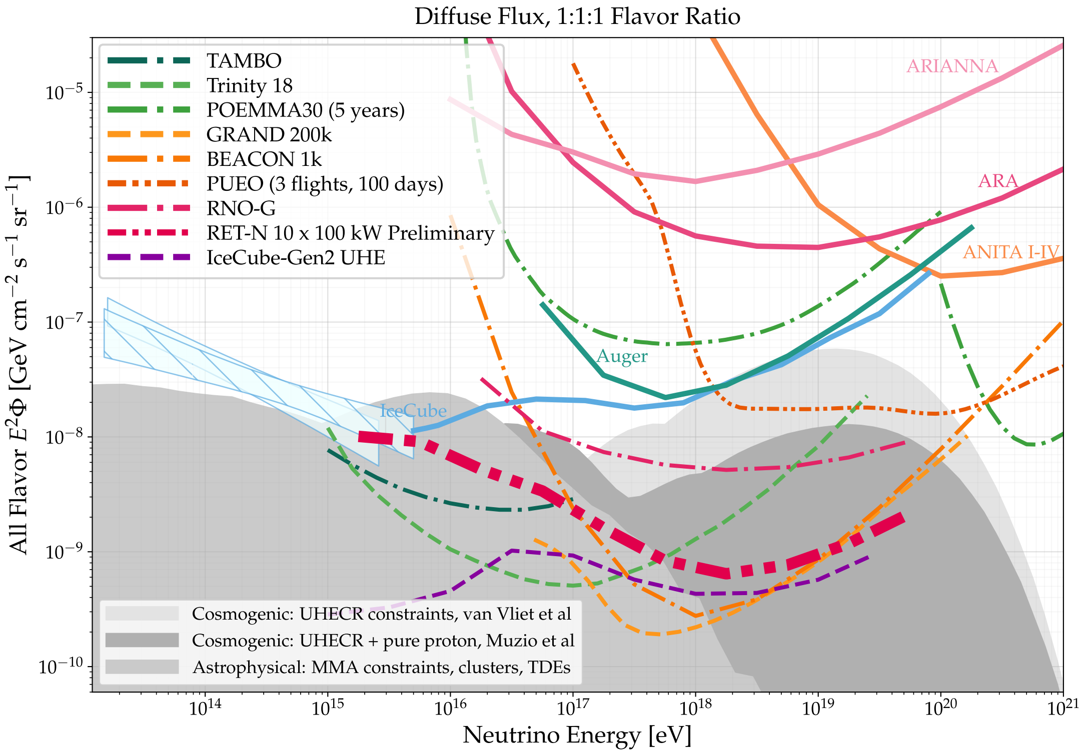


FIGURE 2.11: The expected sensitivities for a variety of neutrino observatories assuming a ten-year integration, unless specified differently in the legend, compared to cosmogenic and astrophysical neutrino flux models. The sensitivity line for RET-N is highlighted for clarity. Figure modified from [62].

# Chapter 3

## Radio Observatories at Summit Station

### 3.1 Introduction

This chapter will focus on the Radio Neutrino Observatory in Greenland (RNO-G) and the Radar Echo Telescope for Cosmic Rays (RET-CR), both located at Summit Station in Greenland.

An overview of the Summit Station site is given in Figure 3.1, showing the RNO-G array currently under construction and the location of RET-CR. It is named after the scientific station it is hosting located close to the highest point of the Greenlandic ice sheet, where it reaches a thickness of more than 3 km. The station itself is based at the end of the so-called skiway, a snow runway that serves as a landing strip for LC-130 Hercules flights provided by the National Guard of the United States. An image of the station is shown in Figure 3.2. Currently it has the capacity to host around 40 people at a time during Arctic summer, usually consisting of technical staff, operations staff, medical staff and scientists. Originally established as a drill site in 1989, it became a long-term science hub with the goal of offering support to a variety of scientific projects in the fields of meteorology, glaciology, atmospheric chemistry, and astrophysics [137].

The Summit Station site offers great possibilities for radio observatories using ice as a detector medium. As one of the most remote places on Earth it is radio quiet, while it still provides the necessary accommodations to support deployment, calibration and maintenance of large-scale detector arrays. Compared to sites in Antarctica, the amount of days with sufficient daylight for autonomous solar-powered stations is higher [58]. Furthermore, as explained in the previous chapter, the IceCube Neutrino Observatory located at the South Pole has the highest sensitivity for neutrinos passing through the Earth, coming from the Northern sky. At ultra-high energies however the Earth becomes opaque for neutrinos, as in this energy range the neutrino interaction probability is significantly higher. Consequently, detecting neutrinos at the opposite hemisphere is no longer possible. A radio detector array extending IceCube's sky coverage towards higher energies therefore has to be build on Earth's Northern hemisphere. In addition, at a latitude of 72° N, the field of view of detector arrays located at Summit Station is affected by Earth's rotation, which leads to an increased sky coverage.

The following sections will give an overview of both the RNO-G observatory and the RET-CR detector, and highlight the on-site installation, maintenance and calibration efforts of RNO-G during the summer of 2023 and RET-CR during the deployment season of 2024, performed as part of this thesis work.

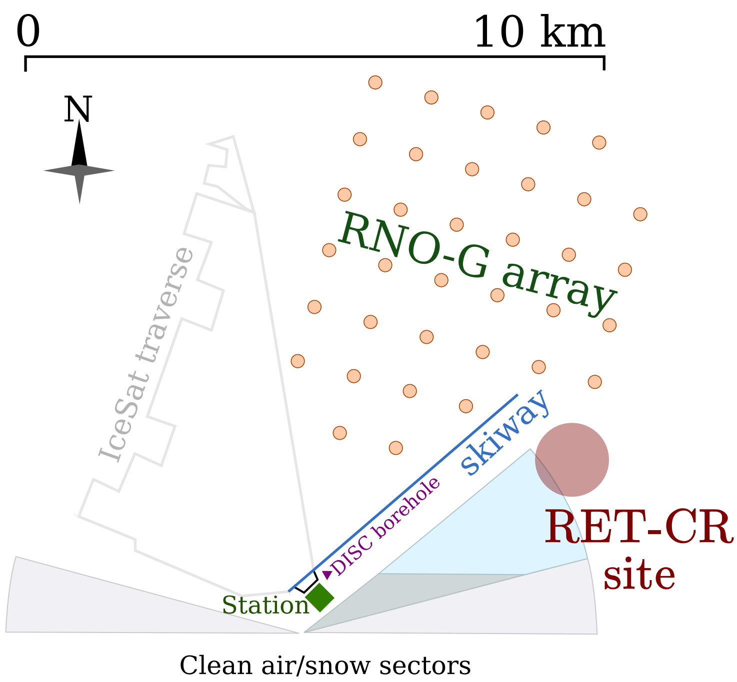


FIGURE 3.1: An overview of the Summit Station site, showing the RNO-G array currently under construction and the location of RET-CR. Figure modified from [58].

FIGURE 3.2: An image of Summit Station, with the Big House in the foreground. The Big House serves as the primary building for operations, and houses the kitchen, dining area and bathroom facility. Picture taken by B. Young, 2023.

## 3.2 Radio Neutrino Observatory Greenland

### 3.2.1 Station Design

The Radio Neutrino Observatory Greenland (RNO-G) is an Askaryan neutrino detector targeting astrophysical neutrinos at energies around several PeV up to the EeV range [58]. Its construction started in 2021, and at the time of writing 7 out of the 35 foreseen detector units have been successfully deployed. As explained in Chapter 2, the antennas of Askaryan neutrino detectors can be deployed deep in the ice or close to the surface, each approach having its advantages and disadvantages. RNO-G uses a hybrid layout for its detector units, combining the deep-ice approach from RICE and ARA with the surface design of ARIANNA, as shown in Figure 3.3.

#### Deep-ice component

The deep-ice component of an RNO-G station consists of 3 vertical strings going 100 m down in the ice. One string holds 7 vertically polarized (Vpol) antennas and 2 horizontally polarized (Hpol) antennas, called the power string. The other two strings are referred to as the helper strings and hold 2 Vpol antennas, 1 Hpol antenna and 1 calibration pulser each. This results in a total of 24 deep-ice readout channels per station. The boreholes are made using a custom-designed mechanical drill, which forms the main constraint on the depth of the channels.

The bottom 4 Vpol antennas on the power string form a phased trigger array. This array is designed to lower the signal trigger threshold by adding up the single waveforms of each channel with certain phase shifts, leading to coherent sums at a predefined range of angles of incident plane waves. This process is often referred to as beamforming. As noise is added up incoherently, this significantly reduces the signal-to-noise ratio. The viability of this technique has been demonstrated by the most recently deployed station of ARA [138]. The 2 Hpol antennas close to the phased trigger array allow for the reconstruction of the total electric field. The additional 3 Vpol antennas higher up on the power string are not part of the phased array, but instead are added to determine the neutrino interaction point and the zenith angle of the signal arrival direction more accurately.

The channels on the helper strings are necessary for a full neutrino direction reconstruction, as they provide additional azimuthal information. Furthermore, they are equipped with a pulser used for calibration of the antenna positions and regular monitoring of the station performance.

#### Surface component

The surface component consists of 9 log-periodic dipole antennas (LPDAs), distributed in sets of 3 around the data acquisition system (DAQ) box. Each set consists of 2 downward-pointing LPDAs and 1 upward-pointing LPDA. By adding a surface component, the total number of expected neutrino detections only increases slightly. However, for events detected in both the deep-ice and surface component the surface antennas add valuable timing information, and can perform precise polarization measurements. Moreover, since LPDAs have a good sensitivity over a larger range of frequencies, they significantly improve energy and direction reconstruction.

The upward-pointing LPDAs are used for the detection of radio emission from air showers. Although not the primary goal of the detector, the detection of cosmic-ray cascades can serve as an independent cross-check of up-time and efficiency, and

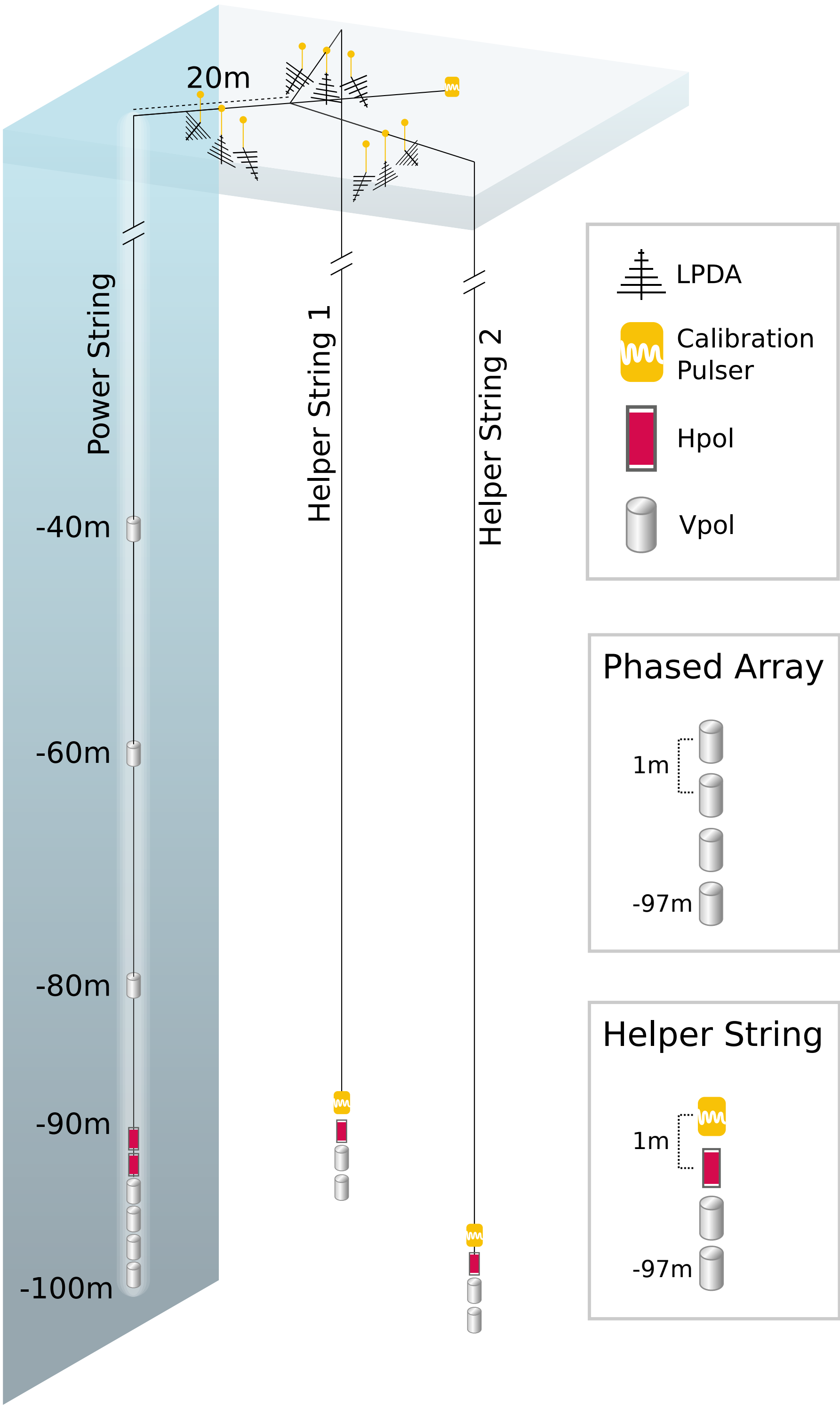


FIGURE 3.3: An RNO-G detector unit, combining surface antennas (LPDAs) with three strings of deep-ice antennas. A similar figure is given in [106]. The string on the left is called the power string, which holds 7 vertically polarized (Vpol) antennas and 2 horizontally polarized (Hpol) antennas. The bottom 4 Vpol antennas form a phased array trigger. The two other strings are referred to as the helper strings, which hold 2 Vpol antennas and 1 Hpol antenna each, as well as a calibration pulser.

can be used for calibration of the system. Moreover, it can help with identifying atmospheric muons triggering the deep-ice channels, which may form an important background for neutrino detection. As such, they can be used as a cosmic-ray veto system.

**Power consumption**

Emphasis lies on the scalability of the detector array. With 35 units and a grid spacing of roughly 1.25 km, RNO-G will monitor an area of around 50 km$^2$. Each station will function autonomously, powered by two 150 W solar panels and relying on a wireless LTE network for communication and data transfer.

Depending on the availability of sunlight, a station can switch between 4 different operation modes. During 'full-station mode' a station will be able to use the low-threshold trigger relying on the beamforming of the phased array, consuming about $\sim$ 24 W. At 'high-threshold mode', power consumption of the station is lowered down to $\sim$ 17 W by disabling the beamforming of the phased array, which increases the trigger threshold. The power consumption of the station can be reduced even further down to $\sim$ 6 W by switching to 'surface-only mode', in which only the 9 surface channels are considered for triggering and data acquisition. Finally, in 'winter-over mode' the station is turned off almost completely. Only the necessary data for housekeeping is being recorded, which consumes about 70 mW. A station should be able to run in full-station mode around 60% of the year, with the high-threshold and surface-only modes increasing the total uptime to roughly 70% of the year.

In order to decrease the time spent in winter-over mode, 2 stations are currently equipped with a wind turbine. The turbines are custom-designed to minimize the generation of radio background, to perform at low winds and to endure the harsh weather and climate. Similar turbines have already been deployed and tested at Moore's Bay in Antarctica by ARIANNA [139]. The effectiveness of the turbines and possible improvements are still under investigation.

### 3.2.2 Field Season of 2023

Following the successful deployment efforts in 2021 and 2022, RNO-G has managed to install a total of 7 out of 35 stations in the ice. During the summer of 2023 no additional units were deployed. Instead the collaboration shifted their focus temporarily towards maintenance, improvement and calibration of the existing detectors in preparation for intensive deployment seasons starting in 2024. In 2023 a field team of four members, including the author of this thesis, was sent to Summit Station from 06/15 to 07/17. Two additional members were on site from 06/15 to 06/28, with a focus on the main maintenance and calibration tasks.

**Maintenance tasks**

A picture of an RNO-G station site at the start of the Arctic summer season can be seen in Figure 3.4. During deployment of a station, all the components of the detector are either installed deep in the ice up to a depth of 100 m or buried in the snow close to the surface, with the exception of the two solar panels and the wind turbines. Flags are placed to mark the locations of the different parts, such as the central DAQ box, the three deep-ice strings and the surface antennas. Due to the accumulating drift of snow, the effective snow surface at a station site rises around the order of $1-2$ m per year. One of the key yearly maintenance tasks is therefore to raise the solar panels, wind turbines and flags, to prevent them from snowing in completely. Figure 3.5 shows a solar panel after being raised onto extended masts, ensuring its functionality for the subsequent seasons.

FIGURE 3.4: A picture of the RNO-G station "Nanoq", which is Inuit for polar bear, taken at the start of the Arctic summer season in 2023. The two solar panels (left) and the wind turbine (right) are clearly visible, as well as several flags marking the locations of different components of the detector.

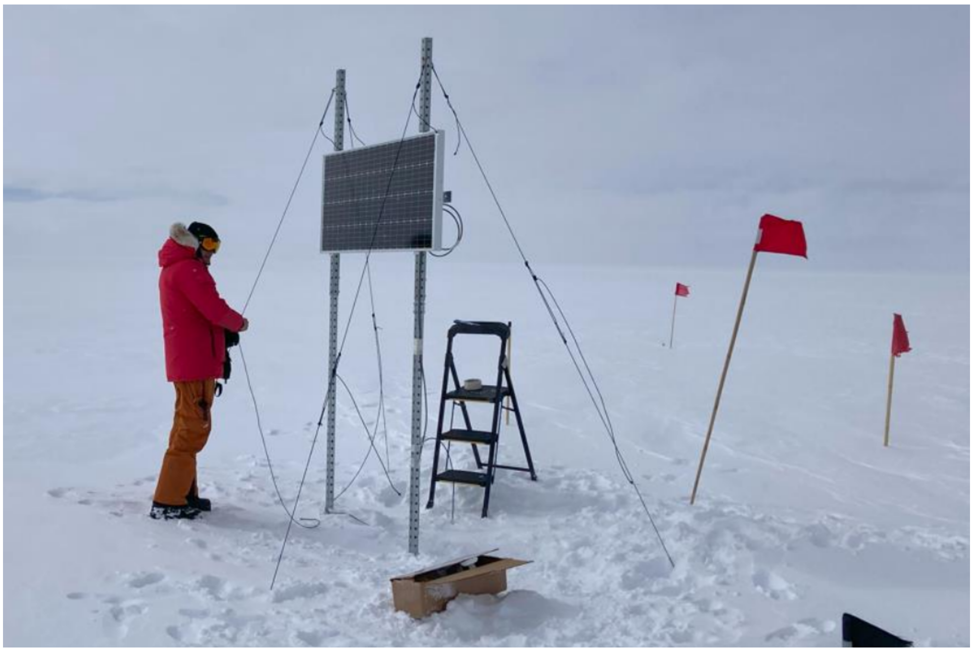

FIGURE 3.5: One of the solar panels at the Nanoq site after being raised onto the extended masts. Picture taken by E. Oberla.

An extra maintenance task in 2023 was to dig out the DAQ boxes of 3 stations and swap out the memory cards. This had to be done on-site, as disconnecting the box and transporting it back to Summit Camp would be a precarious undertaking. To avoid snow blowing into the DAQ box, this task could only be performed during favorable weather conditions, as shown in Figure 3.6.

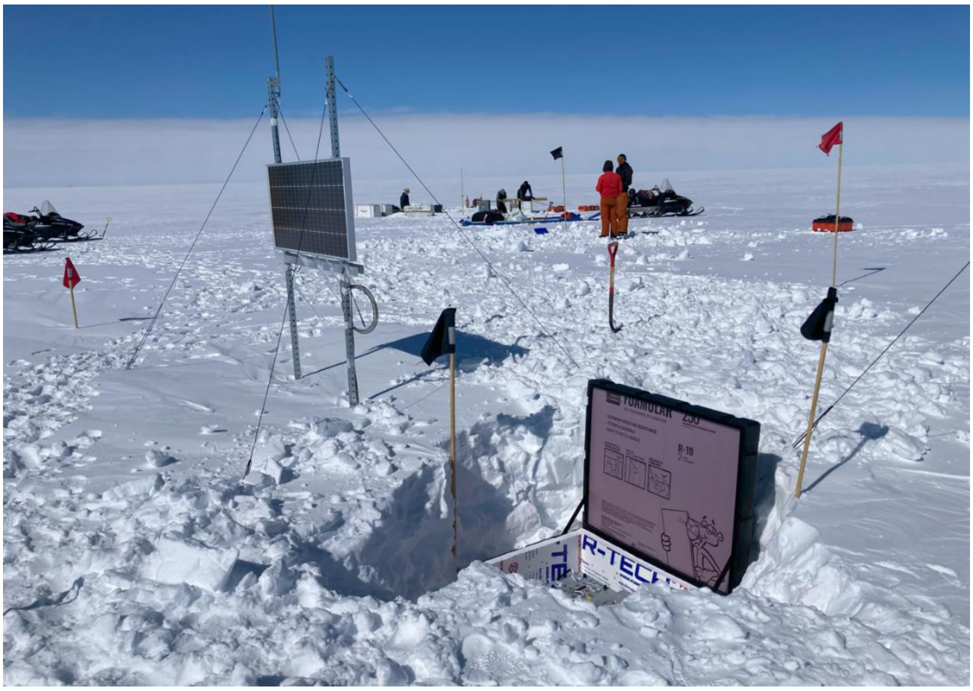

FIGURE 3.6: The DAQ box of station "Ukaliatsiaq", which is Inuit for ermine, dug up and opened at the detector site during favorable weather conditions to swap out the SD-card inside. Picture taken by E. Oberla.

**Calibration tasks**

One of the major calibration tasks of the 2023 field season was to determine the precise location of the different components of the 7 deployed stations, and to mark the location of the different components of 7 new stations with flags as preparation for the deployment season of 2024. To this end a GPS survey kit was used, which applies real-time kinematic positioning (RTK) corrections to achieve high accuracy. It consists of a base receiver for GPS measurements of a fixed reference point at Summit Station, and a rover receiver used for GPS measurements of locations in the field. Since the base receiver is fixed, its location can be surveyed for a long time, and it can therefore be determined with high accuracy. When performing a GPS survey in the field, the base station can compare real-time measurements of its position to the previously determined value of its position, and send the corresponding corrections to the rover. This increases the precision of the measurements down to the order of 1 cm, which is well within the uncertainty on the position of each component relative to its associated flag. Figure 3.7 shows the rover receiver being used in the field to determine the position of a previously deployed detector component.

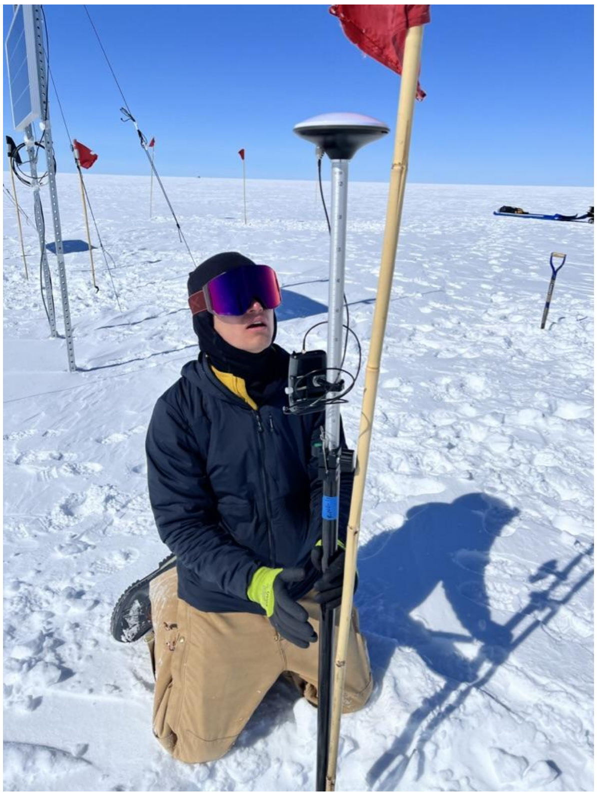

FIGURE 3.7: The GPS rover receiver being used in the field to determine the position of a previously deployed detector component. Picture taken by K. Hughes.

As a second calibration task, a mobile surface pulser was used to study the sensitivity of the existing stations. The pulser consisted of a vertically polarized antenna, connected to an oscilloscope and power source secured in a hard-case enclosure mounted on a sled. The antenna was buried in a shallow hole of roughly 0.5 m deep at different locations on each detector site, covering a range of distances and azimuth angles with respect to the station. Particularly of interest was the determination of the shadow zone horizon on the ice surface, i.e. the distance on the ice surface from which no radio emission can reach the station due to ray bending. The surface pulser setup can be seen in Figure 3.8. A similar setup was also used to send radio pulses from an elevated snow berm at Summit Station, illuminating several stations at the same time using a large horn antenna. The horn antenna installed on the snow berm is shown in Figure 3.9.

A third major calibration task was the use of a ground penetrating radar system (GPR) at the different station sites to study radio properties of the ice, as shown in Figure 3.10. The GPR is controlled with a tablet running dedicated software. It sends radio waves into the ice, and measures reflections from the cables and antennas deployed below the surface.

At the time of writing, a reconstruction of the antenna positions, the cable delays and the refractive index profile of the ice using the calibration data taken during the field season of 2023 is still ongoing. The results will be reported in a future publication.

FIGURE 3.8: The surface pulser setup used to study the sensitivity of the stations, in particular to determine the shadow zone horizon on the ice surface.

FIGURE 3.9: The horn antenna installed on the snow berm, used to send calibration radio pulses to several stations at the same time.

FIGURE 3.10: The ground penetrating radar system (GPR) being used at a station site to study radio properties of the ice.

**Melting probe testing**

The deployment of a single RNO-G station requires the drilling of three 100 m deep holes. This is achieved by using a large mechanical drill, which requires the full-time attention of an experienced group of three people. It would be valuable if in addition smaller and shallower holes of $\sim$ 20 m deep could be drilled to deploy calibration pulsers close to the detector units. To this end a custom designed melting probe was tested during the 2023 field season, which could offer an interesting drilling technique suitable for calibration holes that requires significantly less time and effort from the deployment team. To start the drilling, the melting probe needs to be mounted on a tripod while gently resting on the ice surface. Once turned on, the probe will heat up and start melting down into the ice. The meltwater dissipates into the firn, which means no effort is needed to clear the drilling hole. The melting probe can therefore operate autonomously, only requiring part-time attention of a single person monitoring the process. The melting probe mounted to its tripod during an initial performance test can be seen in Figure 3.11.

The goal of the 2023 field season was to drill two holes with a depth of 20 m each at a single station site. After some initial tests, the probe was successfully deployed to create a 10 m deep hole after about 2 hours of melting. However, when the probe was redeployed the day after to resume the drilling, a technical failure caused the probe to freeze in at the bottom of the hole. Fortunately the melting probe was retrieved, but as the cause of the failure was not clear the probe was no longer used for drilling.

Even though the melting probe did not manage to deliver the two planned boreholes, a single hole of 20 m deep was drilled close to one of the stations by a collegial science team looking for a suitable remote location to retrieve a clean ice core sample. This hole was then used to deploy a vertically polarized calibration antenna.

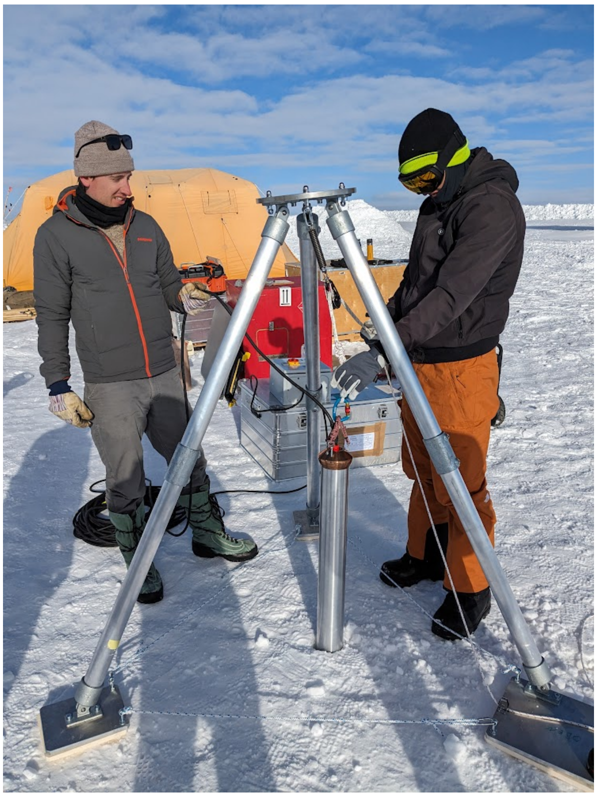

FIGURE 3.11: The melting probe mounted to a tripod during an initial performance test.

## 3.3 Radar Echo Telescope for Cosmic Rays

### 3.3.1 Station Design

The Radar Echo Telescope for Cosmic Rays (RET-CR) is a detector designed to demonstrate the viability of the radar echo method to detect ultra-high-energy neutrinos [133]. As explained in Chapter 2, this method relies on the reflection of radio waves off of the ionization trail created by neutrinos interacting in ice. Several studies as well as the recent results from the T576 experiment at SLAC are showing promising results in favour of the technique, yet a proof-of-principle in nature is still missing.

At altitudes of the order of 3 km, such as at Summit Station or the South Pole, ultra-high-energy cosmic rays can serve as an interesting natural test beam. Air showers initiated by these cosmic rays develop deep in the atmosphere. As will be shown later in Chapter 4, the energy contained within the core of the particle cascade when it reaches the ice surface is around $10 - 30$ % of the primary energy. Ultra-high-energy cosmic-ray air showers propagating through ice should therefore create very similar ionization trails when compared to neutrino-induced particle cascades. Cosmic rays are however much more likely to interact, and the corresponding observed flux is significantly higher. In addition, cosmic-ray air showers can be detected by complementary techniques, which can be used to tag cosmic-ray events and characterize the cosmic-ray properties.

The RET-CR detector was deployed at the Summit Station site during the field seasons of 2023 and 2024, as shown in Figure 3.1. Its primary goal is to detect ultra-high-energy cosmic-ray air showers penetrating the ice using the radar echo method.

It relies on surface scintillator panels and radio antennas to provide an external trigger to the radar data acquisition system (DAQ), as well as an independent reconstruction of the air shower characteristics. This concept is illustrated in Figure 3.12. As of 2024 the detector includes a phased transmitter array, 4 receiving antennas and 5 surface stations, as shown in Figure 3.13.

#### Radar System

The radar system is formed by a phased transmitter array at the center of the station site, surrounded by 4 receiver antennas. The transmitter array consists of 8 vertically polarized dipole antennas identical to the receiver antennas, with a vertical separation length of $\sim 0.25$ m. The transmitter array and the three closest receivers were deployed in 2023, at a depth of approximately 10 m in the ice. A fourth receiver was added in 2024 roughly 12 m below the ice surface, at an increased distance from the transmitter array.

The receivers are constantly being illuminated by the transmitter, both via emission directly reaching the receivers as well as radio waves reflecting off of the ice-air boundary. Therefore the receivers need to apply a filtration process to avoid saturation of their amplifiers. As a simple passive filter at the transmitter frequency would also remove interesting echo events, this process needs to be active. The active transmitter cancellation essentially injects a phase-shifted copy of the transmitter signal into the receiver, optimizing the cancellation using a two-stage minimization process. Once an appropriate phase-shift and amplitude are found for the injection, the transmitter signal can be reduced down to the thermal noise level. This procedure is then repeated several times throughout the day to account for changes in the environment influencing the signal propagation, such as the accumulation of snow on the ice surface.

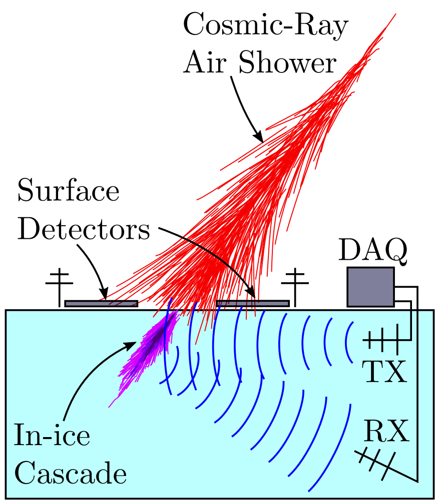


FIGURE 3.12: The concept of the RET-CR detector [133]. The radar system consists of a transmitter (TX) and receiver (RX) component, which are constantly monitoring the ice. A cosmic-ray air shower passes through the scintillator panels of the surface stations, triggering the radar DAQ. The shower propagates further into the ice, reflecting the radio emission from the transmitter into the receiver, which is recorded by the DAQ. The surface antennas measure the radio emission created directly by the air shower, providing additional information for the reconstruction of the air shower characteristics.

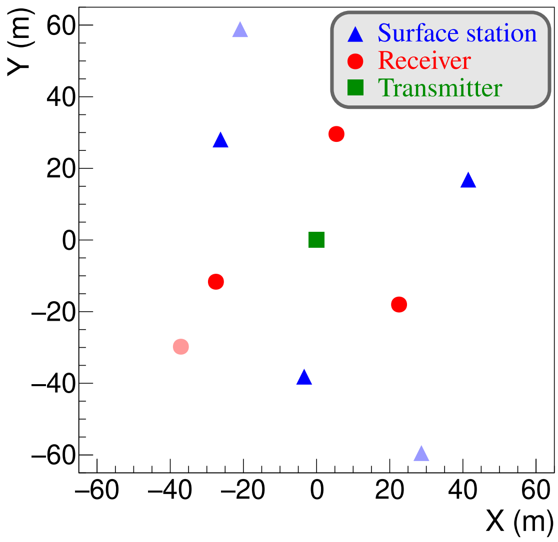


FIGURE 3.13: The station layout of RET-CR, at the end of the 2024 deployment season. The phased transmitter array located in the center is surrounded by 4 receiving antennas and 5 surface stations. The three components added in 2024 are indicated in lighter colors.

The radar system is powered by a solar panel array set up in a triangular formation, each side capable of delivering 1.2 kW of power. This is the only power source provided, as the experiment is designed to run during the Arctic summer, when the sun does not set below the horizon. Communication and data transfer with the radar DAQ is done over a WLAN connection with Summit Station.

#### Surface Stations

Each surface station consists of two scintillator panels and a log-periodic dipole antenna (LPDA), deployed on the ice surface. The scintillator panels form the main external trigger for the radar system, and combined with the LPDA provide extra information for the reconstruction of the air shower properties. The LPDA was originally designed for the Square Kilometer Array (SKA) [140], while its data acquisition system was repurposed from the CODALEMA experiment [32]. The three surface stations closest to the transmitter location were deployed in 2023, with the addition of two more stations farther away from the detector center in 2024. Each surface station is powered by a single 4-faced solar tower.

### 3.3.2 Field Season of 2024

The first field season of RET-CR took place during 2023, which resulted in the successful deployment of the transmitter array, 3 receiver antennas, 3 surface stations and a first data taking run. Due to overheating of the radar DAQ enclosure, the data taking run was shorter than initially planned. Nevertheless it demonstrated the viability of some key features, such as the operation of the phased transmitter array and the active transmitter signal cancellation. Therefore a second field season was approved to implement several improvements to the detector, to deploy two additional surface stations and an extra receiver, to perform ice density studies and to determine the GPS positions of the different components of the detector using a similar setup as described in Section 3.2.2. The 2024 field team consisted of five members in total. Three members, including the author of this thesis, were sent to

Summit Station from 05/01 to 05/21. Two additional members joined the team from 05/09 to 05/21, focusing on the ice density studies and the GPS measurements.

**Relocation of the solar array**

At the end of the 2023 season all surface components of the detector were retrieved, with the exception of the LPDA antennas, the scintillator panels and the large solar array. The first major task of 2024 was to relocate the solar array, as during the winter period about 2 m of snow had accumulated at the detector site. Fortunately most of the accumulation is due to snow drift, which created a well surrounding the array. This made it possible to dismantle the array, lift the components out of the well and reassemble it at a new location within the first two days of the field season. Pictures of the solar array before and after relocation are shown in Figure 3.14. The LPDAs and the scintillator panels deployed in the previous season were not relocated. The antennas were raised onto bamboo sticks during the 2023 deployment season to counter the accumulation, while the snow on top of the scintillator panels does not significantly affect their performance.

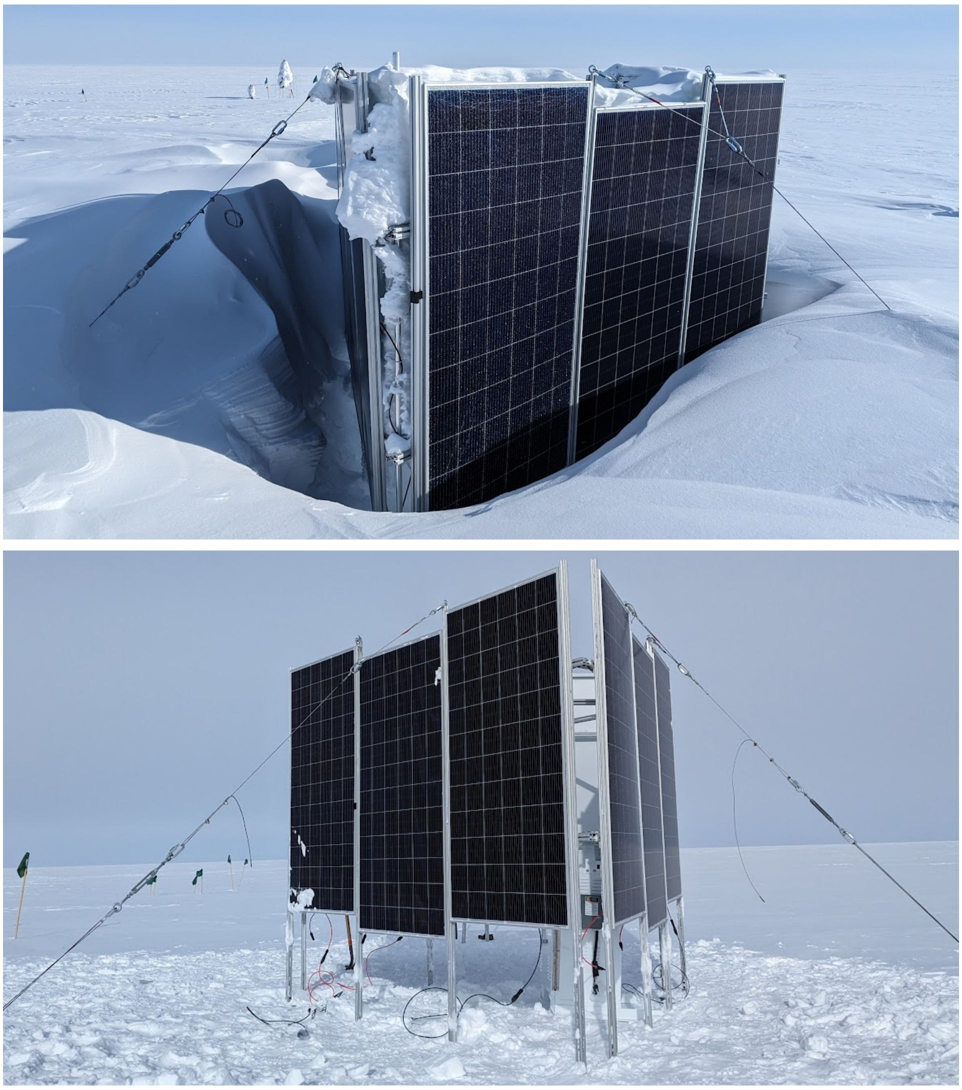

FIGURE 3.14: The solar panel array powering the radar system, before relocation at the start of the 2024 field season (top) and after relocation (bottom).

### Deployment of the radar DAQ

The radar DAQ enclosure was redesigned for the new season, now featuring a large heat sink on top of the box to avoid overheating of the instrument. Furthermore, the enclosure was raised onto a wooden platform to prevent the instrument from melting down into the snow. The platform was built close to the solar panel array to ensure the connection to the enclosure could be made, but far enough to avoid a significant shadow being cast onto the panels. A picture of the raised radar DAQ box can be seen in Figure 3.15.

FIGURE 3.15: The radar DAQ enclosure equipped with a large heat sink on top, raised onto a wooden platform to prevent the instrument from melting down into the snow.

### Deployment of the surface stations

To redeploy the three surface stations, the read-out electronics were prepared and installed into single enclosures. These enclosures where then connected to their corresponding scintillator panels and LPDA, as well as the main radar DAQ box mounted on the wooden platform. Two additional surface stations were deployed farther away from the detector center, which required the excavation of the unused scintillator panels that were left at the site during the 2023 season, as well as the assembly of two additional LPDAs. For each of the 5 surface stations a solar tower was constructed, holding 8 solar panels distributed over 4 sides. Furthermore, a significant amount of time was dedicated to the testing and adjusting of the individual surface stations, as well as the combination of the surface stations with the radar system as a whole. A picture of a surface station can be seen in Figure 3.16.

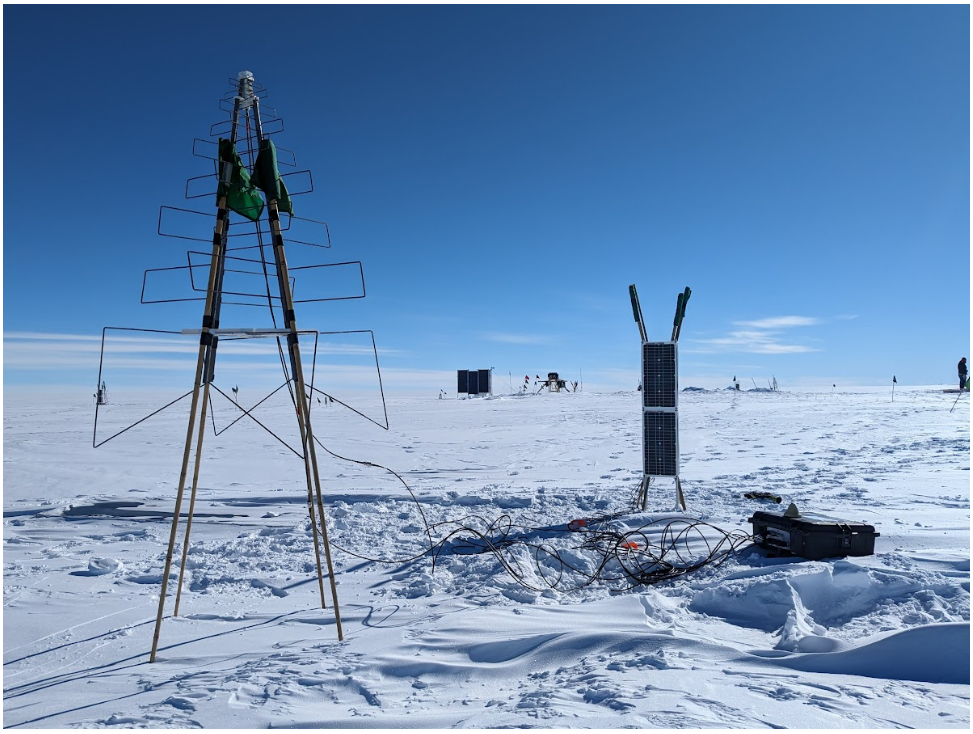

FIGURE 3.16: A completed RET-CR surface station. It consists of two scintillator panels, a raised LPDA, a solar tower and an electronics enclosure connected to the radar DAQ in the background.

**Deployment of the extra receiver**

During the 2024 season a fourth receiver antenna was added to the detector, introducing a channel located farther away from the transmitter array. A new borehole was created using a Kovacs ice core drill, able to drill holes with a depth of the order of $\sim 10$ m. A vertically polarized dipole antenna was lowered down to the bottom of the hole and connected to the radar DAQ. Figure 3.17 shows a picture of the drilling process, with the result shown in Figure 3.18.

FIGURE 3.17: The Kovacs ice core drill being used to create the fourth receiver borehole.

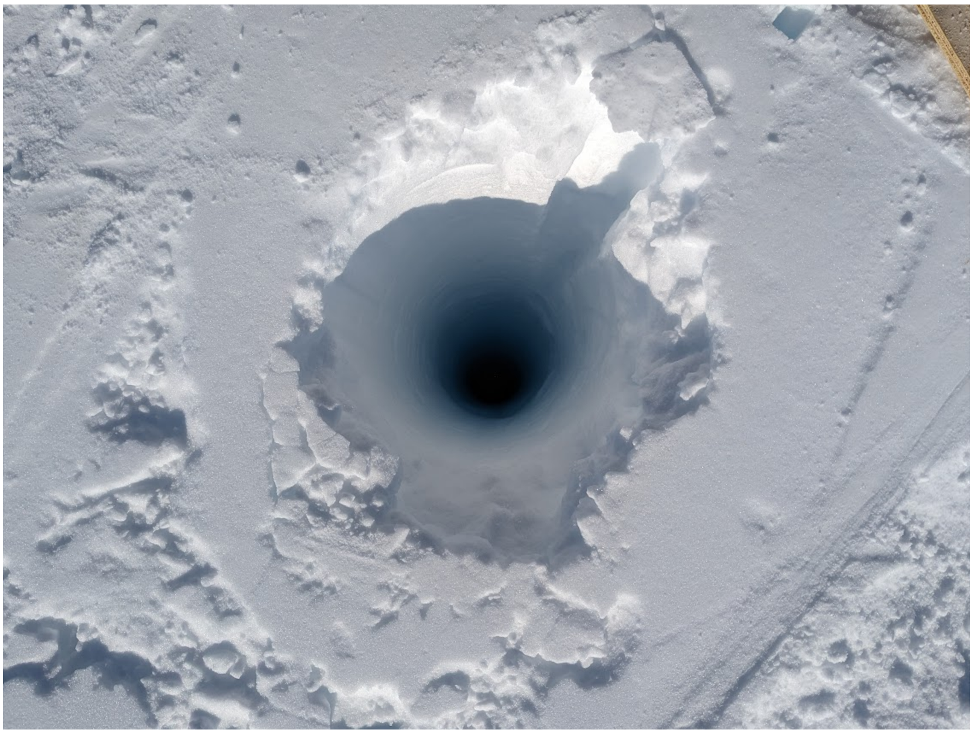

FIGURE 3.18: The borehole of the extra receiver installed during the 2024 field season.

# Chapter 4

## Cosmic-Ray Particle Cascades in Ice

### 4.1 Introduction

As outlined in the previous chapters, several projects are currently exploring the viability of observing ultra-high-energy neutrinos using radio antennas in ice. A neutrino interacting in the ice will induce a particle cascade, which generates radio emission through the Askaryan effect. Furthermore, radio waves emitted by an active transmitter could reflect off of the ionization trail associated with the cascade, providing an alternative method for neutrino detection.

Theoretical studies and simulations of both methods show promising results. Moreover, several experiments have observed Askaryan emission from cosmic-ray air showers, even though the geomagnetic component is usually much stronger. However, radar echoes and Askaryan emission from particle cascades in denser media have so far only been detected by experiments relying on particle accelerators. At the time of writing, a real proof-of-principle in nature is still missing.

This chapter will present simulations of ultra-high-energy cosmic-ray air showers propagating through ice at an altitude of 2.4 km above sea level. The altitude was chosen to correspond to Taylor Dome, an ice dome in East Antarctica which for some time was identified as a possible location for the RET-CR detector. Nevertheless, this altitude represents a typical value for many polar regions in general, such as the Summit Station site in Greenland (3.2 km) and the South Pole (2.8 km). At these altitudes, cosmic-ray air showers with primary energies of $10^{16}$ eV and more and zenith angles up to $\sim 30°$ will reach a maximum number of particles close to the surface, indicating that a significant portion of the energy of the primary particle will propagate through the ice. As most of the energy in the air shower is in the electromagnetic component, which is more densely concentrated around the core, the transition from air to ice will create an in-ice particle cascade similar to those initiated by neutrino interactions. However, cosmic rays are much more likely to interact, and the corresponding observed flux is significantly higher. Cosmic rays could therefore be a valuable test beam in nature, to verify both the Askaryan radio detection technique as well as the radar echo method.

In addition, the radio emission from cosmic-ray particle cascades in ice forms an important background for Askaryan radio neutrino observatories. Although neutrinos usually interact deeper in the ice, inhomogeneities in the ice can cause radio waves to change propagation direction. This can make a cosmic-ray cascade in ice look like a deep-ice event, and vice-versa. Furthermore, given a good understanding of the radio emission from cosmic-ray cascades, the corresponding signals could be used for calibration purposes.

Currently, only a limited amount of studies exist that investigate the propagation of cosmic-ray air showers into ice or other media [141–150]. High-energy neutrino observatories such as the IceCube Neutrino Observatory rely on the detection of

Cherenkov light, and as such are only sensitive to atmospheric muons propagating deep in the ice. The primary goal of the work presented in this chapter is to understand the key features of cosmic-ray particle cascades in ice, relevant for the Askaryan radio emission of such events. Chapter 5 will present the Framework for the simulation of Air shower Emission of Radio for in-Ice Experiments (FAERIE), which combines the simulation software presented in this chapter with the existing CORSIKA and CoREAS codes to simulate the radio emission of cosmic-ray air showers, including both the emission in air and in ice.

Most of the content of this chapter is published as part of this thesis work in a peer-reviewed article [1].

## 4.2 Simulation of Cosmic-Ray Air Showers

At primary energies of $10^{16}$ eV and above, the center-of-mass energies of the first interactions of cosmic-ray air showers start to surpass the current limit of particle accelerators on Earth. Moreover, accelerators need to rely on collisions between two moving beams to achieve high center-of-mass energies, while the particles in air shower cascades collide with fixed targets in the atmosphere. In short, simulations of ultra-high-energy cosmic-ray air showers need to take into account particle interactions in a center-of-mass energy and momentum range which is currently not explored by accelerator experiments. Simulating cosmic-ray air showers therefore requires dedicated software, optimized for these regimes.

A computationally-heavy but accurate approach is to simulate the air shower on the level of the individual particles. The general idea is to follow each single particle in the cascade while it propagates through the medium in discrete steps. Random numbers decide at which point the particle interacts, and determine the characteristics of the interaction. The distributions used to generate the various processes follow from the interaction models implemented in the code. The hadronic interaction models suffer the most from the lack of accelerator data, and therefore carry the largest uncertainties [16]. Codes relying on the sampling of random numbers are called Monte Carlo codes, named after a district in Monaco famous for its casino. Several Monte Carlo codes have been developed for the simulation of cosmic-ray air showers, such as CORSIKA (COsmic Ray SImulations for KAscade) [151] and AIRES (AIRshower Extended Simulations) [152]. Note that random numbers in this context are in fact pseudorandom, in the sense that they follow from complex but deterministic algorithms designed to mimic the properties of truly random numbers. Such algorithms start with a predetermined number, called the random number seed, and using the same seed will always results in the same sequence of pseudorandom numbers.

Monte Carlo air shower simulations are usually very computationally heavy. At ultra-high energies they involve millions to billions of particles, which all need to be taken into account. The computation cost and simulation time can be reduced by using energy cuts, either in the form of tracking cuts or production cuts. In the case of tracking cuts, a particle is discarded during the simulation of the cascade as soon as it falls below the corresponding kinetic energy threshold. When using production cuts, each particle in the cascade is tracked down until it has no kinetic energy left. However, particles are only tracked down if the kinetic energy with which they are produced is above the corresponding energy threshold. Energy cuts are in fact indispensable, as they also avoid infrared divergence [153, 154].

In addition to energy cuts, the computation cost and simulation time can be reduced further by applying statistical thinning [155, 156]. The general idea of statistical thinning is to introduce an artificial acceptance probability, which determines whether newly produced particles are selected for further tracking or not. The particles that are accepted are assigned a weight, which accounts for the particles that are not being tracked. Thinning leads to non-physical clustering, by introducing single weighted particles that in some sense represent multiple particles. Therefore thinning is only applied to particles below a given energy threshold, and the weights assigned to particles are restricted to a certain maximum value.

Below, the global properties of ultra-high-energy cosmic-ray air showers will be illustrated. The focus will lie on the simulation results of a cascade initiated by a $10^{17}$ eV proton with a zenith angle $\theta = 0°$, which will be referred to as the reference air shower. The air shower was simulated with the CORSIKA 7.7100 Monte Carlo code, the QGSJETII-04 high-energy hadronic interaction model [157], the GHEISHA 2002d low energy hadronic interaction model [158] and a MSIS-90-E atmospheric model for South Pole on December 31, 1997 [159]. More information on the modeling of the atmosphere can be found in Appendix A. Tracking cuts were used, set at 0.3 GeV for hadrons (without $\pi^0$'s) and 0.003 GeV for electrons, positrons, photons and $\pi^0$'s. Thinning was only applied to photons, electrons and positrons below $10^{10}$ eV, and the weight limit was set to 10.

It is important to keep in mind that global properties fluctuate from shower to shower, even if the primary particle type, energy and zenith angle are the same. These arise from fundamental physical fluctuations during the interactions of the primary and secondary particles. A good example of a global variable that fluctuates from shower to shower is the depth $X_{\text{max}}$, where the shower reaches the maximum number of electrons and positrons. The depth $X$ of a particle cascade represents the amount of mass traversed in the medium. It can be found by integrating the density of the medium along the shower axis, and is usually expressed in units of g/cm$^2$. Figure 4.1 shows the depth of shower maximum $X_{\text{max}}$ as a function of primary energy, measured by the Pierre Auger Observatory, compared to predictions

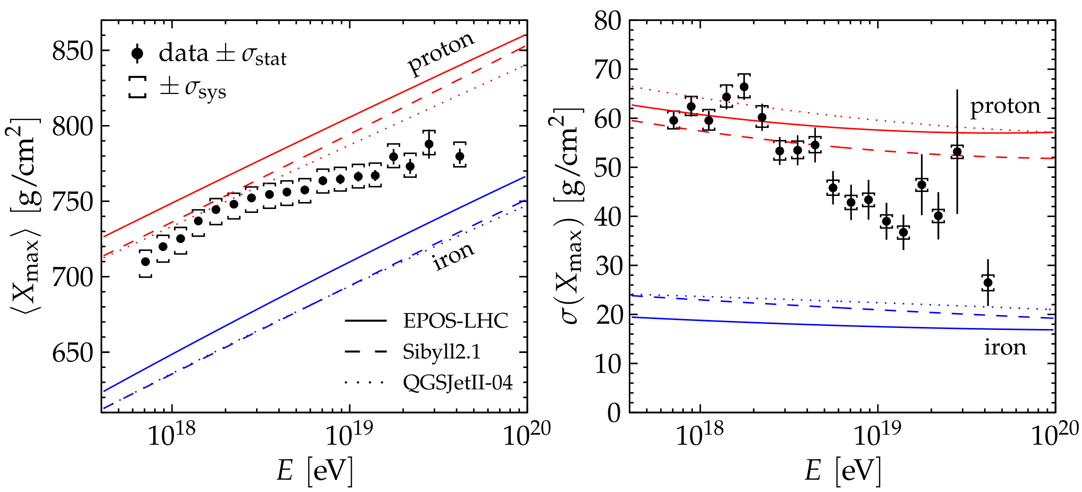


FIGURE 4.1: The mean depth of shower maximum $X_{\text{max}}$ as a function of primary energy (left) and the corresponding dispersion corrected for the reconstruction resolution (right), measured by the Pierre Auger Observatory. The data is compared to predictions from simulations for proton and iron primaries, using different hadronic interaction models. Figure modified from [160].

from simulations for proton and iron primaries. As illustrated by the right panel, even when the primary particle type and energy are fixed during the simulations, shower-to-shower fluctuations lead to a dispersion of $X_{\text{max}}$ of the order of 60 g/cm$^2$ for proton primaries and 20 g/cm$^2$ for iron primaries. As $X_{\text{max}}$ is measured along the shower axis, it does not depend on the zenith angle $\theta$ of the primary particle. The dispersion is therefore due to fluctuations of particle interaction characteristics, such as depth of interaction, multiplicity and elasticity [16]. Interestingly, the magnitude of the dispersion depends on the primary type, which means it can be used for cosmic-ray composition studies [161].

### 4.2.1 Longitudinal Shower Profile

Figure 4.2 shows the number of particles and the energy distribution as a function of depth of the reference air shower, simulated using a proton primary with a primary energy $E_p = 10^{17}$ eV and zenith angle $\theta = 0°$. The total number of electrons and positrons of the shower reaches its maximum at a shower depth $X_{\text{max}} = 680$ g/cm$^2$. As shown by Figure 1.9, this is close to the average value for simulated proton-induced showers at the given primary energy.

The black vertical line indicates an altitude of 2.4 km above sea level, which corresponds to a depth of 734 g/cm$^2$. At this altitude, the number of particles in the electromagnetic part of the cascade (gammas, electrons and positrons) heavily outnumber the particles in the hadronic part of the cascade (muons, antimuons and hadrons). However, looking at the energy distribution, the difference between both components is less extreme. Most of the energy is in the electromagnetic part of the shower, but the hadronic part also carries a significant fraction. Added up together, the cascade particles contain about 50% of the energy of the primary particle, of which roughly 75% is in the electromagnetic part and 25% is in the hadronic part. The remaining 50% of the primary energy is dissipated in the atmosphere, mostly due to ionization energy losses of the electromagnetic component.

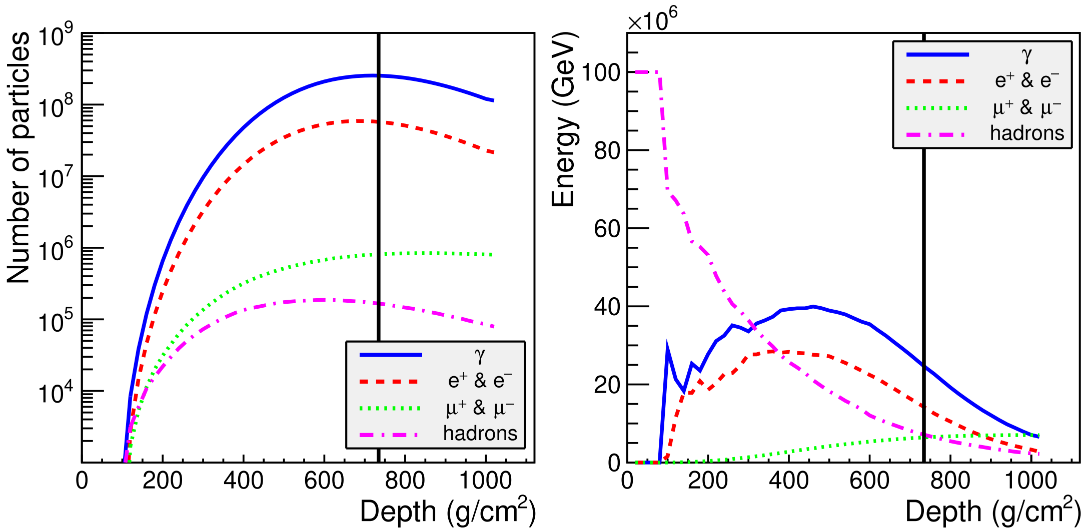


FIGURE 4.2: The number of particles (left) and the energy distribution (right) of the reference air shower ($E_p = 10^{17}$ eV, $\theta = 0°$) as a function of depth, simulated using CORSIKA 7.7100 [1]. The black vertical line indicates an altitude of 2.4 km above sea level, which corresponds to a depth of 734 g/cm$^2$.

In summary, an ice sheet located 2.4 km above sea level would be struck by the air shower close to shower maximum, where the cascade still carries a significant portion of the energy of the primary particle. The development of the in-ice cascade will be determined mainly by the electromagnetic part of the shower, which dominates in terms of number of particles and carries most of the energy of the shower. The hadrons will interact with the medium, adding to the electromagnetic component of the in-ice cascade through $\pi^0$ decay, while the muons will propagate through the ice sheet.

### 4.2.2 Lateral Shower Profile

Figure 4.3 shows the energy in the simulated reference air shower as a function of radius at an altitude of 2.4 km above sea level. Looking at the total energy shown in the left side of the figure, we see that the air shower contains a very energy-dense core. The particles in the first 1 m from the shower core contain about 40% of the cascade energy, which translates to 20% of the energy of the primary particle. The remaining 60% of the cascade energy is spread out over the rest of the air shower footprint, which has a radius of the order of 5 km.

The right side of the figure shows the average kinetic energy per particle. Indicated by a black horizontal line is the value of 80 MeV, which is a reasonable value for the critical energy for electrons in ice [162]. Above this threshold radiation energy losses dominate, which leads to pair production. Therefore, as a rule of thumb, above the critical energy electrons are expected to generate showers. Below the critical energy ionization losses start to dominate, which means that electrons falling below this threshold no longer contribute to the particle shower development. The figure shows that only close to the shower axis the electrons, positrons and gammas have energies above the critical energy. At distances beyond $\sim 1$ m, most particles will vanish after a few radiation lengths equal to $X_{rad} \approx 40$ g/cm$^2$ [163]. As such, we use a radius of 1 m to define the so-called shower core.

Figure 4.4 shows the energy fraction of the shower core at an altitude of 2.4 km above sea level relative to the primary energy $E_p$, as a function of primary energy $E_p$ and zenith angle $\theta$ of the cascade. Here the energy of the core $E_c$ is defined as the energy within 1 m of the shower axis in the shower plane. Each point represents the average of 10 CORSIKA simulations. It drops rapidly with increasing zenith angle, as more inclined air showers need to propagate longer through the atmosphere to reach the given altitude. Furthermore, at higher primary energies, the fraction of the energy of the primary particle contained within the core is larger. Showers at higher primary energies develop deeper into the atmosphere, and are therefore sampled by the observer plane at an earlier stage in their development. At zenith angles up to $\sim 30°$ and primary energies above $10^{16}$ eV, the core of the shower carries around $10 - 30$ % of the energy of the primary particle.

We conclude that at an altitude of 2.4 km, around $10 - 30$ % of the energy of the primary particle is located within 1 m from the shower axis, for showers with primary energies above $10^{16}$ eV and zenith angles up to $\sim 30°$. When propagating through ice this energy-dense core will induce an in-ice particle shower, mimicking a high-energy neutrino-induced cascade. Particles outside the air shower core will quickly disappear, barely influencing the in-ice cascade development.

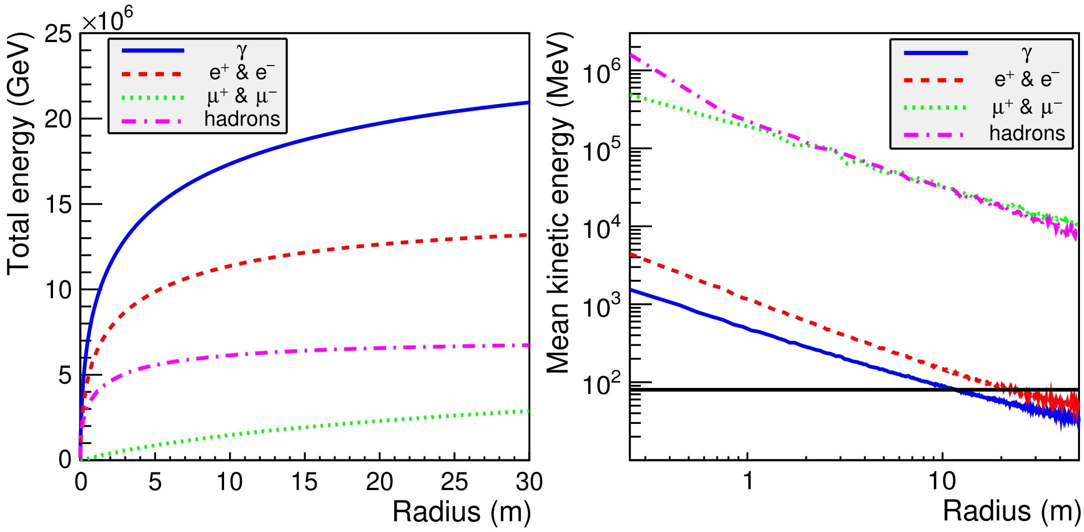


FIGURE 4.3: The energy in the simulated reference air shower ($E_p = 10^{17}$ eV, $\theta = 0°$) at an altitude of 2.4 km above sea level [1]. Left: the total energy within a given radius for the different particle types. Right: the average kinetic energy per particle in function of radius for the different particle types. The black horizontal line indicates the value of 80 MeV. For the electromagnetic part ($\gamma$, $e^-$, $e^+$) the average was calculated over radial bins with a bin width $\Delta r = 0.1$ m. For the hadronic part ($\mu^-$, $\mu^+$, hadrons), $\Delta r = 0.5$ m was used.

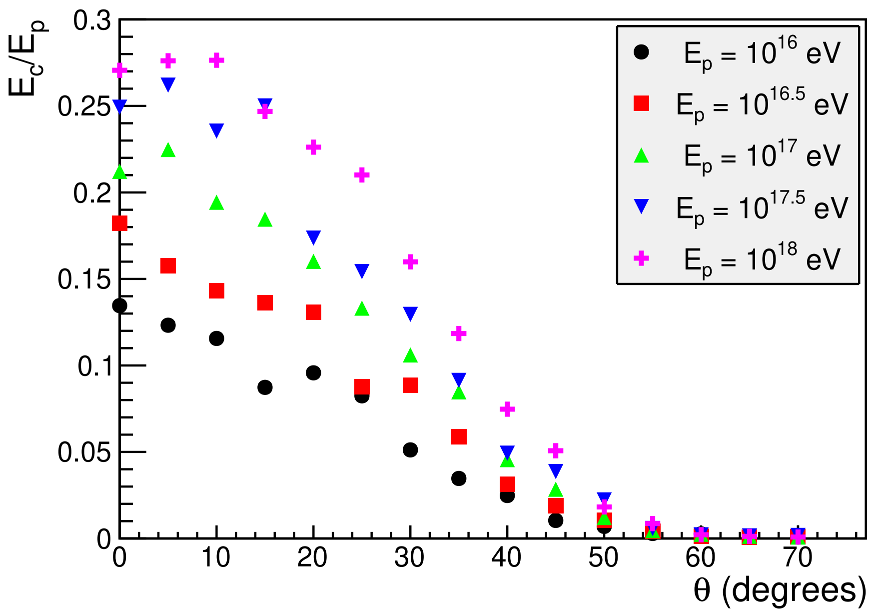


FIGURE 4.4: The energy fraction of the shower core at an altitude of 2.4 km above sea level relative to the primary energy $E_p$, as a function of primary energy $E_p$ and zenith angle $\theta$ of the cascade. The energy of the core $E_c$ is defined as the energy within 1 m of the shower axis in the shower plane. The value of the primary energy of the cascade is indicated by the marker symbol. Each point is averaged over 10 CORSIKA air shower simulations. Thinning was applied for showers with $E_p \geq 10^{17}$ eV on electromagnetic particles below $10^{-7}E_p$, with maximum weights of 10 ($E_p = 10^{17}$ eV and $E_p = 10^{17.5}$ eV) and 100 ($E_p = 10^{18}$ eV).

## 4.3 Propagation of Air Showers in Ice

In this section some key features of the in-ice particle cascades created by ultra-high-energy cosmic-ray air showers propagating through ice at an altitude of 2.4 km above sea level will be discussed. First the focus will lie on the reference air shower described in the previous section, and will then be shifted towards a more general analysis.

As shown by Figure 4.3, by the time the cascade front reaches the altitude of 2.4 km above sea level, most particles in the shower have a kinetic energy below 1 TeV. To simulate the propagation of the cascade through ice, we can therefore use the Geant4 Monte Carlo simulation toolkit [164]. This toolkit was developed to simulate the propagation of particles and radiation through matter at energies up to the TeV scale, and is widely used by the high-energy physics community, such as the Large Hadron Collider (LHC) experiments at the European Council for Nuclear Research (CERN). It provides functionalities that can be implemented in C++ software projects to simulate physics processes for a variety of applications.

The Geant4-based software developed for this work uses the output from the CORSIKA Monte Carlo code, which contains the position, momentum, arrival time and thinning weight for each individual particle, as an input to simulate the propagation of the cascade through ice. The ice is modeled as a multi-layered medium of $H_2O$ molecules. Each layer has a thickness of 1 cm and a constant density determined by the depth of the layer, determined by the relation

$$\rho(z) = \rho_{\text{ice}} - (\rho_{\text{ice}} - \rho_{\text{surface}}) \exp\left(-\frac{1.9}{t_{\text{firn}}}|z|\right). \tag{4.1}$$

We use the values $\rho_{\text{ice}} = 928\ \text{kg/m}^3$, $\rho_{\text{surface}} = 460\ \text{kg/m}^3$ and $t_{\text{firn}} = 95$ m, which follow from a fit to data taken from an ice core retrieved at the Taylor Dome site, measured in the field within a few hours of core recovery [165, 166]. In contrast to air shower simulations with CORSIKA, we do not include Earth's magnetic field for the simulations in ice. We expect the lifetime of the particle cascade in ice to be too short for the magnetic field to have any influence on its development, similar to neutrino-induced particle cascades in ice.

The physical processes included in the simulation are the Geant4 standard electromagnetic processes, the decay physics of particles and radioactive decay processes. The Geant4 standard electromagnetic processes include $e^+/e^-$ pair production, Compton scattering, Coulomb scattering, bremmstrahlung and ionisation, taking into account the LPM effect at high energies. A full description of the electromagnetic processes can be found at [167, 168].

Geant4 uses production cuts, defined in units of length. Secondary particles are only tracked down in the simulation if at production they are able to travel a larger distance than their corresponding cut-off length. The cut-off lengths used in the simulations are the default values, which is 1 mm for gammas, electrons and positrons. No extra thinning is applied, and the thinning weights from the CORSIKA simulation are directly passed on to the corresponding secondaries in the ice.

To decrease the computation costs of the simulations, only particles within a radius of 5 m from the shower axis are propagated into the ice. As demonstrated in the previous section, we do not expect any significant contribution to the in-ice shower development from particles beyond this region.

### 4.3.1 Deposited Energy

Figure 4.5 shows the energy deposited by the reference air shower described in the previous section when propagating through the ice at an altitude of 2.4 km, simulated with the Geant4-based software.

As discussed above, we expect ionization losses to dominate over radiation losses at meter distances from the shower core. In this regime, particles should vanish after several radiation lengths of $X_{rad} \approx 40\ \mathrm{g/cm^2}$, which for the density profile given by Equation 5.26 translates to a distance of 0.86 m in the upper layers of the ice. Closer to the core the energy of the particles is still well above the critical energy, and we expect the shower to continue developing. This picture is confirmed by the figure. The core of the cascade is still growing when propagating through the ice, reaching its maximum a few meters below the ice surface, while the rest of the shower is dying out. Note that the core of the particle cascade extends down to about 20 m in the ice, which is orders of magnitudes smaller than the longitudinal dimension of showers in air.

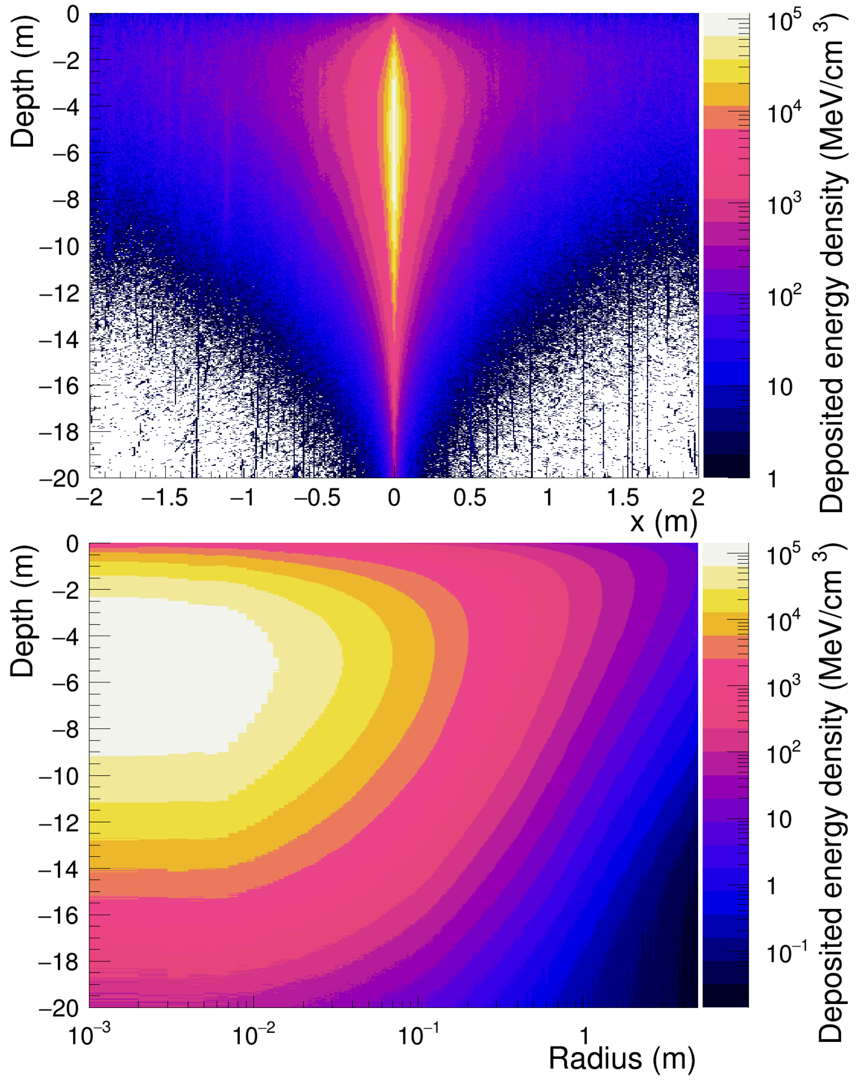


FIGURE 4.5: The energy deposited in the ice by the reference air shower ($E_p = 10^{17}$ eV, $\theta = 0°$) [1]. Top: the deposited energy density within a vertical 1-cm wide slice going through the center of the particle shower. Bottom: the radial energy density profile.

An interesting quantity to describe the lateral scale of the energy deposition is the Molière radius, defined as the radius of the cylinder needed to contain 90% of the deposited energy of an electromagnetic cascade, which for ice is about 10.35 g/cm$^2$ [169]. For densities in the range $460 - 615$ kg/m$^3$, which corresponds to the range of the simulated ice volume, this translates to lengths of $22.5 - 16.8$ cm. For air however, the Molière radius is of the order of 100 m [170]. The radius of the cylinder needed to contain 90% of the energy deposited in the ice by the air shower particles within 5 m from the shower axis is found to be 3.3 m, as shown in Figure 4.6, which in terms of order of magnitude lies in between the values for air and ice.

Appendix B shows the deposited energy density distributions for different values of the primary energy $E_p$ and zenith angle $\theta$, while keeping the random number seeds for the CORSIKA shower simulations fixed.

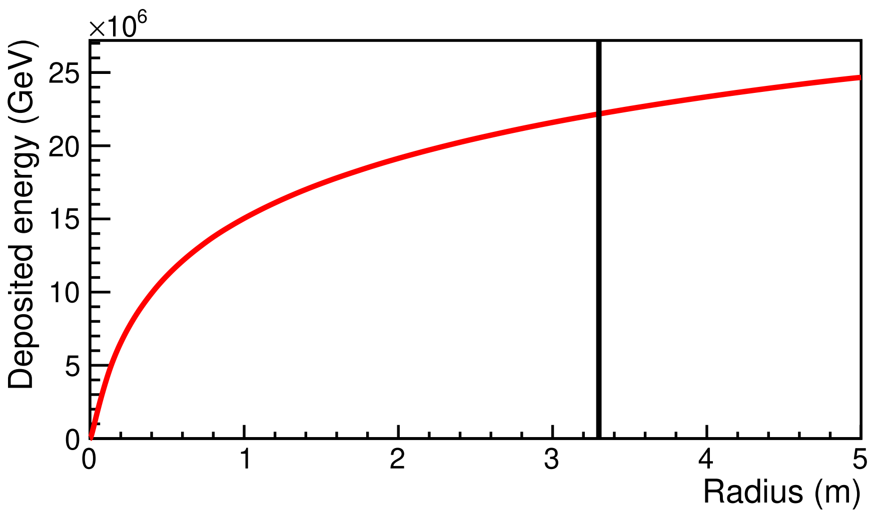


FIGURE 4.6: The total energy deposited in the ice by the reference air shower within a given radius from the shower axis. Indicated by the black line is the value $r = 3.3$ m where the distribution reaches 90% of the total deposited energy within 5 m of the shower axis.

### 4.3.2 Plasma Frequency

The reflective properties of the ionization trail created during the propagation of a cosmic-ray particle cascade through ice can, to a first order, be described by the associated plasma frequency $\omega_p$, which scales with the charged particle density. In the so-called overdense regime, where the plasma frequency is much larger than the frequency of the reflecting radio waves and the collision frequency of the free ionization charges, the trail can be considered as a perfect reflector. The plasma frequency can be calculated from the free charge density $n_q$ using [127],

$$\omega_p = 8980\sqrt{n_q[\text{cm}^{-3}]}\ \text{Hz}. \quad (4.2)$$

Assuming a typical ionization energy of 50 eV, the free charge density $n_q$ can be derived from the deposited energy density $\rho_E$ in the ice as $n_q = \rho_E/(50\ \text{eV})$.

The plasma frequency calculated from the deposited energy density profile of the reference air shower is shown in Figure 4.7. Close to the energy-dense core

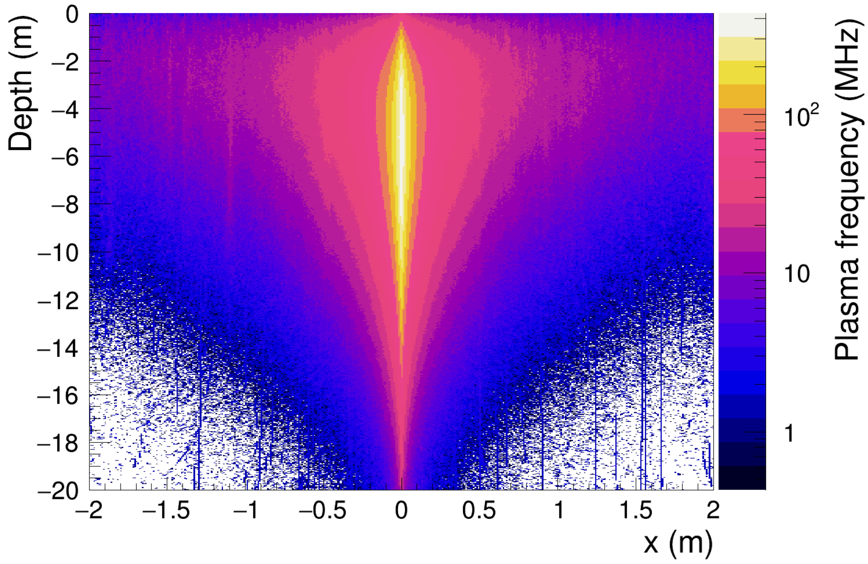


FIGURE 4.7: The estimated plasma frequency $\omega_p$ of the ionization trail created during the propagation of the reference air shower through ice [1].

the plasma frequency reaches values of 100 MHz and more, which is the right order of magnitude for the detection of the ionization trail with the radar echo technique [133]. Note however that the collision frequency of electrons in ice is of the order of $10 - 100$ THz, which means collisions can not be ignored [130]. Nevertheless, a similar conclusion can be drawn when taking into account the collisions of the free ionization charges [128–130].

### 4.3.3 Longitudinal Shower Profile in Ice

Figure 4.8 shows the number of particles of the reference air shower as a function of depth, given earlier in the left side of Figure 4.2, extended towards higher depth values. The dashed line shows the case where the particle shower propagates through the air until reaching sea level, which is at a depth of around 1010 g/cm$^2$. The solid lines show the case where the particle shower propagates through ice at an altitude of 2.4 km above sea level, indicated by the black vertical line, which corresponds to a depth of 734 g/cm$^2$. For this figure specifically, the in-ice simulation did not only propagate the particles within a radius of 5 m from the shower axis, but included the whole particle footprint. Furthermore, in order to have comparable distributions, the kinetic energy tracking cuts used in the CORSIKA simulation were also applied during the in-ice simulations.

The main difference between air and ice is the density. Since depth is expressed in units of mass per area, this should in principle have no effect on the longitudinal particle distribution. Comparing both cases presented in the figure, we see that the longitudinal development of the electromagnetic cascade is indeed not affected by the change of the medium. The distributions for the in-ice cascade follow the ones obtained when simulating the shower cascade in air down to sea level. Existing parameterizations describing longitudinal profiles of air showers, such as the Gaisser-Hillas function [171], could therefore be applied to showers propagating through ice as well. Additionally, simulations using the atmosphere as the only medium could be used to determine parameters such as $X_{\max}$ of showers propagating through ice, irrespective of the altitude of the air-ice boundary. Interestingly, Figure 4.5 clearly

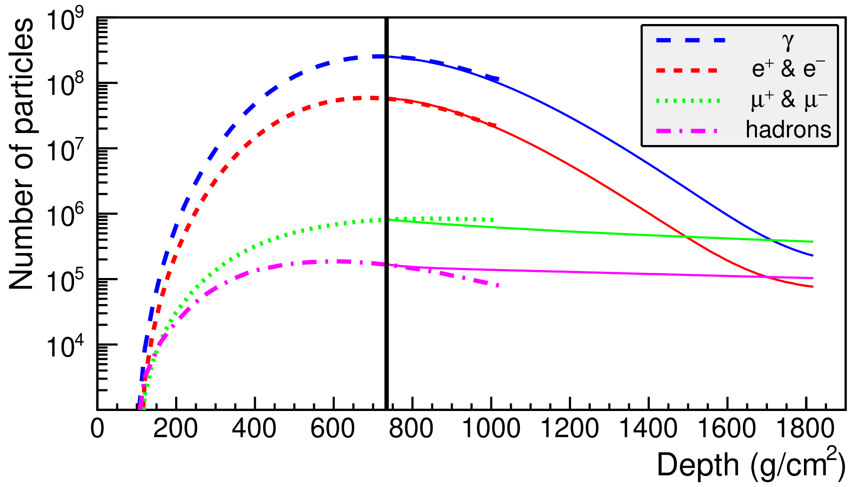


FIGURE 4.8: The number of particles of the reference air shower as a function of depth [1]. The dashed lines show the case where the particle shower propagates through air until reaching sea level. The solid lines show the case where the particle shower propagates through ice at an altitude of 2.4 km above sea level, which corresponds to 734 g/cm$^2$ (indicated by the black vertical line). For this figure specifically, the in-ice simulations propagated the complete particle footprint through the ice and applied the same kinetic energy tracking cuts as the CORSIKA simulation, mentioned in Section 4.2

shows that the core of the particle cascade is still growing during the first few meters in the ice, while Figure 4.8 shows that the shower as a whole has already reached shower maximum at the ice surface.

Important to note is that the Geant4-based simulations of the in-ice propagation of the particle cascade do not include hadronic interactions, which means the muonic and hadronic components of the distribution are hard to interpret. As the density increases when the shower moves from air to ice, the probability of charged pions interacting with the medium before decaying increases. This leads to a suppression of the muonic component, while the hadronic component is boosted. The additional neutral pions created by these interactions subsequently decay into gammas, feeding the electromagnetic component. The same holds for showers propagating from air into soil, as discussed in [146]. The boost in the hadronic component is not visible in Figure 4.8. Instead it is declining, as during the simulations the hadrons can only interact electromagnetically, or decay.

A new version of the CORSIKA Monte Carlo code is currently in development, moving from a Fortran-based design towards a more modern and flexible C++ framework [172]. Thanks to its flexibility this new version, referred to as CORSIKA 8, will be able to simulate cross-media particle showers. Recently, a CORSIKA 8 simulation of a cosmic-ray air shower propagating through ice was performed, aiming to verify the functionalities of the new framework by reproducing the reference particle cascade discussed in this chapter [173]. A good agreement was found, showing a similar deposited energy density profile and longitudinal particle distribution. Interestingly, the CORSIKA 8 simulation does include hadronic interactions and produces the expected boost in the hadronic component, the decline in the muonic component and a softer decline in the tail of the distribution of the electromagnetic component.

It is good to keep in mind that the length scales presented in Figure 4.8 differ significantly. The solid lines in the plot represent 20 m of ice, while the corresponding dashed lines on the right side of the plot represent 2.4 km of air.

### 4.3.4 Lateral Charge Distribution in Ice

As mentioned in Chapter 1, at any moment in time during the development of the air shower most of the particles are located in the shower front, resembling a pancake moving down the direction of the shower axis with a typical thickness of the order of 1 m. In ice, the particles are even more densely concentrated in the cascade front, forming a pancake with a typical thickness of the order of 10 mm. This is illustrated in Figure 4.9, which shows a snapshot of the reference air shower propagating through the ice. The depth of the cascade front with respect to the ice surface at this time is 300 g/cm$^2$, which in units of length translates to 6.2 m.

The radial dimension of the cascade can be described by the lateral distribution function $w_1(r)$, where $r$ is the radius in the shower plane. By definition, $w_1(r)dr$ represents the number of charged particles in the interval $[r, r + dr[$ at a given time, normalized so $\int_0^{R_0} w_1 dr = 1$. We set the value of $R_0$ to 0.2 m, which captures the region where the particle density is the highest. In order to calculate the $w_1(r)$ function at a given time $t$, a histogram with a bin width $\Delta r = 1$ mm is constructed during the simulation. Every bin represents the total number of charges at time $t$ with a radius $r$ within the corresponding bin limits. The $w_1(r)$ function can then be deduced from the histogram by dividing each bin value by the bin width $\Delta r$, and the total amount of charges at time $t$ with $r < R_0$.

The $w_1(r)$ function of the reference air shower at different times of the shower development in ice is shown in Figure 4.10. The time values are indicated by the corresponding values of the depth $X$ of the cascade front with respect to the ice surface. The time $t$ can be related to the depth $X$ of the cascade front by integrating the density profile along the shower axis over a distance $L = c_0 t$, with $c_0$ the speed of light in vacuum. From Figure 4.10, we see that at earlier stages of the cascade development in the ice the $w_1(r)$ function is rather broad, showing an on-set effect

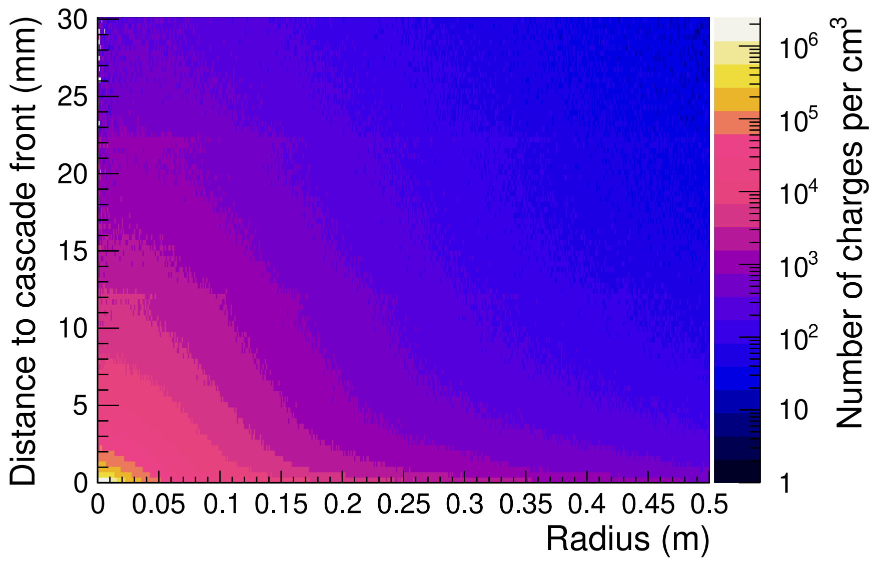


FIGURE 4.9: A snapshot of the simulated reference air shower in the ice, showing the radial profile of the number of charges per unit volume versus the distance along the shower axis to the cascade front [1]. Most of the charges are concentrated within $\sim$ 10 mm from the cascade front. The depth of the cascade front with respect to the ice surface at this time is 300 g/cm$^2$, which in units of length translates to 6.2 m. The total depth including the traversed atmosphere is 1034 g/cm$^2$.

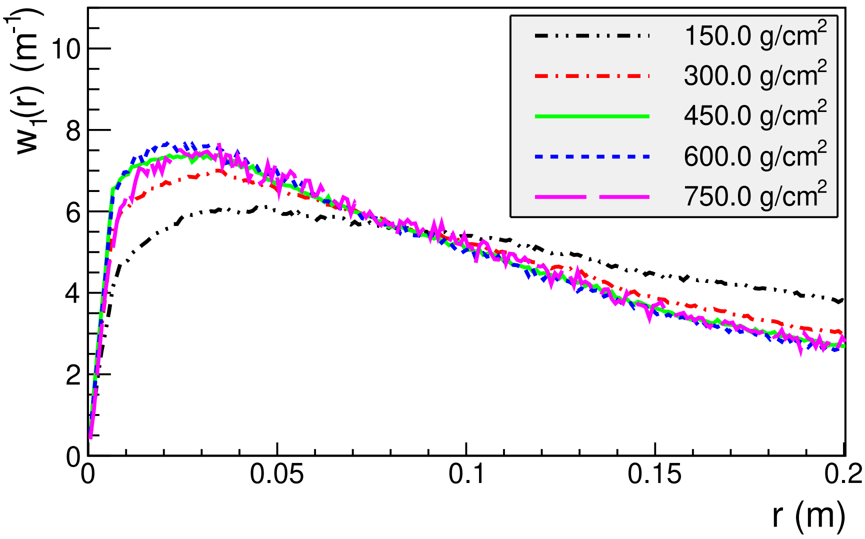


FIGURE 4.10: The lateral distribution function for the reference air shower, at different times of the shower development in ice [1]. The legend indicates the depth of the shower front with respect to the ice surface at each time instance, varying from 150 g/cm$^2$ (3.2 m) down to 750 g/cm$^2$ (14.4 m).

toward larger radii. As the cascade propagates deeper into the ice, particles at larger radii vanish and a stable, more narrow distribution is found.

The exact shape of the $w_1(r)$ function can be expected to depend on the primary energy $E_p$ and zenith angle $\theta$ of the cosmic-ray air shower, as changing these parameters will change the stage of development of the particle cascade at the air-ice boundary. Moreover, as mentioned before, global properties can fluctuate from shower to shower, even if the primary particle type, energy and zenith angle are the same. Although the reference air shower that has been discussed so far has an $X_{\text{max}}$ value close to the average value for proton-induced showers, it does not in any way indicate how large possible fluctuations on the $w_1(r)$ function can be.

Therefore 10 different sets of 15 air showers were simulated, each covering values for $E_p$ ranging from $10^{16}$ eV up to $10^{18}$ eV in steps of half a decade, and values for $\theta$ of 0°, 15° and 30°. Within each set the same CORSIKA random number seeds were used for the different primary energy and zenith angle combinations. Thinning was applied for showers with $E_p \geq 10^{17}$ eV on electromagnetic particles below $10^{-7}E_p$, with maximum weights of 10 ($E_p = 10^{17}$ eV and $E_p = 10^{17.5}$ eV) and 100 ($E_p = 10^{18}$ eV).

Different values for $E_p$, $\theta$ and shower-to-shower fluctuations will primarily influence the stage of the shower development, which to a first approximation can be quantified by the value of $X_{\text{max}}$, defined as the slant depth at which point the shower reaches its maximum number of electrons and positrons. Independent of the value of $E_p$ and $\theta$ the showers were grouped based on their $X_{\text{max}}$ value, which was calculated by simulating each shower down to sea level. As described in Section 4.2.1, ignoring the air-ice boundary does not affect the value of $X_{\text{max}}$. For each shower the $w_1(r)$ function was constructed, from which an average $w_1(r)$ function per $X_{\text{max}}$ group was calculated, defined as

$$\overline{w_1}(r) = \frac{1}{N}\sum_{i}^{N} w_{1,i}(r), \tag{4.3}$$

with $N$ the number of simulated air showers in the $X_{\max}$ group.

Figures 4.11 and 4.12 show the average $w_1(r)$ functions at a cascade front depth of 450 g/cm$^2$ with respect to the ice surface for the different $X_{\max}$ groups. The grey bands in Figure 4.12 represent the dispersion on the average $w_1(r)$ functions within each $X_{\max}$ group, given by

$$\sigma(r) = \sqrt{\frac{1}{N-1}\sum_{i}^{N}(w_{1,i}(r) - \overline{w_1}(r))^2}. \tag{4.4}$$

As expected, there is a clear trend between the distributions and $X_{\max}$. Cosmic-ray air showers with a lower value of $X_{\max}$ will reach the air-ice boundary at a later stage in their development. They will propagate through the ice with a less energy-dense core, resulting in a broader lateral distribution function.

As shown in for example [36, 174], a parameterization of the lateral distribution function can be used to describe the radio emission of the particle cascade analytically. Although numerical Monte Carlo simulations are in general more accurate, analytical descriptions of the emission do not require as much computational resources, and can lead to valuable insights in the radiation processes involved. We found that the $w_1(r)$ functions can be well described by the analytical expression

$$W(r) = \frac{1}{A}\sqrt{r}e^{-(r/b)^c}, \tag{4.5}$$

with the values of the fit parameters $b$ and $c$ depending on $X_{max}$ of the shower. The value of $A$ is determined by the normalization and is given by

$$A = \frac{b^{3/2}}{c}\left\{\Gamma\left(\frac{3}{2c}\right) - \Gamma\left(\frac{3}{2c}, \left(\frac{R_0}{b}\right)^c\right)\right\},$$

with $\Gamma(x)$ the gamma function and $\Gamma(a,x)$ the upper incomplete gamma function. The fits to the average $w_1(r)$ functions are shown in Figure 4.12. Figure 4.13 shows

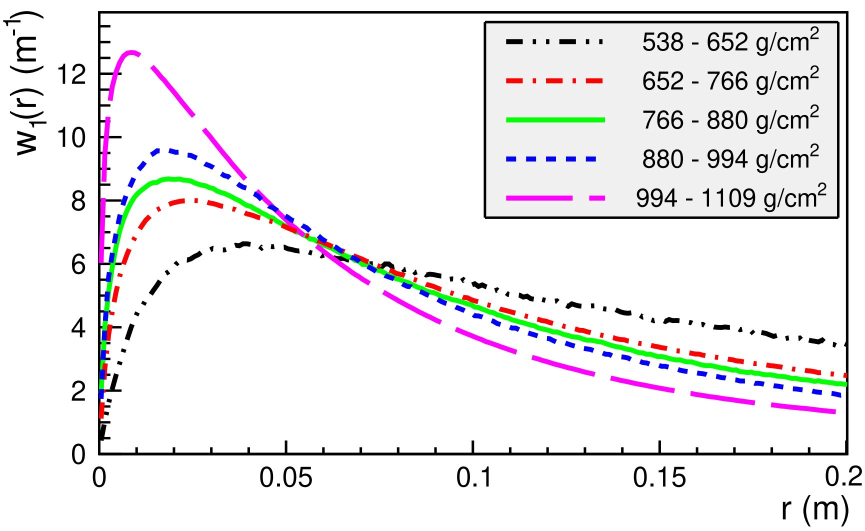


FIGURE 4.11: The average lateral distribution function for each $X_{\max}$ group at a cascade front depth of 450 g/cm$^2$ with respect to the ice surface [1]. The legend indicates the $X_{\max}$ interval for each group. The air-ice boundary sits at a depth of 734 g/cm$^2$ in the atmosphere.

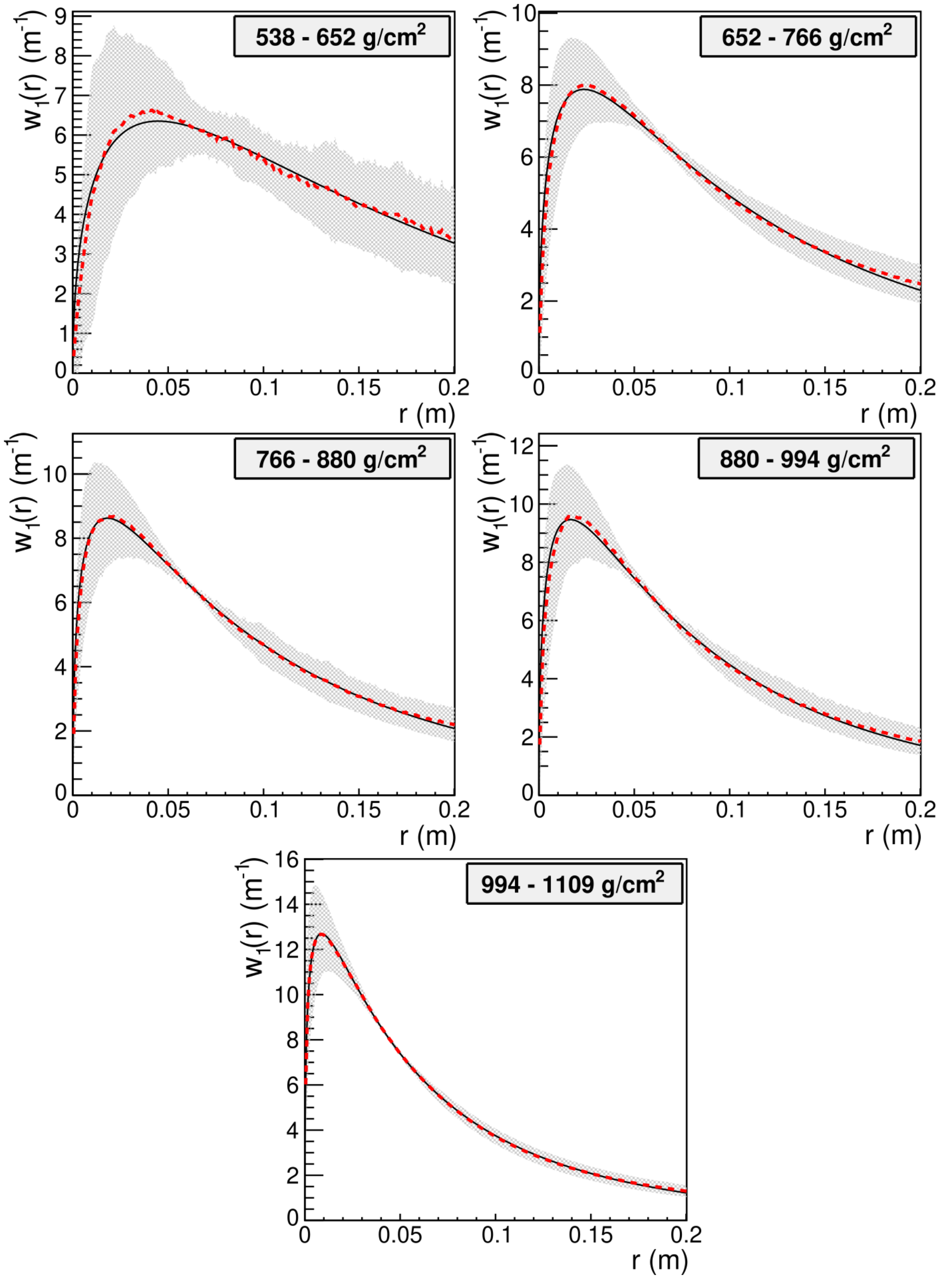


FIGURE 4.12: The average lateral distribution function for each $X_{max}$ group at a cascade front depth of 450 g/cm$^2$ with respect to the ice surface, shown by the red dashed curves [1]. The legends indicate the $X_{max}$ interval for each group. The grey bands represent the dispersion on the average $w_1(r)$ functions, as defined by Equation 4.4. The solid black lines show the fits to the average distributions following Equation 4.5. The dispersion represented by the grey bands is interpreted as the standard deviation during the fitting procedure. The air-ice boundary sits at a depth of 734 g/cm$^2$ in the atmosphere.

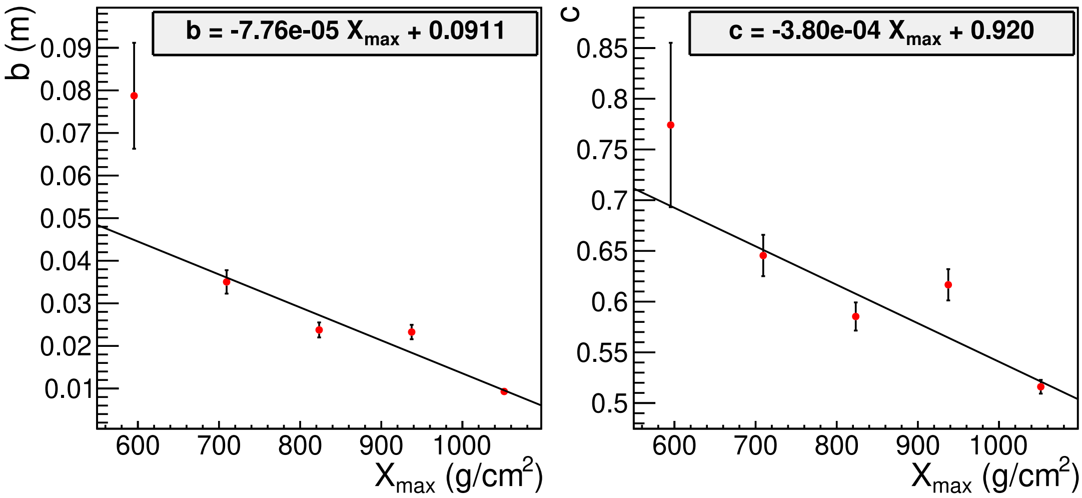


FIGURE 4.13: The values of the fit parameters $b$ (left) and $c$ (right) of Equation 4.5 for each $X_{\mathrm{max}}$ group, for a cascade front depth of 450 g/cm$^2$ with respect to the ice surface [1]. The horizontal axis indicates the mean value of the $X_{\mathrm{max}}$ interval of each group. The error bars are calculated by interpreting the dispersion defined in Equation 4.4 as the standard deviation on the average $w_1(r)$ function values. The black lines show the linear extrapolations, which are given in the legends.

the corresponding values of the fit parameters $b$ and $c$ for each $X_{\mathrm{max}}$ group, where the horizontal axis indicates the mean value of the $X_{\mathrm{max}}$ interval of each group. The error bars are calculated by interpreting the dispersion defined in Equation 4.4 as the standard deviation on the average $w_1(r)$ function values. At lower $X_{\mathrm{max}}$ values the cascades contain less particles when reaching the ice surface, leading to larger statistical fluctuations and therefore significantly larger error bars on the $b$ and $c$ parameters.

Finally, we present linear extrapolations to both fit parameters that can be used to construct the lateral distribution function for any given value of $X_{\mathrm{max}}$. Evaluating the linear extrapolations for a given $X_{\mathrm{max}}$ value will result in a value for $b$ and $c$, which can be used in Equation 4.5 to determine the $w_1(r)$ function. The extrapolations presented here are in principle only valid for the $w_1(r)$ function at a cascade front depth of 450 g/cm$^2$ in the ice, but as shown in Figure 4.10 at this point in the shower development the distribution is largely independent of the shower depth.

Figure 4.14 demonstrates the result of using the linear extrapolations together with Equation 4.5 to construct the $w_1(r)$ function for 4 particle showers from the simulation set, including the reference air shower discussed in more detail above. We see that the parameterization fails to reconstruct the lateral distribution function for some of the particle cascades, suggesting that a more detailed parameterization is required. This could be done by including more simulations to the simulation set, which would allow for a larger number of $X_{\mathrm{max}}$ groups covering smaller $X_{\mathrm{max}}$ intervals. Alternatively, additional information such as the primary energy $E_p$ and zenith angle $\theta$ could be taken into account explicitly in the parameterization.

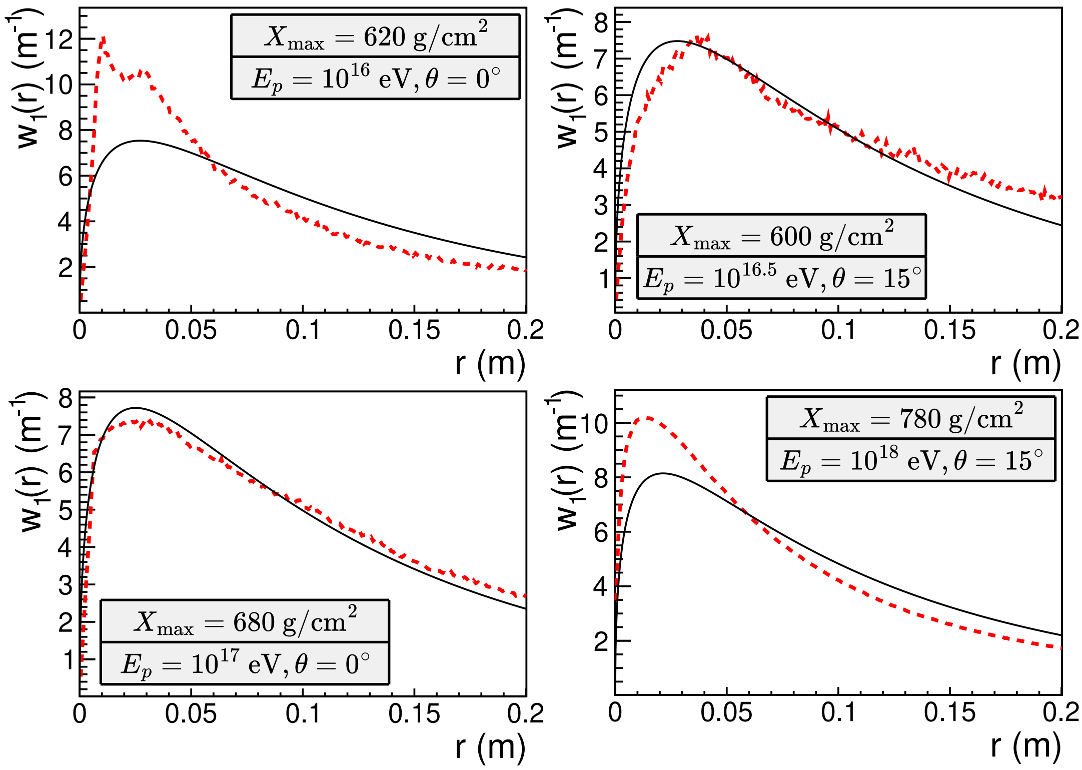


FIGURE 4.14: The $w_1(r)$ functions at a cascade front depth of 450 g/cm$^2$ with respect to the ice surface for 4 particle showers from the simulation set, including the reference air shower discussed in more detail above [1]. The red dashed lines show the $w_1(r)$ functions derived directly from the simulations. The black solid lines show the reconstructed $w_1(r)$ functions using the linear extrapolations from the fit parameters together with Equation 4.5. The legends indicate the values for $X_{\max}$, the primary energy $E_p$ and zenith angle $\theta$.

## 4.4 Conclusion

This chapter demonstrated the properties of ultra-high-energy cosmic-ray air showers at an altitude of 2.4 km, using a reference air shower with primary energy $E_p = 10^{17}$ eV and zenith angle $\theta = 0°$ simulated with the CORSIKA Monte Carlo code. The longitudinal shower profile showed that at this altitude the shower is close to shower maximum, where it reaches the maximum number of electrons and positrons. The shower still contains about 50% of the primary energy, most of which is carried by the electromagnetic component. The lateral shower profile showed that a large fraction of the energy of the cascade is concentrated around the shower axis. Approximately 20% of the primary energy is located within a radius of 1 m, which we defined as the shower core. Analysing a larger simulation set demonstrated that this is indeed a general feature for air showers with primary energies of $10^{16}$ eV and higher, and zenith angles up to $\sim 30°$.

Next, the features of in-ice particle cascades that develop when ultra-high-energy cosmic-rays propagate through ice at an altitude of 2.4 km above sea level were illustrated. To this end a Geant4-based Monte Carlo program was developed, which uses the particle output from CORSIKA as an input to simulate the particle propagation through ice. We expected that the shower core would continue to develop in the ice, while at the same time the particles outside the core would disappear after a few radiation lengths. The deposited energy density profile in the ice confirmed this expectation. Looking at the longitudinal shower profile of the whole particle cascade, we saw that the number of electromagnetic particles as a function of depth does not change when introducing ice as a second medium. The lateral charge distribution showed that the typical thickness of the in-ice cascade is about $\sim$ 10 mm. The radial dimension is described by the lateral distribution function $w_1(r)$, which starting around values of 300 g/cm$^2$ (6.2 m) is largely independent of the cascade depth in the ice. Finally, using a larger simulation set the correlation of the $w_1(r)$ function with $X_{\mathrm{max}}$ of the particle cascade was demonstrated, and a parameterization to calculate the $w_1(r)$ function from the value of $X_{\mathrm{max}}$ was presented.

# Chapter 5

## Radio Signals from Cosmic-Ray Cascades Observed in Ice

### 5.1 Introduction

The main goal of the work presented in this thesis is to compute the radio emission of ultra-high-energy cosmic-ray showers, including both the component emitted in air as well as in ice. In principle the radio emission could be described analytically based on distribution functions extracted from the simulated particle cascades. However, we decided to adopt an existing formalism designed to calculate the radio emission of the particle cascades numerically, directly into the Monte Carlo simulation code.

This chapter will present FAERIE - the Framework for the simulation of Air shower Emission of Radio for in-Ice Experiments. This framework uses the CORSIKA Monte Carlo code to simulate particle cascades in air, and relies on the Geant4-based software described in Chapter 4 to propagate the air showers through ice. The radio emission of both the in-air and the in-ice components of the particle cascades is calculated using the so-called endpoint formalism. For the in-air component, the implementation of the endpoint formalism is provided by the CoREAS simulation code (CORSIKA-based Radio Emission from Air Showers), which is compiled alongside the CORSIKA base code [175]. For the radio emission of the in-ice component, the endpoint formalism was implemented directly in the Geant4-based software, similar to the implementation developed for the work presented in [176, 177].

The endpoint formalism was developed to present a general description of electromagnetic radiation from a collection of charged particles moving through a uniform medium, by calculating the contribution of each single particle. It is set up in such a way that it can be applied directly in Monte Carlo simulations of particle cascades, which will become clear from the description of the formalism in Section 5.2. However, it is important to notice that the medium of interest in this work is not uniform at all. It exists of a combination of air and ice, both of which have a density that increases with depth. This influences the radio propagation, leading to bent trajectories as well as reflections and refractions at the air-ice interface. To account for these effects ray tracing was included in the framework, which required a revision of the endpoint formalism.

The following section gives a summary of the endpoint formalism. Next, the general features of ray tracing will be discussed, as well as how ray tracing can be included in the endpoint formalism, and how the different concepts are implemented in FAERIE. Finally, the first results of FAERIE will be presented. Most of the content of this chapter is published as part of this thesis work in a peer-reviewed article [2]. A description of the ray tracer and the adjustments made to the CoREAS can be found in [178, 179]. The main contributions from this thesis work are the development of the Geant4-based module used for the simulation of the in-ice particle cascade and the corresponding radio emission, and the subsequent merging of the different software components into a single framework.

## 5.2 Endpoint Formalism

The endpoint formalism was developed as a means to calculate the electromagnetic radiation created by a charged particle propagating through a medium [180]. It does so by describing the trajectory of the particle as a sequence of small straight segments, during which the velocity of the particle can be considered constant. The particle motion over each segment is treated as the combination of two instantaneous acceleration events, one at each endpoint of the segment. At the starting point the particle is instantaneously accelerated from rest to the segment velocity, while it is instantaneously decelerated to rest again at the ending point.

The electric field $\vec{E}$ at a position $\vec{x}$ and time $t$ associated with a moving charged particle in a dielectric medium can be derived from Maxwell's equations, and can be expressed as a combination of two components [141],

$$\vec{E}(\vec{x},t) = q\left[\frac{\hat{r}-n\vec{\beta}}{\gamma^2(1-n\vec{\beta}\cdot\hat{r})^3R^2}\right]_{\text{ret}} + \frac{q}{c}\left[\frac{\hat{r}\times[(\hat{r}-n\vec{\beta})\times\dot{\vec{\beta}}]}{(1-n\vec{\beta}\cdot\hat{r})^3R}\right]_{\text{ret}}, \tag{5.1}$$

with $q$ the charge of the particle, $\hat{r}$ the unit vector pointing from particle to observer, $n$ the index of refraction of the medium, $\beta = v/c$ with $v$ the velocity of the particle and $c$ the speed of light in vacuum, $R$ the distance from the particle to the observer and $\gamma = (1-\beta^2)^{-1/2}$ the relativistic factor. Both terms are evaluated at the retarded time

$$t' = t - nR/c, \tag{5.2}$$

as indicated by the subscripts.

The first term is proportional to $R^{-2}$, which indicates it corresponds to the static Coulomb field. As such it does not have radiation associated to it, and it is neglected in the formalism. The second term is called the radiation field. It scales with $R^{-1}$ and therefore has a corresponding flux following the $R^{-2}$ dependence that is expected for spherical waves. The radiation field disappears from the expression for particles with a constant velocity.

In practice an observer system will always be limited by a certain time scale $\Delta t$, determined by the sampling rate at which measurements can be made. The quantity of interest is therefore not the exact value of the radiation field at a given position and time, but instead the time-averaged electric field over the observation-time window $\Delta t$, given by

$$\frac{1}{\Delta t}\int_{\Delta t}\vec{E}_{rad}(\vec{x},t)dt = \frac{1}{\Delta t}\frac{q}{c}\int_{\Delta t}\left[\frac{\hat{r}\times[(\hat{r}-n\vec{\beta})\times\dot{\vec{\beta}}]}{(1-n\vec{\beta}\cdot\hat{r})^3R}\right]_{\text{ret}} dt \tag{5.3}$$

Since the observation time $t$ and the retarded time $t'$ follow the relation $t = t' + nR/c$, we know that

$$\frac{dt}{dt'} = 1 + \frac{n}{c}\frac{dR}{dt'} = 1 - n\vec{\beta}\cdot\hat{r}, \tag{5.4}$$

where we used $dR = -(\vec{v}\cdot\hat{r})dt'$. Note that this expression simplifies to the one given by Equation 1.21, for the case where $\beta = 1$. We can now write Equation 5.3 as

$$\frac{1}{\Delta t}\int_{\Delta t}\vec{E}_{rad}(\vec{x},t)dt = \frac{1}{\Delta t}\frac{q}{c}\int_{\Delta t'}\frac{\hat{r}\times[(\hat{r}-n\vec{\beta})\times\dot{\vec{\beta}}]}{(1-n\vec{\beta}\cdot\hat{r})^2R}dt', \tag{5.5}$$

where $\Delta t'$ is the retarded-time window corresponding to the observer-time window $\Delta t$.

During an instantaneous acceleration event a particle accelerates or decelerates at a certain time $t'_0$. In case of a starting point, it will be at rest for $t' < t'_0$ and have a velocity $\vec{\beta}^*$ for $t' > t'_0$. The opposite is true for an ending point. It can be shown that for this type of events Equation 5.5 simplifies to

$$\frac{1}{\Delta t}\int_{\Delta t} \vec{E}_{rad}(\vec{x},t)dt = \pm \frac{1}{\Delta t}\frac{q}{c}\left(\frac{\hat{r}\times[\hat{r}\times\vec{\beta}^*]}{(1-n\vec{\beta}^*\cdot\hat{r})R}\right), \tag{5.6}$$

if the retarded-time window $\Delta t'$ encompasses the acceleration process at time $t'_0$ [180]. The plus sign is used for starting points, while the minus sign is used for ending points. In both cases, the time-averaged electric field will be perpendicular to the unit vector $\hat{r}$ and the plane spanned by $\hat{r}$ and $\beta^*$, which means that the electromagnetic radiation is radially polarized.

During Monte Carlo simulations individual particles are followed while they take discrete steps through the medium. Applying the endpoint formalism amounts to evaluating Equation 5.6 twice for each step, once in the starting point and once in the ending point. The observation times of the starting point emission and the ending point emission follow from Equation 5.2, each of which falls within a certain observation-time window during which the corresponding field is observed. In each of the observer-time windows all the contributions from the different steps of every particle in the shower are added together, resulting in the total electric field as a function of time. This is illustrated in Figure 5.1.

Note that the so-called boost factor $B = 1 - n\vec{\beta}^* \cdot \hat{r}$ in the denominator of Equation 5.6 corresponds to $\frac{dt}{dt'}$, given by Equation 5.4. As explained in Chapter 1, the

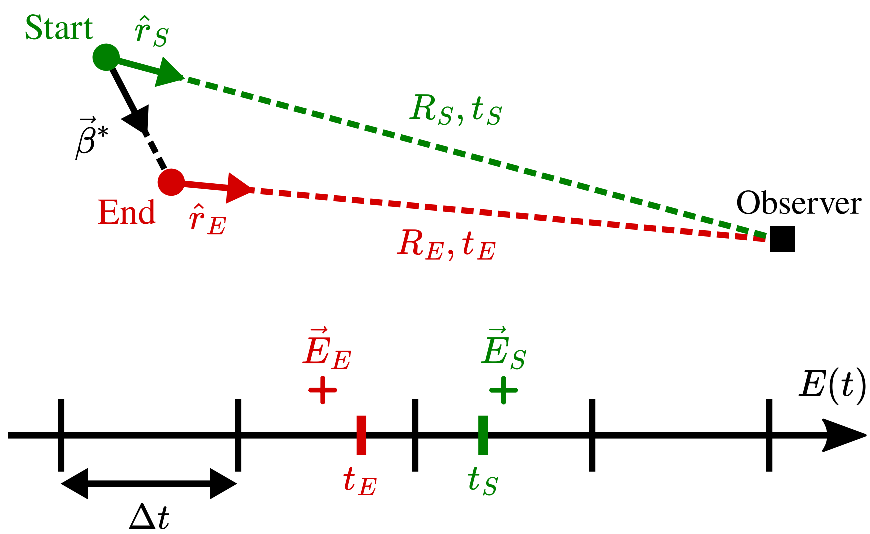


FIGURE 5.1: An illustration of the endpoint formalism. The starting point (green) and the ending point (red) of the particle step are indicated with circles. The observer location is indicated with a square. The quantities with a subscript 'S' refer to the starting point emission, while those with a subscript 'E' refer to the ending point emission. For both points the emitted electric field and observation time are calculated with respectively Equation 5.6 and Equation 5.2. Each observation time corresponds to a certain observer-time window, to which the electric fields are added.

radiation will be the strongest and most coherent when $\frac{dt}{dt'} = 0$, resulting in the expression for the Cherenkov angle

$$\cos(\theta_c) = \frac{1}{n\beta}. \tag{5.7}$$

When the observation angle approaches the Cherenkov angle $\theta_c$ the formalism diverges [181, 182]. In this case the finite time resolution of the observer needs to be taken into account explicitly, as discussed in [175].

Several theory-oriented studies have demonstrated the reliability of the endpoint formalism [180–182]. Furthermore it has been compared to experimental data on several different occasions, including data from air shower experiments as well as a lab experiment at the SLAC National Accelerator Laboratory [55, 175, 177, 183]. Interestingly, it was shown that the formalism is able to reproduce transition radiation accurately [180]. Transition radiation arises when a charged relativistic particle moves between two media with different refractive indices, such as air and ice [184].

## 5.3 Ray Tracing

In a medium with a constant index of refraction, electromagnetic radiation will propagate along straight lines. However, when moving through a medium with a changing index of refraction, a more complicated path is followed. A gradually changing index of refraction will lead to bent trajectories, while a hard transition boundary causes reflections and refractions. Ray tracing takes these effects into account by modeling the electromagnetic radiation with rays, and calculating the corresponding ray paths through the medium. To calculate these paths ray tracing relies on the laws of geometrical optics, such as Fermat's principle and Snell's law [101, 178]. Treating electromagnetic radiation as rays is in principle only valid when the wavelength of the radiation is much smaller than the typical size of structures in the medium. Studies have shown that especially in the firn, ray tracing does not reproduce second-order effects, such as the propagation of radiation into shadow-zones [84, 185, 186]. The modeling of these second-order effects however also requires a good understanding of the firn itself, which considering the typical size of neutrino observatories is not straightforward to achieve. Other more computationally-heavy methods of calculating the propagation of electromagnetic radiation through non-uniform media exist, such as finite-difference-time-domain (FDTD) methods or parabolic equation methods [84, 187], but will not be discussed here any further. Due to the related processing time, these approaches are not feasible in the case of FAERIE.

Traditional ray tracers determine the propagation of rays based on discretization techniques, such as the Runge-Kutta method [188]. The differential equations derived from the laws of geometrical optics are solved locally, and the trajectory of the ray is literally traced out step by step. Through a process of trial and error, the path between a transmitter and a receiver can then be found. Rays are launched in different directions from the transmitter and gradually converge towards the solution through a minimization procedure. An example of such a numerical ray tracer is described in [189].

By assuming a cylindrical symmetry for the medium, the problem of ray tracing becomes somewhat less complicated. Moreover, if the index of refraction $n$ as a function of the depth in the medium $z$ follows an exponential profile

$$n(z) = A + Be^{-C|z|}, \tag{5.8}$$

an analytical solution for the ray path as a function of the launching angle can be derived, as done in for example [101, 178]. Similar to traditional ray tracers, the correct value for the launching angle of the ray is then determined through a minimization process.

The main advantage of analytical ray tracers is their computation speed, which is significantly higher compared to traditional ray tracers. Traditional ray tracers on the other hand do not impose any restrictions on the refractive index profile. Alternatively, a combination of both types of ray tracers can be made, to allow for some more flexibility in the refractive index profile without making the ray tracing process too slow. In this case the medium is described with consecutive layers, each with an exponential refractive index profile. Ray tracing is performed analytically layer by layer, and through trial and error the correct launching angle is found.

In the case of FAERIE, the simulated volume consists of a combination of air and ice. The transmitter points correspond to the endpoints of the particle segments, which can be either in air or in ice. The receiver points on the other hand will always be in ice. The relevant ray tracing scenarios are therefore air-to-ice ray tracing, and ice-to-ice ray tracing. Air-to-ice ray tracing includes ray bending in air, followed by refraction at the air-ice boundary and further bending in the ice. For ice-to-ice ray tracing generally two solutions are found. The solution that corresponds to the shortest ray path will be called the direct ray. The second solution will be called the indirect ray, which can be either a ray refracting downwards or a ray reflecting on the ice-air boundary. All three types of rays are shown in Figure 5.2.

Note that the ray-bending effect is much stronger in ice than it is in air. The index of refraction of ice at the South Pole starts around $n = 1.35$ at the surface, and increases up to $n = 1.75$ within the first 150 m [100]. For air, the index of refraction starts at $n = 1$ in the topmost layer, increasing only by about $3 \times 10^{-4}$ over a range of several kilometers down to sea level. This small increase is however still relevant, as only for $n > 1$ the emission forms a Cherenkov cone. Additionally, especially for very inclined showers, it can lead to a so-called refractive displacement of the radio emission [190].

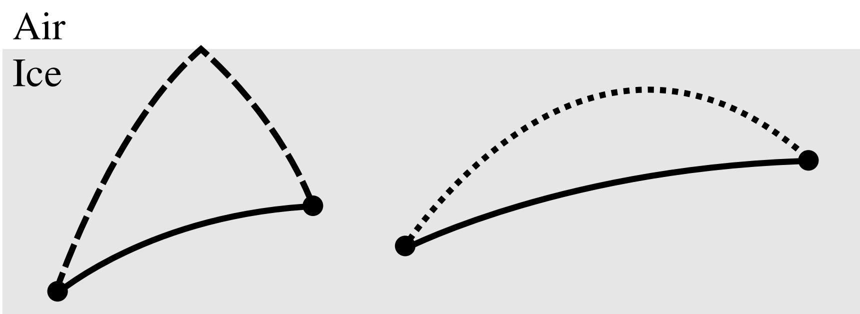


FIGURE 5.2: A sketch of the three different types of rays: a direct ray (solid line) shown in both cases, an indirect reflected ray (dashed line) shown in the left case, and an indirect refracted ray (dotted line) shown in the right case.

### 5.3.1 Ray Tracing in the Endpoint Formalism

Originally, the endpoint formalism was developed assuming radio emission propagates on straight lines from emitter to observer, as shown in Figure 5.1. When evaluating Equation 5.6 in an endpoint, the unit vector $\hat{r}$ points directly from the endpoint to the observer, $n$ is evaluated at the location of the endpoint, and $R$ represents the length of the straight path connecting endpoint and observer. When including ray tracing in the formalism, we have to reconsider the interpretation of these variables.

The boost factor $B = 1 - n\vec{\beta}^* \cdot \hat{r}$ that appears in the denominator of Equation 5.6 corresponds to the derivative $\frac{dt}{dt'}$. As demonstrated in [191], only when interpreting $\hat{r}$ as the propagation direction of the ray at the endpoint and evaluating $n$ at the endpoint location, this relation still holds. In this work, ray tracing for a collection of endpoints and observer locations was performed to calculate the derivative $\frac{dt}{dt'}$ numerically. This was then directly compared to the value for $B = 1 - n\vec{\beta}^* \cdot \hat{r}$ under different interpretations for $\hat{r}$ and $n$.

As explicitly stated in [141], the variable $R$ in Equation 5.1 satisfies the relation $t = t' + nR/c$. This can be rewritten as

$$R = \int_{t'}^{t} \frac{c}{n} dt, \tag{5.9}$$

which can readily be generalized to a non-constant refractive index profile. In this form it is clear that $R$ represents the distance traveled by the electromagnetic radiation when propagating from the endpoint towards the receiver.

An intuitive approach to include ray tracing in the endpoint formalism is therefore the following. Instead of pointing directly from endpoint to observer, the unit vector $\hat{r}$ in Equation 5.6 now corresponds to the launching direction of the ray, defined as the direction of propagation of the ray at the endpoint. The index of refraction $n$ is evaluated at the location of the endpoint, and the variable $R$ corresponds to the length of the curved ray path. Finally, the resulting electric field is rotated in the plane of the ray, such that its component in the plane of the ray is perpendicular to the receiving direction $\hat{r}_{obs}$, i.e. the propagation direction of the ray at the observer. Following Equation 5.6, it will be perpendicular to the launching direction $\hat{r}$ at first. This approach is illustrated in Figure 5.3.

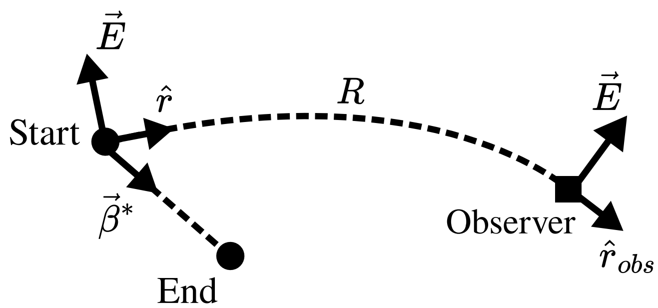


FIGURE 5.3: An illustration of the endpoint formalism including ray tracing, in the specific case where the starting point, ending point and observer coincide in the same plane. The circles represent the endpoints of the particle step. The square represents the observer. All vectors shown in the illustration lie in the same plane.

### 5.3.2 Fresnel Coefficients

When electromagnetic radiation strikes the interface between two different media, it will reflect back into the first medium and refract into the second medium, dividing the energy of the radiation over both components. How much of the energy goes to the reflected component and how much of it goes to the refracted component depends on the refractive indices of both media $n_1$ and $n_2$, as well as the angle of incidence on the interface $\theta_i$. This can be quantified using the Fresnel coefficients. In the context of FAERIE this is important for air-to-ice ray tracing, as well as ice-to-ice ray tracing in case the indirect ray reflects on the ice-air boundary.

The electric field of a plane wave can be decomposed at the interface in two orthogonal components. The P component is the component in the plane of incidence, i.e. the plane that contains the incoming ray. The S component is the component perpendicular to that plane. This is illustrated in Figure 5.4. The Fresnel coefficients represent scaling factors for the amplitude of the P and S components of the electric field. Applying these factors to the components of the incoming wave, results in the components for the reflected and refracted wave.

If the permeabilities of both media can be approximated by the permeability of free space $\mu_0$, which is the case for air and ice, the reflection coefficients can be expressed as [192]

$$r_{\mathrm{P}} = -\frac{n_1\sqrt{1-\left(\frac{n_1}{n_2}\sin(\theta_i)\right)^2} - n_2\cos(\theta_i)}{n_1\sqrt{1-\left(\frac{n_1}{n_2}\sin(\theta_i)\right)^2} + n_2\cos(\theta_i)}, \tag{5.10a}$$

$$r_{\mathrm{S}} = \frac{n_1\cos(\theta_i) - n_2\sqrt{1-\left(\frac{n_1}{n_2}\sin(\theta_i)\right)^2}}{n_1\cos(\theta_i) + n_2\sqrt{1-\left(\frac{n_1}{n_2}\sin(\theta_i)\right)^2}} \tag{5.10b}$$

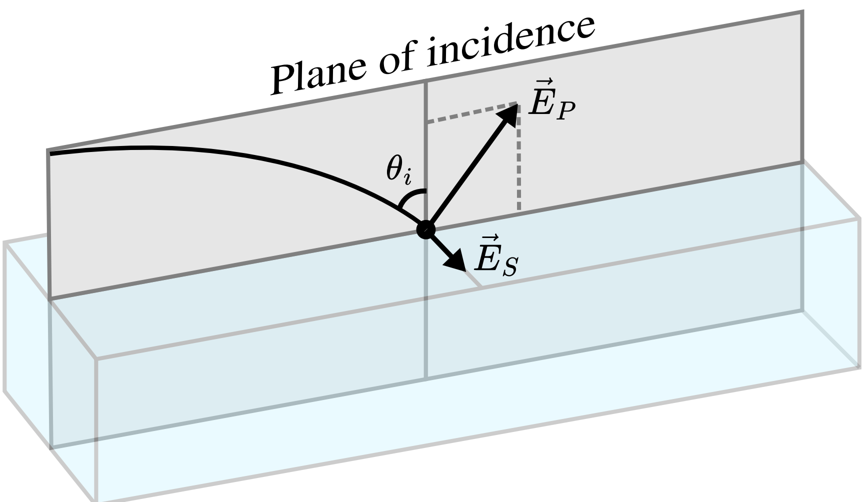


FIGURE 5.4: An illustration of the P and S components of the electric field of a plane wave at the interface of two media.

while the transmission coefficients can be found using

$$t_{\mathrm{P}} = (1 + r_{\mathrm{P}}) \frac{n_1}{n_2}. \tag{5.11a}$$

$$t_{\mathrm{S}} = 1 + r_{\mathrm{S}} \tag{5.11b}$$

Here Snell's law was used to express the angle of refraction as a function of the angle of incidence $\theta_i$. For air-to-ice rays the transmission coefficients $t_S$ and $t_P$ are relevant, while for ice-to-ice rays reflecting on the ice-air boundary the reflection coefficients $r_S$ and $r_P$ should be applied. In case of air-to-ice rays $n_1$ and $n_2$ correspond to the index of refraction of air and ice respectively, which is reversed in the case of ice-to-ice reflected rays. For ice-to-ice reflected rays this means that $n_1 > n_2$, and therefore a critical angle exists at which point the expressions for the reflection coefficients break down. When $\sin\theta_i > \frac{n_2}{n_1}$, total internal reflection occurs, which means the wave reflects completely and no refraction takes place. In principle this introduces a non-trivial phase shift, which is not included in FAERIE.

### 5.3.3 Focusing Factor

Bending of rays introduces a convergence or divergence of the rays, when compared to straight-line propagation. In case of convergence the intensity of the radiation should increase, while it should decrease for divergence. This does not come out naturally when ray tracing is included in the endpoint formalism, since the observer is represented as a single point. The amount of rays going through a single point will always be at most two. Rays will never converge into or diverge out of a single point. This means that the amplitude of the electric field needs to be corrected with a so-called focusing factor, as discussed in [101].

Below the focusing factor is derived assuming a cylindrical symmetry of the medium. In this case the associated refractive index profile only depends on the depth in the medium, and bending does not influence the azimuthal direction of the rays. As illustrated by Figure 5.5, when following bent trajectories the distance between two rays changes from $a$ to $a'$. Given the cylindrical symmetry, the intensity $I$ of the radiation scales as

$$\frac{I'}{I} = \frac{a}{a'}. \tag{5.12}$$

For the case of straight-line propagation, we have

$$a = R d\theta_l. \tag{5.13}$$

In case of ray bending, we see that

$$a' = dz \sin\theta_r. \tag{5.14}$$

Combining both, we find

$$\frac{I'}{I} = \frac{R}{\sin(\theta_r) \frac{dz}{d\theta_l}}. \tag{5.15}$$

The intensity $I$ and the amplitude of the electric field $\epsilon$ follow the relation

$$I \propto \frac{n\epsilon^2}{c_0}, \tag{5.16}$$

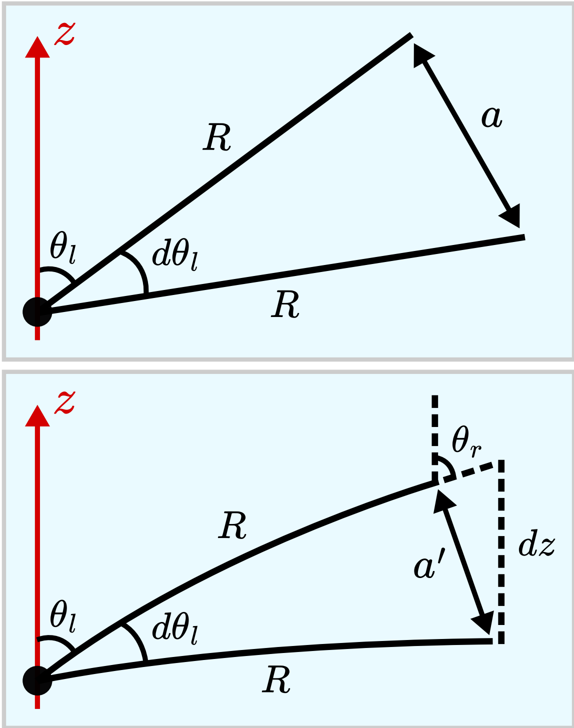


FIGURE 5.5: An illustration of rays propagating on a straight path (top) and rays propagating on bent trajectories (bottom).

with $n$ the index of refraction and $c_0$ the speed of light in vacuum. This means that the focusing factor for the amplitude of the electric field is given by

$$F = \frac{\epsilon'}{\epsilon} = \sqrt{\frac{n}{n'}\frac{I'}{I}} = \sqrt{\frac{n}{n'}\frac{R}{\sin(\theta_r)\frac{dz}{d\theta_l}}}, \tag{5.17}$$

where $n$ and $n'$ correspond to the index of refraction at the emitter and observer respectively. To be more precise, $n$ refers to the index of refraction at the observer in the case of straight-line propagation, which is the same as the index of refraction at the emitter.

Within the context of ray tracing, Equation 5.17 is rewritten in the more practical form

$$F = \sqrt{\frac{n}{n'}\frac{R}{\sin(\theta_r)}\frac{\Delta\theta_l}{\Delta z}}. \tag{5.18}$$

The term $\frac{\Delta\theta_l}{\Delta z}$ can be calculated numerically using ray tracing, by varying the observer position over a small distance $\Delta z$ and calculating the corresponding variation on the launching angle $\theta_l$.

The effect of the focusing factor will be the strongest for ice-to-ice ray tracing, were significant bending of the rays occurs. For air-to-ice ray tracing the effect will be negligible. Most of the radio emission is concentrated around the Cherenkov cone, which for air is around 1°. Since we are not considering very inclined air showers in this work, the angle of incidence $\theta_i$ on the ice surface for the bulk of the in-air emission will be small. Therefore, focusing effects due to refraction and ray bending in the ice will be limited. Currently, FAERIE does not include a focusing factor for in-air radio emission, although a similar approach as presented in [193] could be followed.

## 5.4 Implementation in FAERIE

The Framework for the simulation of Air shower Emission of Radio for in-Ice Experiments (FAERIE) is a Monte Carlo framework for the simulation of radio emission from cosmic-ray air showers propagating through ice. The in-air cascade development and the associated radio emission are simulated with the CORSIKA Monte Carlo and CoREAS codes, while the in-ice cascade development and the associated radio emission are simulated with a Geant4-based module. Both the in-air and in-ice component of FAERIE rely on the endpoint formalism including ray tracing for the calculation of the radio emission, and use similar implementations of the associated concepts.

### 5.4.1 Application of the Ray Tracer

The ray tracer currently implemented in FAERIE is a combination of a traditional ray tracer and an analytical ray tracer, as described in Section 5.3. This means that the refractive index profile only depends on the depth in the medium, which implies that both the air and the ice are assumed to be cylindrically symmetric. The atmosphere is described by 5 consecutive layers, each of which follow a different exponential refractive index profile. For the ice a single exponential refractive index profile is used. The ray tracer does not take into account the curvature of Earth's surface, which should only be important for very inclined air showers. More detailed information on the ray tracer can be found in [178, 194].

The emission from a single endpoint is calculated using Equation 5.6, where the unit vector $\hat{r}$ now represents the launching direction of the ray, $R$ the length of the ray path and $n$ the index of refraction at the endpoint. Relevant parameters that are determined by the ray tracer are therefore the launching angle at the endpoint and the length of the ray path. Furthermore, it provides the receiving angle at the observer to account for the rotation of the electric field. In case of air-to-ice rays and ice-to-ice reflected rays, also the incident angle on the air-ice interface needs to be known, as it determines the corresponding Fresnel coefficients. Finally, as discussed in Section 5.3, in case of ice-to-ice ray tracing the ray tracer also calculates the focusing factor, accounting for convergence or divergence of the rays in the ice. Below a technical overview of the implementations within the Geant4-based in-ice module is given. More information on the adjustments made to the CoREAS code can be found in [178, 179].

#### Evaluating the endpoint formula

Even though the ray tracer assumes cylindrical symmetry of the ice, the calculation of the radio emission from an endpoint is in general a three-dimensional problem. Only in the special case shown in Figure 5.3, in which the starting point, ending point and observer point coincide in the same plane, the problem is reduced to two dimensions. In this case, the electric fields associated with the endpoints are restricted within this plane as well. Relying mainly on geometric vectors defined in a global Cartesian coordinate system ensures the generality of the calculations. In the following we will assume a right-handed coordinate system. The $x$-axis and $y$-axis form the horizontal plane of the coordinate system, parallel to the air-ice interface, and the $z$-axis is perpendicular to this plane. A visualization of ray tracing in the global Cartesian coordinate system is shown in Figure 5.6. The launching direction $\hat{r}$ can then be calculated by rotating the unit vector $\hat{z}$, originally aligned with the

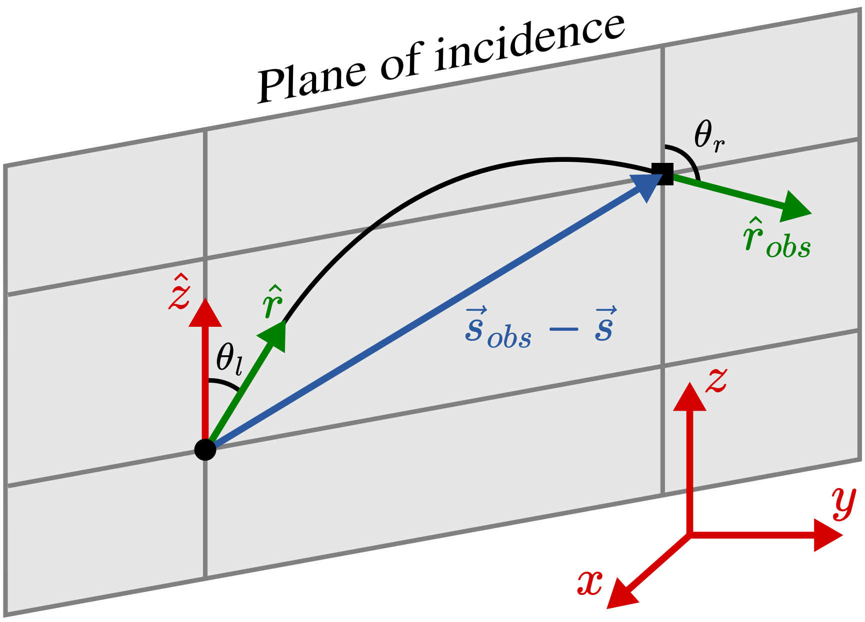


FIGURE 5.6: An illustration of ray tracing in the global Cartesian coordinate system. The vectors $\hat{z}$, $\hat{r}$, $\vec{s}_{obs} - \vec{s}$ and $\hat{r}_{obs}$ all lie in the same plane.

$z$-axis, over the launching angle $\theta_l$ using the rotation axis

$$\hat{u} = \hat{z} \times \frac{(\vec{s}_{obs} - \vec{s})}{||\vec{s}_{obs} - \vec{s}||}, \tag{5.19}$$

while following the right-hand rule to determine the direction of rotation. Here $\vec{s}_{obs}$ is the position of the observer in the Cartesian coordinate system, and $\vec{s}$ that of the endpoint. The receiving direction $\hat{r}_{obs}$ can be calculated in a similar way, rotating the unit vector $\hat{z}$ over the receiving angle instead. A right-hand rotation over an angle $\theta$ around the unit vector $\hat{u}$ is in the global Cartesian coordinate system given by the rotation matrix

$$\begin{bmatrix} \cos\theta + u_x^2(1-\cos\theta) & u_x u_y(1-\cos\theta) - u_z\sin\theta & u_x u_z(1-\cos\theta) + u_y\sin\theta \\ u_y u_x(1-\cos\theta) + u_z\sin\theta & \cos\theta + u_y^2(1-\cos\theta) & u_y u_z(1-\cos\theta) - u_x\sin\theta \\ u_z u_x(1-\cos\theta) - u_y\sin\theta & u_z u_y(1-\cos\theta) + u_x\sin\theta & \cos\theta + u_z^2(1-\cos\theta) \end{bmatrix}$$

which can be deduced from the so-called Rodrigues' rotation formula [195–198].

Once the launching direction $\hat{r}$ is known, Equation 5.6 can be evaluated to calculate the electric field at the observer associated with the radio emission from the endpoint. The field is then rotated so that its component in the plane of incidence is perpendicular to the receiving direction $\hat{r}_{obs}$, instead of the launching angle $\hat{r}$. The same rotation axis $\hat{u}$ can be used, again following the right-hand rule to determine the direction of rotation, while the rotation angle is simply given by $\theta_r - \theta_l$. The rotation matrix however effectively depends on the cosine and sine value of the rotation angle. It is therefore numerically more efficient to directly calculate the cosine of the rotation angle as

$$\cos|\theta_r - \theta_l| = \hat{r} \cdot \hat{r}_{obs}, \tag{5.20}$$

as a scalar product of two vectors can be easily calculated by multiplication and addition of the components in the global Cartesian coordinate system. The sine of the rotation angle follows from

$$\sin|\theta_r - \theta_l| = \sqrt{1 - \cos|\theta_r - \theta_l|^2}. \tag{5.21}$$

Following Equations 5.20 and 5.21, the rotation matrix can be constructed, using $\vec{u}$ as the rotation axis if $\theta_r - \theta_l > 0$, while using $-\vec{u}$ as the rotation axis if $\theta_r - \theta_l < 0$. Note that for a single exponential refractive index profile rays will in principle always bend downward, but for more generic ray tracers the condition $\theta_r - \theta_l < 0$ can occur.

### Applying the Fresnel coefficients

As discussed in Section 5.3.2, when considering ice-to-ice rays reflecting on the ice-air boundary, the Fresnel reflection coefficients need to be taken into account. The Fresnel reflection coefficients are scaling factors applied to the P and S component of the electric field at the ice-air boundary, shown in Figure 5.4, which determine the amplitude of electric field of the ray reflecting back into the ice. The P and S component of the electric field in an observer point can be constructed by switching from the global Cartesian coordinate system to a local spherical coordinate system, defined by the receiving direction of the ray $\hat{r}_{obs}$ and two additional orthonormal vectors $\hat{\theta}$ and $\hat{\phi}$. The relation between the global Cartesian coordinate system and such a local spherical coordinate system is illustrated in Figure 5.7. Since we know that the electric field does not have a component along the direction of $\hat{r}_{obs}$, the P and S components of the electric are given by $E_P = E_\theta$ and $E_S = E_\phi$.

From the vector $\hat{r}_{obs} = (r_x, r_y, r_z)$ given in the global Cartesian coordinate system the two other orthonormal vectors can be calculated. The vector $\hat{\phi}$ is confined to the

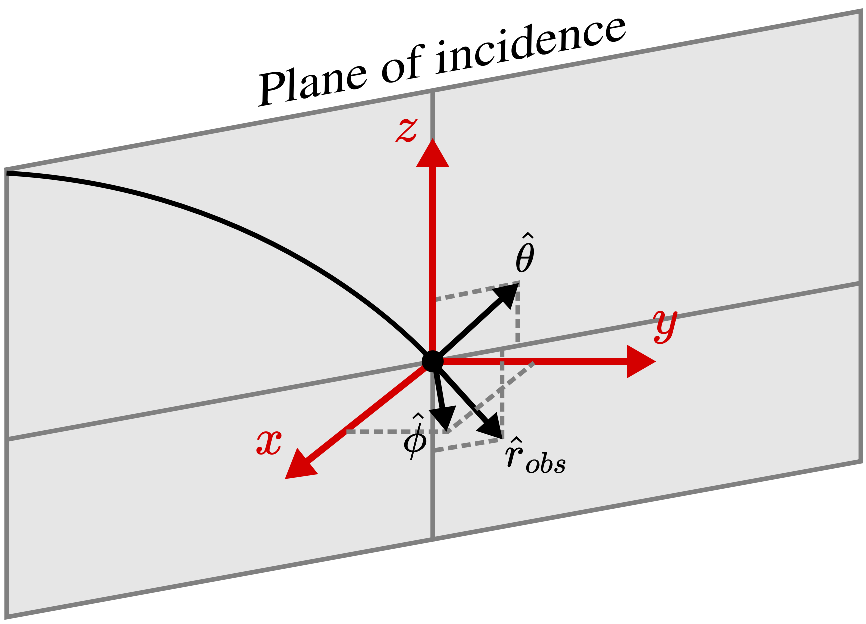


FIGURE 5.7: A visualization of the relation between a global Cartesian coordinate system and a local spherical coordinate system, defined by the incoming direction of the ray. The spherical coordinate system is given by the orthonormal vectors $\hat{r}_{obs}$, $\hat{\theta}$ and $\hat{\phi}$.

$xy$-plane and meets the condition $\hat{\phi} \cdot \hat{r} = 0$, which means

$$\hat{\phi} = \frac{1}{\sqrt{r_x^2 + r_y^2}} \left(-r_y, r_x, 0\right). \tag{5.22}$$

The unit vector $\hat{\theta}$ can be found by $\hat{\theta} = \hat{\phi} \times \hat{r}$, which gives

$$\hat{\theta} = \frac{1}{\sqrt{r_x^2 + r_y^2}} \left(r_x r_z, r_y r_z, -(r_x^2 + r_y^2)\right) \tag{5.23}$$

The electric field $\vec{E}_C$ corrected for the reflection coefficients can then be derived from the uncorrected electric field $\vec{E}$ using

$$\vec{E}_C = r_S(\hat{\phi} \cdot \vec{E})\hat{\phi} + r_P(\hat{\theta} \cdot \vec{E})\hat{\theta}. \tag{5.24}$$

Equation 5.24 can be applied directly to the electric field at the observer, and does not need to be applied to the electric field at the ice-air boundary. When viewed from within the global Cartesian coordinate system, the electric field at the observer is smaller than that at the ice-air boundary due to a larger path length $R$, and orientated differently due to the change in receiving direction $\hat{r}_{obs}$. This follows directly from the endpoint formula given by Equation 5.6. The Fresnel reflection coefficients are however applied in the local spherical coordinate system, which is aligned with $\hat{r}_{obs}$. When comparing the electric fields to each other in their respective local systems, the only difference is the magnitude due to the different path lengths. Applying the Fresnel reflection coefficients in the local coordinate system at the ice-air boundary is therefore equivalent to simply applying the Fresnel coefficients in the local coordinate system at the observer. Whether the Fresnel reflection coefficients scale down the electric field before or after the propagation scaling does not affect the final result. The only relevant variable associated with the reflection point at the ice-air boundary is the incidence angle $\theta_i$, which follows directly from ray tracing.

#### Applying the focusing factor

Finally, the electric field is multiplied by the focusing factor $F$, calculated using the form given in Equation 5.18. For FAERIE the value $\Delta z = 1$ cm is used. The factor is restricted to

$$0.5 \leq F \leq 2.0, \tag{5.25}$$

to be consistent with the approach outlined in [101].

### 5.4.2 Interpolation Tables

The ray tracer currently implemented in FAERIE relies on an analytical solution of the ray paths, which means it is significantly faster than traditional ray tracers. Given the huge amount of particles and corresponding endpoints in the simulation, the ray tracer has nonetheless proven to be too slow, driving up the total simulation time beyond what is practically acceptable for both the in-air as well as the in-ice component of the cascade.

Therefore, the ray tracing in FAERIE is performed before the actual particle cascade simulation starts. The ray tracer calculates the ray tracing parameters for a predetermined set of emitter positions and observer positions, and stores the results in tables. For each observer position one table is constructed, covering the expected range of relevant emitter positions. Since the ray tracer assumes cylindrical symmetry such a table can be visualized as a two-dimensional grid, each point representing an emitter position. The first axis of the grid indicates its horizontal distance to the given observer point, while the second axis indicates its depth. In case of ice-to-ice ray tracing the relevant emitter positions are determined by the in-ice particle cascade, and are captured by a grid that spans 40 m on the first axis and 20 m on the second axis. This is visualized in Figure 5.8. The larger range on the first axis ensures also inclined showers with zenith angle $\theta \geq 30°$ are contained in the grid. In case of air-to-ice ray tracing the scale on the first axis is set by performing ray tracing with different values for the launching angle, starting at 89.9° (almost horizontal) and ending with 0° (vertically down). The second axis of the grid starts at the altitude of the ice surface, typically around 3 km above sea level, and goes up to 100 km above sea level. Since the ray tracer assumes cylindrical symmetry, the air-to-ice ray tracing tables constructed in this way only depend on the depth of the observer point. Observer points at the same depth in the ice therefore share a single air-to-ice ray tracing table, which reduces the memory usage.

Once the tables are constructed, the particle cascade simulation starts. For every endpoint in the simulation the ray tracer parameters are then calculated from linear interpolation of the tables. Interpolating the tables is roughly 100 times faster than the actual ray tracing calculations, making simulating the required amount of endpoints possible. The relative error for the interpolated results is of the order of $10^{-7} - 10^{-8}$ [179, 199]. Note that the use of ray tracing tables allows for the implementation of slower ray tracers, which are usually more accurate. The time it takes to construct a ray tracing table does not influence the speed with which it is interpolated during the particle cascade simulation. Breaking the assumed cylindrical symmetry would however require three-dimensional ray tracing tables, which needs significantly more memory, as well as a revision of the focusing factor.

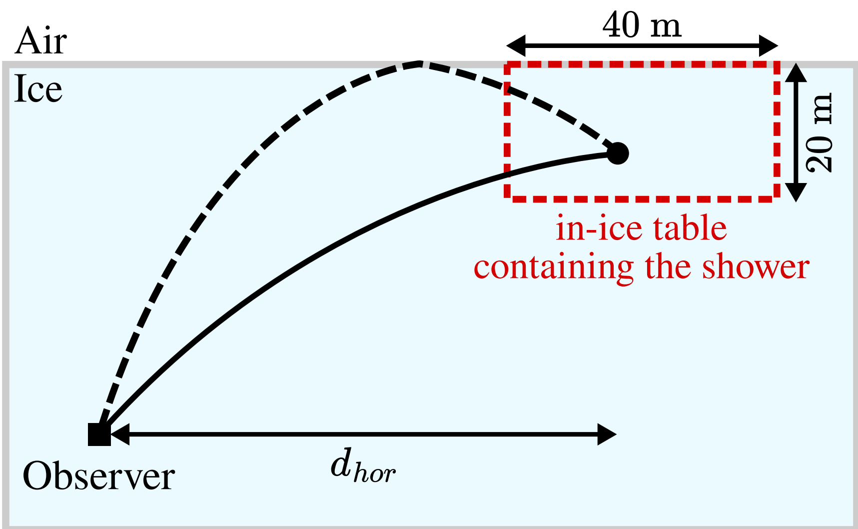


FIGURE 5.8: A visualization of an interpolation table used for the in-ice ray tracing, for a given observer position. Interpolation tables for the in-air ray tracing follow a similar structure, but instead cover a much larger area in air. A single in-air table is used for multiple receivers at the same depth in the ice.

## 5.5 Simulation Results

In this section the first results of FAERIE are presented. The parameters of the framework are set to correspond to the South Pole. For the density of the atmosphere we use the five-layer model for the South Pole described by Table A.2 in Appendix A, which follows from a fit to a database used by the National Center for Environmental Predictions Global Forecast System in weather forecasting. The refractive index profile of the atmosphere consists of five consecutive exponential functions, each function corresponding to one of the density layers. They are determined by matching the refractive index profile to the density profile of the atmosphere, as described in Appendix C. The density of the ice follows a typical polar ice density profile given by

$$\rho(z) = \rho_{\text{ice}} - (\rho_{\text{ice}} - \rho_{\text{surface}}) \exp\left(-\frac{1.9}{t_{\text{firn}}}|z|\right), \tag{5.26}$$

with $\rho_{\text{ice}} = 917$ kg m$^{-3}$, $\rho_{\text{surface}} = 359$ kg m$^{-3}$ and $t_{\text{firn}} = 100$ m [200]. The refractive index profile of the ice is described by a single exponential profile,

$$n(z) = 1.78 - 0.43 \exp\left(-(0.0132\ \text{m}^{-1})|z|\right), \tag{5.27}$$

which corresponds to the model used by the Askaryan Radio Array at the South Pole outlined in [201]. Note that in FAERIE the ice density profile only influences the particle cascade development in the ice, and not the radio emission propagation. This means that it is only relevant down to $\sim 20$ m, even though observers can be located deeper below the surface. The ice surface is set at an altitude of 2.835 km. For the given atmospheric density profile this corresponds to a vertical depth of 729 g/cm$^3$, which is close to that of the reference shower discussed in the previous chapter.

The CORSIKA code was updated to version 7.7500. For hadrons (except $\pi^0$'s) and muons the threshold of the tracking cut was set to 0.3 GeV. For electrons and photons (including $\pi^0$'s) the threshold was set to 0.401 MeV. We use the QGSJETII-04 high-energy hadronic interaction model [157] and the UrQMD low-energy hadronic interaction model [202, 203]. Thinning was applied during the CORSIKA air shower simulation on electromagnetic particles falling below $10^{-6}E_p$, using a weight limit of $w = 100$. The geomagnetic field was set to $\vec{B} = (16.7525\ \mu\text{T}, -52.0874\ \mu\text{T})$, corresponding to the values at a latitude of 89.9588° south following the IGRF12 model [204]. The first component indicates the horizontal component of the magnetic field, which defines the geomagnetic north. The second component indicates the vertical component of the magnetic field, which is upward for negative values.

The production cut-off lengths for the Geant4-based module are set to the default values, which is 1 mm for gammas, electrons and positrons. Furthermore, for the calculation of the radio emission only charged particles with a kinetic energy above 0.1 MeV were taken into account. To minimize the processing time, hadronic interactions are not included in the simulations of the in-ice particle cascade, since the radio emission will be dominated by the electromagnetic part of the cascade. As mentioned in Chapter 4, hadronic interactions only affect the tail of the electromagnetic particle distribution, while most of the radiation will be generated around shower maximum. Moreover, as was also demonstrated in the previous chapter, at the ice surface altitude we expect about 50% of the energy of the particle cascade to be contained within a radius of 1 m from the shower axis. We defined this as the core of the shower, and demonstrated that particles outside of the core will not contribute significantly to the development of the in-ice cascade. Therefore, only the air shower core is propagated through the ice and contributes to the in-ice radio emission. Note however that for the in-air radio emission, the whole air shower is accounted for.

To confirm that only the core of the air shower needs to be propagated through the ice for the calculation of the in-ice radio emission, we show the results of simulations that did not include ray tracing. Instead the index of refraction of the ice was fixed at a value $n = 1.52$, which allows to estimate the location of the Cherenkov cone. The calculations where made for the proton-induced reference air shower from Chapter 4 ($E_p - 10^{17}$ eV, $\theta = 0°$) with an observer placed close to the Cherenkov cone. The radius of the air shower footprint propagated through the ice was repeatedly increased by an amount $\Delta r = 1$ cm, and at each increment the electric field was calculated. Figure 5.9 shows the intensity of the vertical (VPol) and horizontal (HPol) component of the electric field as a function of the radius of the particle footprint that was propagated through the ice, where we defined the intensity of the emission as

$$I = \int E(t)^2 dt. \tag{5.28}$$

The intensity of both components stops increasing around a radius of $r \sim 10$ cm, which shows that including only the particles within a radius of $r = 1$ m during the in-ice simulations is indeed sufficient to calculate the corresponding radio emission.

Below, the general properties of the radio emission of a cosmic-ray air shower propagating through ice will be illustrated, using the setup described above. In line with the discussion in Chapter 4, we will focus on the results of a proton-induced particle shower with primary energy $E_p = 10^{17}$ eV and zenith angle $\theta = 0°$. Distributions describing the particle cascade development of the simulated particle shower can be found in Appendix D. More information about the computation time of the simulation can be found in Appendix E.

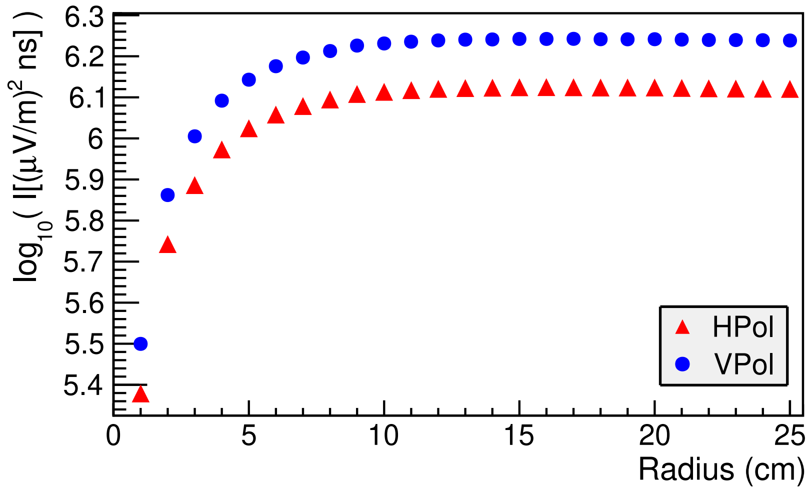


FIGURE 5.9: The intensity $I = \int E(t)^2 dt$ of the in-ice radio emission as a function of the radius of the particle footprint that was propagated through the ice of both the vertical component (VPol) and horizontal component (HPol), for an observer close to the Cherenkov cone [1]. The index of refraction of the ice was fixed at $n = 1.52$, and therefore no ray tracing was included. Shown here are the results for the proton-induced reference air shower discussed in Chapter 4 ($E_p = 10^{17}$ eV, $\theta = 0°$).

### 5.5.1 Radio Footprint

The fluence footprint of the radio emission at a depth of 100 m below the ice surface is given in Figure 5.10. The figure separately shows the component of the emission created by the particle shower in air, the component of the emission created during propagation of the cascade through ice, and the combination of both components. The vertical axis is aligned with the horizontal component of the magnetic field and defines the south-north direction, while the horizontal axis indicates the west-east direction. Fluence is defined as

$$\Phi = \epsilon_0 c_0 \int E^2(t)\mathrm{d}t, \tag{5.29}$$

with $\epsilon_0$ the vacuum permittivity, $c_0$ the speed of light in vacuum and $E(t)$ the magnitude of the electric field at time $t$. To calculate the fluence footprint a simulation for 121 observer points at a depth of 100 m below the ice surface was performed. The points were placed in a star-shape pattern with 8 arms and a spacing of 10 m, including an extra observer point at the center of the grid. The center of the grid lies on the shower axis of the particle cascade. The complete footprint was then determined through interpolation, using the code described in [205].

The Cherenkov angle in air is of the order of 1°, which means most of the in-air radiation is concentrated around the shower axis. Taking into account the refraction following the propagation into ice we can expect the emission to be even more concentrated around the axis, although this effect should be rather small. The radiation created during the cascade development in air is a combination of geomagnetic emission and Askaryan emission. The superposition of both leads to a bean-shaped asymmetry of the fluence footprint along the $\vec{v} \times \vec{B}$ axis, as discussed in Chapter 1. As mentioned above, the horizontal component of the magnetic field is aligned with the north axis of the coordinate system. Since $\theta = 0°$, the particles in the air shower are mainly moving vertically downwards. The direction of $\vec{v} \times \vec{B}$ is therefore from west to east. This means that we expect a west-east asymmetry in the footprint corresponding to the emission created in air, with more energy distributed over the east side of the footprint than over the west side of the footprint. This is clearly visible in Figure 5.10.

Once propagating through the ice the transverse current in the shower cascade front is suppressed, which means the particle cascade only emits Askaryan radiation. Looking at the footprint corresponding to the emission created in ice, we clearly see the associated symmetric Cherenkov ring. The radiation is now concentrated further out from the shower axis, as the Cherenkov angle in ice is of the order of $40° - 45°$ in the first 20 m below the surface. The combination with the emission in air results in a unique footprint. It consists of the bean-like shape from the in-air emission close to the shower axis, surrounded by the Cherenkov ring from the in-ice emission further out. The geomagnetic component of the in-air emission creates a subtle west-east asymmetry in the Cherenkov ring.

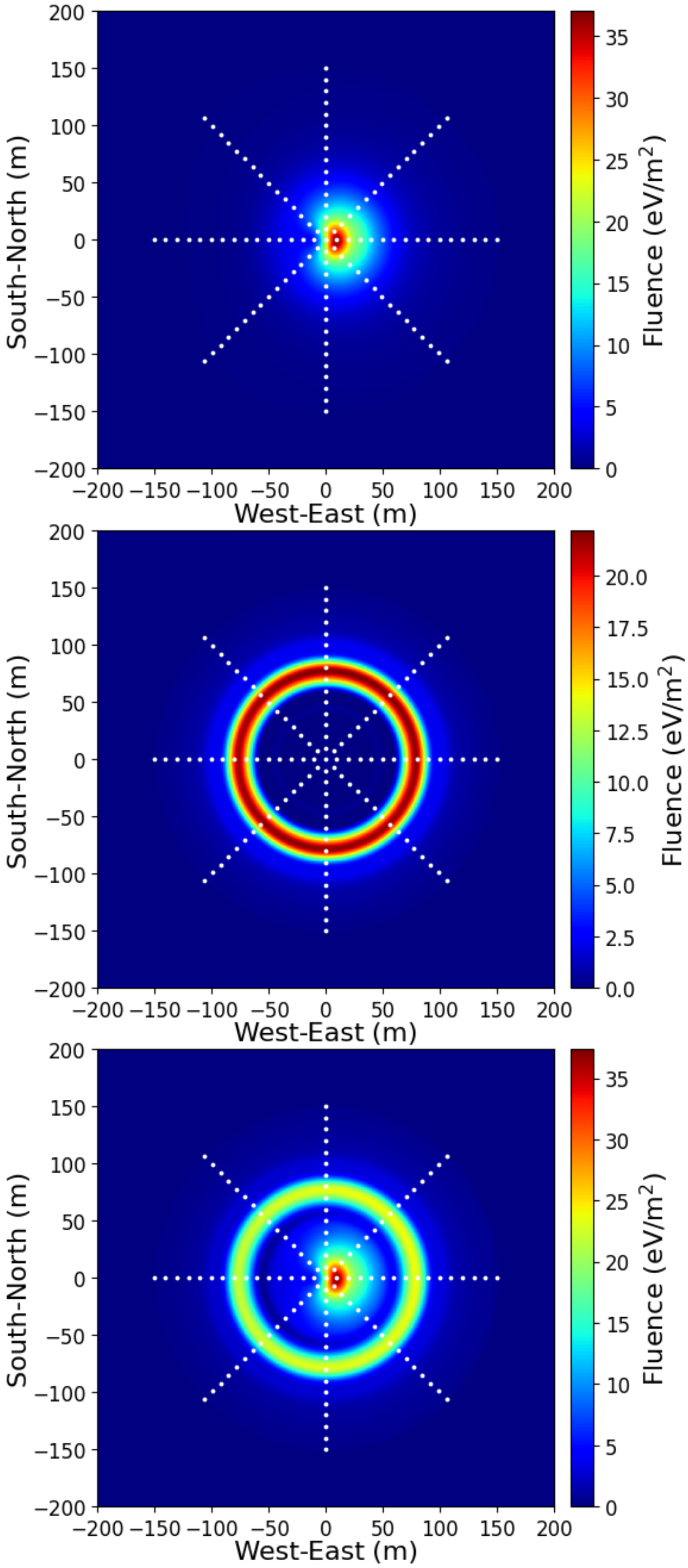


FIGURE 5.10: The fluence footprint of the simulated cosmic-ray air shower propagating through ice at a depth of 100 m below the ice surface for the in-air emission (top), in-ice emission (middle) and the combined emission (bottom), with $E_p = 10^{17}$ eV and $\theta = 0°$ [2]. The simulation included observer positions distributed over a star-shaped grid with 8 arms and a spacing of 10 m, as indicated by the white dots. The interpolation was performed with the code described in [205].

### 5.5.2 Electric Field Traces

**In-air emission**

Figure 5.11 shows the electric field components as a function of time at a depth of 100 m from the ice surface, for two observer points located 20 m away from the shower axis. At this distance to the shower axis the in-air emission is the strongest. One observer point lies on the south axis, while the other observer point lies on the north axis. In Figure 5.12 the same is shown, now placing the observer points along the west and east axes. The blue lines indicate the emission created in air, while the red lines indicate the emission created in ice. The component $E_{\text{north}}$ is the component along the south-north axis, and positive when pointing to the north. The component $E_{\text{east}}$ is the component along the west-east axis, and positive when pointing to the east. The component $E_{\text{vert}}$ is the component perpendicular to the air-ice interface, and is positive when pointing upwards.

As mentioned earlier, the direction of $\vec{v} \times \vec{B}$ is from west to east. For the in-air emission we expect the geomagnetic radiation to be more important than the Askaryan radiation, and therefore the east component to be the strongest. Furthermore it should be negative, indicating an antiparallel orientation with respect to the $\vec{v} \times \vec{B}$ direction. This is clearly the case in both figures.

Nevertheless, we do expect a non-zero component of the in-air emission associated with the Askaryan radiation. For the observers on the south-north axis this translates to a non-negligible north component, negative on the northern side of the footprint and positive on the southern side of the footprint. For the west and east observer points there is almost no contribution to the north component, as in these cases the in-air Askaryan radiation is polarized along the west-east axis. The bean-shaped west-east asymmetry of the radio footprint resulting from the superposition of the geomagnetic and Askaryan radiation is clearly visible in the traces. The corresponding peak amplitudes are higher for the observer point on the eastern side of the footprint, compared to those for the observer on the western side of the footprint.

The vertical component of the in-air emission should be the smallest, since we can expect most of the radiation created in air to be described by downward going rays. The electric field of the emission is perpendicular to the rays, and therefore mostly horizontal. This is indeed what is shown by the figures. Furthermore, the pulse shape of the in-air emission is very similar to that obtained for observer positions in air. It is characterized by a strong and sharp peak, followed by a long tail of opposite polarization [36]. This indicates that the shape of the pulse is largely unaffected by ray tracing.

Interestingly, the shape of the pulse of the vertical component shows an additional sharp peak for observer points on the west-east axis, compared to those on the south-north axis. The difference between both pulse shapes could be another consequence of geomagnetic emission. If we model the geomagnetic emission as the radiation generated by a changing current along the west-east axis, an observer in the plane perpendicular to the current and intersecting the current halfway through will not see any vertical component of the electric field. Instead, the electric field will be perfectly aligned with the current. Observer points on the south-north axis lie in this plane. Observer points along the west-east axis however will in general see a vertical component of the electric field, as they are located in the vertical plane aligned with the current. It is therefore not surprising to find a difference in the shape pulse of the vertical component of the electric field, when comparing observer points on the south-north axis with observer points on the west-east axis. The similarities between both pulse shapes could then be attributed to the Askaryan emission.

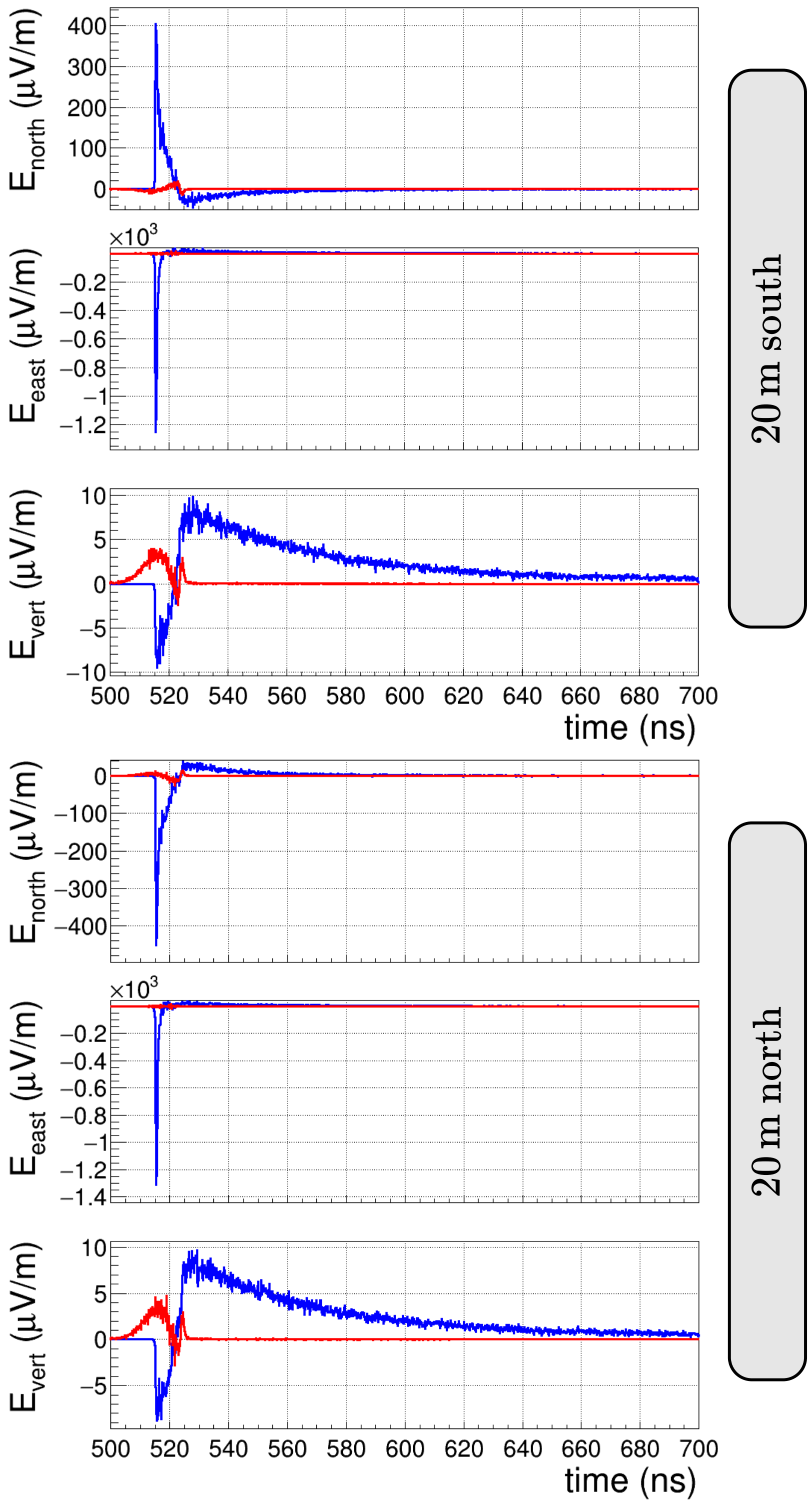


FIGURE 5.11: The electric field components as a function of time for 2 different observer positions, for the cosmic-ray air shower with $E_p = 10^{17}$ eV and $\theta = 0°$ [2]. The observers are located 20 m away from the shower axis on the south-north axis, at a depth of 100 m below the ice surface. The blue lines indicate the in-air emission, while the red lines indicate the in-ice emission. Note that the range on the $y$-axis is not fixed.

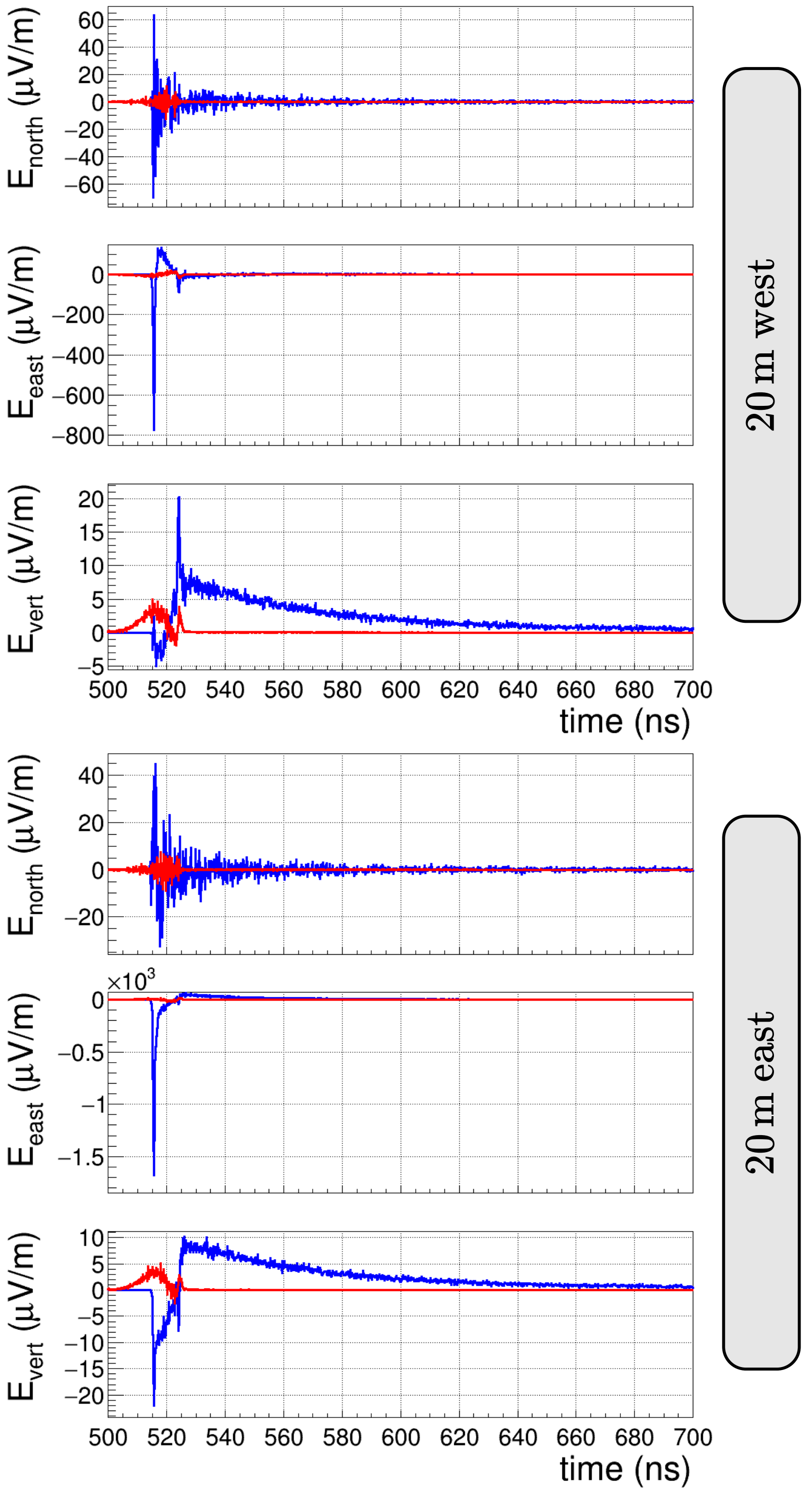


FIGURE 5.12: The electric field components as a function of time for 2 different observer positions, for the cosmic-ray air shower with $E_p = 10^{17}$ eV and $\theta = 0°$ [2]. The observers are located 20 m away from the shower axis on the west-east axis, at a depth of 100 m below the ice surface. The blue lines indicate the in-air emission, while the red lines indicate the in-ice emission. Note that the range on the $y$-axis is not fixed.

### In-ice emission

Figure 5.13 shows the electric field components as a function of time at a depth of 100 m from the ice surface, for two observer points located 80 m away from the shower axis. They are both situated within the Cherenkov ring of the emission created by the in-ice particle cascade. Again one observer point lies on the south axis, while the other observer point lies on the north axis. In Figure 5.14 the same is shown, now placing the observer points along the west and east axes.

The in-ice emission is purely Askaryan, which means it should be radially polarized. Indeed, for the observers on the south-north axis we see that its north component is the strongest, showing a polarization flip when moving from one side of the footprint to the other side of the footprint. The small contribution to the east component of the electric field can be attributed to the lateral momentum within the particle cascade in the ice. For the west-east observers the roles are reversed, showing a strong east component with a flipping polarization and a negligible north component. In contrast to the in-air emission, the in-ice emission does have a significant vertical component. For an observer point located 100 m below the ice surface and 80 m from the shower axis, the rays describing the direct in-ice emission propagate at angles around 50° with respect to the surface. Since the electric field of the emission is perpendicular to the rays, it should indeed have a vertical component that is comparable in size to its horizontal component. The launching angles associated with the indirect rays are in the given geometry far off from the Cherenkov angle, which means the contribution of the indirect radiation is negligible.

### Equivalent neutrino energy

When a neutrino with an energy of $10^{16}$ eV interacts in the ice and creates an electromagnetic shower, it leads to Askaryan radio emission with a typical amplitude of around 1000 $\mu$V/m close to the Cherenkov cone [101]. This corresponds to the peak amplitude of the signals shown in the figures discussed above. As a rule of thumb, we can therefore state that the signal of a cosmic-ray cascade with a primary energy $E_p$ and zenith angle $\theta = 0°$ observed in ice translates to a signal from a neutrino with an energy of $0.1 \times E_p$. As shown by Figure 4.4, this indeed corresponds to the typical energy within the core of cosmic-ray air shower at altitudes around 3 km above sea level.

### Double pulse signature

Comparing Figures 5.11 and 5.12 with Figures 5.13 and 5.14, we clearly see that the arrival time difference between the in-air signal and the in-ice signal strongly depends on the position of the observer. Observer points close to the shower axis will receive the in-air and in-ice signal almost simultaneously, as both the emission created in air and that created in ice travel approximately the same distance through the ice. For observers moving away from the shower axis however, the in-ice signal will be delayed compared to the in-air signal. The emission created in air will propagate through the air and refract into the ice somewhere close to the observer position. The emission created in ice has to travel a much larger distance through the ice, as the full path between the in-ice cascade and the observer lies below the surface. Since the speed of light in ice is significantly lower than it is in air, the in-ice signal will be delayed, while the in-air signal is hardly affected. The arrival time of the in-air signal is mostly determined by the depth of the observer point.

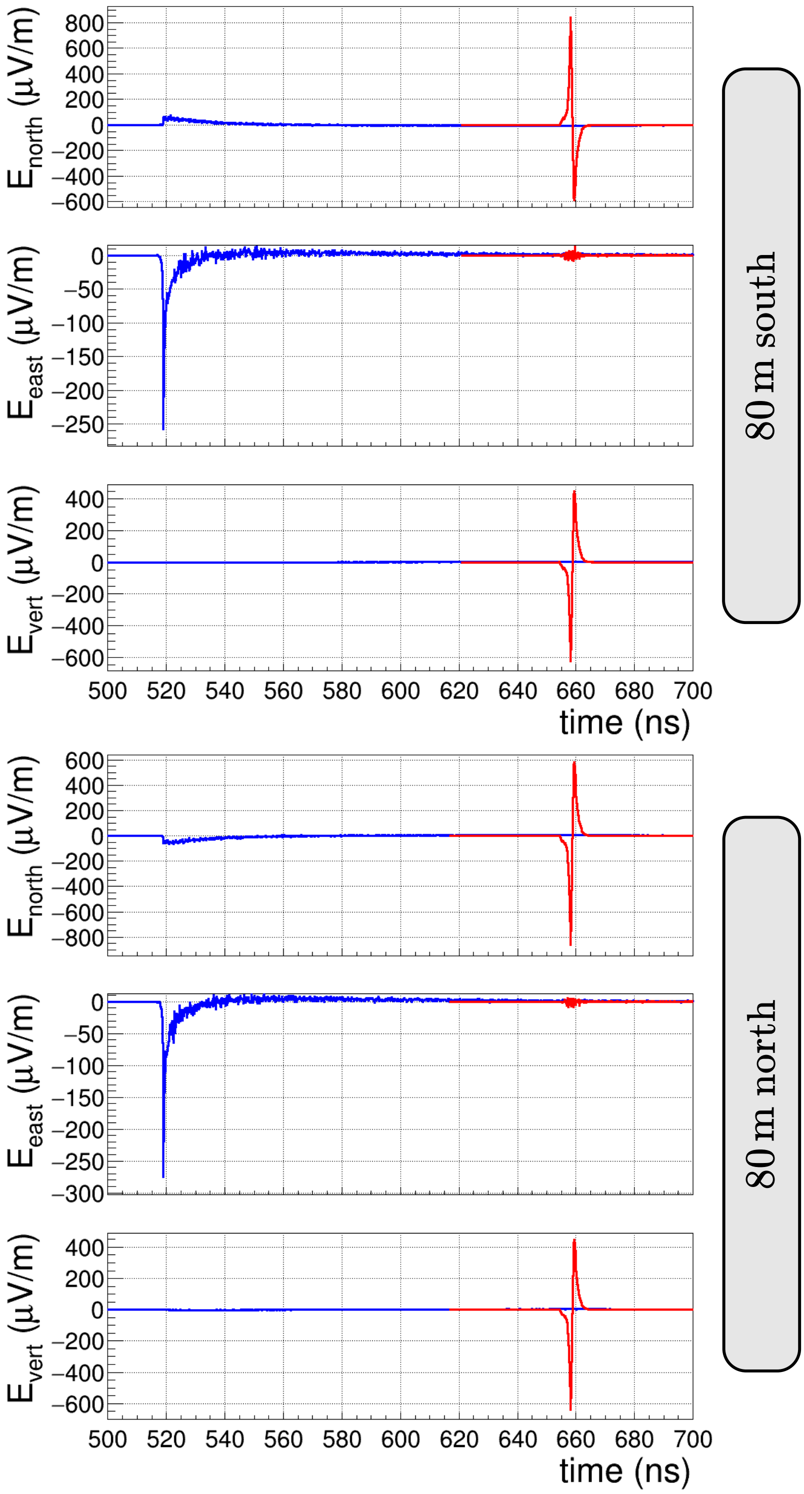


FIGURE 5.13: The electric field components as a function of time for 2 different observer positions, for the cosmic-ray air shower with $E_p = 10^{17}$ eV and $\theta = 0°$ [2]. The observers are located 80 m away from the shower axis on the south-north axis, at a depth of 100 m below the ice surface. The blue lines indicate the in-air emission, while the red lines indicate the in-ice emission. Note that the range on the $y$-axis is not fixed.

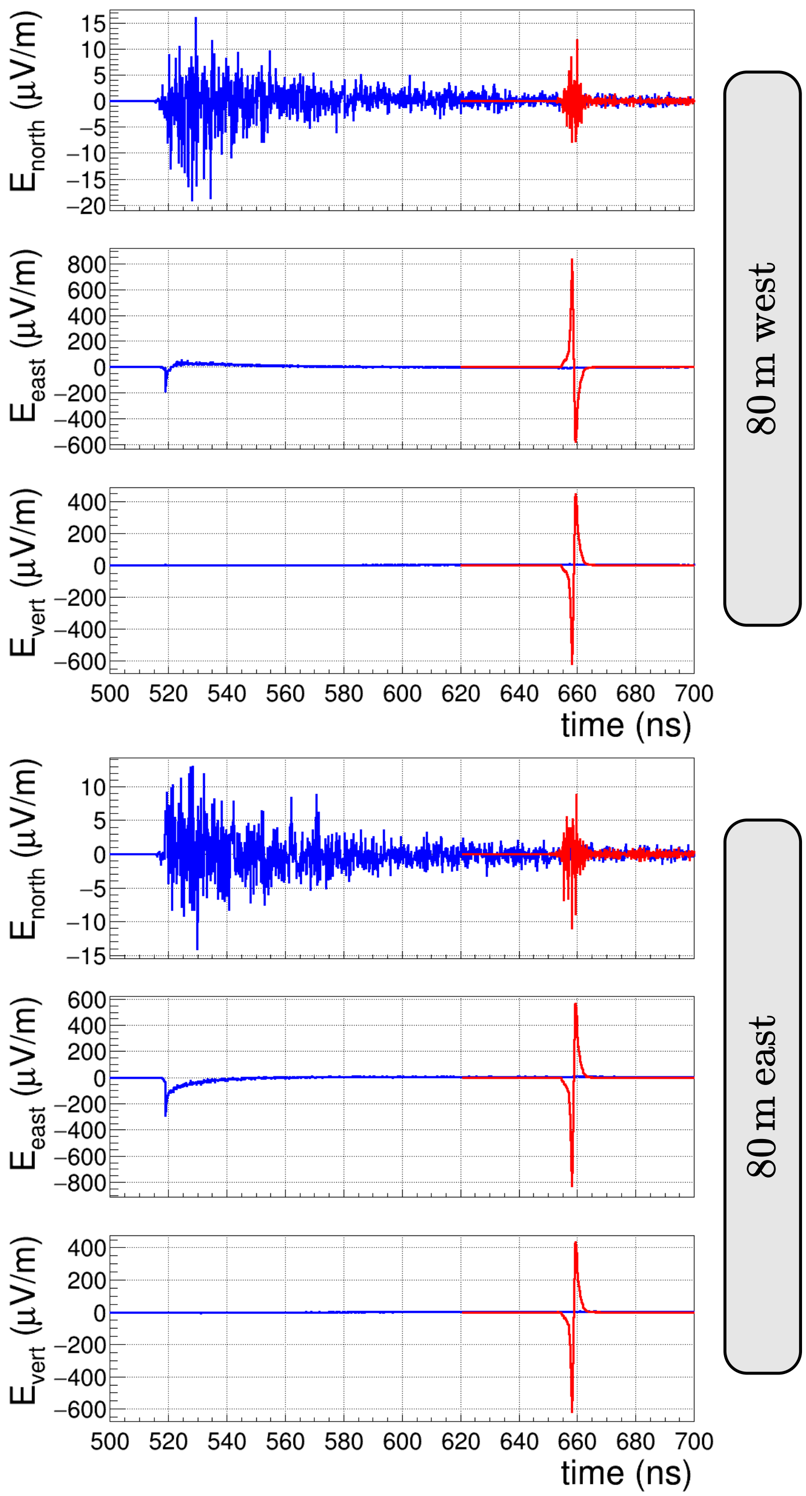


FIGURE 5.14: The electric field components as a function of time for 2 different observer positions, for the cosmic-ray air shower with $E_p = 10^{17}$ eV and $\theta = 0°$ [2]. The observers are located 80 m away from the shower axis on the west-east axis, at a depth of 100 m below the ice surface. The blue lines indicate the in-air emission, while the red lines indicate the in-ice emission. Note that the range on the $y$-axis is not fixed.

Figure 5.15 shows the time difference between the in-air signal and in-ice signal as a function of distance to the shower axis, for observer points at different depths below the ice surface. The arrival time was defined as the time where the Hilbert envelope of the signal reaches 33% of its maximum value, after passing an 8th order digital Butterworth bandpass filter for the frequency band $30 - 1000$ MHz, averaged over the three components. As explained above, the time difference between both signals increases as the observer moves away from the shower axis, as the in-ice signal is delayed. The figure also illustrates that this time difference depends on the depth of the observer point. For observers deep below the ice surface, the distance propagated through ice by the in-air emission becomes comparable to that of the in-ice emission. As a consequence, the time difference between both signals is smaller.

For observers on the shower axis, the in-ice signal arrives before the in-air signal. As the particle cascade in air moves downward faster than the speed of light in air, it will reach the ice surface slightly before the associated radio emission. As such the in-ice emission will have a small head start propagating down to the observer, closely followed by the in-air emission. This effect is small and barely noticeable in the figure, as the index of refraction in air is close to unity.

The total signal of a cosmic-ray event observed in ice therefore in general consists of two pulses. As shown by Figure 5.13 and 5.14, for some observers both pulses are strong enough to be detected. This double pulse signature could be used by in-ice radio experiments to search for cosmic-ray particle cascade signals, combined with other properties such as arrival direction. Furthermore, the in-air emission will be polarized in the $\vec{v} \times \vec{B}$ direction, while the in-ice emission will be radially polarized. Taking into account polarization measurements would therefore make the double pulse signature an even stronger discriminator. Moreover, Figure 5.15 illustrates that from the time difference of both signals in principle the distance to the shower axis can be determined. The results shown in this figure however are derived for a particle shower with zenith angle $\theta = 0°$, and a degeneracy might arise when considering other zenith angles.

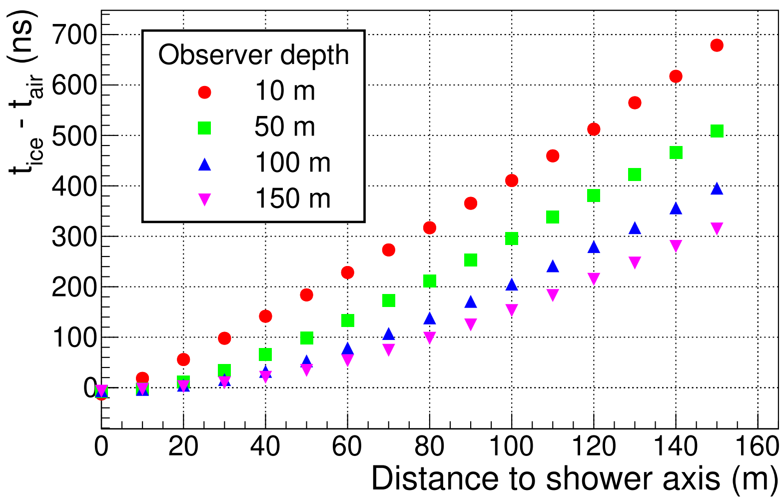


FIGURE 5.15: The difference in arrival time of air and ice radio pulses as a function of distance to the shower axis for varying depths, with $E_p = 10^{17}$ eV and $\theta = 0°$ [2]. The depth of the observer is indicated by the legend. The arrival time was defined as the time where the Hilbert envelope of the signal reaches 33% of its maximum value, after passing an 8th order digital Butterworth bandpass filter for the frequency band $30 - 1000$ MHz, averaged over the three components.

### 5.5.3 Frequency Dependence

In practice radio emission is measured by antennas, which are only sensitive to radiation within a certain frequency range. It is therefore valuable to study the frequency dependence of the radio emission of a cosmic-ray event. Furthermore, the response of the antenna to the electric field is determined by the specific antenna design, and usually depends on the arrival direction of the radiation. Predicting how the exact signal of a cosmic-ray event would look like for a given detector however falls out of the scope of this thesis.

Figure 5.16 and Figure 5.17 show the fluence for three different frequency bands along the south-north axis and the west-east axis respectively, simulated using 201 observer points separated by 1.5 m at a depth of 100 m below the ice. For each of the three frequency bands an 8th order digital Butterworth bandpass filter was applied. The low frequency band was limited to $30 - 100$ MHz, the middle frequency band was limited to $100 - 300$ MHz, and the high frequency band was limited to $300 - 1000$ MHz. The two outer fluence peaks in the figures are associated with the in-ice emission concentrated in the Cherenkov ring. The inner fluence peak is associated with the in-air emission, which is concentrated around the shower axis. The west-east asymmetry due to the superposition of the in-air geomagnetic and in-air Askaryan emission is clearly visible in Figure 5.17.

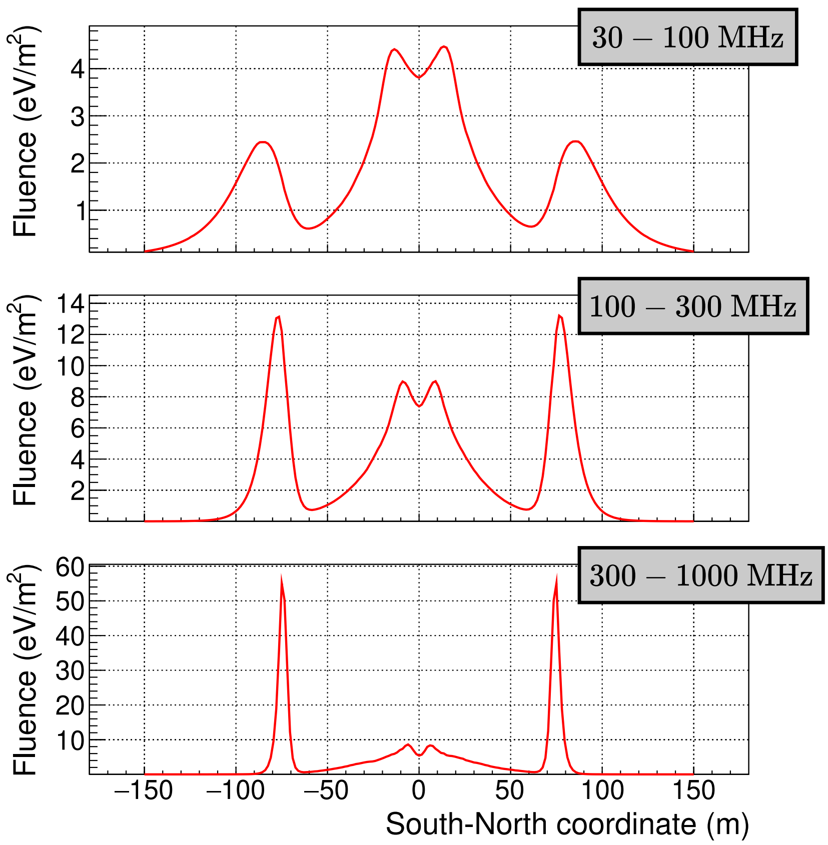


FIGURE 5.16: The fluence on the south-north axis at a depth of 100 m below the ice surface for the combined in-air and in-ice emission for different frequency bands, with $E_p = 10^{17}$ eV and $\theta = 0°$ [2]. For each of the three frequency bands an 8th order digital Butterworth bandpass filter was applied, using the frequency range indicated by the labels. The simulation was performed using 201 observer points on the south-north axis, placed 1.5 m apart.

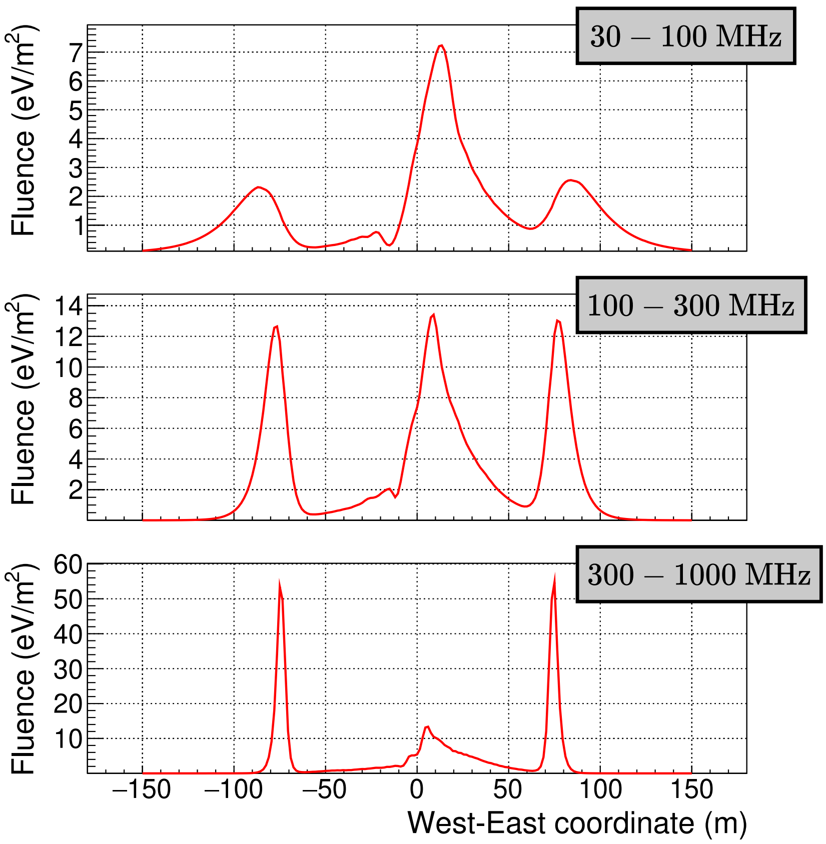


FIGURE 5.17: The fluence on the west-east axis at a depth of 100 m below the ice surface for the combined in-air and in-ice emission for different frequency bands, with $E_p = 10^{17}$ eV and $\theta = 0°$ [2]. For each of the three frequency bands an 8th order digital Butterworth bandpass filter was applied, using the frequency range indicated by the labels. The simulation was performed using 201 observer points on the west-east axis, placed 1.5 m apart.

In the low frequency band the in-air emission reaches higher fluence values than the in-ice emission, as we would expect from Figure 5.10. Shifting toward higher frequencies however, we see that the situation is reversed. This indicates that the in-ice emission is more coherent at higher frequencies, compared to the in-air emission. In principle full coherence is only achieved at the Cherenkov angle, where the radiation emitted over a finite time interval is observed simultaneously. The condition for coherence can however be relaxed in the case where the wavelength of the radiation is much larger than the dimensions of the emission region. The emission region of the in-ice particle cascade is much smaller compared to the region of the in-air particle cascade, which explains why it is more coherent at higher frequencies.

From the figures we also see that the width of the Cherenkov ring is smaller at higher frequencies. As the frequency increases, the wavelength decreases and approaches the dimensions of the emission region. As such, the region in which the radiation is observed coherently becomes smaller, closing in around the Cherenkov cone. In the limit where the frequency goes to infinity the radiation is only coherent on the Cherenkov cone, which is in principle not exactly defined for a cascade of moving particles.

### 5.5.4 Effect of Ray Tracing

To illustrate the effect of ray tracing using an exponential refractive index profile, we performed an in-ice simulation of the shower discussed above using a fixed value for the density and the index of refraction. Both variables were fixed to their values at the surface following Equations 5.26 and 5.27, given by $\rho = 359\ \mathrm{kg/m^3}$ and $n = 1.35$.

Figure 5.18 shows the fluence along the west-east axis using a constant refractive index profile, compared to the case where the exponential profile was used. In both cases an 8th order digital Butterworth bandpass filter for a frequency band of $300 - 1000$ MHz was applied. The simulations were performed using 201 observer points on the west-east axis, placed 1.5 m apart. We see that the Cherenkov ring corresponding to the constant index of refraction has a larger radius, compared to the Cherenkov ring associated with the exponential refractive index profile. In the case of a constant index of refraction the radiation propagates on straight lines. Using an exponential profile however will cause the rays to bend towards the shower axis, decreasing the radius of the Cherenkov ring.

Moreover, as a result of the bending the radio emission converges, which could explain why also the width of the Cherenkov ring seems slightly smaller. Following Equation 5.16, the fluence should be multiplied by the index of refraction $n$ at the observer to obtain the intensity of the radiation. For the constant refractive index profile this is simply $n = 1.35$, while for the exponential profile we have $n = 1.67$. As the peak fluence values are similar for both cases, this means that the peak intensity in the Cherenkov ring corresponding to the exponential refractive index profile is the highest.

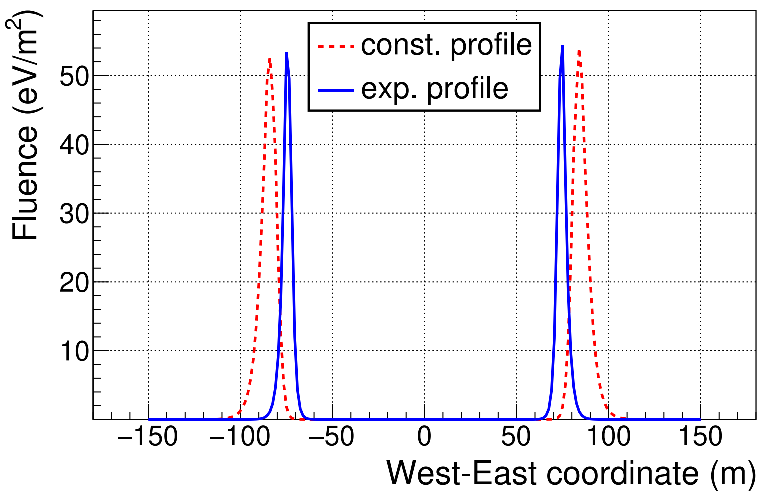


FIGURE 5.18: The fluence along the west-east axis using a constant refractive index profile (red dashed line) compared to the case where the exponential profile was used (solid blue line), with $E_p = 10^{17}$ eV and $\theta = 0°$ [2]. In both cases an 8th order digital Butterworth bandpass filter for a frequency band of $300 - 1000$ MHz was applied. The simulations were performed using 201 observer points on the west-east axis, placed 1.5 m apart.

### 5.5.5 Primary Energy Dependence

As discussed in Chapter 1, the number of particles in the air shower scales with primary energy. In case of coherent radiation, we can therefore expect that the amplitude of the electric field will scale with primary energy as well. Following Equation 5.29, increasing the energy of the primary particle by a factor of 10 should thus increase the fluence of the coherent radiation by a factor of 100. Figure 4.4 however clearly shows that for higher primary energies, the fraction of the energy of the primary particle contained within the core of the air shower at the ice surface is generally higher. Increasing the energy of the primary particle by an order of magnitude scales up the core energy of the air shower by more than just a factor of 10, which means the fluence of the coherent in-ice radio emission should increase by more than a factor of 100.

Figure 5.19 shows the fluence footprint of the radio emission at a depth of 100 m below the ice surface, for a simulated proton-induced particle cascade with primary energy $E_p = 10^{18}$ eV and zenith angle $\theta = 0°$. We follow the structure from Figure 5.10, with the component of the emission created by the particle shower in air at the top, the component of the emission created during propagation of the cascade through ice in the middle, and the combination of both components at the bottom. Distributions describing the particle cascade development of the simulated particle shower can be found in Appendix D. They show profiles very similar to the distributions obtained for the shower with primary energy $E_p = 10^{17}$ eV, scaled up by a factor of 10.

To first order the fluence footprints shown in Figure 5.19 indeed correspond to the footprints shown in Figure 5.10, scaled up by a factor of 100. However, as expected, the fluence of the in-ice emission increased by more than a factor of 100, which is especially clear from the combined footprint. In Figure 5.10 the highest fluence values correspond to the in-air emission footprint, while for Figure 5.10 the Cherenkov ring of the in-ice emission is leading. Comparing the energy in the core at the ice surface of the air shower with primary energy $E_p = 10^{18}$ eV to that of the air shower with primary energy $E_p = 10^{17}$ eV, we find that it has increased by a factor of 15. The fluence of the in-ice emission integrated over the given footprints has increased by a factor of 240, which is indeed close to the expected $15^2$. The integrated fluence of the in-air emission has only increased by a factor of 85, as a larger part of the shower development has now been shifted into the ice.

Figure 5.20 shows the electric field components as a function of time for the shower with $E_p = 10^{18}$ eV at a depth of 100 m from the ice surface, for two observer points located on the east axis. The first observer is placed 20 m away from the shower axis, where the in-air emission dominates. The second observer is placed 80 m away from the shower axis, inside the Cherenkov ring from the in-ice emission. The general features of the signals are similar to the corresponding signals shown in Figures 5.12 and 5.14. For the in-air emission the amplitude of the electric field components has overall increased by a factor of 10, while for the in-ice emission the amplitude of the electric field components has generally increased by more than a factor of 10. This is in line with the behavior of the fluence footprints.

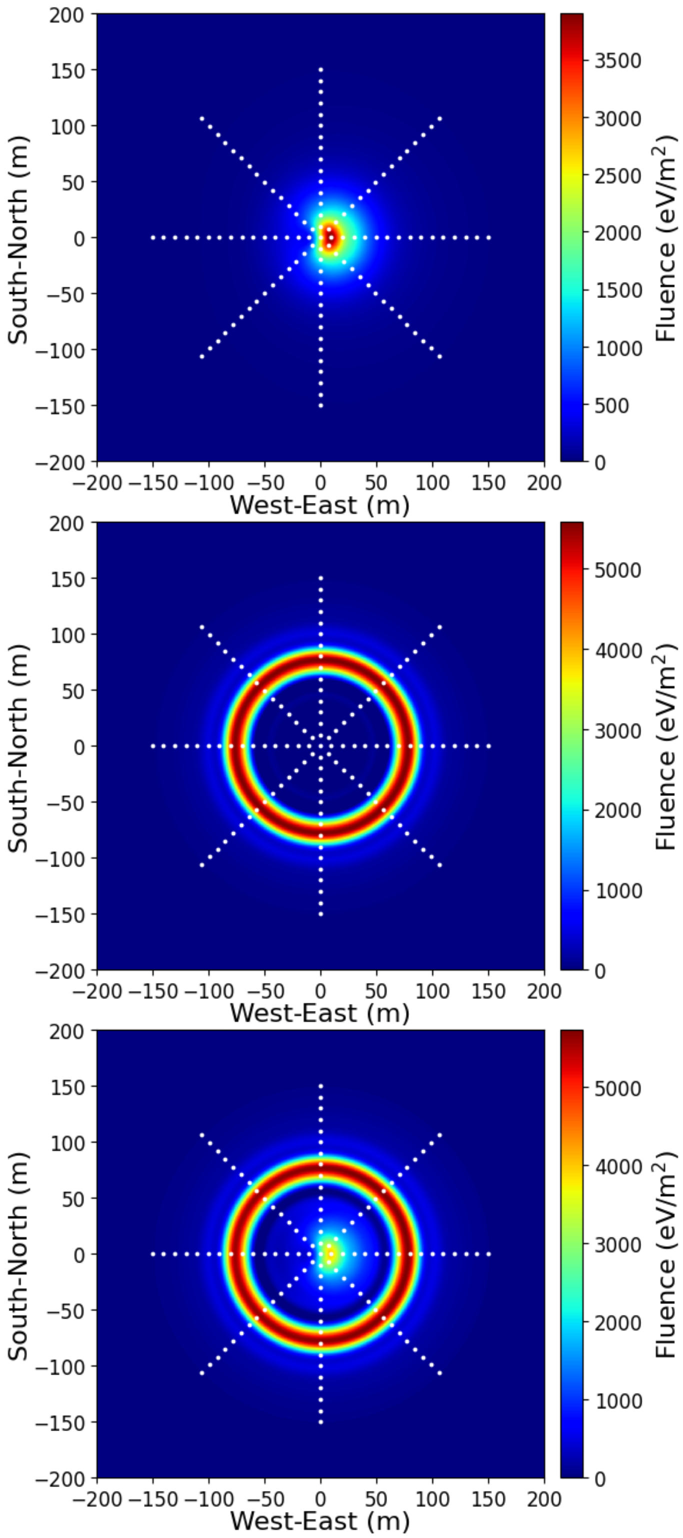


FIGURE 5.19: The fluence footprint of the simulated cosmic-ray air shower propagating through ice at a depth of 100 m below the ice surface for the in-air emission (top), in-ice emission (middle) and the combined emission (bottom), with $E_p = 10^{18}$ eV and $\theta = 0°$ [2]. The simulation included observer positions distributed over a star-shaped grid with 8 arms and a spacing of 10 m, as indicated by the white dots. The interpolation was performed with the code described in [205].

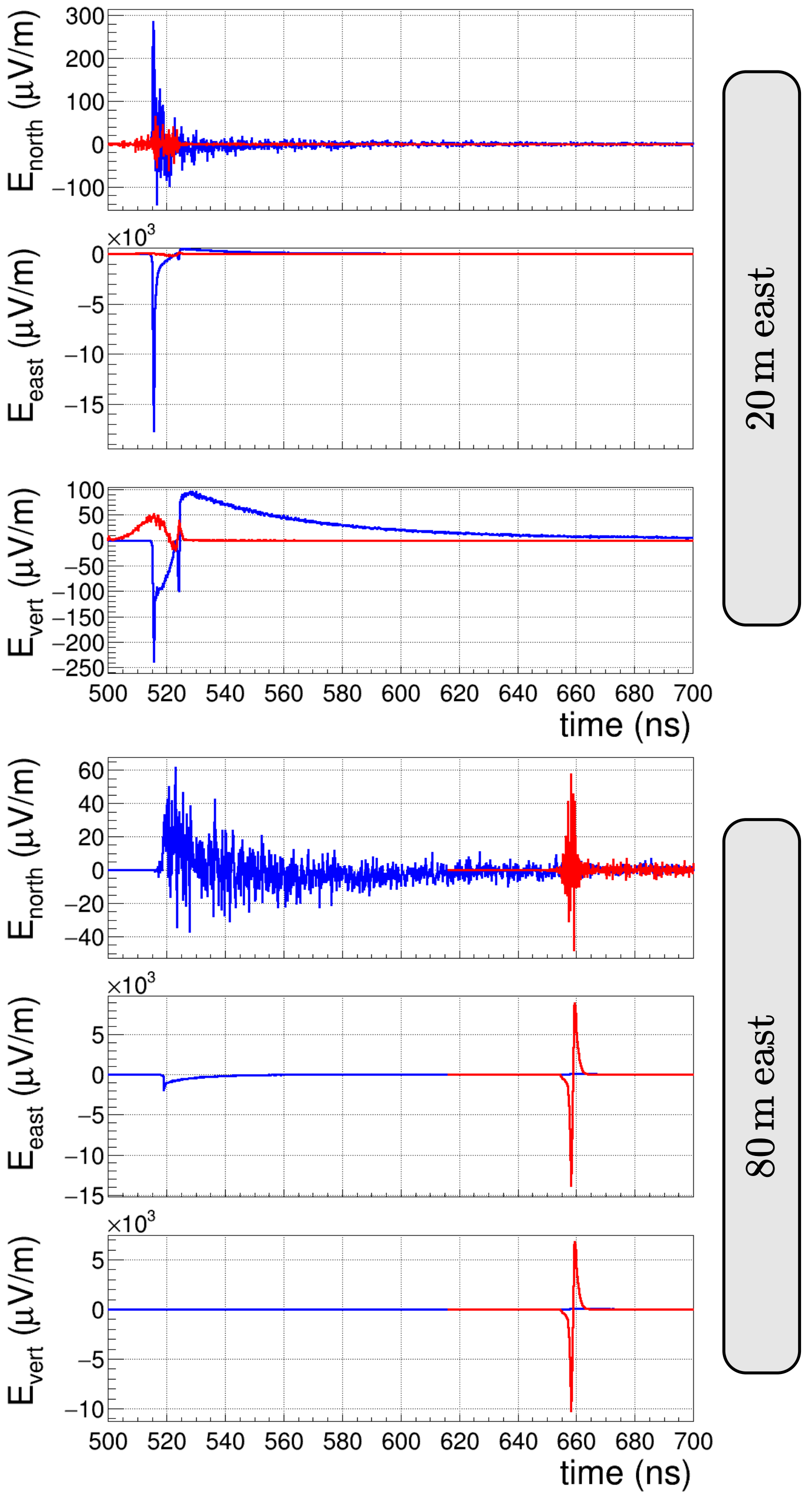


FIGURE 5.20: The electric field components as a function of time for 2 different observer positions on the east axis at a depth of 100 m, for the cosmic-ray air shower with $E_p = 10^{18}$ eV and $\theta = 0°$ [2]. The position on the axis is given on the right of the plots. The blue lines indicate the in-air emission, while the red lines indicate the in-ice emission. Note that the range on the $y$-axis is not fixed.

## 5.6 Conclusion

This chapter presented FAERIE - the Framework for the simulation of Air shower Emission of Radio for in-Ice Experiments. It combines the CORSIKA Monte Carlo and CoREAS codes with a Geant4-based module to simulate the radio emission of cosmic-ray air showers propagating through ice, for observers located below the ice surface. The framework tracks the individual particles of the cascade and relies on the endpoint formalism for the radio calculations. It is the first Monte Carlo simulation framework to include both the radio emission created in air and in ice.

The propagation of the radiation through the medium is described by ray tracing, which takes into account the bending, reflecting and refracting of the rays associated with the radio emission. The endpoint formalism was generalized to include ray tracing by using the index of refraction at the emitter, the launching direction of the ray and the path length of the ray, followed by a rotation along the ray path. The framework includes the Fresnel coefficients to account for energy losses during reflection and refraction of the radiation, as well as a focusing factor to describe the effect of convergence and divergence of the rays. The implementation in FAERIE relies on geometric vectors defined in a global Cartesian coordinate system, which ensures the generality of the calculations. To speed up the calculations interpolation tables for the relevant ray tracing variables are being used, which are created before the actual particle cascade simulation starts. The current ray tracer used by FAERIE assumes a cylindrical symmetry, and uses a combination of different exponential functions to describe the refractive index profile of the medium. The use of interpolation tables implies that also slower, more accurate ray tracers could be implemented without increasing the actual particle cascade simulation time. However, three-dimensional ray tracing tables will be needed for ray tracers that do not assume cylindrical symmetry, as well as a different approach for the calculation of the focusing factor.

The first results of the framework were presented, using a simulation of a cosmic-ray air shower with a primary energy $E_p = 10^{17}$ eV and zenith angle $\theta = 0°$. The ice surface was set at an altitude of 2.835 km, which corresponds to that of the South Pole. The fluence footprints at a depth of 100 m were shown for the emission created in air, the emission created in ice and the combination of both components. The in-air emission is concentrated around the shower axis, marked by the bean-shaped asymmetry following the superposition of the in-air geomagnetic and in-air Askaryan radiation. The in-ice emission has no geomagnetic component, leading to a symmetric Cherenkov ring farther away from the shower axis.

Next, the features of the electric field traces observed at different points in the footprint were discussed. As a rule of thumb, the peak amplitude of a signal from a cosmic-ray cascade with primary energy $E_p$ and zenith angle $\theta = 0°$ corresponds to that of a neutrino with an energy of $0.1 \times E_p$. For most geometries, the in-ice emission will be delayed with respect to the in-air emission, which means the signal of a cosmic-ray event observed in ice in general consists of two pulses. The time difference between the two pulses depends on the position of the observer, which could potentially be used to reconstruct the distance to the shower axis.

To study the frequency dependence of the radio emission, Butterworth bandpass filters were applied using three different frequency ranges. This showed that the in-ice emission is more coherent at higher frequencies than the in-air emission, as a consequence of the emission region in ice being much smaller. The effect on ray tracing on the in-ice emission was illustrated by comparing the results with a simulation using a constant index of refraction. Ray tracing decreases the radius and width of the Cherenkov ring, while it increases the peak intensity in the ring.

Finally, the dependence of the emission on the primary energy of the particle cascade was discussed. To first approximation, increasing the energy of the primary particle by an order of magnitude increases the fluence of the coherent radiation by a factor of 100. However, at higher primary energies, the fraction of the energy of the primary particle contained within the core is larger. As a result, the factor by which the fluence of the in-ice emission increases is actually larger than 100, while it is smaller than 100 for the in-air emission.

# Summary and Outlook

## Summary

High-energy neutrino observatories have delivered important milestones during the past decades, and have proven to be an important piece in the puzzle of multi-messenger astronomy. The move towards ultra-high-energy neutrino astronomy however poses a big challenge, that has not yet been overcome. Radio detection techniques relying on the observation of Askaryan radiation or radar echoes show promising results, but at the time of writing no evidence of any detection of astrophysical neutrinos has been presented. In fact, both the observation of Askaryan radiation from particle cascades in dense media as well as radar echoes from the associated ionization trail have only been realized in controlled environments, relying on particle accelerators. Any demonstration of their viability in nature is still missing.

Cosmic rays are much more likely to interact than these elusive neutrinos, and the observed cosmic-ray flux is significantly higher. As such, they form a suitable test beam that can be exploited to verify the feasibility of these radio detection techniques. Furthermore, they present an important background for radio neutrino observatories, and could potentially serve as an in situ calibration source. The radio emission from cosmic-ray air showers is a well-researched topic, supported by several established simulation frameworks. These frameworks are however mainly restricted to air, focusing on the cosmic-ray induced particle cascade in air and the radio emission observed by ground-based detectors. When considering detector units deployed in ice these frameworks need to be extended, accounting for the propagation of the radio emission into ice. Furthermore, as a significant amount of radio neutrino projects are currently running at altitudes around 3 km above sea level, simulations also need to include the propagation of the particle cascade into ice. This in turn will lead to a second radio emission component, mimicking the signal of a neutrino-induced particle cascade.

This work presents FAERIE - the Framework for the simulation of Air shower Emission of Radio for in-Ice Experiments. It combines the CORSIKA Monte Carlo and CoREAS codes with a Geant4-based module to simulate the radio emission of cosmic-ray air showers propagating through ice, for observers located below the ice surface. The framework tracks the individual particles of the cascade and relies on the endpoint formalism for the radio calculations. As such it is the first Monte Carlo simulation framework to include both the radio emission created in air and in ice.

Chapter 4 demonstrated the properties of ultra-high-energy cosmic-ray air showers at altitudes around 3 km above sea level. In particular, it focused on the results of a FAERIE simulation of a proton-induced particle cascade with primary energy $E_p = 10^{17}$ eV and zenith angle $\theta = 0°$, fixing the air-ice interface at 2.4 km above sea level. It was shown that at this point the air shower is close to shower maximum, where it reaches the maximum number of electrons and positrons. The shower still contains about 50% of the primary energy, most of which is carried by the electromagnetic component of the cascade. We defined the core of the shower as all the particles within 1 m from the shower axis, and found that about 20% of the primary energy is contained within this region. Results from a larger set of simulations confirmed that at these altitudes in general around $10 - 30\%$ of the energy of the primary particle is located in the core of the air shower, for primary energies of $10^{16}$ eV and higher and zenith angles up to $\sim 30°$.

Next, we studied the properties of the in-ice cascade. The lateral profile of the air shower indicated that most of the particles outside of the core disappear after a few radiation lengths, while the core itself continues to develop in the ice. This behavior was confirmed by the deposited energy density profile. It showed us that during the first few meters the core of the in-ice cascade is still growing, while the rest of the shower is dying out. When taking into account the full extend of the shower, we saw that introducing ice as a second medium did not have any significant effect on the number of electromagnetic particles in the cascade as a function of depth. When looking at the lateral distribution of the in-ice cascade, we found that most of the particles are located within $\sim$ 10 mm of the cascade front. The lateral distribution function of the cascade becomes stable at depths around 300 g/cm$^2$ below the surface, when most of the particles outside the core have vanished. Finally, a correlation between the lateral distribution function and $X_{\max}$ of the shower was demonstrated, which led to the parameterization of the distributions as a function of $X_{\max}$.

The simulation of the radio emission of the particle cascade was covered in Chapter 5. The concept of ray tracing was included in the endpoint formalism, to describe the propagation of radiation through non-uniform media. This includes the calculation of the Fresnel coefficients and the focusing factor. The use of interpolation tables avoids unrealistic computation times, as it requires only a limited amount of calculations that are performed before the actual particle cascade simulation starts. Currently, the refractive index profile of the medium is assumed to be cylindrically symmetric, following a combination of different exponential functions, which makes analytical ray tracing possible. However, the interpolation tables allow for the implementation of slower, more accurate ray tracers, keeping in mind that the assumption of cylindrical symmetry is also made during the derivation of the formula for the focusing factor presented in Section 5.3.3.

We discussed the first results of the framework, focusing on the radio emission of a cosmic-ray particle cascade with primary energy $E_p = 10^{17}$ and zenith angle $\theta = 0°$. The footprint of the radio emission at a depth of 100 m below the ice surface shows a unique pattern. It consists of the bean-shaped asymmetry close to the shower axis associated with the emission in air, surrounded by the symmetric Cherenkov ring created during the propagation of the particle cascade through the ice. Looking at the traces, we found that the peak amplitude of the radio signal corresponds to that of a signal created by an electromagnetic neutrino-induced particle cascade with a neutrino energy of $10^{16}$ eV, i.e. one order of magnitude smaller than the primary energy of the cosmic-ray cascade. The delay of the in-ice emission leads to a double pulse feature in the cosmic-ray signal, which could be used for cosmic-ray event identification and reconstruction. Applying bandpass filters showed that the emission created in ice is more coherent at higher frequencies than the emission created in air, which can be explained by the difference in size of the corresponding emission regions. Calculating the in-ice radio emission using a constant refractive index profile demonstrated that ray tracing decreases the radius and width of the associated Cherenkov ring, while it increases the peak intensity in the ring. Finally, we showed that increasing the primary energy by an order of magnitude roughly increases the fluence in the studied footprint by a factor of 100, which is expected for coherent radiation. A more detailed analysis however revealed that the factor by which the fluence of the in-air emission increases is actually smaller than 100, while it is larger than 100 for the in-ice emission.

The first results from FAERIE presented in this work demonstrate that the radio emission from ultra-high-energy cosmic-ray particle showers should be detectable by radio neutrino observatories deployed in high-altitude polar ice. Both the emission generated during the propagation through the atmosphere and the radiation created by the subsequent in-ice cascade reach peak amplitudes comparable to the radio signals from cascades initiated by ultra-high-energy neutrinos. Furthermore, the framework illustrated that the ionization trail associated with the in-ice cascade shows favorable reflective properties for the radar echo technique, which has been confirmed by more detailed studies. As such, we can conclude that ultra-high-energy cosmic rays indeed present a valuable in-situ test beam to demonstrate the feasibility of neutrino detection methods based on the observation of Askaryan radio emission or radar echoes.

Consequently, they also form an important background signal for neutrino observatories exploring these techniques. Current cosmic-ray data filters applied during neutrino searches only take into account the arrival direction of the radio emission, defining strong geometric cuts that reduce the effective detection volume. Simulations from FAERIE can be used to identify alternative cosmic-ray discriminators, such as the double pulse signature, leading to more refined cosmic-ray data filters. Interestingly, the radio footprints presented in Chapter 5 clearly illustrate that the in-air emission of a cosmic-ray event is concentrated around the shower axis, while deep below the ice most of the in-ice emission is concentrated in a region further out. This means that the surface component of hybrid detectors like RNO-G, that combine deep-ice antennas with surface antennas, cannot serve as a perfect cosmic-ray veto system. Cosmic-ray events creating in-ice emission that triggers the in-ice component, do not necessarily generate in-air emission that reaches the detection threshold of the surface component.

Finally, cosmic-ray signals could be used for calibration of detector units, especially in the case of hybrid detectors. Detecting a cosmic-ray signal in both the deep-ice and surface components could lead to a better understanding of the deep-ice antennas. Additionally, the linear polarization from the in-air emission combined with the radial polarization from the in-ice emission give cosmic-ray events a unique characteristic that could help determine the difference in antenna responses between horizontally and vertically polarized antennas, as well as the effects of cross polarization.

## Outlook

FAERIE has reached a state where it can be used for the construction of simulation libraries, to support in-ice radio detectors with the identification and reconstruction of cosmic-ray events. It is currently in use within the ARA, RNO-G and RET collaborations, showing some interesting first results [206]. Significant efforts are being made to modernize and upgrade the CORSIKA Monte Carlo code, which will be released under the name CORSIKA 8 [172]. With CORSIKA 8 it will be possible to simulate cross-media showers, and to calculate the corresponding radio emission for any observer position. The code is however still in development, and the first simulations for cosmic-ray discrimination with detectors in ice will be provided by

FAERIE. Moreover, it will be interesting to see how the results of CORSIKA 8 and FAERIE compare, and FAERIE will be a valuable tool to evaluate the functionalities of the CORSIKA 8 code [173].

Improvements on the framework can be made, and will need to be taken into account for upcoming simulation codes such as CORSIKA 8. At the moment, indirect ice-to-ice rays reflecting on the ice-air boundary under an angle where total reflection occurs do not undergo the appropriate phase shift in FAERIE. Especially for inclined showers this could be a non-negligible effect. Around zenith angles of $30° - 50°$ the in-ice emission can still be significant, while on one side of the shower axis the indirect emission will be emitted close to the Cherenkov cone. Furthermore, the use of interpolation tables allows for the implementation of slower, more accurate ray tracers in the framework. In particular this would allow the simulation of inhomogeneities in the ice, such as wave guides and reflection layers [191, 200, 207], and could possibly include birefringence effects [101, 207–212]. An additional propagation effect which is not yet taken into account is attenuation, which represents a frequency-dependant power loss of radiation moving through a medium. However, measurements of the attenuation of radio waves in polar ice at high altitudes show that this only becomes important for propagation distances of the order of 1 km and more, when considering the typical frequency ranges relevant for the radio detectors described in this work [92, 207, 208, 211, 213, 214]. More involved ray tracers could also take into account Earth's curvature and the focusing factor for the in-air emission, both of which are important for very inclined air showers.

In this work only the radio emission of vertical showers was discussed, as this provides a convenient geometry in which the properties of the corresponding electric fields can be well understood. Due to the computational costs of the simulations, no other geometries were considered. As mentioned above FAERIE is currently used by several collaborations, and a more extensive study of the radio signal properties of cosmic-ray events is expected in the future.

Moreover, a more thorough study of the charge distribution of the in-ice particle cascade with FAERIE could provide parameterizations suitable for analytic or semi-analytic Askaryan radiation models. Such models already exist for Askaryan radiation of neutrino-induced particle cascades in ice [147, 169, 174, 215–220], and have shown to be valuable for simulation frameworks [101]. By using analytical or semi-analytical models the particle-by-particle simulation of the in-ice cascade can be avoided, reducing the computation time significantly. The accuracy of such simulations can then be verified against the radio calculations from FAERIE.

Finally, as shown in [180], the endpoint formalism naturally includes the emission of transition radiation when the calculations in both media are treated separately, which is the case for FAERIE. Transition radiation arises when a charged relativistic particle moves between two media with different refractive indices [184]. In the results presented in this work, the contribution of transition radiation is however not immediately visible. One possible explanation could be that the charge excess in the cascade front might be too small to create a significant amount of transition radiation, when traversing the air-ice boundary. Furthermore, a large fraction of the energy of the cosmic-ray cascade is carried by gammas. Gammas do not have an electrical charge and therefore do not contribute to transition radiation. Due to time constraints, the contribution of transition radiation to the cosmic-ray signal has not been investigated, but could be an interesting future study.

# Contributions during the PhD

## Research Output

As mentioned in Chapter 5, my main contribution to the FAERIE framework was the development of the Geant4-based module for the simulation of the in-ice particle cascade and the associated radio emission, and the subsequent merging of the different software components into a single framework. The development of the framework resulted in the publication of the peer-reviewed articles [1, 2]. I supported the distribution of the FAERIE software within the ARA and RNO-G collaborations, and subsequently assisted in the verification of simulated data. Furthermore, I was a member of the field team of RNO-G in 2023 and the field team of RET in 2024 sent to Summit Station in Greenland. As such I was involved in the maintenance, calibration and deployment tasks described in Chapter 3. In addition, I participated in the monitoring of the ARA and RET-CR detectors.

Apart from the peer-reviewed articles mentioned above, I regularly presented my work at national and international conferences in the form of talks and poster presentations, including [199, 221–227]. Moreover, I frequently presented progress and results of my research activities at collaboration meetings.

## Teaching & Coordination

As a teaching assistant I was heavily involved in the courses provided by the Department of Physics within the Faculty of Sciences and Bio-engineering Sciences:

- Fysica: inleiding mechanica (1$^{\text{st}}$ Bachelor of Chemistry, Geography, Biology and Bio-engineering, 2018 - 2024)
- Fysica: trillingen, golven & thermodynamica (1$^{\text{st}}$ Bachelor of Chemistry, Geography, Biology and Bio-engineering, 2018 - 2024)
- Fysica: elektromagnetisme (2$^{\text{nd}}$ Bachelor of Chemistry and Bio-engineering, 2018 - 2024)

This included supervision of exercise and lab sessions, as well as general coordination of the courses. With the support of the Department of Physics and the Department of Chemistry, I also acquired funding (€20,000) for a blended-learning project in context of these courses, and coordinated its execution. In addition, I was responsible for the component "Wiskundige Technieken" of the course "Seminarie Actuele Wetenschappen & Samenleving" (1$^{\text{st}}$ Bachelor of Physics & Astronomy, 2018 - 2024). Furthermore, I co-supervised the BSc thesis of Daniel H. Hiel [228] and the MSc thesis of Nicolas Moller [206], and I was a member of the education and research boards of the Department of Physics (2019 - 2024), the education committee of the Faculty of Sciences and Bio-Engineering Sciences (2019 - 2021, 2022 - 2024) and the council of the Faculty of Sciences and Bio-Engineering Sciences (2021 - 2022).

## Outreach

I co-organized the annual astroparticle physics masterclass for secondary school students taking place at the Inter-University Institute For High Energies (IIHE) during the years 2019 - 2024, known as the "IceCube Masterclass" and later renamed to "Particles from the Cosmos Masterclass". Furthermore, I participated in a science workshop organized by "Sport en Opleiding vzw" during the summer of 2019 and in the outreach village connected to the "A Decade of Discoveries in High-Energy Physics" event in 2023, both of which were aimed at an audience of primary school children. In addition, I presented the Department of Physics during the "Studie-informatiedagen (SID-ins)" organized by the Flemish government, where participants are informed about study and career opportunities after secondary school.

# Appendix A

## Atmospheric Density Profiles

The density of the atmosphere is modeled by five consecutive layers. In the lower four layers the density follows an exponential function given by

$$T(h) = a_i + b_i e^{-h/c_i} \quad i = 1, 2, 3, 4, \tag{A.1}$$

with $T$ the mass overburden and $h$ the height [229]. In the fifth, topmost layer the density follows a linear function given by

$$T(h) = a_5 - b_5 h / c_5. \tag{A.2}$$

The parameters for the different models used in this work are given in Table A.1 and Table A.2.

| Layer $i$ | Altitude $h$ (km) | $a_i$ (g/cm$^2$) | $b_i$ (g/cm$^2$) | $c_i$ (cm) |
|---|---|---|---|---|
| 1 | $0 - 4$ | $-128.601$ | 1139.99 | 861913 |
| 2 | $4 - 10$ | $-39.5548$ | 1073.82 | 744955 |
| 3 | $10 - 40$ | 1.13088 | 1052.96 | 675928 |
| 4 | $40 - 100$ | $-0.00264960$ | 492.503 | 829627 |
| 5 | $> 100$ | 0.00192534 | 1 | $5.85870 \times 10^9$ |

TABLE A.1: South Pole atmosphere parameters for Dec. 31, 1997 (MSIS-90-E) [229].

| Layer $i$ | Altitude $h$ (km) | $a_i$ (g/cm$^2$) | $b_i$ (g/cm$^2$) | $c_i$ (cm) |
|---|---|---|---|---|
| 1 | $0 - 3.217$ | $-113.352$ | 1194.39 | 810969 |
| 2 | $3.217 - 8.364$ | $-9.73769$ | 1103.28 | 706357 |
| 3 | $8.364 - 23.142$ | $-0.218461$ | 1109.64 | 686443 |
| 4 | $23.142 - 100$ | $7.95615 \times 10^{-4}$ | 1124.99 | 682494 |
| 5 | $> 100$ | 0.0112829 | 1 | $1 \times 10^9$ |

TABLE A.2: South Pole atmosphere parameters generated with GDAS for the work presented in [178].

# Appendix B

## Deposited Energy Density Profile

Figures B.1, B.2 and B.3 show the energy deposited by the reference air shower described in Chapter 4 when it propagates through the ice at an altitude of 2.4 km above sea level, using different values for the primary energy $E_p$ and zenith angle $\theta$.

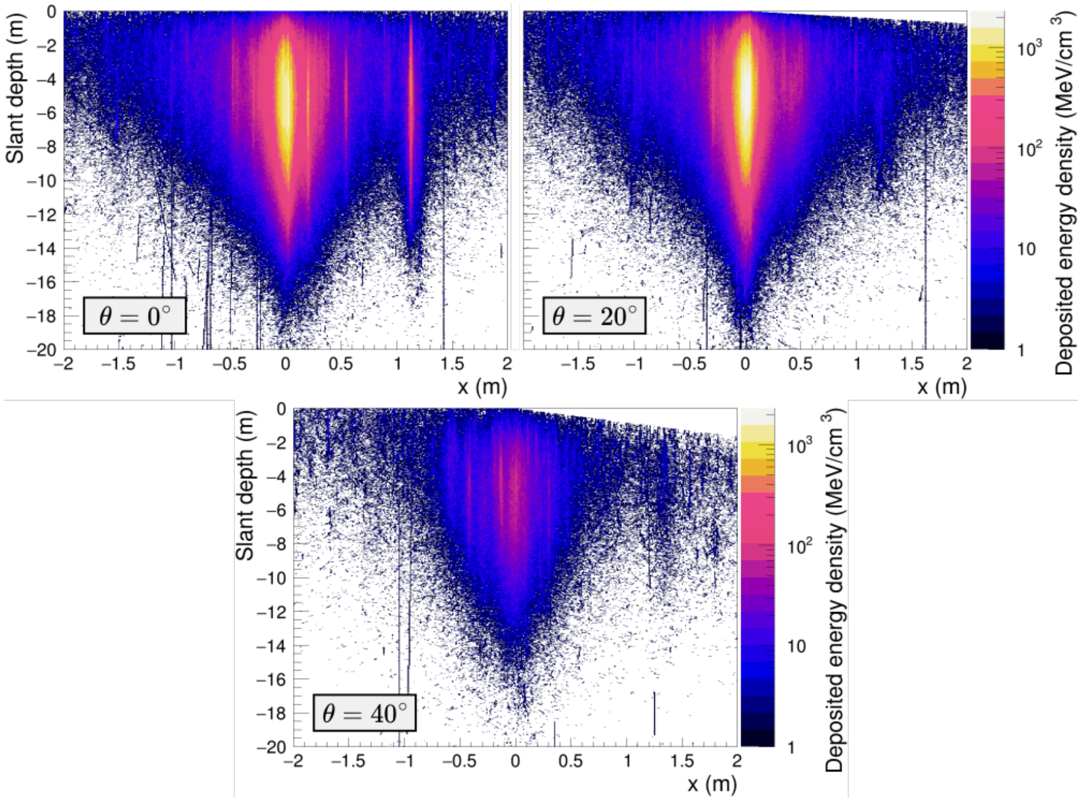


FIGURE B.1: The energy deposited in the ice by the reference cascade within a vertical 1-cm wide slice going through the center of the particle shower using $E_p = 10^{16}$ eV and different zenith angles $\theta$, indicated in the plots [1]. The y-axis shows slant depth, defined as the depth in unit length along the shower axis with respect to the ice surface. In this reference system the ice surface is tilted clockwise over an angle $\theta$, showing up in the upper right corners of the plots.

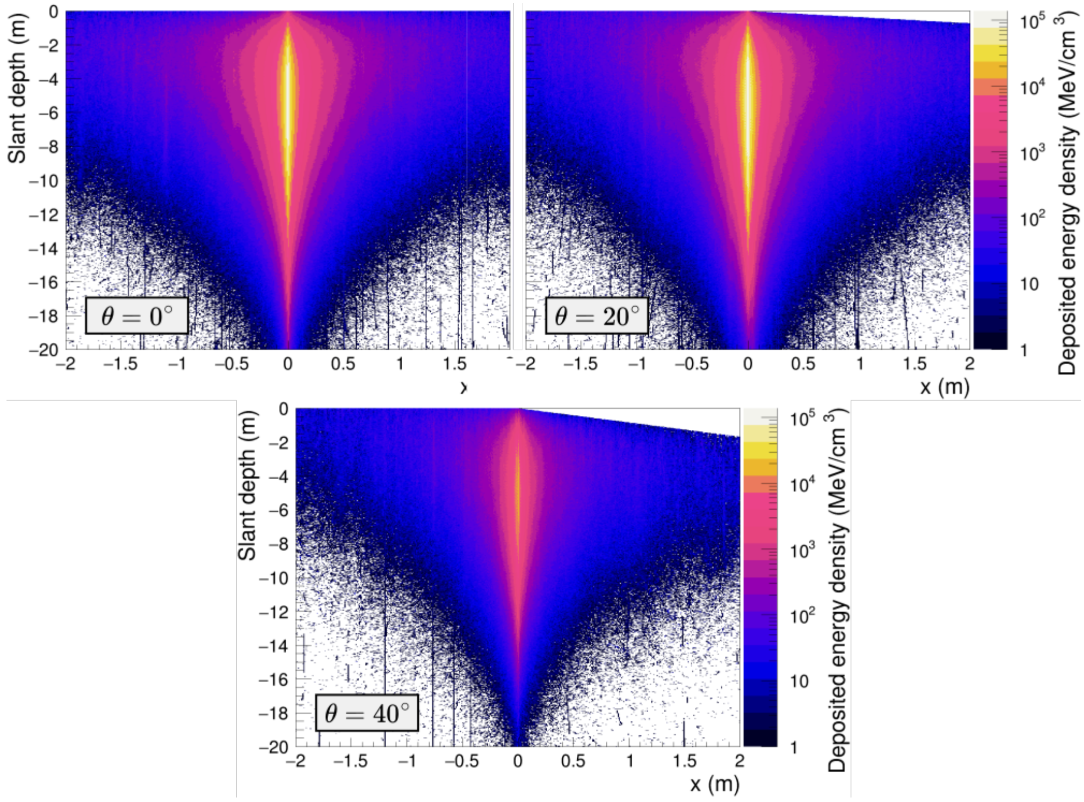


FIGURE B.2: The energy deposited in the ice by the reference cascade within a vertical 1-cm wide slice going through the center of the particle shower using $E_p = 10^{17}$ eV and different zenith angles $\theta$, indicated in the plots [1]. The y-axis shows slant depth, defined as the depth in unit length along the shower axis with respect to the ice surface. In this reference system the ice surface is tilted clockwise over an angle $\theta$, showing up in the upper right corners of the plots.

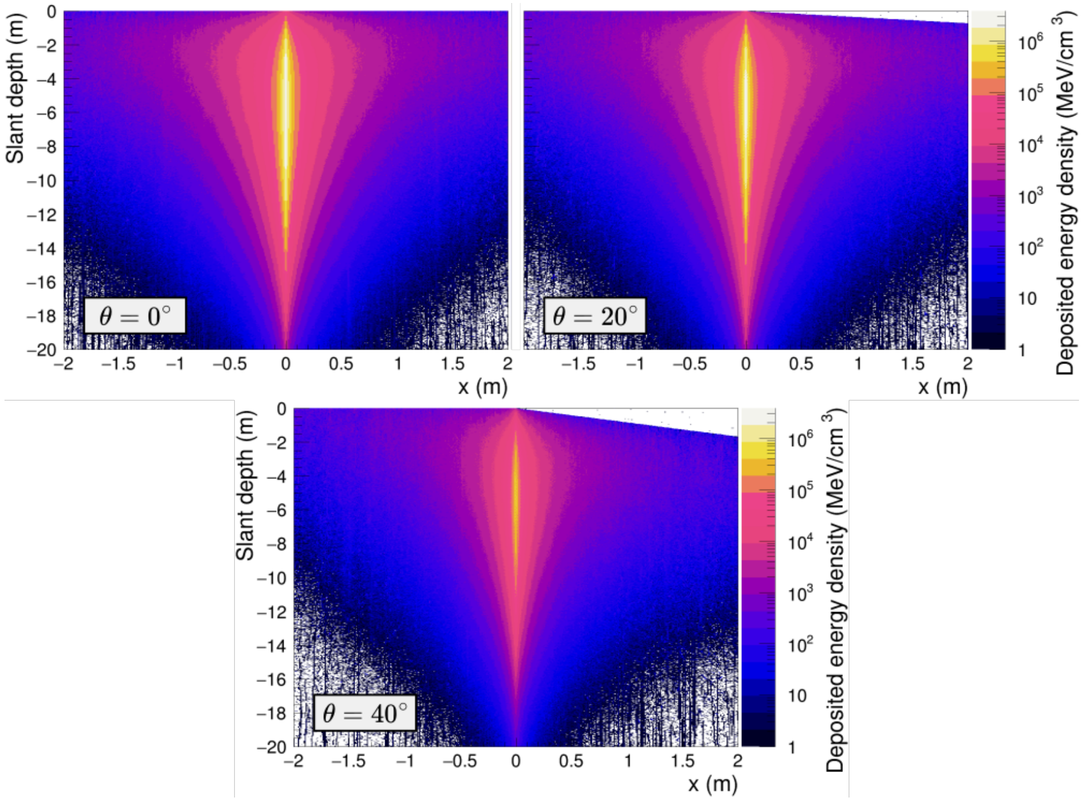


FIGURE B.3: The energy deposited in the ice by the reference cascade within a vertical 1-cm wide slice going through the center of the particle shower using $E_p = 10^{18}$ eV and different zenith angles $\theta$, indicated in the plots [1]. The y-axis shows slant depth, defined as the depth in unit length along the shower axis with respect to the ice surface. In this reference system the ice surface is tilted clockwise over an angle $\theta$, showing up in the upper right corners of the plots.

# Appendix C

## Atmospheric Refractive Index Profile

As described in Appendix A, the density of the atmosphere is modeled by five consecutive layers. The refractive index profile $n(h)$ of the atmosphere consists of five consecutive exponential functions,

$$n(h) = 1 + B_i e^{-h/C_i} \quad i = 1, 2, 3, 4, 5, \tag{C.1}$$

where each function corresponds to one of the density layers. The values for the parameters used in this work are given in Table C.1. They are determined by matching the refractive index profile to the density profile of the atmosphere described by Table A.2 in Appendix B [178, 179].

For the first four layers the parameter $C_i$ is set to the exponential coefficient $c_i$ of the density profile. The value $n(0)$ is set to $n(0) = 1.0003289$, from which the value of $B_1$ can be determined. The values for $B_2$, $B_3$ and $B_4$ then follow from the condition that subsequent functions share the same value on the layer boundaries.

In the fifth layer the density is described by a linear function, and as such the value of $C_5$ is not set to that of $c_5$. Instead it is fixed to $C_5 = C_4$, and the parameter $B_5$ is determined by the condition that the fourth and the fifth refractive index functions share the same value on the transition boundary. The fifth layer corresponds to altitudes of $h > 100$ km, and the details of the refractive index function of this layer are therefore not relevant for the work presented in this thesis.

| Layer | Altitude interval (km) | $B_i$ | $C_i$ (cm) |
|---|---|---|---|
| 1 | $0 - 3.217$ | $3.28911 \times 10^{-4}$ | 810969 |
| 2 | $3.217 - 8.364$ | $3.48817 \times 10^{-4}$ | 706357 |
| 3 | $8.364 - 23.142$ | $3.61006 \times 10^{-4}$ | 686443 |
| 4 | $23.142 - 100$ | $3.68118 \times 10^{-4}$ | 682494 |
| 5 | $> 100$ | $3.68404 \times 10^{-4}$ | 682494 |

TABLE C.1: The numerical values of the parameters in Equation C.1 describing the refractive index of the atmosphere used in this work. They are determined by matching the refractive index profile to the density profile of the atmosphere described by Table A.2 in Appendix B.

# Appendix D

## Shower Profiles

In this Appendix, distributions describing the particle cascade development of the simulated proton-induced air shower discussed in Chapter 5 are shown, both for $E_p = 10^{17}$ eV and $E_p = 10^{18}$ eV. Figure D.1 and Figure D.2 show the longitudinal particle and energy distributions of the particle cascades in air, starting at the top of the atmosphere and ending at the air-ice boundary. Figure D.3 and Figure D.4 show the energy deposited in the ice by the particle cascades.

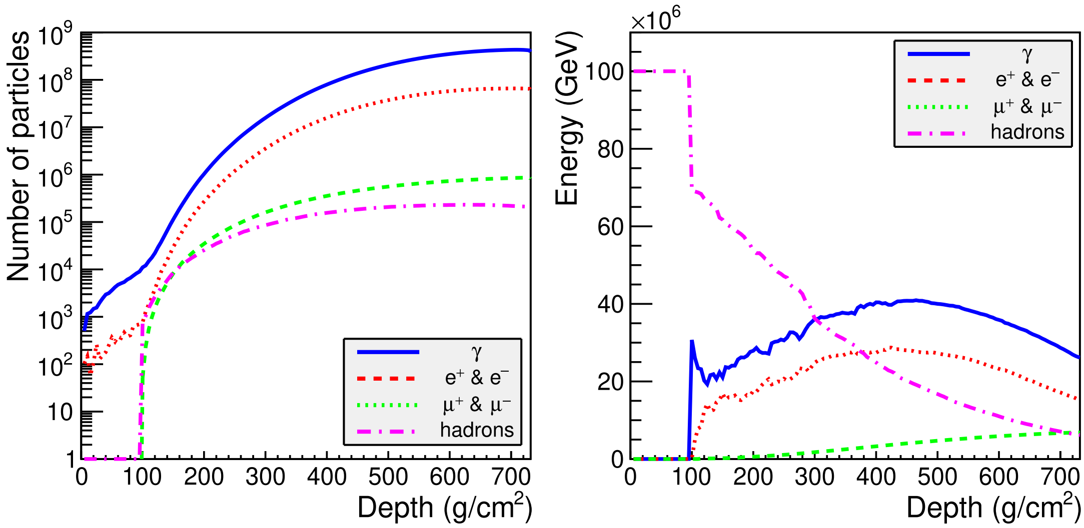


FIGURE D.1: The number of particles (left) and the energy distribution (right) as a function of depth for the simulated proton-induced air shower, with $E_p = 10^{17}$ eV, $\theta = 0°$ and $\phi = 0°$ [2]. The particle distributions are obtained over the full radial extent of the in-air particle cascade.

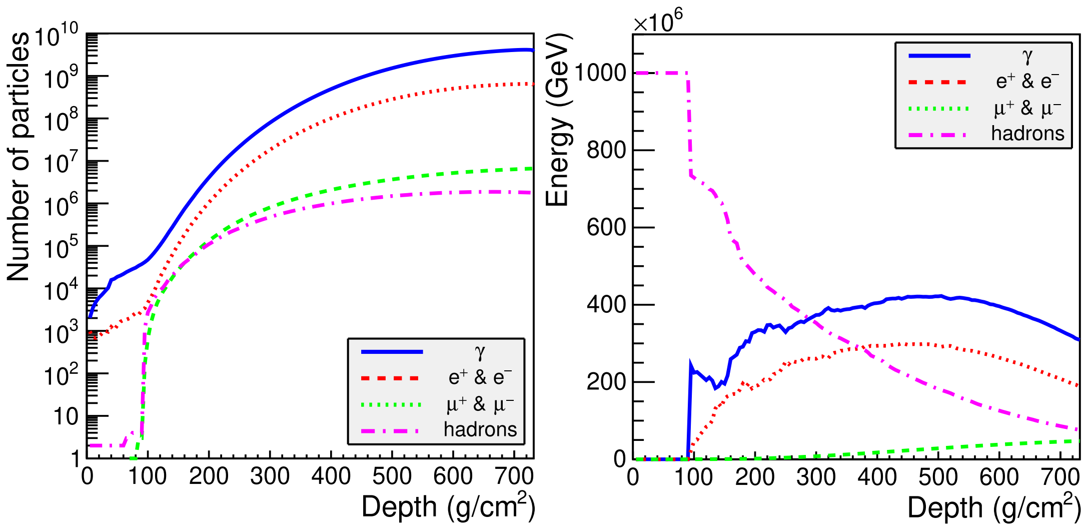


FIGURE D.2: The number of particles (left) and the energy distribution (right) as a function of depth for the simulated proton-induced air shower, with $E_p = 10^{18}$ eV, $\theta = 0°$ and $\phi = 0°$ [2]. The particle distributions are obtained over the full radial extent of the in-air particle cascade.

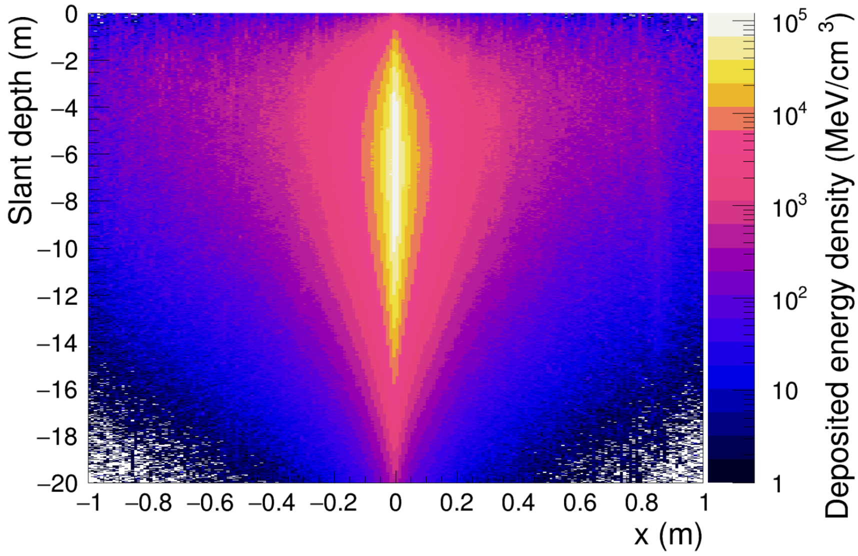


FIGURE D.3: The energy deposited in the ice by the simulated proton-induced air shower, with $E_p = 10^{17}$ eV, $\theta = 0°$ and $\phi = 0°$ [2]. Shown here is the deposited energy density within a vertical 1-cm wide slice going through the center of the particle cascade.

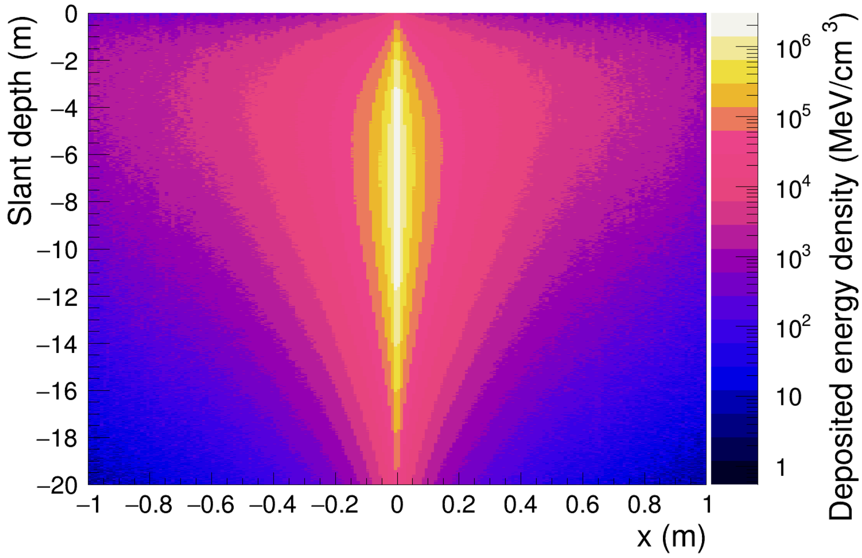


FIGURE D.4: The energy deposited in the ice by the simulated proton-induced air shower, with $E_p = 10^{18}$ eV, $\theta = 0°$ and $\phi = 0°$ [2]. Shown here is the deposited energy density within a vertical 1-cm wide slice going through the center of the particle cascade.

# Appendix E

## Computation Time

Below, the computation time of a cosmic-ray cascade initiated by a $E_p = 10^{17}$ eV proton entering the atmosphere at a zenith angle $\theta = 0^\circ$ using a star-shaped antenna grid of 121 antennas is illustrated. A complete simulation of a cosmic-ray cascade requires the three following steps in FAERIE:

1. simulating the in-air particle cascade and the corresponding radio emission with CORSIKA and CoREAS,
2. generating the input files required for the Geant4-based module using the CORSIKA particle output file,
3. simulating the in-ice particle cascade and the corresponding radio emission with the Geant4-base module.

The process in step 1 was split up over 8 different CPUs. On each CPU the full cosmic-ray air shower and its corresponding radio emission was simulated for 15 of the 121 antennas, with one of the CPUs including a 16th antenna at (0,0). The average CPU time was 21.3h, while the longest CPU time was 26.8h.

During step 2 of the simulation process the CORSIKA particle output from the CORSIKA simulation is split up in different parts, only taking into account the particles within a radius of 1 m of the shower axis. The splitting procedure is based on the energy of the particles. The amount of particles per part varies from $540,000$ (energies below $10^7$ eV) down to 1 (starting at energies of $10^{13}$ eV). During step 3, each part is then used by a different CPU as the input for the Geant4-based module. In contrast to step 1, each CPU now simulates the complete antenna grid of 121 antennas. The distribution of the CPU time of the 591 cores used in step 3 is shown in Figure E.1. The majority of the CPU's finished within a period of 10 h. A small fraction of CPU's took significantly longer, up to approximately 24 h. The computation time can be further optimized by splitting up the parts that correspond to long CPU times, and combining parts that correspond to short CPU times. The longest CPU time for a simulation of the propagation of a single particle was 12.2 h, which can only be reduced by splitting up the antenna grid.

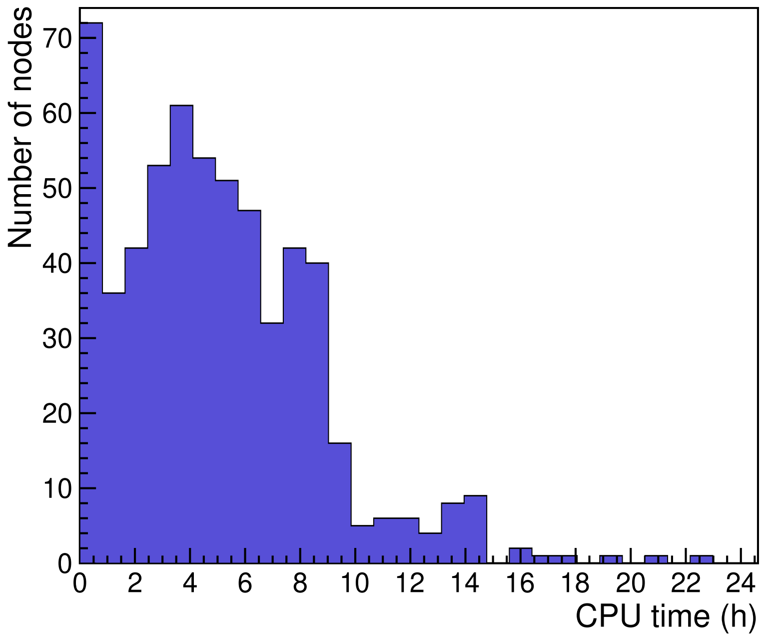


FIGURE E.1: A distribution of the CPU time of 591 cores used for the simulation of the in-ice particle cascade and the corresponding radio emission for 121 antennas in the ice, using a primary energy $E_p = 10^{17}$ eV and zenith angle $\theta = 0$ [2].

# Bibliography


[1] S. De Kockere et al. "Simulation of in-ice cosmic ray air shower induced particle cascades". In: *Physical Review D* 106.4 (Aug. 2022). ISSN: 2470-0029. DOI: 10.1103/physrevd.106.043023.

[2] S. De Kockere et al. "Simulation of radio signals from cosmic-ray cascades in air and ice as observed by in-ice Askaryan radio detectors". In: *Phys. Rev. D* 110 (2 2024), p. 023010. DOI: 10.1103/PhysRevD.110.023010.

[3] V. Hess. *On the Observations of the Penetrating Radiation during Seven Balloon Flights*. 2018. arXiv: 1808.02927.

[4] J. Blümer, R. Engel, and J. R. Hörandel. "Cosmic rays from the knee to the highest energies". In: *Progress in Particle and Nuclear Physics* 63.2 (Oct. 2009), 293–338. ISSN: 0146-6410. DOI: 10.1016/j.ppnp.2009.05.002.

[5] T. K. Gaisser, R. Engel, and E. Resconi. *Cosmic Rays and Particle Physics*. 2nd ed. Cambridge University Press, 2016. ISBN: 9780521016469; 0521016460.

[6] M. S. Longair. *High Energy Astrophysics*. 3rd ed. Cambridge University Press, 2011.

[7] K. Greisen. "End to the Cosmic-Ray Spectrum?" In: *Phys. Rev. Lett.* 16 (17 1966), pp. 748–750. DOI: 10.1103/PhysRevLett.16.748.

[8] G. T. Zatsepin and V. A. Kuz'min. "Upper Limit of the Spectrum of Cosmic Rays". In: *Soviet Journal of Experimental and Theoretical Physics Letters* 4 (Aug. 1966), p. 78.

[9] J. L. Puget, F. W. Stecker, and J. H. Bredekamp. "Photonuclear interactions of ultrahigh energy cosmic rays and their astrophysical consequences." In: *The Astrophysical Journal* 205 (1976), pp. 638–654. DOI: 10.1086/154321.

[10] F. W. Stecker and M. H. Salamon. "Photodisintegration of Ultra-High-Energy Cosmic Rays: A New Determination". In: *The Astrophysical Journal* 512.2 (1999), p. 521. DOI: 10.1086/306816.

[11] E. Khan et al. "Photodisintegration of ultra-high-energy cosmic rays revisited". In: *Astroparticle Physics* 23.2 (2005), pp. 191–201. ISSN: 0927-6505. DOI: https://doi.org/10.1016/j.astropartphys.2004.12.007.

[12] A. Aab et al. "Depth of maximum of air-shower profiles at the Pierre Auger Observatory. I. Measurements at energies above $10^{17.8}$ eV". In: *Physical Review D* 90.12 (Dec. 2014). ISSN: 1550-2368. DOI: 10.1103/physrevd.90.122005.

[13] A. Aab et al. "Features of the Energy Spectrum of Cosmic Rays above $2.5 \times 10^{18}$ eV Using the Pierre Auger Observatory". In: *Physical Review Letters* 125.12 (Sept. 2020). ISSN: 1079-7114. DOI: 10.1103/physrevlett.125.121106.

[14] J. Matthews. "A Heitler model of extensive air showers". In: *Astroparticle Physics* 22.5 (2005), pp. 387–397. ISSN: 0927-6505. DOI: https://doi.org/10.1016/j.astropartphys.2004.09.003.

[15] R. Engel. “Indirect Detection of Cosmic Rays”. In: *Handbook of Particle Detection and Imaging*. Ed. by Claus Grupen and Irène Buvat. Berlin, Heidelberg: Springer Berlin Heidelberg, 2012, pp. 593–632. ISBN: 978-3-642-13271-1. DOI: 10.1007/978-3-642-13271-1_24.

[16] T. Pierog. “Hadronic Interactions and Air Showers: Where Do We Stand?” In: *EPJ Web Conf.* 208 (2019), p. 02002. DOI: 10.1051/epjconf/201920802002.

[17] P. Sommers. “Extensive air showers and measurement techniques”. In: *Comptes Rendus Physique* 5.4 (2004). Ultimate energy particles in the Universe, pp. 463–472. ISSN: 1631-0705. DOI: https://doi.org/10.1016/j.crhy.2004.03.009.

[18] A. Watson. *The future's bright for the Pierre Auger Observatory*. [Online; accessed 7-February-2024]. 2006. URL: https://cerncourier.com/a/the-futures-bright-for-the-pierre-auger-observatory/.

[19] W. Hofmann. *The H.E.S.S. Telescopes*. [Online; accessed 7-February-2024]. 2012. URL: https://www.mpi-hd.mpg.de/HESS/.

[20] H. Kawai et al. “Telescope Array Experiment”. In: *Nuclear Physics B - Proceedings Supplements* 175-176 (2008). Proceedings of the XIV International Symposium on Very High Energy Cosmic Ray Interactions, pp. 221–226. ISSN: 0920-5632. DOI: https://doi.org/10.1016/j.nuclphysbps.2007.11.002.

[21] T. Antoni et al. “The cosmic-ray experiment KASCADE”. In: *Nuclear Instruments and Methods in Physics Research Section A: Accelerators, Spectrometers, Detectors and Associated Equipment* 513.3 (2003), pp. 490–510. ISSN: 0168-9002. DOI: https://doi.org/10.1016/S0168-9002(03)02076-X.

[22] The Pierre Auger Collaboration. “The Pierre Auger Cosmic Ray Observatory”. In: *Nuclear Instruments and Methods in Physics Research Section A: Accelerators, Spectrometers, Detectors and Associated Equipment* 798 (2015), pp. 172–213. ISSN: 0168-9002. DOI: https://doi.org/10.1016/j.nima.2015.06.058.

[23] P. A. Cherenkov. “Visible Radiation Produced by Electrons Moving in a Medium with Velocities Exceeding that of Light”. In: *Phys. Rev.* 52 (4 1937), pp. 378–379. DOI: 10.1103/PhysRev.52.378.

[24] J.A Hinton. “The status of the HESS project”. In: *New Astronomy Reviews* 48.5–6 (Apr. 2004), 331–337. ISSN: 1387-6473. DOI: 10.1016/j.newar.2003.12.004.

[25] D. V. Chernov et al. “The Tunka Experiment: Towards a 1-km2 Cherenkov EAS Array in the Tunka Valley”. In: *International Journal of Modern Physics A* 20.29 (Nov. 2005), 6796–6798. ISSN: 1793-656X. DOI: 10.1142/s0217751x05030119.

[26] H.M.J. Barbosa et al. “Determination of the calorimetric energy in extensive air showers”. In: *Astroparticle Physics* 22.2 (Nov. 2004), 159–166. ISSN: 0927-6505. DOI: 10.1016/j.astropartphys.2004.06.007.

[27] G. A. Askaryan. “Excess Negative Charge of an Electron-Photon Shower and Its Coherent Radio Emission”. In: *Soviet Physics JETP-USSR* 14 (1962), pp. 441–443.

[28] F. D. Kahn and I. Lerche. “Radiation from cosmic ray air showers”. In: *Proc. R. Soc. Lond. A* 289 (1966), 206–213.

[29] J. Jelley, J. Fruin, N Porter, et al. “Radio Pulses from Extensive Cosmic-Ray Air Showers”. In: *Nature* 205 (1965), 327–328.

[30] F. G. Schröder. "Radio detection of cosmic-ray air showers and high-energy neutrinos". In: *Progress in Particle and Nuclear Physics* 93 (2017), pp. 1–68. ISSN: 0146-6410. DOI: https://doi.org/10.1016/j.ppnp.2016.12.002.

[31] H. Falcke et al. "Detection and imaging of atmospheric radio flashes from cosmic ray air showers". In: *Nature* 435.7040 (May 2005), 313–316. ISSN: 1476-4687. DOI: 10.1038/nature03614.

[32] D. Ardouin et al. "Radio-detection signature of high-energy cosmic rays by the CODALEMA experiment". In: *Nuclear Instruments and Methods in Physics Research Section A: Accelerators, Spectrometers, Detectors and Associated Equipment* 555.1–2 (Dec. 2005), 148–163. ISSN: 0168-9002. DOI: 10.1016/j.nima.2005.08.096.

[33] B. Zimmermann. "Cosmic ray physics with the Auger Engineering Radio Array (AERA)". In: *Nuclear and Particle Physics Proceedings* 291-293 (2017), pp. 90–95. DOI: https://doi.org/10.1016/j.nuclphysbps.2017.06.018.

[34] M. P. van Haarlem et al. "LOFAR: The LOw-Frequency ARray". In: *Astronomy and Astrophysics* 556 (2013), A2. DOI: 10.1051/0004-6361/201220873.

[35] S. Lafebre et al. "Universality of electron–positron distributions in extensive air showers". In: *Astroparticle Physics* 31.3 (Apr. 2009), 243–254. ISSN: 0927-6505. DOI: 10.1016/j.astropartphys.2009.02.002.

[36] K. D. de Vries et al. "The lateral distribution function of coherent radio emission from extensive air showers: Determining the chemical composition of cosmic rays". In: *Astroparticle Physics* 34.5 (Dec. 2010), 267–273. ISSN: 0927-6505. DOI: 10.1016/j.astropartphys.2010.08.003.

[37] O. Scholten, K. D. de Vries, and K. Werner. "Coherent radiation from extensive air showers". In: *Nuclear Instruments and Methods in Physics Research Section A: Accelerators, Spectrometers, Detectors and Associated Equipment* 662 (2012). 4th International workshop on Acoustic and Radio EeV Neutrino detection Activities, S80–S84. ISSN: 0168-9002. DOI: https://doi.org/10.1016/j.nima.2010.11.125.

[38] K. D. de Vries et al. "Coherent Cherenkov Radiation from Cosmic-Ray-Induced Air Showers". In: *Physical Review Letters* 107.6 (Aug. 2011). ISSN: 1079-7114. DOI: 10.1103/physrevlett.107.061101.

[39] F. G. Schröder. "Status of the radio technique for cosmic-ray induced air showers". In: *Nuclear and Particle Physics Proceedings* 279-281 (2016). Proceedings of the 9th Cosmic Ray International Seminar, pp. 190–197. ISSN: 2405-6014. DOI: https://doi.org/10.1016/j.nuclphysbps.2016.10.027.

[40] D. Ardouin et al. "Geomagnetic origin of the radio emission from cosmic ray induced air showers observed by CODALEMA". In: *Astroparticle Physics* 31.3 (2009), pp. 192–200. ISSN: 0927-6505. DOI: https://doi.org/10.1016/j.astropartphys.2009.01.001. URL: https://www.sciencedirect.com/science/article/pii/S0927650509000140.

[41] K. Werner, K. D. de Vries, and O. Scholten. "A realistic treatment of geomagnetic Cherenkov radiation from cosmic ray air showers". In: *Astroparticle Physics* 37 (Sept. 2012), 5–16. ISSN: 0927-6505. DOI: 10.1016/j.astropartphys.2012.07.007.

[42] S. Chiche et al. "Loss of Coherence and Change in Emission Physics for Radio Emission from Very Inclined Cosmic-Ray Air Showers". In: *Phys. Rev. Lett.* 132 (23 2024), p. 231001. DOI: 10.1103/PhysRevLett.132.231001.

[43] I. M. Frank and I. E. Tamm. "Coherent visible radiation of fast electrons passing through matter". In: *Compt. Rend. Acad. Sci. URSS* 14.3 (1937), pp. 109–114. DOI: 10.3367/UFNr.0093.196710o.0388.

[44] B. Ratcliff and J. Schwiening. "Cherenkov Radiation". In: *Handbook of Particle Detection and Imaging*. Ed. by Ivor Fleck et al. Cham: Springer International Publishing, 2021, pp. 583–608. DOI: 10.1007/978-3-319-93785-4_18.

[45] T. Winchen et al. "Cosmic Ray Physics with the LOFAR Radio Telescope". In: *Journal of Physics: Conference Series* 1181 (Feb. 2019), p. 012020. ISSN: 1742-6596. DOI: 10.1088/1742-6596/1181/1/012020.

[46] A. Nelles et al. "A new way of air shower detection: measuring the properties of cosmic rays with LOFAR". In: *Journal of Physics: Conference Series* 632.1 (2015), p. 012018. DOI: 10.1088/1742-6596/632/1/012018.

[47] C. Glaser. "The Energy Content of Extensive Air Showers in the Radio Frequency Range of 30-80 MHz". In: *PoS* ICRC2015 (2016), p. 364. DOI: 10.22323/1.236.0364.

[48] W. Apel et al. "A comparison of the cosmic-ray energy scales of Tunka-133 and KASCADE-Grande via their radio extensions Tunka-Rex and LOPES". In: *Physics Letters B* 763 (Jan. 2016). DOI: 10.3204/PUBDB-2016-05881.

[49] V.V. Prosin et al. "Primary CR energy spectrum and mass composition by the data of Tunka-133 array". In: *EPJ Web of Conferences* 99 (Jan. 2015), p. 04002. DOI: 10.1051/epjconf/20159904002.

[50] A. Porcelli. "Measurements of the first two moments of the depth of shower maximum over nearly three decades of energy, combining data from". In: *PoS* ICRC2015 (2016), p. 420. DOI: 10.22323/1.236.0420.

[51] F. G. Schröder et al. "LOPES — Recent Results and Open Questions on the Radio Detection of Air Showers". In: *Journal of Physics: Conference Series* 632.1 (2015), p. 012102. DOI: 10.1088/1742-6596/632/1/012102.

[52] S. Buitink et al. "A large light-mass component of cosmic rays at 1017–1017.5 electronvolts from radio observations". In: *Nature* 531.7592 (Mar. 2016), 70–73. ISSN: 1476-4687. DOI: 10.1038/nature16976.

[53] D. Kostunin. "Reconstruction of air-shower parameters with a sparse radio array". PhD thesis. Karlsruher Institut für Technologie (KIT), 2015. DOI: 10.5445/IR/1000053435.

[54] F. Riehn. "Hadronic multiparticle production with Sibyll". 51.03.03; LK 01. PhD thesis. Karlsruher Institut für Technologie (KIT), 2015. DOI: 10.5445/IR/1000052699.

[55] A. Nelles et al. "A parameterization for the radio emission of air showers as predicted by CoREAS simulations and applied to LOFAR measurements". In: *Astroparticle Physics* 60 (Jan. 2015), 13–24. ISSN: 0927-6505. DOI: 10.1016/j.astropartphys.2014.05.001.

[56] S. Buitink et al. "Xmax reconstruction based on radio detection of air showers". In: *PoS* ICRC2015 (2016), p. 369. DOI: 10.22323/1.236.0369.

[57] A. Coleman et al. "Ultra high energy cosmic rays The intersection of the Cosmic and Energy Frontiers". In: *Astroparticle Physics* 149 (July 2023), p. 102819. ISSN: 0927-6505. DOI: 10.1016/j.astropartphys.2023.102819.

[58] J.A. Aguilar et al. "Design and sensitivity of the Radio Neutrino Observatory in Greenland (RNO-G)". In: *Journal of Instrumentation* 16.03 (Mar. 2021), P03025. ISSN: 1748-0221. DOI: 10.1088/1748-0221/16/03/p03025.

[59] IceCube Collaboration. "Evidence for High-Energy Extraterrestrial Neutrinos at the IceCube Detector". In: *Science* 342.6161 (Nov. 2013). ISSN: 1095-9203. DOI: 10.1126/science.1242856.

[60] C. W. Walter. "The Super-Kamiokande Experiment". In: *Neutrino Oscillations*. WORLD SCIENTIFIC, Mar. 2008, 19–43. DOI: 10.1142/9789812771971_0002.

[61] A. Coleiro et al. "Combining neutrino experimental light-curves for pointing to the next galactic core-collapse supernova". In: *The European Physical Journal C* 80.9 (Sept. 2020). ISSN: 1434-6052. DOI: 10.1140/epjc/s10052-020-8407-7.

[62] M. Ackermann et al. "High-energy and ultra-high-energy neutrinos: A Snowmass white paper". In: *Journal of High Energy Astrophysics* 36 (2022), pp. 55–110. ISSN: 2214-4048. DOI: https://doi.org/10.1016/j.jheap.2022.08.001.

[63] C. Spiering. "Neutrino Detectors Under Water and Ice". In: *Particle Physics Reference Library*. Ed. by C. W. Fabjan and H. Schopper. Springer Cham, 2020, pp. 785–822. ISBN: 978-3-030-35318-6. DOI: 10.1007/978-3-030-35318-6.

[64] M. G. Aartsen et al. "Energy reconstruction methods in the IceCube neutrino telescope". In: *Journal of Instrumentation* 9.03 (Mar. 2014), P03009–P03009. ISSN: 1748-0221. DOI: 10.1088/1748-0221/9/03/p03009.

[65] M. Thomson. *Modern Particle Physics*. 1st ed. Cambridge University Press, 2013. ISBN: 978-1-107-03426-6.

[66] J. G Learned and S. Pakvasa. "Detecting $\nu_\tau$ oscillations at PeV energies". In: *Astroparticle Physics* 3.3 (May 1995), 267–274. ISSN: 0927-6505. DOI: 10.1016/0927-6505(94)00043-3.

[67] R. Abbasi et al. "Search for ultrahigh-energy tau neutrinos with IceCube". In: *Phys. Rev. D* 86 (2 2012), p. 022005. DOI: 10.1103/PhysRevD.86.022005.

[68] M. G. Aartsen et al. "Search for astrophysical tau neutrinos in three years of IceCube data". In: *Phys. Rev. D* 93 (2 2016), p. 022001. DOI: 10.1103/PhysRevD.93.022001.

[69] R. Abbasi et al. "Detection of astrophysical tau neutrino candidates in IceCube". In: *The European Physical Journal C* 82.11 (Nov. 2022). ISSN: 1434-6052. DOI: 10.1140/epjc/s10052-022-10795-y.

[70] M. Meier and J. Soedingrekso. "Search for Astrophysical Tau Neutrinos with an Improved Double Pulse Method". In: *PoS* ICRC2019 (2019), p. 960. DOI: 10.22323/1.358.0960.

[71] N. Geisselbrecht. "First measurement of tau appearance with KM3NeT/ORCA6". In: *PoS* ICRC2023 (2023), p. 1107. DOI: 10.22323/1.444.1107.

[72] M. G. Aartsen et al. "Flavor Ratio of Astrophysical Neutrinos above 35 TeV in IceCube". In: *Phys. Rev. Lett.* 114 (17 2015), p. 171102. DOI: 10.1103/PhysRevLett.114.171102.

[73] M.G. Aartsen et al. "The IceCube Neutrino Observatory: instrumentation and online systems". In: *Journal of Instrumentation* 12.03 (Mar. 2017), P03012–P03012. ISSN: 1748-0221. DOI: 10.1088/1748-0221/12/03/p03012.

[74] M. G. Aartsen et al. "Multimessenger observations of a flaring blazar coincident with high-energy neutrino IceCube-170922A". In: *Science* 361.6398 (2018). ISSN: 1095-9203. DOI: 10.1126/science.aat1378.

[75] M. G. Aartsen et al. "Neutrino emission from the direction of the blazar TXS 0506+056 prior to the IceCube-170922A alert". In: *Science* 361.6398 (2018), 147–151. ISSN: 1095-9203. DOI: 10.1126/science.aat2890.

[76] R. Abbasi et al. "Evidence for neutrino emission from the nearby active galaxy NGC 1068". In: *Science* 378.6619 (2022), 538–543. ISSN: 1095-9203. DOI: 10.1126/science.abg3395.

[77] R. Abbasi et al. "Observation of high-energy neutrinos from the Galactic plane". In: *Science* 380.6652 (June 2023), 1338–1343. ISSN: 1095-9203. DOI: 10.1126/science.adc9818.

[78] A. Margiotta. "The KM3NeT deep-sea neutrino telescope". In: *Nuclear Instruments and Methods in Physics Research Section A: Accelerators, Spectrometers, Detectors and Associated Equipment* 766 (Dec. 2014), 83–87. ISSN: 0168-9002. DOI: 10.1016/j.nima.2014.05.090.

[79] Y. Malyshkin. "Baikal-GVD neutrino telescope: Design reference 2022". In: *Nuclear Instruments and Methods in Physics Research Section A: Accelerators, Spectrometers, Detectors and Associated Equipment* 1050 (2023), p. 168117. ISSN: 0168-9002. DOI: https://doi.org/10.1016/j.nima.2023.168117.

[80] R. Lahmann. "Acoustic Detection of Neutrinos: Review and Future Potential". In: *Nuclear and Particle Physics Proceedings* 273-275 (2016). 37th International Conference on High Energy Physics (ICHEP), pp. 406–413. ISSN: 2405-6014. DOI: https://doi.org/10.1016/j.nuclphysbps.2015.09.059.

[81] T. Karg. "Acoustic neutrino detection in ice: Past, present, and future". In: *AIP Conference Proceedings*. AIP, 2013. DOI: 10.1063/1.4807541.

[82] J. Álvarez Muñiz et al. "The Giant Radio Array for Neutrino Detection (GRAND): Science and design". In: *Science China Physics, Mechanics & Astronomy* 63.1 (Aug. 2019). ISSN: 1869-1927. DOI: 10.1007/s11433-018-9385-7.

[83] D. Southall et al. "Design and initial performance of the prototype for the BEACON instrument for detection of ultrahigh energy particles". In: *Nuclear Instruments and Methods in Physics Research Section A: Accelerators, Spectrometers, Detectors and Associated Equipment* 1048 (2023), p. 167889. ISSN: 0168-9002. DOI: https://doi.org/10.1016/j.nima.2022.167889.

[84] C. Deaconu et al. "Measurements and modeling of near-surface radio propagation in glacial ice and implications for neutrino experiments". In: *Physical Review D* 98.4 (Aug. 2018). ISSN: 2470-0029. DOI: 10.1103/physrevd.98.043010.

[85] M.A. Markov and I.M. Zheleznykh. "Large-scale Cherenkov detectors in ocean, atmosphere and ice". In: *Nuclear Instruments and Methods in Physics Research Section A: Accelerators, Spectrometers, Detectors and Associated Equipment* 248.1 (1986), pp. 242–251. ISSN: 0168-9002. DOI: https://doi.org/10.1016/0168-9002(86)90522-X.

[86] F. Halzen, E. Zas, and T. Stanev. "Radiodetection of cosmic neutrinos. A numerical, real time analysis". In: *Physics Letters B* 257.3 (1991), pp. 432–436. ISSN: 0370-2693. DOI: https://doi.org/10.1016/0370-2693(91)91920-Q.

[87] E. Zas, F. Halzen, and T. Stanev. "Electromagnetic pulses from high-energy showers: Implications for neutrino detection". In: *Phys. Rev. D* 45 (1 1992), pp. 362–376. DOI: 10.1103/PhysRevD.45.362.

[88] J. Alvarez-Muñiz and E. Zas. "Cherenkov radio pulses from EeV neutrino interactions: the LPM effect". In: *Physics Letters B* 411.1–2 (Oct. 1997), 218–224. ISSN: 0370-2693. DOI: 10.1016/s0370-2693(97)01009-5.

[89] J. Alvarez-Muñiz and E. Zas. "The LPM effect for EeV hadronic showers in ice: implications for radio detection of neutrinos". In: *Physics Letters B* 434.3–4 (Aug. 1998), 396–406. ISSN: 0370-2693. DOI: 10.1016/s0370-2693(98)00905-8.

[90] C. Allen et al. "Status of the Radio Ice Cherenkov Experiment (RICE)". In: *New Astron. Rev.* 42 (1998), pp. 319–329. DOI: 10.1016/S1387-6473(98)00017-7.

[91] S. W. Barwick et al. "Constraints on Cosmic Neutrino Fluxes from the Antarctic Impulsive Transient Antenna Experiment". In: *Phys. Rev. Lett.* 96 (17 2006), p. 171101. DOI: 10.1103/PhysRevLett.96.171101.

[92] P. Allison et al. "Design and initial performance of the Askaryan Radio Array prototype EeV neutrino detector at the South Pole". In: *Astroparticle Physics* 35.7 (2012), pp. 457–477. ISSN: 0927-6505. DOI: https://doi.org/10.1016/j.astropartphys.2011.11.010.

[93] S. W. Barwick et al. "Design and Performance of the ARIANNA HRA-3 Neutrino Detector Systems". In: *IEEE Transactions on Nuclear Science* 62.5 (2015), pp. 2202–2215. DOI: 10.1109/TNS.2015.2468182.

[94] D. Saltzberg et al. "Observation of the Askaryan Effect: Coherent Microwave Cherenkov Emission from Charge Asymmetry in High-Energy Particle Cascades". In: *Phys. Rev. Lett.* 86 (13 2001), pp. 2802–2805. DOI: 10.1103/PhysRevLett.86.2802.

[95] S. W. Barwick and C. Glaser. "Radio Detection of High Energy Neutrinos in Ice". In: *The Encyclopedia of Cosmology*. WORLD SCIENTIFIC, Oct. 2023, 237–302. ISBN: 9789811282645. DOI: 10.1142/9789811282645_0006.

[96] I. Kravchenko et al. "Updated results from the RICE experiment and future prospects for ultra-high energy neutrino detection at the south pole". In: *Physical Review D* 85.6 (Mar. 2012). ISSN: 1550-2368. DOI: 10.1103/physrevd.85.062004.

[97] P. Allison et al. "Low-threshold ultrahigh-energy neutrino search with the Askaryan Radio Array". In: *Physical Review D* 105.12 (June 2022). ISSN: 2470-0029. DOI: 10.1103/physrevd.105.122006.

[98] P. Allison et al. "Performance of two Askaryan Radio Array stations and first results in the search for ultrahigh energy neutrinos". In: *Physical Review D* 93.8 (Apr. 2016). ISSN: 2470-0029. DOI: 10.1103/physrevd.93.082003.

[99] C. Glaser. "Results from the ARIANNA high-energy neutrino detector". In: *PoS* ARENA2022 (2023), p. 003. DOI: 10.22323/1.424.0003. arXiv: 2304.07179 [astro-ph.IM].

[100] S. Ali et al. *Modeling the refractive index profile n(z) of polar ice for ultra-high energy neutrino experiments*. 2024. arXiv: 2406.00857 [astro-ph.IM].

[101] C. Glaser et al. "NuRadioMC: simulating the radio emission of neutrinos from interaction to detector". In: *The European Physical Journal C* 80.2 (Jan. 2020). ISSN: 1434-6052. DOI: 10.1140/epjc/s10052-020-7612-8.

[102] A. Anker et al. "A search for cosmogenic neutrinos with the ARIANNA test bed using 4.5 years of data". In: *Journal of Cosmology and Astroparticle Physics* 2020.03 (2020), p. 053. DOI: 10.1088/1475-7516/2020/03/053.

[103] V. Decoene. "Review of Neutrino Experiments Searching for Astrophysical Neutrinos". In: *PoS* ICRC2023 (2023), p. 026. DOI: 10.22323/1.444.0026.

[104] Q. Abarr et al. "The Payload for Ultrahigh Energy Observations (PUEO): a white paper". In: *Journal of Instrumentation* 16.08 (Aug. 2021), P08035. ISSN: 1748-0221. DOI: 10.1088/1748-0221/16/08/p08035.

[105] P. Allison et al. *Observation of Reconstructable Radio Emission Coincident with an X-Class Solar Flare in the Askaryan Radio Array Prototype Station*. July 2018. arXiv: 1807.03335 [astro-ph.HE].

[106] S. Agarwal et al. "Solar flare observations with the Radio Neutrino Observatory Greenland (RNO-G)". In: *Astroparticle Physics* (2024), p. 103024. ISSN: 0927-6505. DOI: https://doi.org/10.1016/j.astropartphys.2024.103024.

[107] D. García-Fernández et al. "Measurement of the cosmic ray flux with the ANITA experiment". In: *EPJ Web Conf.* 136 (2017), p. 02014. DOI: 10.1051/epjconf/201713602014. URL: https://doi.org/10.1051/epjconf/201713602014.

[108] A. Anker et al. "Measuring the polarization reconstruction resolution of the ARIANNA neutrino detector with cosmic rays". In: *Journal of Cosmology and Astroparticle Physics* 2022.04 (Apr. 2022), p. 022. ISSN: 1475-7516. DOI: 10.1088/1475-7516/2022/04/022.

[109] P. W. Gorham et al. "Characteristics of Four Upward-Pointing Cosmic-Ray-like Events Observed with ANITA". In: *Phys. Rev. Lett.* 117 (7 2016), p. 071101. DOI: 10.1103/PhysRevLett.117.071101.

[110] P. W. Gorham et al. "Observation of an Unusual Upward-Going Cosmic-Ray-like Event in the Third Flight of ANITA". In: *Phys. Rev. Lett.* 121 (16 2018), p. 161102. DOI: 10.1103/PhysRevLett.121.161102.

[111] P. W. Gorham et al. "Unusual Near-Horizon Cosmic-Ray-like Events Observed by ANITA-IV". In: *Phys. Rev. Lett.* 126 (7 2021), p. 071103. DOI: 10.1103/PhysRevLett.126.071103.

[112] I. Kravchenko et al. "Limits on the ultra-high energy electron neutrino flux from the RICE experiment". In: *Astroparticle Physics* 20.2 (2003), pp. 195–213. ISSN: 0927-6505. DOI: https://doi.org/10.1016/S0927-6505(03)00181-6.

[113] P. Allison et al. "Constraints on the diffuse flux of ultrahigh energy neutrinos from four years of Askaryan Radio Array data in two stations". In: *Phys. Rev. D* 102 (4 2020), p. 043021. DOI: 10.1103/PhysRevD.102.043021.

[114] P.W. Gorham et al. "Constraints on the ultrahigh-energy cosmic neutrino flux from the fourth flight of ANITA". In: *Physical Review D* 99.12 (June 2019). ISSN: 2470-0029. DOI: 10.1103/physrevd.99.122001.

[115] P. W. Gorham et al. "Observational constraints on the ultrahigh energy cosmic neutrino flux from the second flight of the ANITA experiment". In: *Physical Review D* 82.2 (July 2010). ISSN: 1550-2368. DOI: 10.1103/physrevd.82.022004.

[116] A. Anker et al. "Neutrino vertex reconstruction with in-ice radio detectors using surface reflections and implications for the neutrino energy resolution". In: *Journal of Cosmology and Astroparticle Physics* 2019.11 (2019), p. 030. DOI: 10.1088/1475-7516/2019/11/030.

[117] L. D. Landau and I. Pomeranchuk. “Limits of applicability of the theory of bremsstrahlung electrons and pair production at high-energies”. In: *Dokl. Akad. Nauk Ser. Fiz.* 92 (1953), pp. 535–536.

[118] A. B. Migdal. “Bremsstrahlung and Pair Production in Condensed Media at High Energies”. In: *Phys. Rev.* 103 (6 1956), pp. 1811–1820. DOI: 10.1103/PhysRev.103.1811.

[119] J. A. Aguilar et al. “Reconstructing the neutrino energy for in-ice radio detectors: A study for the Radio Neutrino Observatory Greenland (RNO-G)”. In: *The European Physical Journal C* 82.2 (Feb. 2022). ISSN: 1434-6052. DOI: 10.1140/epjc/s10052-022-10034-4.

[120] B. Lovell. “The Blackett-Eckersley-Lovell Correspondence of World War II and the Origin of Jodrell Bank”. In: *Notes and Records of the Royal Society of London* 47.1 (1993), pp. 119–131. ISSN: 00359149.

[121] T. Matano et al. “Tokyo large air shower project”. In: *Canadian Journal of Physics* 46.10 (1968), S255–S258. DOI: 10.1139/p68-222.

[122] T. Terasawa et al. “Search for radio echoes from EAS with the MU radar, Shigaraki, Japan”. In: *Proceedings of the 31st International Cosmic Ray Conference* 2 (2009), p. 932.

[123] R. Abbasi et al. “Telescope Array Radar (TARA) observatory for Ultra-High Energy Cosmic Rays”. In: *Nuclear Instruments and Methods in Physics Research Section A: Accelerators, Spectrometers, Detectors and Associated Equipment* 767 (Dec. 2014), 322–338. ISSN: 0168-9002. DOI: 10.1016/j.nima.2014.08.015.

[124] R.U. Abbasi et al. “First upper limits on the radar cross section of cosmic-ray induced extensive air showers”. In: *Astroparticle Physics* 87 (Jan. 2017), 1–17. ISSN: 0927-6505. DOI: 10.1016/j.astropartphys.2016.11.006.

[125] J. Stasielak et al. “Feasibility of radar detection of extensive air showers”. In: *Astroparticle Physics* 73 (2016), pp. 14–27. ISSN: 0927-6505. DOI: https://doi.org/10.1016/j.astropartphys.2015.07.003.

[126] M.I. Bakunov et al. “Relativistic effects in radar detection of ionization fronts produced by ultra-high energy cosmic rays”. In: *Astroparticle Physics* 33.5 (2010), pp. 335–340. ISSN: 0927-6505. DOI: https://doi.org/10.1016/j.astropartphys.2010.03.005.

[127] K. D. de Vries, K. Hanson, and T. Meures. “On the feasibility of RADAR detection of high-energy neutrino-induced showers in ice”. In: *Astroparticle Physics* 60 (Jan. 2015), 25–31. ISSN: 0927-6505. DOI: 10.1016/j.astropartphys.2014.05.009.

[128] S. Prohira and D. Besson. “Particle-level model for radar based detection of high-energy neutrino cascades”. In: *Nuclear Instruments and Methods in Physics Research Section A: Accelerators, Spectrometers, Detectors and Associated Equipment* 922 (2019), pp. 161–170. ISSN: 0168-9002. DOI: https://doi.org/10.1016/j.nima.2018.12.027.

[129] E. Huesca Santiago et al. “Macroscopic approach to the radar echo scatter from high-energy particle cascades”. In: *Phys. Rev. D* 109 (8 2024), p. 083012. DOI: 10.1103/PhysRevD.109.083012.

[130] E. Huesca Santiago. "Understanding Radar Echoes from High-Energy Particle Cascades". PhD thesis. Vrije Universiteit Brussel, 2024. URL: https://researchportal.vub.be/en/publications/understanding-radar-echoes-from-high-energy-particle-cascades-a-m.

[131] S. Prohira et al. "Observation of Radar Echoes from High-Energy Particle Cascades". In: *Physical Review Letters* 124.9 (Mar. 2020). ISSN: 1079-7114. DOI: 10.1103/physrevlett.124.091101.

[132] D. Frikken. "The Radar Echo Telescope for Neutrinos: Contribution to ICRC 2023". In: *PoS* ICRC2023 (2023), p. 1135. DOI: 10.22323/1.444.1135.

[133] S. Prohira et al. "The Radar Echo Telescope for Cosmic Rays: Pathfinder experiment for a next-generation neutrino observatory". In: *Phys. Rev. D* 104 (10 2021), p. 102006. DOI: 10.1103/PhysRevD.104.102006.

[134] S. Kunwar et al. "Design, construction and operation of a low-power, autonomous radio-frequency data-acquisition station for the TARA experiment". In: *Nuclear Instruments and Methods in Physics Research Section A: Accelerators, Spectrometers, Detectors and Associated Equipment* 797 (2015), pp. 110–120. ISSN: 0168-9002. DOI: https://doi.org/10.1016/j.nima.2015.05.072.

[135] S. Prohira et al. "Implementation of a custom time-domain firmware trigger for RADAR-based cosmic ray detection". In: *Nuclear Instruments and Methods in Physics Research Section A: Accelerators, Spectrometers, Detectors and Associated Equipment* 890 (2018), pp. 126–132. ISSN: 0168-9002. DOI: https://doi.org/10.1016/j.nima.2018.02.051.

[136] D. García-Fernández, A. Nelles, and C. Glaser. "Signatures of secondary leptons in radio-neutrino detectors in ice". In: *Phys. Rev. D* 102 (8 2020), p. 083011. DOI: 10.1103/PhysRevD.102.083011.

[137] *GEOsummit*. [Online; accessed 17-April-2024]. URL: https://geo-summit.org/.

[138] P. Allison et al. "Design and performance of an interferometric trigger array for radio detection of high-energy neutrinos". In: *Nuclear Instruments and Methods in Physics Research Section A: Accelerators, Spectrometers, Detectors and Associated Equipment* 930 (June 2019), 112–125. ISSN: 0168-9002. DOI: 10.1016/j.nima.2019.01.067.

[139] A. Nelles. "A wind-turbine for autonomous stations for radio detection of neutrinos". In: *PoS* ICRC2019 (2019), p. 968. DOI: 10.22323/1.358.0968.

[140] D. J. Bacon et al. "Cosmology with Phase 1 of the Square Kilometre Array Red Book 2018: Technical specifications and performance forecasts". In: *Publications of the Astronomical Society of Australia* 37 (2020). ISSN: 1448-6083. DOI: 10.1017/pasa.2019.51.

[141] E. Zas, F. Halzen, and T. Stanev. "Electromagnetic pulses from high-energy showers: Implications for neutrino detection". In: *Phys. Rev. D* 45 (1 1992), pp. 362–376. DOI: 10.1103/PhysRevD.45.362.

[142] S. Razzaque et al. "Coherent radio pulses from GEANT generated electromagnetic showers in ice". In: *Physical Review D* 65.10 (May 2002). ISSN: 1089-4918. DOI: 10.1103/physrevd.65.103002.

[143] S. Razzaque et al. "Addendum to "Coherent radio pulses from GEANT generated electromagnetic showers in ice"". In: *Physical Review D* 69.4 (Feb. 2004). ISSN: 1550-2368. DOI: 10.1103/physrevd.69.047101.

[144] S. Bevan et al. “Simulation of ultra high energy neutrino induced showers in ice and water”. In: *Astroparticle Physics* 28.3 (2007), pp. 366–379. ISSN: 0927-6505. DOI: https://doi.org/10.1016/j.astropartphys.2007.08.001.

[145] D. Seckel et al. “In-Ice radio detection of air shower cores”. In: *Proc. 30th ICRC, Ciudad de Mexico: Universidad Nacional Autonoma de Mexico, Merida (Mexico)* 5 (2008), pp. 1029–1032.

[146] M. Tueros and S. Sciutto. “TIERRAS: A package to simulate high energy cosmic ray showers underground, underwater and under-ice”. In: *Computer Physics Communications* 181 (2010), pp. 380–392.

[147] J. Alvarez-Muñiz et al. “Coherent Cherenkov radio pulses from hadronic showers up to EeV energies”. In: *Astroparticle Physics* 35.6 (2012), pp. 287–299. ISSN: 0927-6505. DOI: https://doi.org/10.1016/j.astropartphys.2011.10.002.

[148] A. Javaid. “Monte Carlo simulation for radio detection of Ultra High Energy air shower cores by ANITA-II”. PhD thesis. University of Delaware, Jan. 2012. URL: https://ui.adsabs.harvard.edu/abs/2012PhDT.......59J.

[149] A. Saftoiu et al. “Studies of radio emission from neutrino induced showers generated in rock salt”. In: *Astroparticle Physics* 46 (2013), pp. 1–13. ISSN: 0927-6505. DOI: https://doi.org/10.1016/j.astropartphys.2013.04.002.

[150] K. D. de Vries et al. “The cosmic-ray air-shower signal in Askaryan radio detectors”. In: *Astroparticle Physics* 74 (Feb. 2016), 96–104. ISSN: 0927-6505. DOI: 10.1016/j.astropartphys.2015.10.003.

[151] D. Heck et al. “CORSIKA: A Monte Carlo code to simulate extensive air showers”. In: *FZKA* 6019 (1998). URL: https://publikationen.bibliothek.kit.edu/270043064/3813660.

[152] S. J. Sciutto. *AIRES A system for air shower simulations. User's guide and reference manual*. National University of La Plata, 2019. DOI: 10.13140/RG.2.2.12566.40002.

[153] F. Bloch and A. Nordsieck. “Note on the Radiation Field of the Electron”. In: *Phys. Rev.* 52 (2 1937), pp. 54–59. DOI: 10.1103/PhysRev.52.54.

[154] D. R. Yennie, S. C. Frautschi, and H. Suura. “The infrared divergence phenomena and high-energy processes”. In: *Annals of Physics* 13.3 (1961), pp. 379–452. ISSN: 0003-4916. DOI: https://doi.org/10.1016/0003-4916(61)90151-8.

[155] D. Heck and J. Knapp. *Upgrade of the Monte Carlo Code CORSIKA to simulate extensive air showers with energie* $> 10^{20}$ *eV*. Tech. rep. 51.02.03; LK 01; Wissenschaftliche Berichte FZKA-6097 (Juli 98). 1998. DOI: 10.5445/IR/270043705.

[156] M. Kobal. “A thinning method using weight limitation for air-shower simulations”. In: *Astroparticle Physics* 15.3 (2001), pp. 259–273. ISSN: 0927-6505. DOI: https://doi.org/10.1016/S0927-6505(00)00158-4.

[157] S. Ostapchenko. “Monte Carlo treatment of hadronic interactions in enhanced Pomeron scheme: QGSJET-II model”. In: *Phys. Rev. D* 83 (1 2011), p. 014018. DOI: 10.1103/PhysRevD.83.014018.

[158] H. Fesefeldt. *The Simulation of Hadronic Showers: Physics and Applications*. Tech. rep. PITHA-85-02. Dec. 1985.

[159] A. E. Hedin. "Extension of the MSIS Thermosphere Model into the middle and lower atmosphere". In: *Journal of Geophysical Research: Space Physics* 96.A2 (1991), pp. 1159–1172. DOI: https://doi.org/10.1029/90JA02125.

[160] The Pierre Auger Collaboration. *The Pierre Auger Observatory Upgrade - Preliminary Design Report*. 2016. arXiv: 1604.03637.

[161] F. Schmidt et al. "A model-independent method of determining energy scale and muon number in cosmic ray surface detectors". In: *Astroparticle Physics* 29.6 (July 2008), 355–365. ISSN: 0927-6505. DOI: 10.1016/j.astropartphys.2008.03.004.

[162] M. J. Berger et al. *ESTAR, PSTAR, and ASTAR: Computer Programs for Calculating Stopping-Power and Range Tables for Electrons, Protons, and Helium Ions*. [Version 2.0.1; Online; accessed on 18-June-2024]. National Institute of Standards and Technology, Gaithersburg, MD, 2017. URL: http://physics.nist.gov/Star.

[163] L. Gerhardt and S. R. Klein. "Electron and photon interactions in the regime of strong Landau-Pomeranchuk-Migdal suppression". In: *Physical Review D* 82.7 (Oct. 2010). ISSN: 1550-2368. DOI: 10.1103/physrevd.82.074017.

[164] J. Allison *et al*. "Recent developments in Geant4". In: *Nucl. Instrum. Methods Phys. Res., Sect. A* 835 (2016), pp. 186–225. ISSN: 0168-9002. DOI: https://doi.org/10.1016/j.nima.2016.06.125.

[165] J. J. Fitzpatrick. "Preliminary report on the physical and stratigraphic properties of the Taylor Dome ice core". In: *Antarctic Journal of the U.S.* 29.5 (1994), pp. 84–86.

[166] D.Z. Besson et al. "In situ radioglaciological measurements near Taylor Dome, Antarctica and implications for ultra-high energy (UHE) neutrino astronomy". In: *Astroparticle Physics* 29.2 (Mar. 2008), 130–157. ISSN: 0927-6505. DOI: 10.1016/j.astropartphys.2007.12.004.

[167] Geant4 Collaboration. *Electromagnetic physics constructors - EM Opt0*. [Online; accessed 19-June-2024]. URL: https://geant4-userdoc.web.cern.ch/UsersGuides/PhysicsListGuide/html/electromagnetic/Opt0.html#em-opt0.

[168] Geant4 Collaboration. *Physics Reference Manual*. [Online; accessed 19-June-2024]. URL: https://geant4-userdoc.web.cern.ch/UsersGuides/PhysicsReferenceManual/html/index.html.

[169] J. Alvarez-Muñiz et al. "Coherent radio pulses from showers in different media: A unified parametrization". In: *Physical Review D* 74.2 (July 2006). ISSN: 1550-2368. DOI: 10.1103/physrevd.74.023007.

[170] The Pierre Auger Collaboration. "Atmospheric effects on extensive air showers observed with the surface detector of the Pierre Auger observatory". In: *Astroparticle Physics* 32.2 (2009), pp. 89–99. ISSN: 0927-6505. DOI: https://doi.org/10.1016/j.astropartphys.2009.06.004.

[171] T.K. Gaisser and A.M. Hillas. "Reliability of the Method of Constant Intensity Cuts for Reconstructing the Average Development of Vertical Showers". In: *Proc. 15th ICRC, Bulgarian academy of sciences, Plovdiv (Bulgaria)* 8 (1977), p. 353.

[172] J. Alameddine et al. "The particle-shower simulation code CORSIKA 8". In: *PoS* ICRC2023 (2023), p. 310. DOI: 10.22323/1.444.0310. arXiv: 2308.05475 [astro-ph.HE].

[173] J. Alameddine et al. “Simulations of cross media showers with CORSIKA 8”. In: *PoS* ICRC2023 (2023), p. 442. DOI: 10.22323/1.444.0442. arXiv: 2309.05897 [astro-ph.IM].

[174] J. C. Hanson and R. Hartig. “Complex analysis of Askaryan radiation: A fully analytic model in the time domain”. In: *Physical Review D* 105.12 (June 2022). ISSN: 2470-0029. DOI: 10.1103/physrevd.105.123019.

[175] T. Huege, M. Ludwig, and C. W. James. “Simulating radio emission from air showers with CoREAS”. In: *AIP Conference Proceedings*. Melville (New York): AIP Publishing, 2013. DOI: 10.1063/1.4807534.

[176] A. Zilles. “Emission of Radio Waves in Particle Showers: Validation of microscopic simulations with the SLAC T-510 experiment and their potential in the future Square Kilometer Array”. PhD thesis. Karlsruher Institute of Technology, 2017. URL: https://link.springer.com/book/10.1007/978-3-319-63411-1.

[177] K. Bechtol et al. “SLAC T-510 experiment for radio emission from particle showers: Detailed simulation study and interpretation”. In: *Phys. Rev. D* 105 (6 2022), p. 063025. DOI: 10.1103/PhysRevD.105.063025.

[178] U. A. Latif. “Towards measurement of UHECR with the ARA experiment”. PhD thesis. University of Kansas, 2020. URL: https://kuscholarworks.ku.edu/handle/1808/34559.

[179] U. A. Latif et al. “Propagating air shower radio signals to in-ice antennas”. In: *PoS* ARENA2022 (2023), p. 016. DOI: 10.22323/1.424.0016.

[180] J. W. Clancy et al. “General description of electromagnetic radiation processes based on instantaneous charge acceleration in “endpoints””. In: *Physical Review E* 84.5 (Nov. 2011). ISSN: 1550-2376. DOI: 10.1103/physreve.84.056602.

[181] C. W. James. “Electromagnetic radiation in the Tamm problem”. In: *AIP Conference Proceedings*. AIP, 2013. DOI: 10.1063/1.4807539.

[182] K. Belov. “Radio emission from air showers. Comparison of theoretical approaches”. In: *AIP Conference Proceedings*. AIP, 2013. DOI: 10.1063/1.4807540.

[183] M. Ludwig et al. “Comparison of LOPES measurements with CoREAS and REAS 3.11 simulations”. In: *AIP Conference Proceedings*. AIP, 2013. DOI: 10.1063/1.4807526.

[184] V. L. Ginzburg and I. M. Frank. “Radiation of a uniformly moving electron due to its transition from one medium into another”. In: *J. Phys. (USSR)* 9 (1945), pp. 353–362.

[185] S.W. Barwick et al. “Observation of classically ‘forbidden’ electromagnetic wave propagation and implications for neutrino detection.” In: *Journal of Cosmology and Astroparticle Physics* 2018.07 (July 2018), 055–055. ISSN: 1475-7516. DOI: 10.1088/1475-7516/2018/07/055.

[186] P. Allison et al. “Long-baseline horizontal radio-frequency transmission through polar ice”. In: *Journal of Cosmology and Astroparticle Physics* 2020.12 (Dec. 2020), 009–009. ISSN: 1475-7516. DOI: 10.1088/1475-7516/2020/12/009.

[187] S. Prohira et al. “Modeling in-ice radio propagation with parabolic equation methods”. In: *Physical Review D* 103.10 (May 2021). ISSN: 2470-0029. DOI: 10.1103/physrevd.103.103007.

[188] J. M. Thijssen. *Computational Physics*. Cambridge University Press, 1999.

[189] T. Winchen. "RadioPropa — A Modular Raytracer for In-Matter Radio Propagation". In: *EPJ Web of Conferences* 216 (2019). Ed. by G. Riccobene et al., p. 03002. ISSN: 2100-014X. DOI: 10.1051/epjconf/201921603002.

[190] F. Schlüter et al. "Refractive displacement of the radio-emission footprint of inclined air showers simulated with CoREAS". In: *The European Physical Journal C* 80.7 (July 2020). ISSN: 1434-6052. DOI: 10.1140/epjc/s10052-020-8216-z.

[191] D. Van den Broeck et al. "Radio propagation in non-uniform media". In: *PoS* ARENA2022 (2023), p. 020. DOI: 10.22323/1.424.0020.

[192] E. Hecht. *Optics*. Fourth edition. Addison-Wesley, 2002.

[193] N. G. Lehtinen et al. "FORTE satellite constraints on ultrahigh energy cosmic particle fluxes". In: *Phys. Rev. D* 69 (1 2004), p. 013008. DOI: 10.1103/PhysRevD.69.013008.

[194] U. A. Latif. *IceRayTracing*. https://github.com/uzairlatif90/IceRayTracing. Version 1.0.0. [Online; accessed 19-July-2024]. 2023.

[195] E. Kovács. "Rotation about an arbitrary axis and reflection through an arbitrary plane". In: *Annales Mathematicae et Informaticae* 40 (Jan. 2012), pp. 175–186.

[196] I. R. Cole. "Modelling CPV". PhD thesis. Loughborough University, 2015. URL: https://repository.lboro.ac.uk/articles/thesis/Modelling_CPV/9523520.

[197] Wikipedia. *Rotation matrix — Wikipedia, The Free Encyclopedia*. http://en.wikipedia.org/w/index.php?title=Rotation%20matrix&oldid=1223594989. [Online; accessed 17-July-2024].

[198] Wikipedia. *Rodrigues' rotation formula — Wikipedia, The Free Encyclopedia*. http://en.wikipedia.org/w/index.php?title=Rodrigues'%20rotation%20formula&oldid=1224740055. [Online; accessed 17-July-2024].

[199] U. A. Latif et al. "Simulation of radio signals from cosmic-ray cascades in air and ice as observed by in-ice Askaryan radio detectors". In: *PoS* ICRC2023 (2023), p. 346. DOI: 10.22323/1.444.0346.

[200] I. Kravchenko, D. Besson, and J. Meyers. "In situ index-of-refraction measurements of the South Polar firn with the RICE detector". In: *Journal of Glaciology* 50.171 (2004), 522–532. DOI: 10.3189/172756504781829800.

[201] J. Kelley et al. "Observation of two deep, distant (1.4, 4)km impulsive RF transmitters by the Askaryan Radio Array (ARA)." In: *PoS* ICRC2017 (2017), p. 1030. DOI: 10.22323/1.301.1030.

[202] S Bass. "Microscopic models for ultrarelativistic heavy ion collisions". In: *Progress in Particle and Nuclear Physics* 41 (1998), 255–369. ISSN: 0146-6410. DOI: 10.1016/s0146-6410(98)00058-1.

[203] M. Bleicher et al. "Relativistic hadron-hadron collisions in the ultra-relativistic quantum molecular dynamics model". In: *J. Phys. G: Nucl. Part. Phys.* 25.9 (1999), p. 1859. DOI: 10.1088/0954-3899/25/9/308.

[204] National Centers for Environmental Information (NCEI). *Geomagnetic Calculators*. https://www.ngdc.noaa.gov/geomag/calculators/magcalc.shtml#igrfwmm. [Online; accessed 19-July-2024].

[205] A. Corstanje et al. "A high-precision interpolation method for pulsed radio signals from cosmic-ray air showers". In: *Journal of Instrumentation* 18.09 (2023), P09005. DOI: 10.1088/1748-0221/18/09/P09005.

[206] N. Moller. "Simulating cosmic–ray air shower radio emission for the Askaryan Radio Array". MA thesis. Université Libre de Bruxelles, 2024.

[207] J. A. Aguilar et al. "Radiofrequency ice dielectric measurements at Summit Station, Greenland". In: *Journal of Glaciology* (2023), 1–12. DOI: 10.1017/jog.2023.72.

[208] D.Z. Besson et al. "In situ radioglaciological measurements near Taylor Dome, Antarctica and implications for ultra-high energy (UHE) neutrino astronomy". In: *Astroparticle Physics* 29.2 (2008), pp. 130–157. ISSN: 0927-6505. DOI: https://doi.org/10.1016/j.astropartphys.2007.12.004.

[209] I. Kravchenko et al. "Radio frequency birefringence in south polar ice and implications for neutrino reconstruction". In: *Astroparticle Physics* 34.10 (2011), pp. 755–768. ISSN: 0927-6505. DOI: https://doi.org/10.1016/j.astropartphys.2011.01.008.

[210] T. M. Jordan et al. "Modeling ice birefringence and oblique radio wave propagation for neutrino detection at the South Pole". In: *Annals of Glaciology* 61.81 (Apr. 2020), 84–91. ISSN: 1727-5644. DOI: 10.1017/aog.2020.18.

[211] J. A. Aguilar et al. "In situ, broadband measurement of the radio frequency attenuation length at Summit Station, Greenland". In: *Journal of Glaciology* 68.272 (May 2022), 1234–1242. ISSN: 1727-5652. DOI: 10.1017/jog.2022.40. URL: http://dx.doi.org/10.1017/jog.2022.40.

[212] N. Heyer and C. Glaser. "First-principle calculation of birefringence effects for in-ice radio detection of neutrinos". In: *The European Physical Journal C* 83.2 (Feb. 2023). ISSN: 1434-6052. DOI: 10.1140/epjc/s10052-023-11238-y.

[213] S. Barwick et al. "South Polar in situ radio-frequency ice attenuation". In: *Journal of Glaciology* 51.173 (2005), 231–238. DOI: 10.3189/172756505781829467.

[214] J. Avva et al. "An in situ measurement of the radio-frequency attenuation in ice at Summit Station, Greenland". In: *Journal of Glaciology* 61.229 (2015), 1005–1011. DOI: 10.3189/2015JoG15J057.

[215] J. Alvarez-Muñiz, R. A. Vázquez, and E. Zas. "Calculation methods for radio pulses from high energy showers". In: *Phys. Rev. D* 62 (6 2000), p. 063001. DOI: 10.1103/PhysRevD.62.063001.

[216] R. V. Buniy and J. P. Ralston. "Radio detection of high energy particles: Coherence versus multiple scales". In: *Phys. Rev. D* 65 (1 2001), p. 016003. DOI: 10.1103/PhysRevD.65.016003.

[217] J. Alvarez-Muñiz et al. "Thinned simulations of extremely energetic showers in dense media for radio applications". In: *Astroparticle Physics* 32.2 (2009), pp. 100–111. ISSN: 0927-6505. DOI: https://doi.org/10.1016/j.astropartphys.2009.06.005.

[218] J. Alvarez-Muñiz, A. Romero-Wolf, and E. Zas. "Čerenkov radio pulses from electromagnetic showers in the time domain". In: *Phys. Rev. D* 81 (12 2010), p. 123009. DOI: 10.1103/PhysRevD.81.123009.

[219] J. C. Hanson and A. L. Connolly. "Complex analysis of Askaryan radiation: A fully analytic treatment including the LPM effect and Cascade Form Factor". In: *Astroparticle Physics* 91 (2017), pp. 75–89. ISSN: 0927-6505. DOI: https://doi.org/10.1016/j.astropartphys.2017.03.008.

[220] P. Windischhofer, C. Welling, and C. Deaconu. "Eisvogel: Exact and efficient calculations of radio emissions from in-ice neutrino showers". In: *PoS* ICRC2023 (2023), p. 1157. DOI: 10.22323/1.444.1157.

[221] S. De Kockere et al. *The Radar Echo Telescope: Simulation and Optimization*. Neutrino (virtual). 2020.

[222] S. De Kockere, K. D. de Vries, and N. van Eijndhoven. "Simulation of the propagation of CR air shower cores in ice". In: *Proceedings of 37th International Cosmic Ray Conference — PoS(ICRC2021)*. ICRC2021. Sissa Medialab, July 2021. DOI: 10.22323/1.395.1032.

[223] S. De Kockere. *Simulation of the propagation of cosmic ray air shower cores in ice*. Neutrinos in the Multi-Messenger Era. 2022.

[224] S. De Kockere et al. "Simulation of the propagation of cosmic ray air showers in ice". In: *PoS* ARENA2022 (2023), p. 015. DOI: 10.22323/1.424.0015.

[225] S. De Kockere. *Simulation of the propagation of cosmic ray air shower cores in ice*. CORSIKA 8 Air-Shower Simulation and Development Workshop. 2022.

[226] S. De Kockere. *Simulation of the propagation of cosmic ray air shower cores in ice*. 22nd International School of Cosmic Ray Astrophysics. 2022.

[227] S. De Kockere. *Simulation of radio signals from cosmic-ray cascades in air and ice as observed by in-ice Askaryan radio detectors*. Belgian Neutrino Meeting. 2024.

[228] D. H. Hiel. "Investigation of the Polarisation of the Signals in the Askaryan Radio Array". BA thesis. Vrije Universiteit Brussel, 2021.

[229] D. Heck and T. Pierog. *Extensive Air Shower Simulation with CORSIKA: A User's Guide*. Version 7.7500. Karlsruher Institut für Technologie (KIT). 2024. URL: https://www.iap.kit.edu/corsika/70.php.